Spin dynamics calculations applied to systems of potential biological significance

Thomas Christopher Player

Keble College
University of Oxford

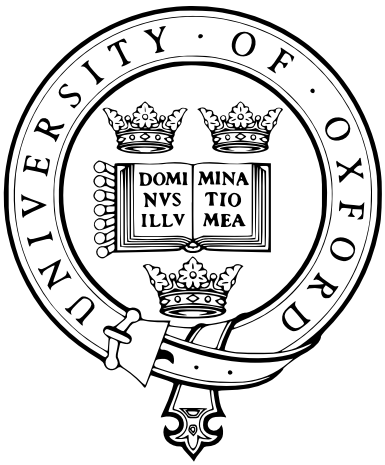

A thesis submitted in partial fulfilment
of the requirements for the degree of

Doctor of Philosophy

in

Physical and Theoretical Chemistry

Physical and Theoretical Chemistry Laboratory

Hilary Term 2021

Spin dynamics calculations applied to systems of potential biological significance

Thomas Christopher Player

Abstract

of a thesis submitted for the degree of

Doctor of Philosophy

Magnetic fields interact with biological systems, often in unexplored and surprising ways. In this thesis I develop and employ a range of quantum mechanical spin dynamics tools for simulating these magnetic spin interactions, modelling a diverse set of systems of potential biological relevance.

Nuclear spins in calcium phosphates known as Posner molecules form the basis of a proposed mechanism for human neural processing. This theory requires that phosphorus nuclei in different Posner molecules become entangled and remain so for periods far longer than typical nuclear spin relaxation times. In Chapter 3 I model the coherent and relaxation spin dynamics of this molecule, deriving a strict upper bound on the entanglement lifetime and arguing that other relaxation effects will further limit this lifetime.

Spin relaxation is also relevant to studies into the chemical compass sense possessed by migratory birds. Certain evidence indicates that a flavin-superoxide radical pair may be better suited for detecting the Earth's magnetic field than the flavin-tryptophan system more commonly assumed. Studies into this alternative radical pair often ignore the particularly rapid electron spin relaxation expected for superoxide. In Chapter 4 I simulate the sensitivity of this superoxide radical pair to an Earth-strength magnetic field, deriving a set of strict conditions on the local environment and molecular dynamics of the radicals that will need to be satisfied if it does play a role in geomagnetic sensing.

In Chapter 5 I simulate the effect of a magnetic field on the electrocatalytic reduction of carbon dioxide, demonstrating that an experimentally observed field effect cannot be accounted for by the mechanism originally proposed. By including spin relaxation, I am able to fit the experimental results and derive a set of physically reasonable parameters that quantitatively account for the observed field effect.

In many systems these observed magnetic effects are of a relatively small magnitude. In Chapter 6 I examine autocatalysis in oscillating chemical reactions as a means of amplifying weak field effects. A minute change in one of the rate constants for the initiation step in a model oscillating system that involves a radical pair is found to produce a dramatically large change in the amplitude of reaction intermediate oscillations.

Publications

The theoretical work and calculations described in this thesis were completed by the author and have formed the basis for four journal articles. The work described in:

- Chapter 3 forms the basis of reference [1]: "Posner qubits: spin dynamics of entangled $Ca_9(PO_4)_6$ molecules and their role in neural processing", published in the *Journal of The Royal Society Interface* (2018).
- Chapter 4 forms the basis of reference [2]: "Viability of superoxide-containing radical pairs as magnetoreceptors", published in the *Journal of Chemical Physics* (2019).
- Chapter 5 forms the basis of reference [3]: "Source of magnetic field effects on the electrocatalytic reduction of CO_2", published in the *Journal of Chemical Physics* (2020).
- Chapter 6 forms the basis of reference [4]: "Amplification of weak magnetic field effects on oscillating reactions", published in *Scientific Reports* (2021).

Acknowledgements

My first thanks go to Peter Hore, for welcoming me into his research group over the past five years. He has been an insightful mentor who has given me both the freedom to explore and the guidance to improve, for which I am equally grateful.

Thanks to all members of the Hore research group, past and present, for being good company in the office, friendly travelling companions, and willing listeners to my opinions about movies.

A particular mention goes to: Susannah Bourne-Worster, for reinstating regular and diverting teatimes; Hamish Hiscock, for demonstrating the construction potential of peanut butter jars; Daniel Kattnig, for a tip-off about a good room to rent; Jiate Luo, who started his DPhil at the same time as me and was my sole office-mate for the better part of a year; and Rachel Henning, for her help re-reinstating teatimes. Or should that be "acrid-coffee-times"?

Thanks to all of my teachers and tutors, especially Stephen Faulkner, whose calm and friendly manner meant that I learnt a great deal about Chemistry, and perhaps a greater deal yet about all manner of other things. Also to Melissa Barkan and my fellow "peer supporters", whose training, support, and (dare I say it?) advice have broadened and transformed my experience as a DPhil student.

My friends at Keble—from the JCR, MCR, and SCR alike—have been a stimulating and varied group of people, and one of the nicest ongoing surprises about being a postgraduate student. I have had the opportunity to learn, to teach, and to have an obscene amount of fun. Thanks to all of the people with whom I've shared brunch, bops, birthdays, boardgames, balls, book clubs, and much more besides. A particular thank you to Ellen, a postcard pal and editing expert (what do you think of my font choices—pretty good, right?) whose finger is very often on the buzzer.

Thanks also to all of my friends from home and from my undergraduate days—when I decided to stay in Oxford for four *more* years I knew I would need to escape sometimes, and you have provided the means, motive, and opportunity to do so. Recently this has been more online than I would have liked, and I can't

wait to see you all in person soon. A special mention goes to Justin; after our undergraduate interviews I couldn't get rid of you, and you've not been able to get rid of me ever since. Over the past year we're probably the only people we've each seen much *more* of than we would have chosen. Oh, and how about that dilapidated octahedron (see Fig. 3.3)?

Ben—firstly, thanks for the perceptive proofreading, I'm looking forward to returning the favour. Thanks also for all of your support while I've been writing this, and always. I've been trying to think of something to write here that doesn't resort to referencing some quote or trend that makes us both laugh. In any case: thank you for being a friend.

A final, especially large, thank you goes to my supportive family, and above all to my brothers, Samuel and Benjamin, and to my parents, Leslie and Tracey. You have always been there for me, whether at home or away, and for the last part of my time in Oxford your unwavering time, attention, and humour from all-too-great a distance have made all the difference.

Thomas Player
Oxford, April 2021

> "I don't know half of you half as well as I should like; and I like less than half of you half as well as you deserve." This was unexpected and rather difficult. There was some scattered clapping, but most of them were trying to work it out and see if it came to a compliment.
>
> J.R.R. Tolkien
> *The Fellowship of the Ring* [5]

This thesis is fondly dedicated to the memory of

my grandfather, Fred Player (1925–2019),
my grandmother, June Player (1931–2019), and
my great-grandfather, Bernard "Alf" Pearman (1922–2020).

I would have loved the chance to try to explain it to you.

Contents

1 Introduction

> . . . living matter, while not eluding the 'laws of physics' as established up to date, is likely to involve 'other laws of physics' hitherto unknown, which, however, once they have been revealed, will form just as integral a part of this science as the former.
>
> Erwin Schrödinger
> *What Is Life?* [6]

It is well known that electromagnetic interactions between molecules drive the set of processes that we call life. From hydrogen bonding between DNA base pairs [7, 8] to the release of calcium ions in synapses [9], innumerable critical biological phenomena rely on electromagnetic forces.

In the same way that the dawn of electromagnetic theory in the 17$^{\text{th}}$ century[1] helped us understand a host of biological processes, possible non-trivial effects of quantum mechanics in biology have been debated since the earliest quantum theories were formulated in the 1920s [6, 11]. Quantum effects are often defined as those that have no classical analogue, but what do we mean by *non-trivial* quantum effects?

It is clear that quantum mechanics has a role to play in biology, in the same way that it has a role to play in all empirical science, being the set of tools built

[1] Certain branches of what we would now call physics—astronomy, mechanics, optics—have been studied for millennia, but this is not true for electricity and magnetism. Effects now described as electromagnetic, such as the static charge that builds up on amber when it is rubbed with fur, have been well known since antiquity, but these phenomena were not studied quantitatively until the 17$^{\text{th}}$ century and the publication of *On the Magnet and Magnetic Bodies, and on That Great Magnet the Earth* by English physician William Gilbert [10]. He coined the term "electricus" to describe these observations, which is ultimately derived from the Greek word for amber, ἤλεκτρον (ēlektron), giving rise to the term electricity today.

up to explain the quantized behaviour we observe on the scale of atoms and subatomic particles. Quantum mechanics clearly plays a non-trivial role in even the simplest chemical bonds, and we can use its tools to describe in amazing detail the behaviour of the bonding electrons. In many cases, however, we can use a classical analogue to adequately explain observed effects—to continue the example of chemical bonding, a simple harmonic oscillator model that treats chemical bonds like classical springs is often sufficient to explain even complex bonding patterns and molecular behaviours, being routinely used today in the field of molecular mechanics to model systems from small molecules all the way up to large biological assemblies.

For the purposes of this thesis, non-trivial quantum effects are therefore those that cannot be adequately described and explained without invoking quantum mechanical tools. In practice, there will clearly be a large grey area between trivial and non-trivial quantum effects, with the suitability of a classical approximation often not obvious at first glance. It has also been suggested that if a quantum effect in biology is non-trivial then it may have been exploited by evolution, rather than simply arising because a material is made up of atoms, molecules, and electrons [12]. On a practical level, uncovering and understanding a non-trivial quantum effect requires using the theoretical tools of quantum mechanics to solve biological problems, which is the focus of this thesis.

Potential quantum effects in the natural world are becoming better and better understood, and this emergent field is therefore full of both discoveries and unanswered questions [12]. Efficient energy transfer in photosynthesis [13], phototransduction in vision [14], magnetic field effects in avian magnetoreception [15], and even inelastic tunnelling in olfaction [16], are all areas where it has been suggested that non-trivial quantum effects may exist.

The first step to answering questions in these fields is understanding how interactions that occur on energy scales much smaller than the thermal energy

available from the surroundings persist and cause measurable effects in the noisy environments found in nature. Many of these interactions are thought to rely on spin.

Spin 1.1

In the early 20th century, several experimental results led to the conclusion that certain properties of the smallest known particles at the time could not be fully explained by classical mechanics. One such discovery was that, as well as their charge, electrons and protons (and indeed neutrons, which make up much of the mass of nuclei but have no charge) exhibit a quantized angular momentum that has no classical counterpart. The discovery of this intrinsic property of matter was one of the most fundamental in the burgeoning field of quantum mechanics.

On the atomic scale, matter clearly exhibits orbital angular momentum, for instance due to the orbital motion of electrons about nuclei. Pauli first described "a strange two-valuedness which cannot be described classically" [17], which would become the basis of his famous exclusion principle. The presence of a second intrinsic type of angular momentum in atomic scale systems was first demonstrated by Stern and Gerlach in 1922 with their now famous experiment in which silver atoms were deflected by a magnetic field [18]. This result was later shown to be consistent with Uhlenbeck and Goudsmit's hypothesis that electrons possessed a quantized angular momentum [19]. Speaking towards the end of his scientific career, Goudsmit described the difficulty he had explaining the concept of spin to the sceptical Pauli, trying his best but saying that "because I did not really understand it myself I, naturally, was unable to explain it to Pauli" [20].

Spin angular momentum, often referred to simply as spin, is possessed by quarks and leptons and hence by the protons, neutrons, and electrons that make up matter. Despite the name it does not directly relate to motion of any kind, rather it is an intrinsic property of these elementary particles. In many ways,

however, it behaves analogously to classical angular momentum, not least in its magnetic properties.

A spin-carrying particle can be thought of like a small bar magnet, which will tend to align itself with an external magnetic field. Unlike a macroscopic magnet, the projection of this spin magnetic moment onto a fixed axis is quantized such that it can only take certain values. A spin quantum number describes these possible values, of which there are two for particles such as the electron and proton. The two options, which will be described in more detail in Chapter 2, can be thought of for the moment as spin-up (↑) or spin-down (↓). The energy gap between these two states tells us something about how the quantum state of a spin system can change over time.

Spin dynamics 1.2

The energy of a molecule can generally be divided into a sum of contributions from its different degrees of freedom: translational, rotational, vibrational, and electronic, $E = E_{\text{tr}} + E_{\text{rot}} + E_{\text{vib}} + E_{\text{elec}}$ [21]. Gaps between energy levels associated with each of these degrees of freedom can be expressed in frequency units of hertz ($1\,\text{Hz} = 1\,\text{s}^{-1}$) by dividing the Bohr condition for radiation absorption or emission through by Planck's constant: $\Delta E_i / h = \nu_i$ [22].

Consider the simple hydrogen molecule H_2, which is made up of two protons and two electrons. The frequencies associated with the gap between the ground and first excited energy levels for each of its degrees of freedom[2] are shown in Fig. 1.1. These modes are not completely independent, but the approximation that they are very often holds [21]. In particular, the translational energy levels are so closely spaced that we can think of them as a continuum.

[2]These frequencies are $\nu_{\text{tr}} \simeq 74\,\text{mHz}$, $\nu_{\text{rot}} \simeq 3600\,\text{GHz}$, $\nu_{\text{vib}} \simeq 130\,\text{THz}$, and $\nu_{\text{elec}} \simeq 2700\,\text{THz}$. The energy levels were taken to be the ground and first excited energy level associated with the usual expressions [21] for: a particle in a 3D box of dimension 1 cm; a rigid rotor; a simple harmonic oscillator; and the electronic excitation energy for the Lyman band in H_2 [23]. The choice of the side length for the particle in a box is somewhat arbitrary—a shorter length would give a larger energy gap, and vice versa.

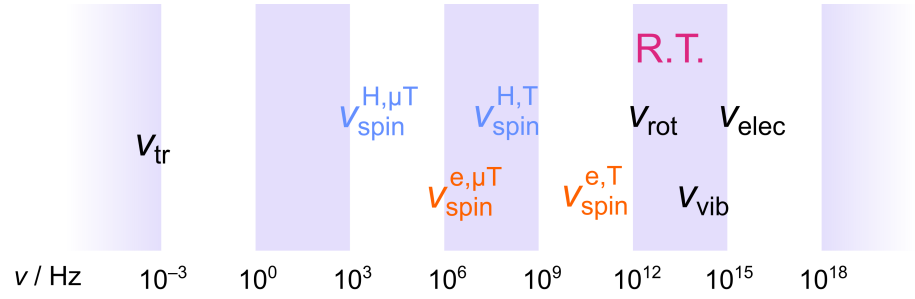

Figure 1.1 Frequencies representing transitions that can be associated with translational, rotational, vibrational, electronic, electron spin, and nuclear spin degrees of freedom in H_2 at two different magnetic field strengths: 50 μT, indicated by a superscript μT, and 1 T, indicated by a subscript T. These are representative values that show how the energy scales associated with spin-possessing particles compare to the energy scales accessible through other degrees of freedom for small molecules such as hydrogen. Also indicated is the frequency associated with thermal energy $k_B T/h$ at room temperature (R.T., $T = 298$ K)

How do the energies of spin interactions compare? The energy of interaction between an external magnetic field and a spin's magnetic moment is directly proportional to the magnitude of the field, as will be explained in Chapter 2. The total magnetic field magnitude (more technically the magnetic flux density), is represented by the symbol B and measured in units of tesla ($1\,\mathrm{T} = 1\,\mathrm{kg\,s^{-2}\,A^{-1}}$).

This direct proportionality between field strength and interaction energy means that in a 1 T magnetic field the energy splitting between the ↑ and ↓ energy levels for the electron and proton,[3] which are also shown in Fig. 1.1, would be exactly 20 000 times greater than the same splitting in an Earth's strength field of 50 μT.

These values illustrate two principles. Firstly, that the degrees of freedom associated with spin can largely, but not exclusively, be thought of as separate from other degrees of freedom in a molecule [22]. Two examples where this separation breaks down are the significant spin–orbit coupling that sometimes exists between electronic orbital and spin degrees of freedom, which will be important in Chapter 4, and the joint rotational-nuclear spin wavefunction that couples nuclear spin states with rotations and must be considered for small symmetric molecules, which we will touch upon in Chapter 3.

[3] These frequencies are $\nu_{spin}^{e}(50\,\mu\mathrm{T}) \simeq 1.4\,\mathrm{MHz}$, $\nu_{spin}^{e}(1\,\mathrm{T}) \simeq 28\,\mathrm{GHz}$, $\nu_{spin}^{H}(50\,\mu\mathrm{T}) \simeq 2.2\,\mathrm{kHz}$, and $\nu_{spin}^{H}(1\,\mathrm{T}) \simeq 43\,\mathrm{MHz}$.

Secondly, the idea that we even need consider quantum effects related to spin when studying biologically relevant systems in geomagnetic fields may come as a surprise [11, 12, 15]. The thermal energy at room temperature, $T = 298\,\mathrm{K}$, can also be expressed as a frequency using the Boltzmann constant: $k_\mathrm{B}T/h \simeq 66.2\,\mathrm{THz}$, shown in Fig. 1.1. Because thermal energy is so much larger than the transition frequencies for electrons and protons (and other nuclei, which have even smaller transition frequencies still), all spin states are broadly equally populated at physiologically relevant temperatures [24].

How, then, could a magnetic field as weak as the Earth's influence the outcome of a chemical reaction? Firstly we must establish what we mean by the Earth's *weak* magnetic field. The convective motion of an electrically conductive iron-nickel alloy in the Earth's outer core induces and maintains a magnetic field, which can for the most part be thought of as a magnetic dipole at the centre of the Earth [25]. The strength of the Earth's magnetic field is non-uniform, varying both in space (between ~24 μT in South America and ~66 μT in central Russia and the southern Indian Ocean, see Fig. 1.2) and in time (by up to approximately ±0.1 μT per year) [26]. By way of comparison, the strength of a typical fridge magnet is ~5 mT, and magnetic fields generated for magnetic resonance experiments typically vary between 0.3 T and 17 T.

We have seen that the energy of interaction between the Earth's field and an electron is far weaker than thermal energy at physiological temperatures, and conventional wisdom would therefore dictate that any effects of this field on a chemical reaction would be washed out by thermal noise [15].

The solution to this apparent contradiction is that the reactants have been brought to a state that is far from equilibrium; often this is a radical pair.

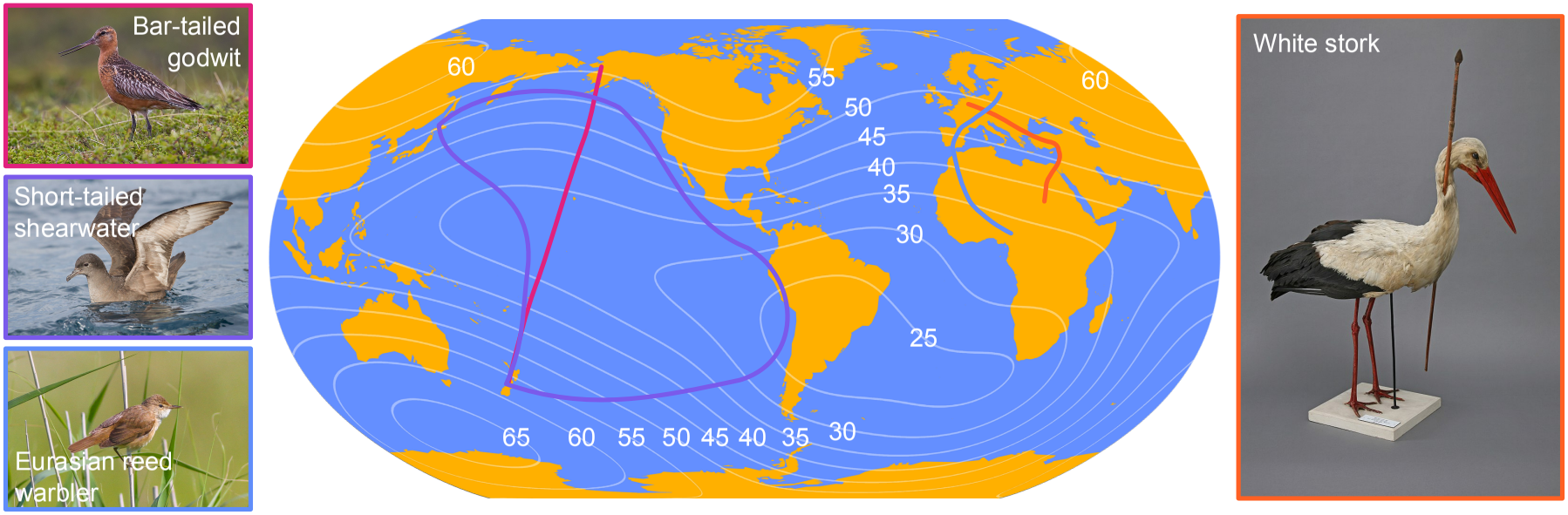

Figure 1.2 Contour plot showing spatial variation in the magnitude of the Earth's magnetic field, in μT, with coloured lines showing the approximate migratory routes of four bird species: the bar-tailed godwit [27], short-tailed shearwater [28], Eurasian reed warbler [29], and white stork [30]. The white stork shown is the *Rostocker Pfeilstorch*—found near the German village of Klütz in 1822 with a central-African hunting spear lodged in its neck, it was one of the earliest pieces of proof that birds migrate long distances to their wintering grounds, and can be seen in the zoological collection of the University of Rostock. Photos taken from [31].

The radical pair mechanism 1.2.1

A *radical* is a chemical species that contains at least one unpaired electron, indicated by a dot, for instance the hydrogen atom $H^{\bullet}$. Radicals can be formed via thermally or photochemically induced homolytic bond breaking or from single electron transfers, among other mechanisms [32]. A *radical pair* is made up of two radicals that have either been generated simultaneously, often by a chemical reaction (as we will see in Chapter 4), or diffused together (as we will see in Chapter 5).

In Section 1.1 we saw that a single electron spin can have two orientations—as a consequence of the Pauli exclusion principle, a pair of electrons in the same bonding orbital will always have opposite orientations. Specifically, they are in an antisymmetric linear combination of states that could be described as $\uparrow\downarrow$ and $\downarrow\uparrow$, where the direction of each arrow represents the orientation of a single electron.[4] We call this linear combination the singlet state, since it has a spin multiplicity of one, whereas a symmetric linear combination of the same two states is one of three possible triplet states. The other two triplet states are when the two electrons have the same orientation: either $\uparrow\uparrow$ or $\downarrow\downarrow$.

Triplets (sometimes labelled T) are distinguished from singlets (S) by the total spin angular momentum, which for triplets is equal to one and for singlets is zero. Depending on the electronic state of its precursor, a radical pair is often created as either pure singlet or pure triplet. Non-uniform magnetic interactions for the two partner radicals in this initial state will cause it to interconvert between singlet and triplet states, a process known as singlet–triplet mixing.

This is shown in Fig. 1.3 for a simple model radical pair that has two spin-$1/2$ nuclei interacting with one of the radicals and none with the other. The singlet probability (see Section 2.2.1) and triplet probability can be calculated as a function of time t for this radical pair, which is initially in a singlet state. Therefore the

[4] These states will be more fully introduced in Section 2.1.

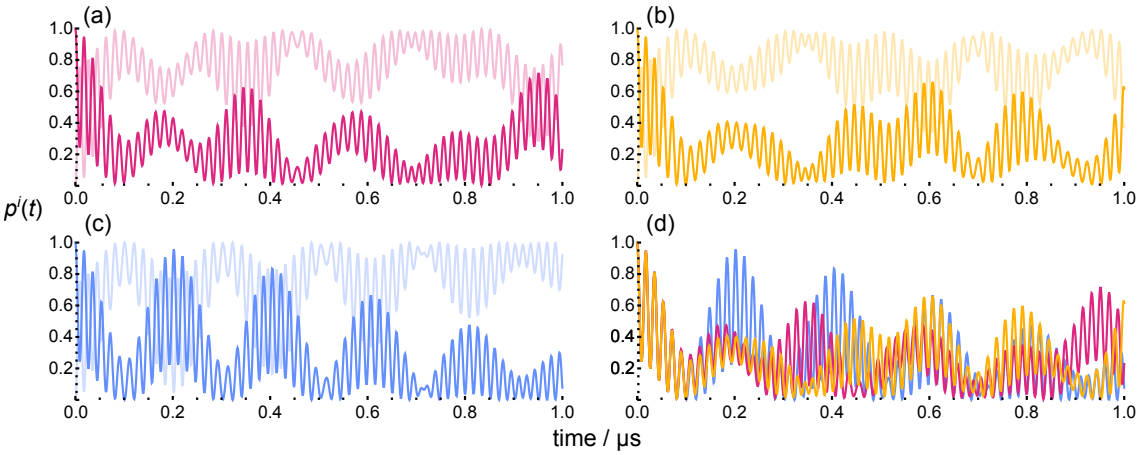

Figure 1.3 Oscillations in singlet probability ($p^{\mathrm{S}}(t)$, heavier lines) and triplet probability ($p^{\mathrm{T}}(t)$, lighter lines) for a simple radical pair, both calculated according to Eq. (2.46). The radical pair is initially in a pure singlet state. One of the partner radicals is coupled to two spin-1/2 nuclei with rhombic anisotropic hyperfine couplings of ~1 mT (see Section 2.2.2) and the other to none. No relaxation or reactivity was included. An applied magnetic field of strength $B = 50\,\mu\mathrm{T}$ in the z-direction is included in (a), and the same strength field but in a perpendicular direction (x-direction) is included in (b). In (c) there is no applied magnetic field. (d) shows all three singlet traces superimposed.

singlet probability at $t = 0$ equals one, and over time the singlet and triplet states interconvert, with the probabilities for the four states always summing to one.

In panels (a) and (b) an Earth-strength magnetic field is applied to the radical pair. This changes the dynamics, as can be seen by comparing with (c), where the field is not present. Furthermore, the orientation of this magnetic field changes the probabilities over time, as can be seen by comparing (a), where the magnetic field is parallel to an axis fixed within the radical pair, with (b), where it is perpendicular.

Over time the radical pair will reach a thermally equilibrated state, via relaxation processes that couple the spin system to its surroundings. Before it relaxes, the product quantum yields of onward reactions from this radical state can be affected by an applied magnetic field. This is because the interconversion of singlet and triplet can be affected by the direction and magnitude of an applied magnetic field, as we have already seen in Fig. 1.3.

A simple reaction scheme demonstrating this principle is shown in Fig. 1.4. A

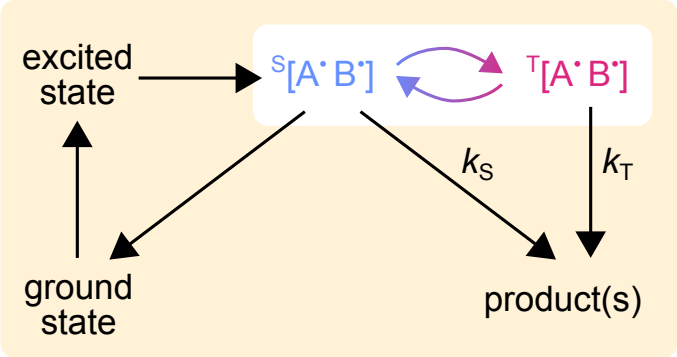

Figure 1.4 Simple model showing the radical pair mechanism for a radical pair $[A^{\bullet}\ B^{\bullet}]$ that can be characterised as either singlet or triplet. Both of these can react to form products, with rate constants k_S and k_T respectively, whereas only the singlet can return to the ground state. An applied magnetic field can affect the product yields of this reaction by altering the rates of singlet–triplet interconversion, represented by the blue/red arrows.

singlet radical pair is formed from some excited state molecule, perhaps produced via electron transfer or homolytic bond cleavage. Over time singlet and triplet will interconvert, and the rate of this interconversion can be affected by an applied magnetic field, as shown in Fig. 1.3 and indicated by the blue/red arrows in Fig. 1.4. Both singlet and triplet can react to give products—perhaps the same product, or different—with rate constants k_S and k_T, which may or may not be equal. Only the singlet state can return to the ground state, due to spin conservation.

This imbalance in reactivity means the radical pair mechanism can lead to a magnetic field effect (MFE) on the product yields. For instance, if the applied magnetic field increases the likelihood of the radical pair being in the triplet state then this may decrease the amount of singlet product/ground state generated.

In this thesis we will consider MFEs caused both by introducing a magnetic field (i.e. comparing panels (a) or (b) to panel (c) in Fig. 1.3—this type of MFE will be seen in Chapter 5) or by changing the angle of a fixed-magnitude field relative to the radical pair (i.e. comparing panel (a) to panel (b)—this type of MFE will be seen in Chapter 4).

In order that an MFE buids up, the radical pair must exist for sufficiently long that significant singlet–triplet mixing can occur. In panel (d) all three singlet traces from (a–c) are superimposed, and we can see that for the first ~0.1 μs the behaviour under all three field conditions is essentially identical. If the radical pair equilibrates before the singlet–triplet mixing has any chance to build up—i.e. the spin relaxation is rapid compared to other magnetic interactions—then there can be no MFE. Therefore, an understanding of the relaxation processes that can occur in radical pairs will be critical to the modelling in Chapters 4 and 5. This type of relaxation will also be important in Chapter 3, which considers a singlet state similar to a radical pair but composed of two nuclei instead of electrons.

Although the energy gaps for spin transitions are small, they are not so small as to be unobservable. These transitions form the basis for the powerful techniques of nuclear magnetic resonance (NMR) and electron spin resonance (ESR). Because the equilibrium population difference between the upper lower and energy levels is so small, strong magnetic fields and many other tools are used to optimize signal strengths in these spectroscopic techniques [24].

The spin effects we have outlined can have profound influences on physical and chemical molecular properties, many of which have been uncovered using the tools of NMR and ESR. The field of spin chemistry was born out of the observation of unexpected non-equilibrium intensities in the magnetic resonance spectra of chemical reaction systems [33–35]. It was subsequently found that the rates and product yields of these reactions could be affected by applied magnetic fields in the way we have discussed, often involving the radical pair mechanism—for an introduction see reference [36]. Recently there has also been much research into pairs of nuclear spins in the singlet state, which may exhibit long-lived and useful experimental properties [37].

In what ways could effects like these play a non-trivial role in *biological* processes? In Chapters 3–6 we will consider four specific questions related to this

field from a theoretical standpoint, using the tools of spin dynamics outlined in Chapter 2.

Quantum processing in the brain 1.2.2

The biochemical workings of the human brain have interested scientists for decades. Several proposed theories have invoked the tools of quantum mechanics to explain the workings of neural processing—perhaps most famous among these is Penrose and Hameroff's theory that relies on quantum states of microtubules [38]. This theory is frequently refuted on many counts, not least that quantum decoherence would quickly destroy any possible effects in the warm, wet, and noisy environment of the brain [39–41].

Recently it has been proposed [42–44] that "cognition" in the human brain could non-trivially rely on quantum mechanics. The hypothesis involves a system of quantum computing-like neural processing [43], whereby the nuclear spins in small calcium phosphate molecules (the building blocks of bones and teeth) are implicated as quantum bits, analogous to the ones and zeros used by a conventional computer. When it was proposed there was no direct experimental evidence to support this hypothesis, which was arrived upon by a process of "reverse-engineering" [42] by the proposer, Matthew Fisher. Two experimental studies (on model organisms) have since found contradictory evidence about whether quantum processing with nuclear spins may operate in the mammalian brain [45, 46].

A key part of the proposed hypothesis is that two such molecules would need to become entangled—a state whereby two parts of a system cannot be described separately but only as part of a whole, of which the singlet is an example, see Section 2.1.1—and remain so in the thermally noisy environment of the human body.

When this hypothesis was proposed, it was suggested that entanglement lifetimes for the calcium phosphate molecules will be anywhere from around 24 hours all the way up to 21 days [42, 47]. Lifetimes for this kind of entanglement are more typically on the order of seconds [48]. Chapter 3 will look more closely at the processes that will destroy entanglement in these molecules, and the rate at which these processes will occur.

Magnetoreception 1.2.3

Every autumn, billions of birds make awe-inspiring migratory journeys (see Fig. 1.2). The bar-tailed godwit, a long-legged wading bird, flies from Alaska to New Zealand over nine straight days without stopping [27]. Short-tailed shearwaters migrate all the way round the Pacific with pinpoint accuracy, returning to the same burrow each year [28].

One of the earliest pieces of evidence that pointed towards annual migration was the so-called Pfeilstorch ("arrow-stork" in German). In 1822, near the German village of Klütz, a white stork appeared with an African hunting spear embedded in its neck (see Fig. 1.2). It had been injured while wintering in Africa, and somehow managed to make its way back to its breeding grounds. Evidence like this eventually led to the conclusion that birds must migrate, searching for better shelter, richer food supplies, and suitable breeding grounds.[5] How these birds navigate on their long journeys is not yet fully understood [15, 51, 52].

Some birds, and many other migratory animals, possess a sense that detects the Earth's magnetic field, providing information that they use for both orientation and navigation [52–57]. As well as compass information, some birds learn a magnetic map during their lifetime [52]. Reed warblers in Russia usually migrate south-west towards sub-Saharan Africa, but in one virtual displacement exper-

[5] Centuries ago, there was not a clear explanation for the bewildering seasonal disappearance of many bird species. Charles Morton, a 17th century English minister, believed that birds flew to the moon and back each winter [49]. Other theories included birds hibernating at the bottom of the sea, or even turning into other species on an annual basis [50].

iment they were kept in a magnetic field of the same strength and direction as found in Scotland. This changed the behaviour of adult birds completely, which set off in the appropriate direction to get to their destination from Scotland (south-east) [29]. Juveniles were instead randomly oriented, showing that the birds must learn this magnetic map on their first migration.

There are two main theories behind how this compass-map sense works: the first involves biogenic magnetite particles in the bird's body aligning with the Earth's magnetic field [58], like a traditional compass, whereas the second relies on a light-dependent chemical reaction in the bird's eyes for compass information [15, 59–63] (see reference [64] for a recent discussion of the two together). This second theory, which is the focus of Chapter 4, suggests that the distribution of the products of a radical pair chemical reaction in the bird's eyes depends on the orientation of the bird's head with respect to the Earth's magnetic field [15].

Although the radical pair mechanism as a compass sensor was first proposed in 1978 [59], it is only during the past twenty years that the idea has seriously gathered support. This is because, in 2000, a specific radical pair magnetosensitive molecule was proposed: cryptochrome [60]. Highly homologous to photolyases, which form radical pairs upon light-excitation, and found in the eyes of several bird species, cryptochrome proteins remain the most likely candidate for the magnetically sensitive material that interacts with the Earth's field to provide a compass bearing [15, 63, 65]. Within this theory, excited states that lead to the radical pair are formed when light of a particular wavelength enters the birds' eyes [66]. We know that light is important for navigation because migrating birds such as European robins can orient themselves in their migratory direction under blue or green light, but not red or yellow [67–69].

There are still many unanswered questions in this field [15, 51, 62], two of which relate to the work in this thesis. In Chapter 4 we will directly address the question of which specific molecules detect the magnetic field, focusing on a

proposed alternative radical pair involving superoxide radicals [2]. In Chapter 6 we will indirectly, and from a theoretical perspective, address the ways in which small MFEs may be processed and amplified, considering a model of an oscillating chemical reaction [4].

Electrochemical reactions 1.2.4

Reactions that happen at an electrode involve the use of an electric potential to cause a chemical change, and clearly the electrodynamic properties of the reactants and products can be influenced by magnetic fields [70]. One way in which magnetic fields can influence electrochemical reactions is via the Lorentz force (see Eq. (2.5)). This force can act on electrically charged particles to cause convection near the surface of the electrode, influencing processes such as nucleation, bubble formation, and even the shapes and chirality of crystals that form [71].

Electrochemical reactions may also be of biological relevance. For instance, recent experiments have demonstrated that *in situ* electrochemical generation of nitric oxide in the (mouse) brain can stimulate nearby cation channels, resulting in an influx of Ca^{2+} ions into neuronal cells [72, 73].

The effects of magnetic fields on electrochemical reactions such as these is speculative, but nevertheless an area of growing interest [70]. Much is not yet understood about the way that magnetic fields affect biological electrochemical systems. We know, for instance, that neuronal excitation can be induced externally using magnetic fields, most famously in the method of transcranial magnetic stimulation (TMS) [74]. TMS can be used as both a therapeutic and a diagnostic tool, but its effect on neuronal activity is poorly understood because the microelectrodes that are normally used to monitor neuronal activity are massively disrupted by a strong applied magnetic field [75]. Theoretical study of model systems will help uncover the range of possible effects magnetic fields may have on electrochemical systems *in vivo*.

The radical pair mechanism is one further way in which magnetic fields may potentially affect electrochemical reactions. In Chapter 5 we will model an experimentally observed MFE on the electrocatalytic conversion of CO_2 into formic acid [76]. The serious risks of irreversible climate change and increasing sea levels presented by the build-up of CO_2 in the atmosphere are well understood by many [77], and the efficient conversion of carbon dioxide into useful small organic molecules is of obvious appeal as a way to reduce this accumulation, presenting an added benefit by making use of a waste product [78–84].

Thesis outline 1.3

Having given an overview of the areas considered in this thesis, in Chapter 2 we present the theoretical tools that will be used throughout, and in particular the mathematical framework of spin dynamics calculations.

Chapter 3 considers the nuclear spin dynamics of a calcium phosphate cluster that has been indicated as a potential component of a system of neural processing [42]. The lifetime of the singlet state in these clusters is critical to this hypothesis, and we will model coherent and relaxation spin processes in order to set a strict upper limit on this lifetime [1].

Chapter 4 treats the radical pair model of avian magnetoreception [15], investigating the potential magnitude of MFEs exhibited by a flavin-superoxide radical pair that is sometimes considered as an alternative [85–88] to the flavin-tryptophan one usually indicated within this model [15, 51, 60, 89]. We will identify strict conditions on the physical environment of this radical pair that must be met if it were to be used as a compass sensor [2].

Chapter 5 examines an experimentally reported MFE on an electrocatalytic reaction of carbon dioxide [76], fitting the experimental data with variable parameters related to the dynamic processes of the reactants [3].

Finally, Chapter 6 explores a model oscillating chemical reaction [90] as a potential method of amplifying small magnetic field effects, fully characterising for the first time [4] a feature known as a canard explosion [91] in this model system.

Does anyone still wear a hat?

STEPHEN SONDHEIM in *The Ladies Who Lunch* [92]

2 Theory

Any rotating body possesses angular momentum, which can be visualised as a vector pointing along the axis about which the body rotates. This angular momentum is defined as the cross product of position and linear momentum vectors, $\mathbf{L} = \mathbf{r} \times \mathbf{p}$.

In quantum systems, the angular momentum of a particle is quantized and can be described by two integers, l and m_l, which are good quantum numbers. A good quantum number is an eigenvalue of the system Hamiltonian, i.e. it describes a stationary state (see Section 2.2.2). These quantum numbers correspond to the eigenvalues of the states $|l, m_l\rangle$, which are simultaneous eigenstates of the operators for the square of the total angular momentum and its z-component:

$$\begin{aligned} \hat{L}^2 |l, m_l\rangle &= \hbar^2 l(l+1) |l, m_l\rangle \quad && l \in \{0, 1, 2, \ldots\}, \\ \hat{L}_z |l, m_l\rangle &= \hbar m_l |l, m_l\rangle && m_l \in \{-l, -l+1, \ldots, l-1, l\}, \end{aligned} \tag{2.1}$$

where $\hbar = h/2\pi$ is the reduced Planck constant and we have used Dirac's elegant ⟨bra|ket⟩ notation [93]. We draw a distinction between an operator (indicated by a hat over the symbol, $\hat{L}$) and the vector or matrix representing that operator in a particular basis (indicated by a bold symbol, $\mathbf{L}$). In this chapter we will be particularly explicit about whether we are considering operators or their matrix representations, in later chapters treating them more interchangeably.

The magnetic quantum number, l, describes the magnitude of the angular momentum, and the azimuthal quantum number, m_l, describes its projection onto a fixed axis (arbitrarily chosen as the z-axis, see Fig. 2.1(a)). Since, in this represen-

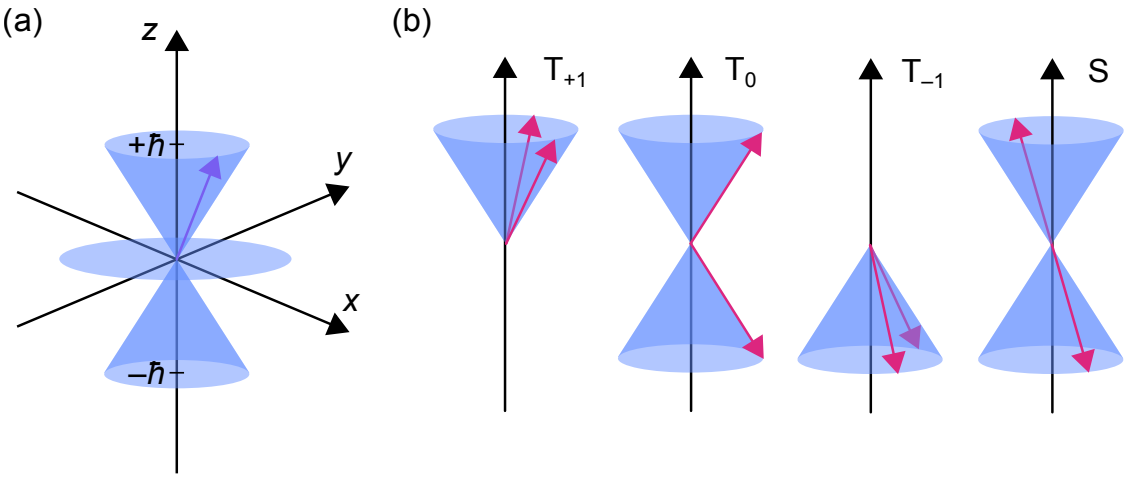

Figure 2.1 Vector representations of quantum mechanical angular momentum. (a) The blue planes indicate possible orientations of an angular momentum vector (purple) with quantum number $l = 1$ and $m_l = -1, 0, +1$. (b) Two coupled spin-1/2 particles ($s = \frac{1}{2}$, pink). The triplet states, T_{+1}, T_0, and T_{-1}, and singlet state, S, are shown. For the triplets the angle between the vectors is the same, such that the resultant is the same, in all three cases, although we cannot know the orientation of the spin vectors on the cones [21]. (a) and (b) are not drawn to scale.

tation, we have specified the angular momentum's magnitude and z-component, we cannot also specify its x- or y-components. This is because the operators $\hat{L}_x$, $\hat{L}_y$, and $\hat{L}_z$ do not commute, and is reflected in Fig. 2.1(a) by blue cones/planes that indicate the range of possible orientations of the angular momentum for a given projection onto the z-axis.

By analogy with orbital angular momentum and Eq. (2.1), spin angular momentum can also be fully described using two quantum numbers: s, the spin quantum number, and m_s, the spin projection (or magnetic) quantum number, such that

$$\begin{aligned} \hat{S}^2 \left|s, m_s\right\rangle &= \hbar^2 s\,(s+1) \left|s, m_s\right\rangle \quad & s &\in \left\{0, \tfrac{1}{2}, 1, \tfrac{3}{2}, \ldots\right\}, \\ \hat{S}_z \left|s, m_s\right\rangle &= \hbar\, m_s \left|s, m_s\right\rangle & m_s &\in \{-s, -s+1, \ldots, s-1, s\}. \end{aligned} \tag{2.2}$$

These quantum numbers clearly relate to the eigenvalues of states $|s, m_s\rangle$, which are simultaneous eigenstates of $\hat{S}^2$ (total squared spin angular momentum operator), and $\hat{S}_z$ (the z-component).

The key difference between Eq. (2.1) and Eq. (2.2) is that s can take half-integer values—a manifestation that spin is not a classical angular momentum resulting from an object spinning about an axis.

Electrons have an intrinsic spin quantum number $s = \frac{1}{2}$. Since atomic nuclei are made up of protons and neutrons, they can have spin quantum number with integer or half-integer values. Table A.1 (in Appendix A) gives examples of nuclear isotopes that will appear in this thesis, along with their spin quantum numbers (often labelled I to indicate a nuclear spin, as opposed to s for electron spin), spin state degeneracies $Z = 2I + 1$, nuclear g-factors g_N, and natural abundances.

A magnetic moment can be associated with an isolated spin labelled i:

$$\boldsymbol{\mu}_i = \gamma_i \mathbf{S}_i, \tag{2.3}$$

where γ_i is the spin's gyromagnetic ratio. This is a proportionality constant that varies from spin to spin but always has the form

$$\gamma_i = (-)\frac{g_i \mu_i}{\hbar}. \tag{2.4}$$

In Eq. (2.4) the minus sign appears in the case of electrons only, g_i is the g-factor for the spin of interest, and μ_i is either μ_N (the nuclear magneton, which is used for nuclear spins) or μ_B (the Bohr magneton, which is used for electron spins). μ_B is larger than μ_N by a factor equal to the ratio of the proton to electron mass, such that interactions for nuclei are significantly weaker than for electrons, all other things being equal.

An isolated electron has the g-factor $g_\mathrm{e} \simeq 2.0023$, and the g-factors for nuclei are given in Table A.1. In almost all chemical environments, spin–orbit coupling between the electron's orbital and angular momenta changes this value or makes it anisotropic. If this anisotropy has significant effects then g may be represented by a tensor, for instance this can be seen in Chapter 5 for the $CO_2^{\bullet -}$ radical.

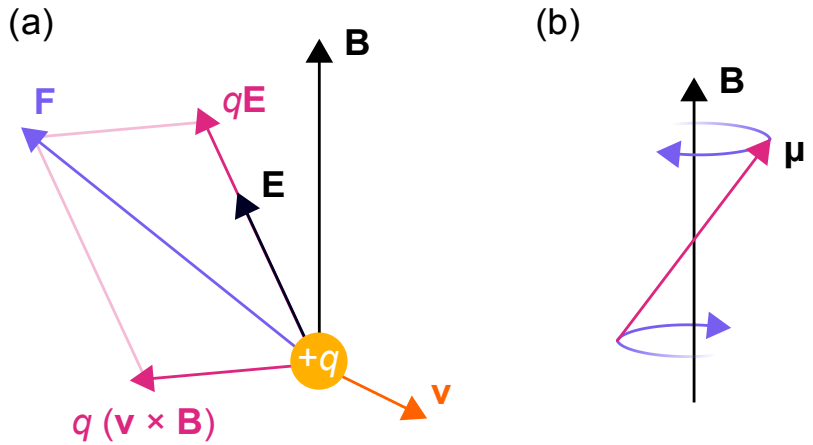

Figure 2.2 The magnetic field vector $\mathbf{B}$ can be defined in terms of (a) the Lorentz force $\mathbf{F} = q\,(\mathbf{E} + \mathbf{v} \times \mathbf{B})$ on a particle of charge q moving at a velocity $\mathbf{v}$ in an electric field $\mathbf{E}$ or (b) the Larmor precession of a magnetic dipole $\boldsymbol{\mu}$ experiencing a torque $\boldsymbol{\tau} = \boldsymbol{\mu} \times \mathbf{B}$.

The Lorentz force law [94] states that the electromagnetic force (a vector quantity $\mathbf{F}$) on a charge is a function of its charge (a scalar, q) and velocity (a vector, $\mathbf{v}$) and can be parametrised by exactly two vectors $\mathbf{E}$ and $\mathbf{B}$ as

$$\mathbf{F} = q\,(\mathbf{E} + \mathbf{v} \times \mathbf{B})\,, \tag{2.5}$$

where $\times$ is the cross product (see Fig. 2.2(a)). The units of Eq. (2.5) imply that the force is produced by the motion of the particle in the case of a magnetic field $\mathbf{B}$, but not for an electric field $\mathbf{E}$. This is simply a question of relativity—in a reference frame moving at the same velocity as the particle, the magnetic field would not be seen. As Richard Feynman described it: "One part of the force between moving charges we call the *magnetic* force. It is really one aspect of an electrical effect" [94]. A second way of defining the magnetic field vector $\mathbf{B}$ is in terms of the torque it produces on a magnetic dipole $\boldsymbol{\mu}$

$$\boldsymbol{\tau} = \boldsymbol{\mu} \times \mathbf{B}, \tag{2.6}$$

which can cause Larmor precession about an applied magnetic field (see Fig. 2.2(b)).

The potential energy of a magnetic dipole moment in a field $\mathbf{B}$ can be calculated using the work done when rotating the magnetic moment against the torque caused by the field [94]. The magnitude of this torque from Eq. (2.6) is the rate of change of this energy with angle, $\frac{\mathrm{d}E}{\mathrm{d}\theta} = \tau$, which we can integrate to give

$$\begin{aligned} E(\theta) = \int \mathrm{d}E = \int \tau \,\mathrm{d}\theta &= |\boldsymbol{\mu}_i||\mathbf{B}| \int \sin\theta \,\mathrm{d}\theta \\ &= -|\boldsymbol{\mu}_i||\mathbf{B}| \cos\theta + c \\ &= -\boldsymbol{\mu}_i \cdot \mathbf{B} + c, \end{aligned} \tag{2.7}$$

correct within a constant of integration. The negative sign makes sense, since the torque acts to align the magnetic moment with the field, such that the minimum energy is when they are parallel.

This derivation ignores part of the potential energy, and without going through the details[1] we can set the constant of integration equal to zero. We can also rewrite the energy in terms of Eq. (2.3), introducing the Larmor frequency $\omega_i = -\gamma_i B$, which describes the rate at which the spin precesses about the magnetic field vector:

$$\begin{aligned} E &= -\gamma_i \mathbf{B} \cdot \mathbf{S}_i \\ &= \boldsymbol{\omega}_i \cdot \mathbf{S}_i. \end{aligned} \tag{2.8}$$

[1] When the magnetic moment is perpendicular to the field the torque it experiences is maximal (see Eq. (2.6)), and according to Eq. (2.7) the potential energy at that angle is simply equal to c. So, we can define the energy of interest as the difference between the energy at maximum torque and the energy at an angle θ. However, this still glosses over some of the details, which can be found in reference [94].

	$\lvert S, M_S\rangle$	$\left\lvert m_{s_j}, m_{s_k}\right\rangle$
$\lvert \mathrm{T}_{+1}\rangle$	$\lvert 1, +1\rangle$	$\lvert \alpha\alpha\rangle$
$\lvert \mathrm{T}_{0}\rangle$	$\lvert 1, 0\rangle$	$\frac{1}{\sqrt{2}}(\lvert \alpha\beta\rangle + \lvert \beta\alpha\rangle)$
$\lvert \mathrm{T}_{-1}\rangle$	$\lvert 1, -1\rangle$	$\lvert \beta\beta\rangle$
$\lvert \mathrm{S}\rangle$	$\lvert 0, 0\rangle$	$\frac{1}{\sqrt{2}}(\lvert \alpha\beta\rangle - \lvert \beta\alpha\rangle)$

Table 2.1 Possible triplet and singlet states formed from two coupled spins. The single spin $\lvert s, m_s\rangle$ eigenstates, $\left\lvert \frac{1}{2}, +\frac{1}{2}\right\rangle$ and $\left\lvert \frac{1}{2}, -\frac{1}{2}\right\rangle$, are labeled $\lvert \alpha\rangle$ and $\lvert \beta\rangle$ respectively.

Spin-½ particles 2.1

For much of this thesis we will be concerned with spin-1/2 particles, especially the electron when discussing radical pairs in Chapters 4, 5, and 6, but also other magnetic nuclei, in particular ^{31}P in Chapter 3. We will often consider coupled pairs of spin-½ particles, and it is worth exploring the ways in which these pairs of spins can interact.

Two spins labelled j and k can couple, according to the Clebsch–Gordan series, to form states with total spin angular momentum S and total spin projection M_S:

$$\begin{aligned} S &= s_j + s_k, s_j + s_k - 1, \ldots, \lvert s_j - s_k\rvert, \\ M_S &= -S, -S+1, \ldots, S-1, S. \end{aligned} \tag{2.9}$$

We use s and S to label these states, which is often used to indicate electron spins, but the argument applies equally well to spin-½ nuclei.

Eq. (2.9) implies two possible complete descriptions of two spins: an uncoupled representation with states $\left\lvert s_j, m_{s_j}, s_k, m_{s_k}\right\rangle$, and a coupled representation with states $\left\lvert S, M_s, s_j, s_k\right\rangle$. For the spins j and k, s_j and s_k are fixed and the same no matter the representation, so the two representations are more simply referred to as $\left\lvert m_{s_j}, m_{s_k}\right\rangle$ and $\lvert S, M_s\rangle$. The correspondence between the two representations is summarised in Table 2.1, where the $\lvert s, m_s\rangle$ eigenstates, $\left\lvert \frac{1}{2}, +\frac{1}{2}\right\rangle$ and $\left\lvert \frac{1}{2}, -\frac{1}{2}\right\rangle$, are labeled $\lvert \alpha\rangle$ and $\lvert \beta\rangle$ respectively. These are also often referred to as spin-up (α)

or spin-down (β), indicating the direction of the angular momentum vector along the fixed z-axis. The three states $|\mathrm{T}_{+1}\rangle, |\mathrm{T}_0\rangle, |\mathrm{T}_{-1}\rangle$ are known as triplet states, with three possible projections of the total spin angular momentum: $M_S = -1, 0,$ or +1. The state $|\mathrm{S}\rangle$ is known as the singlet state, in which the two spin angular momentum vectors are precisely antiparallel, and therefore the resultant can only have the projection $M_S = 0$. Vector representations of these states are shown in Fig. 2.1(b).

Matrix formalism 2.1.1

We define the Pauli matrices

$$\boldsymbol{\sigma}_x = \begin{pmatrix} 0 & 1 \\ 1 & 0 \end{pmatrix}, \quad \boldsymbol{\sigma}_y = \begin{pmatrix} 0 & -i \\ i & 0 \end{pmatrix}, \quad \boldsymbol{\sigma}_z = \begin{pmatrix} 1 & 0 \\ 0 & -1 \end{pmatrix}, \tag{2.10}$$

which are self-inverse, and alongside the 2×2 identity matrix $\mathbb{1}_2$ form a basis set for the vector space of 2×2 Hermitian matrices, which can be used to build up a matrix representation of spin-1/2 operators.

As in Eq. (2.2), the $\hat{S}_z$ operator should act on the $|\alpha\rangle$ and $|\beta\rangle$ states to give

$$\hat{S}_z \left|\frac{1}{2}, \pm\frac{1}{2}\right\rangle = \pm\frac{\hbar}{2}\left|\frac{1}{2}, \pm\frac{1}{2}\right\rangle, \tag{2.11}$$

such that, in the basis $\{|\alpha\rangle, |\beta\rangle\}$, the matrix representation of $\hat{S}_z$ is $\frac{\hbar}{2}\boldsymbol{\sigma}_z$. The matrices for operators $\hat{S}_x$ and $\hat{S}_y$ can be similarly formed from the corresponding Pauli matrices, with the $\hat{S}^2$ operator:

$$\begin{aligned} \hat{S}^2 &= \hat{\mathbf{S}} \cdot \hat{\mathbf{S}} \\ &= \hat{S}_x^2 + \hat{S}_y^2 + \hat{S}_z^2, \end{aligned} \tag{2.12}$$

i.e. the dot product of a vector $\hat{\mathbf{S}} = \left(\hat{S}_x, \hat{S}_y, \hat{S}_z\right)$ with itself, where $\hat{S}_i$ are the operators for the x, y, and z components of the spin. This makes the matrix

representation of the total squared angular momentum operator

$$\begin{aligned}\mathbf{S}^2 &= \frac{\hbar^2}{4}\left(\sigma_x^2 + \sigma_y^2 + \sigma_z^2\right) \\ &= \frac{3}{4}\hbar^2\,\mathbb{1}_2.\end{aligned} \tag{2.13}$$

Spin operators are often written in angular frequency units where $\hbar = 1$, as is conventional in the field and will be done throughout the rest of this thesis for all spin operators, and therefore all spin Hamiltonians and derived superoperators.

Multi-spin operators

The Hilbert space for a system of N spin-1/2 nuclei can be written in the same $\{|\alpha\rangle, |\beta\rangle\}$ basis, such that it has dimension 2^N. For instance, two spin-1/2 particles have individual Hilbert spaces H_1 and H_2 of dimension two, and the direct product, $\otimes$, of these individual Hilbert spaces gives a combined Hilbert space H of dimension four:

$$\begin{aligned}H_i &\rightarrow \{|\alpha_i\rangle, |\beta_i\rangle\}, \\ H = H_1 \otimes H_2 &\rightarrow \{|\alpha_1\alpha_2\rangle, |\alpha_1\beta_2\rangle, |\beta_1\alpha_2\rangle, |\beta_1\beta_2\rangle\}.\end{aligned} \tag{2.14}$$

Observables are represented by self-adjoint operators, which can be formed from the single-spin matrix operators described above. These product operators are formed by taking the direct product of the appropriate single spin operators:

$$\hat{P}_i = \hat{S}_1 \otimes \hat{S}_2 \otimes \cdots \otimes \hat{S}_N = \bigotimes_{n=1}^{N} \hat{S}_n. \tag{2.15}$$

The $\bigotimes$ notation for direct products is entirely analogous to the $\prod$ notation for ordinary products. Since the direct product is not necessarily commutative, it is important that this multiplication is carried out in an arbitrary but consistent

order. The matrix representation is formed by taking the Kronecker product,

$$\mathbf{A} \otimes \mathbf{B} = \begin{pmatrix} a_{11}\mathbf{B} & \cdots & a_{1n}\mathbf{B} \\ \vdots & \ddots & \vdots \\ a_{n1}\mathbf{B} & \cdots & a_{nn}\mathbf{B} \end{pmatrix}, \tag{2.16}$$

of the corresponding $n \times n$ matrices in the same (fixed) order.

An equivalent way to build up these operators is via ordinary matrix products of single-spin operators:

$$\hat{P}_i = \prod_{n=1}^{N} \hat{S}_n \tag{2.17}$$

that have been scaled up to the size of the full Hilbert space by taking direct products in the usual order and using the identity matrix for all other spins.

We have considered the spin-$1/2$ case in detail since it applies to electrons, protons, and ^{31}P nuclei, all of which will be of concern in this thesis. It can easily be extended to spin systems containing nuclei with $I > 1/2$, as will be seen in later Chapters. The individual spin operators will be of dimension $2I_n + 1$ to reflect the possible values of m_I, such that the Hilbert space of n spins has dimension $\prod_{n=1}^{N}(2I_n + 1)$.

Expectation values

The expectation value of any operator $\hat{P}$ is

$$\left\langle \hat{P} \right\rangle = \left\langle \Psi \middle| \hat{P} \middle| \Psi \right\rangle \tag{2.18}$$

where $|\Psi\rangle$ is the normalized total wavefunction. This wavefunction can be expressed as a sum over the set of stationary orthogonal basis states $\{|n\rangle\}$,

$$|\Psi\rangle = \sum_n c_n |n\rangle , \tag{2.19}$$

which, when substituted into Eq. (2.18) gives the expectation value as

$$\left\langle \hat{P} \right\rangle = \sum_{n,m} c_n c_m^* \left\langle m \left| \hat{P} \right| n \right\rangle . \tag{2.20}$$

The product $\left\langle m \left| \hat{P} \right| n \right\rangle$ can be thought of as the elements of a matrix, $\mathbf{P}_{mn}$. The usual basis we will work in is the one containing the states $\{|\alpha\rangle, |\beta\rangle\}$ for each spin-1/2 in the system. For a pair of spins another possible basis would be $\{|\mathrm{S}\rangle, |\mathrm{T}_{+1}\rangle, |\mathrm{T}_0\rangle, |\mathrm{T}_{-1}\rangle\}$ (see Table 2.1).

Density matrix

An isolated system in a pure state can be described by a wavefunction $|\Psi\rangle$, which is a vector in the Hilbert space of all possible states for the system. For instance, for a system of two spins a general wavefunction can be written in a basis of α and β states as

$$|\Psi\rangle = c_{\alpha\alpha} |\alpha\alpha\rangle + c_{\alpha\beta} |\alpha\beta\rangle + c_{\beta\alpha} |\beta\alpha\rangle + c_{\beta\beta} |\beta\beta\rangle . \tag{2.21}$$

We define a density operator, for now simply a mathematical object, as the product

$$\hat{\sigma} = |\Psi\rangle \langle\Psi| = \sum_{n,m} c_n c_m^* |n\rangle \langle m| , \tag{2.22}$$

such that the elements of a density matrix can be written in terms of the coefficients of the orthogonal basis states,

$$\sigma_{ij} = \langle i| \hat{\sigma} |j\rangle = \sum_{n,m} c_n c_m^* \langle i \mid n\rangle \langle m \mid j\rangle = c_i c_j^* . \tag{2.23}$$

In the case of Eq. (2.21), the indices n and m would run over the four possible combinations of α and β for the two spins. From Eq. (2.23) it is clear that the density matrix is Hermitian, i.e. $\sigma_{ij} = \sigma_{ji}^*$, and that $\mathrm{Tr}[\sigma] = 1$ for a correctly

normalized wavefunction, where Tr represents the matrix trace, that is the sum of diagonal elements.

Rather than just being a convenient way of storing the coefficients of the basis states in a wavefunction, the particular use of the density matrix is when we consider ensembles. For a macroscopic ensemble of N identical, independent, microscopic systems, each of which is in a state $\left|\Psi_j\right\rangle = \sum_n c_{n,j} \left|n\right\rangle$, the ensemble expectation value of an observable is simply an average of the expectation value of the observable for each system, labelled j:

$$\begin{aligned}
\overline{\left\langle \hat{P} \right\rangle} = \frac{1}{N} \sum_{j=1}^{N} \left\langle \Psi_j \middle| \hat{P} \middle| \Psi_j \right\rangle &= \frac{1}{N} \sum_{j=1}^{N} \sum_{n,m} c_{n,j} c^*_{m,j} \left\langle m \middle| \hat{P} \middle| n \right\rangle \\
&= \frac{1}{N} \sum_{j=1}^{N} \sum_{n,m} \mathbf{P}_{mn} \boldsymbol{\sigma}_{nm,j} \\
&= \frac{1}{N} \sum_{j=1}^{N} \sum_{m} \left(\mathbf{P}\boldsymbol{\sigma}_j\right)_{mm} \\
&= \mathrm{Tr}\left[\mathbf{P} \frac{1}{N} \sum_{j=1}^{N} \boldsymbol{\sigma}_j\right] \\
&= \mathrm{Tr}\left[\mathbf{P}\boldsymbol{\rho}\right],
\end{aligned} \tag{2.24}$$

where we have used Eqs. (2.20) and (2.23).

In the last two lines of Eq. (2.24) it is clear that all we need to find the ensemble average expectation value of the observable represented by $\hat{P}$ is the ensemble average density operator:

$$\hat{\rho} = \frac{1}{N} \sum_{j=1}^{N} \hat{\sigma}_j. \tag{2.25}$$

This can be restated as a sum over all of the possible states, labelled i, of the microscopic system, rather than a sum over all of the systems:

$$\hat{\rho} = \sum_i p_i \hat{\sigma}_i = \sum_i p_i \left|\Psi_i\right\rangle \left\langle\Psi_i\right| = \overline{\left|\Psi\right\rangle \left\langle\Psi\right|}, \tag{2.26}$$

where the overbar represents an ensemble average, p_i is the probability of a microscopic system being in the state represented by the density operator $\hat{\sigma}_i$, and $\sum_i p_i = 1$ [95]. We will often refer to the ensemble average expectation value in Eq. (2.24), which is both a quantum average over possible states and a statistical average over systems, as a probability: for instance $p^{\mathrm{S}} = \overline{\left\langle \hat{P}^{\mathrm{S}} \right\rangle}$ may be called the singlet probability.

For a pure state, which can be defined by a wavefunction, the density matrix is idempotent, i.e. $\rho^2 = \rho$, such that $\mathrm{Tr}\left[\rho^2\right] = 1$. For a mixed state this idempotency property does not hold, and so $\mathrm{Tr}\left[\rho^2\right] < 1$. Since the trace is invariant under a similarity transform, $\mathrm{Tr}\left[\rho^2\right]$ can be used to distinguish between pure and mixed states no matter the basis in which the density matrix is written. This is equivalent to the observation that, in the eigenbasis of the density matrix, a pure state will have one non-zero element, which will be equal to one, whereas a mixed state will have several non-zero diagonal elements that sum to one.

The explicit density matrix for the general state in Eq. (2.21) is

$$\sigma = \begin{pmatrix} c_{\alpha\alpha}c^*_{\alpha\alpha} & c_{\alpha\alpha}c^*_{\alpha\beta} & c_{\alpha\alpha}c^*_{\beta\alpha} & c_{\alpha\alpha}c^*_{\beta\beta} \\ c_{\alpha\beta}c^*_{\alpha\alpha} & c_{\alpha\beta}c^*_{\alpha\beta} & c_{\alpha\beta}c^*_{\beta\alpha} & c_{\alpha\beta}c^*_{\beta\beta} \\ c_{\beta\alpha}c^*_{\alpha\alpha} & c_{\beta\alpha}c^*_{\alpha\beta} & c_{\beta\alpha}c^*_{\beta\alpha} & c_{\beta\alpha}c^*_{\beta\beta} \\ c_{\beta\beta}c^*_{\alpha\alpha} & c_{\beta\beta}c^*_{\alpha\beta} & c_{\beta\beta}c^*_{\beta\alpha} & c_{\beta\beta}c^*_{\beta\beta} \end{pmatrix}, \tag{2.27}$$

where the diagonal elements can be identified as the probabilities of finding the system in the corresponding state, sometimes referred to as *populations*. The density matrix clearly, in general, contains surplus information than is strictly needed for defining a pure state. In the case of Eq. (2.21) the state of the system is defined using four coefficients, whereas the corresponding density matrix in Eq. (2.27) has 16 elements. This extra capacity is what allows the density matrix to describe mixed states, which can arise when the preparation of the system is not fully known, or when describing quantum entanglement.

In a particular basis, off-diagonal elements in the density matrix are known as *coherences*—they arise from systems in superposition states, and are only non-zero in an ensemble of microscopic systems if there is phase coherence between the system states [95]. These coherences cause the system to oscillate between the basis states. Singlet–triplet coherences are essential in the radical pair mechanism for magnetoreception that will be discussed in Chapter 4, whereby the Earth's field is detected via its influence on the rate of coherent oscillations between singlet and triplet states [96].

Projection operators

A particularly useful operator is the projection operator $\hat{P}^i$, which projects an arbitrary state onto a particular state $|i\rangle$, or equivalently gives the component of a particular state in an arbitrary state. It has the form:

$$\hat{P}^i = \frac{|i\rangle \langle i|}{\langle i \mid i\rangle}, \tag{2.28}$$

such that the projection operator for a basis state i acts on the wavefunction in Eq. (2.19) to give the coefficient of that state multiplied by the state vector,

$$\begin{aligned} \hat{P}^i |\Psi\rangle = \sum_n c_n \frac{|i\rangle \langle i \mid n\rangle}{\langle i \mid i\rangle} &= c_i \frac{|i\rangle \langle i \mid i\rangle}{\langle i \mid i\rangle} \\ &= c_i |i\rangle . \end{aligned} \tag{2.29}$$

However, the use of projection operators is not limited to basis states. For instance, we can construct the singlet projection operator for a singlet involving spins j and k using the form of the singlet wavefunction in Table 2.1 as

$$\begin{aligned} \hat{P}^{\mathrm{S}}_{j,k} &= \left|\mathrm{S}_{j,k}\right\rangle \left\langle \mathrm{S}_{j,k}\right| \\ &= \frac{1}{2} \left(|\alpha\beta\rangle - |\beta\alpha\rangle\right) \left(\langle\alpha\beta| - \langle\beta\alpha|\right) \\ &= \frac{1}{2} \left(|\alpha\beta\rangle \langle\alpha\beta| - |\alpha\beta\rangle \langle\beta\alpha| - |\beta\alpha\rangle \langle\alpha\beta| + |\beta\alpha\rangle \langle\beta\alpha|\right) , \end{aligned} \tag{2.30}$$

where we have assumed that $\langle S_{j,k} | S_{j,k} \rangle = 1$ and dropped the j, k labelling of the α and β states for simplicity. This can be written as a density matrix using Eq. (2.27),

$$\mathbf{P}^{S}_{j,k} = \frac{1}{2}\begin{pmatrix} 0 & 0 & 0 & 0 \\ 0 & +1 & -1 & 0 \\ 0 & -1 & +1 & 0 \\ 0 & 0 & 0 & 0 \end{pmatrix}, \tag{2.31}$$

equivalent to the operator form

$$\hat{P}^{S}_{j,k} = \frac{1}{4}\hat{\mathbb{1}} - \hat{\mathbf{S}}_j \cdot \hat{\mathbf{S}}_k, \tag{2.32}$$

where $\hat{\mathbb{1}}$ is an identity operator.

Since the singlet and triplet states span the Hilbert space of two spin-1/2 particles, the triplet projection operator can be identified as

$$\begin{aligned} \hat{P}^{T}_{j,k} &= \hat{\mathbb{1}} - \hat{P}^{S}_{j,k} \\ &= \frac{3}{4}\hat{\mathbb{1}} + \hat{\mathbf{S}}_j \cdot \hat{\mathbf{S}}_k, \end{aligned} \tag{2.33}$$

where we have used the completeness relation:

$$\sum_i |i\rangle \langle i| = \hat{\mathbb{1}}. \tag{2.34}$$

Entanglement

Entanglement occurs when groups of particles interact such that the quantum state of each part of a system cannot be described separately, but rather the system must be described as a whole. Einstein famously referred to entanglement as "spooky action at a distance" [97].

A particular quantum state is entangled if it cannot be factorised as a product of individual states for each of its constituents, i.e. if it is not separable. Consider

the product of two Hilbert spaces, H_j and H_k, with bases:

$$\begin{aligned} H_j &\rightarrow \left\{\left|1_j\right\rangle, \cdots, \left|n_j\right\rangle\right\}, \\ H_k &\rightarrow \left\{\left|1_k\right\rangle, \cdots, \left|n_k\right\rangle\right\}, \\ H = H_j \otimes H_k &\rightarrow \left\{\left|1_j 1_k\right\rangle, \cdots, \left|1_j n_k\right\rangle, \cdots, \left|n_j 1_k\right\rangle, \cdots, \left|n_j n_k\right\rangle\right\}. \end{aligned} \tag{2.35}$$

If a particular state in H, $\left|\phi\right\rangle = \sum_{n,m} c_{nm} \left|n_j m_k\right\rangle$, is separable it can be written as $\left|\phi\right\rangle = \left|\phi_j\right\rangle \left|\phi_k\right\rangle$, i.e. the product of two separate states in each individual Hilbert space, $\left|\phi_j\right\rangle = \sum_n c_n \left|n_j\right\rangle$ and $\left|\phi_k\right\rangle = \sum_m c_m \left|m_k\right\rangle$, such that the coefficients $c_{nm} = c_n c_m \; \forall \; n, m$. If this decomposition is not possible then it is not separable, and is therefore an entangled state.

From Table 2.1, it is clear that the triplet states $|\mathrm{T}_{+1}\rangle$ and $|\mathrm{T}_{-1}\rangle$ are not entangled—in a basis of α and β states for each spin these are just the product states where both spins are α, or both β. The other two states $|\mathrm{T}_0\rangle$ and $|\mathrm{S}\rangle$ are entangled, since they are not separable—if the first spin is α then the second will be β, and vice versa, in each case.

Given a particular density matrix, it is often useful to quantify the entanglement of that particular state, especially since it is rarely obvious if or how it can be written out in terms of basis states. Entanglement measures is an active area of research, with no one agreed upon standard measure [98].

We will make use of the concurrence measure of entanglement. This is a measure of bipartite entanglement, i.e. entanglement between two spins, as exists in the $|\mathrm{S}\rangle$ and $|\mathrm{T}_0\rangle$ states previously mentioned. The measure ranges from 0 (not entangled) to 1 (fully entangled), where the $|\mathrm{S}\rangle$ state would have a value of 1 and an identity matrix would have a value of 0. For a pair of spins j and k the concurrence can be calculated by first tracing out the other spins in the system to give the reduced density matrix $\rho_{\mathrm{red}}(t) = \mathrm{Tr}_{i \neq \{j,k\}} \left[\hat{\rho}(t)\right]$. The concurrence is then

calculated as in reference [99]:

$$C_{j,k}(t) = \max\{0, \lambda_1 - \lambda_2 - \lambda_3 - \lambda_4\}, \tag{2.36}$$

where λ_i are the eigenvalues of the matrix $\rho_{\text{red}}(t)\left(\sigma_y \otimes \sigma_y\right)\rho_{\text{red}}(t)\left(\sigma_y \otimes \sigma_y\right)$ in decreasing order, and σ_y is the second Pauli matrix.

Spin interactions 2.2

Often a spin system will begin in a defined state, and we will be interested in its evolution under the system Hamiltonian $\hat{\mathcal{H}}$ (see Section 2.2.2). This is given by the time-dependent Schrödinger equation (TDSE):

$$\begin{aligned} \frac{\mathrm{d}}{\mathrm{d}t}|\Psi(t)\rangle &= -\mathrm{i}\hat{\mathcal{H}}|\Psi(t)\rangle \\ \implies |\Psi(t)\rangle &= \mathrm{e}^{-\mathrm{i}\hat{\mathcal{H}}t}|\Psi(0)\rangle, \end{aligned} \tag{2.37}$$

where the solution is valid if the Hamiltonian contains no time-dependent terms.

The TDSE can be recast in terms of a density operator by differentiating Eq. (2.26) and using the complex conjugate of the TDSE, $\frac{\mathrm{d}}{\mathrm{d}t}\langle\Psi(t)| = +\mathrm{i}\langle\Psi(t)|\hat{\mathcal{H}}$:

$$\begin{aligned} \frac{\mathrm{d}\hat{\rho}(t)}{\mathrm{d}t} = \frac{\mathrm{d}}{\mathrm{d}t}\overline{|\Psi(t)\rangle\langle\Psi(t)|} &= \left(\frac{\mathrm{d}}{\mathrm{d}t}\overline{|\Psi(t)\rangle}\right)\overline{\langle\Psi(t)|} + \overline{|\Psi(t)\rangle}\left(\frac{\mathrm{d}}{\mathrm{d}t}\overline{\langle\Psi(t)|}\right) \\ &= -\mathrm{i}\left(\hat{\mathcal{H}}\overline{|\Psi(t)\rangle\langle\Psi(t)|} - \overline{|\Psi(t)\rangle\langle\Psi(t)|}\hat{\mathcal{H}}\right) \\ &= -\mathrm{i}\left(\hat{\mathcal{H}}\hat{\rho}(t) - \hat{\rho}(t)\hat{\mathcal{H}}\right). \end{aligned} \tag{2.38}$$

This is the Liouville-von Neumann equation,

$$\frac{\mathrm{d}\hat{\rho}(t)}{\mathrm{d}t} = -\mathrm{i}\left[\hat{\mathcal{H}}, \hat{\rho}(t)\right]_-, \tag{2.39}$$

where $\left[\hat{A}, \hat{B}\right]_\pm = \hat{A}\hat{B} \pm \hat{B}\hat{A}$ are the commutator and anticommutator—as well as the (subtractive) commutator in Eq. (2.39), sometimes we will make use of the (additive) anticommutator, which can be indicated by the subscript. Solving

this equation allows us to calculate time-dependent observables and explore the dynamics of the system of interest. Using the solution of Eq. (2.37), it has a simple solution for a time-independent Hamiltonian:

$$\begin{aligned}\hat{\rho}(t) = |\Psi(t)\rangle\langle\Psi(t)| &= \mathrm{e}^{-\mathrm{i}\hat{\mathcal{H}}t}\,|\Psi(0)\rangle\langle\Psi(0)|\,\mathrm{e}^{+\mathrm{i}\hat{\mathcal{H}}t} \\ &= \mathrm{e}^{-\mathrm{i}\hat{\mathcal{H}}t}\,\hat{\rho}(0)\mathrm{e}^{+\mathrm{i}\hat{\mathcal{H}}t}.\end{aligned} \tag{2.40}$$

Liouville space 2.2.1

So far we have been working in the system Hilbert space, which is spanned by a basis of orthogonal wavefunctions. Liouville space, also known as operator space, is spanned by a basis of orthogonal spin operators. The density matrices from the Hilbert space are row-wise flattened to form state vectors representing the density operators, such that an n-dimensional Hilbert space produces an n^2-dimensional Liouville space. We use the notation $|\rho(t)\rangle$ if we want to explicitly invoke this form:

$$\rho(t) = \begin{pmatrix} \rho_{11} & \cdots & \rho_{1n} \\ \rho_{21} & \cdots & \rho_{2n} \\ \vdots & \ddots & \vdots \\ \rho_{n1} & \cdots & \rho_{nn} \end{pmatrix} \quad\Longleftrightarrow\quad |\rho(t)\rangle = \begin{pmatrix} \rho_{11} \\ \vdots \\ \rho_{1n} \\ \rho_{21} \\ \vdots \\ \rho_{2n} \\ \vdots \\ \rho_{n1} \\ \vdots \\ \rho_{nn} \end{pmatrix}. \tag{2.41}$$

The Liouville-von Neumann equation can then be re-written as

$$\frac{\mathrm{d}}{\mathrm{d}t}\hat{\rho}(t) = -\mathrm{i}\hat{\hat{\mathcal{H}}}\left[\hat{\rho}(t)\right], \tag{2.42}$$

where the Hamiltonian superoperator is

$$\hat{\hat{\mathcal{H}}}\left[\hat{\rho}(t)\right] \Longleftrightarrow \hat{\mathcal{H}}\hat{\rho}(t) - \hat{\rho}(t)\hat{\mathcal{H}} = \left[\hat{\mathcal{H}}, \hat{\rho}(t)\right]_{-}, \tag{2.43}$$

or, equivalently,

$$\hat{\hat{\mathcal{H}}} = \hat{\mathcal{H}} \otimes \hat{\mathbb{1}} - \hat{\mathbb{1}} \otimes \hat{\mathcal{H}}^{\mathrm{T}}. \tag{2.44}$$

Superoperators, denoted by a double hat, operate on spin operators. We will indicate this using square-bracket function notation: $\hat{\hat{\mathcal{L}}}\left[\hat{\rho}(0)\right]$. In terms of practically performing calculations, this involves transforming the density matrix to the vector form $|\rho\rangle$, pre-multiplying it by the Liouville space matrix $\mathcal{L}$, and then (if necessary) transforming it back into square density matrix form. The utility of Liouville space is that it allows us to describe non-coherent and relaxation evolution processes involving transfers of populations and coherences between elements of the density matrix.

Stochastic Liouville equation

The coherent spin dynamics, reactivity, and spin relaxation for a system of interacting electronic and/or nuclear spins together determine the time dependence of the density operator describing that spin system. This time dependence can be calculated by solving a stochastic Liouville master equation [100–103] for the spin density matrix $\hat{\rho}(t)$,

$$\begin{aligned} &\frac{\mathrm{d}}{\mathrm{d}t}\hat{\rho}(t) = -\hat{\hat{\mathcal{L}}}\left[\hat{\rho}(t)\right] \\ \Longrightarrow\ &\hat{\rho}(t) = \exp\left(-\hat{\hat{\mathcal{L}}}t\right)\left[\hat{\rho}(0)\right], \end{aligned} \tag{2.45}$$

where the Liouvillian $\hat{\hat{\mathcal{L}}} = \mathrm{i}\hat{\hat{\mathcal{H}}}_0 + \hat{\hat{\mathcal{K}}} + \hat{\hat{\Gamma}}$ contains the commutator superoperator corresponding to the coherent Hamiltonian $\hat{\mathcal{H}}_0$, the reaction superoperator $\hat{\hat{\mathcal{K}}}$, and the relaxation superoperator $\hat{\hat{\Gamma}}$ (which can often be related to stochastic time-dependent processes described by a time-dependent Hamiltonian $\hat{\mathcal{H}}_1(t)$). This

solution is valid because $\hat{\hat{\mathcal{L}}}$ contains no time dependent terms. The superoperators $\hat{\hat{\mathcal{H}}}_0$, $\hat{\hat{\mathcal{K}}}$, and $\hat{\hat{\Gamma}}$ will be introduced in Sections 2.2.2, 2.2.4, and 2.2.5.

Combining the ensemble average expectation value in Eq. (2.24) and the solution to Eq. (2.45) allows us to calculate the time-dependent probability $p^i(t)$ for an operator $\hat{P}^i$:

$$\begin{aligned} p^i(t) &= \mathrm{Tr}\left[\hat{P}^i\,\hat{\rho}(t)\right] \\ &= \mathrm{Tr}\left[\hat{P}^i\,\exp\left(-\hat{\hat{\mathcal{L}}}t\right)[\hat{\rho}(0)]\right]. \end{aligned} \tag{2.46}$$

If we consider a simple process whereby singlet radical pairs undergo a first order reaction with rate constant k_S to form a singlet-derived product, the final fractional yield of this singlet product (which we label Φ_S) can be calculated via a rate equation:

$$\begin{aligned} \frac{\mathrm{d}\Phi_\mathrm{S}(t)}{\mathrm{d}t} &= k_\mathrm{S}\,p^\mathrm{S}(t) \\ \implies \Phi_\mathrm{S} = \Phi_\mathrm{S}(\infty) &= k_\mathrm{S}\int_0^\infty p^\mathrm{S}(t)\,\mathrm{d}t, \end{aligned} \tag{2.47}$$

where the rate of change of $\Phi_\mathrm{S}(t)$ is proportional to the singlet reaction rate constant and the fractional population of the singlet state $p^\mathrm{S}(t)$. This is the same as the probability of the system being in the singlet state, and so substitution of Eq. (2.46) allows us to write the final fractional yield of singlet products after all radical pairs have disappeared (often referred to simply as the *singlet yield*) as

$$\Phi_\mathrm{S} = k_\mathrm{S}\int_0^\infty \mathrm{Tr}\left[\hat{P}^\mathrm{S}\,\exp\left(-\hat{\hat{\mathcal{L}}}t\right)[\hat{\rho}(0)]\right]\,\mathrm{d}t. \tag{2.48}$$

Only the exponential term in Eq. (2.48) is time-dependent, and since $\hat{\hat{\mathcal{L}}}$ contains no time-dependent terms the integral has a simple solution:

$$\begin{aligned} \Phi_\mathrm{S} &= k_\mathrm{S}\mathrm{Tr}\left[\hat{P}^\mathrm{S}\int_0^\infty \exp\left(-\hat{\hat{\mathcal{L}}}t\right)\,\mathrm{d}t\;[\hat{\rho}(0)]\right] \\ &= k_\mathrm{S}\mathrm{Tr}\left[\hat{P}^\mathrm{S}\,\hat{\hat{\mathcal{L}}}^{-1}\,[\hat{\rho}(0)]\right]. \end{aligned} \tag{2.49}$$

Spin Hamiltonian 2.2.2

The TDSE, Eq. (2.37), states that the Hamiltonian operator governs the time evolution of the system of interest, and we now consider the form of this spin Hamiltonian in more detail.

The spin Hamiltonian $\hat{\mathcal{H}}^i(t)$ for a molecule i can often be divided into two components

$$\hat{\mathcal{H}}^i(t) = \hat{\mathcal{H}}^i_0 + \hat{\mathcal{H}}^i_1(t), \tag{2.50}$$

where $\hat{\mathcal{H}}^i_0$ describes coherent interactions, while $\hat{\mathcal{H}}^i_1(t)$ describes time-dependent interactions and is responsible for equilibration of the spin states.

Whether coherent or time-independent, the Hamiltonian contains terms of the form

$$\hat{\mathcal{H}} = \hat{\mathbf{S}}_i \cdot \mathbf{A} \cdot \hat{\mathbf{R}}_j \tag{2.51}$$

where $\hat{\mathbf{S}}_i$ is the vector of spin operators for the spin of interest, $\mathbf{A}$ is an interaction tensor, and $\hat{\mathbf{R}}_j$ is a vector of either scalars or operators describing the interaction partner.

The spin Hamiltonian for a pair of non-interacting molecules a and b can be written as

$$\hat{\mathcal{H}}(t) = \hat{\mathcal{H}}^a(t) \oplus \hat{\mathcal{H}}^b(t), \tag{2.52}$$

where $\oplus$ is the direct sum $\hat{\mathrm{A}} \oplus \hat{\mathrm{B}} = \hat{\mathrm{A}} \otimes \hat{\mathbb{1}}_{\mathrm{B}} + \hat{\mathbb{1}}_{\mathrm{A}} \otimes \hat{\mathrm{B}}$ and $\hat{\mathbb{1}}_i$ is of a size appropriate for molecule i. This is applicable to both coherent and time-dependent interactions, and could easily be generalised to more than two molecules (in this thesis we will consider two at most).

Zeeman interaction

Following Eq. (2.8), the Hamiltonian describing the Zeeman interaction between a spin and a magnetic field is

$$\begin{aligned}\hat{\mathcal{H}}_Z &= -\gamma_i \mathbf{B}\left(\theta,\phi\right)\cdot\hat{\mathbf{S}}_i \\ &= \boldsymbol{\omega}_i\left(\theta,\phi\right)\cdot\hat{\mathbf{S}}_i.\end{aligned} \tag{2.53}$$

The vector $\mathbf{B}\left(\theta,\phi\right)$ describes the orientation of the spin system with respect to the external magnetic field axis, and varies with the polar angles θ and ϕ:

$$\mathbf{B}\left(\theta,\phi\right) = B_0\begin{pmatrix}\sin\theta\cos\phi\\ \sin\theta\sin\phi\\ \cos\theta\end{pmatrix}, \tag{2.54}$$

where B_0 is the magnitude of the external field, θ is the polar angle and ϕ the azimuthal angle describing the relative orientation of the field and the z-axis.

Often we define an external magnetic field as aligned entirely with the z-axis, with no components in the x or y directions. In this case the Zeeman interaction becomes a scalar interaction with only the z-component of the spin:

$$\begin{aligned}\hat{\mathcal{H}}_Z &= -\gamma_i\, B_0\,\hat{S}_{iz} \\ &= \omega_0\,\hat{S}_{iz}.\end{aligned} \tag{2.55}$$

Spin–spin coupling

In a multi-spin system, the magnetic moments associated with the spins also interact with each other. The subtleties of these interactions are complex, and for our purposes we focus on two types of interaction. The magnetic dipole–dipole interaction, often called dipolar coupling, occurs because electrons and nuclei behave as dipoles in the presence of each other's magnetic fields. Spins may also

interact via the Fermi contact interaction, which arises from the electron–nuclear dipolar interaction when taking into account the finite radius of the nucleus.

The result of these interactions can be seen in the nucleus–nucleus J-coupling, the electron–nucleus hyperfine coupling, and the nucleus–nucleus dipolar coupling.

J-coupling

The Hamiltonian describing J-coupling between two nuclei j and k has the form

$$\hat{\mathcal{H}}_{\mathrm{J}} = 2\pi\, \hat{\mathbf{I}}_j \cdot \mathbf{J}_{jk} \cdot \hat{\mathbf{I}}_k \tag{2.56}$$

where the tensor $\mathbf{J}_{jk}$ describes this internuclear coupling, mainly caused by the isotropic Fermi contact interaction. The interaction tensor may also have small anisotropic components—these have the same form as the direct dipolar coupling (see below), alongside which they are sometimes treated [104–106]. In an isotropic liquid we consider the orientational average of this tensor, i.e. an average of the diagonal elements of the J-coupling tensor in Eq. (2.56) [104], such that the coupling between nuclei j and k is given by $\hat{\mathcal{H}}_{\mathrm{J}} = 2\pi\, J_{jk}\, \hat{\mathbf{I}}_j \cdot \hat{\mathbf{I}}_k$.

Hyperfine coupling

The Hamiltonian describing hyperfine coupling between an electron j and nucleus k has the form

$$\hat{\mathcal{H}}_{\mathrm{HF}} = \gamma_i\, \hat{\mathbf{S}}_j \cdot \mathbf{A}_k \cdot \hat{\mathbf{I}}_k, \tag{2.57}$$

where the interaction tensor $\mathbf{A}_k$ is labelled only with the nuclear spin index k, since in general a radical will contain only one electron but potentially multiple nuclei. A symmetric hyperfine tensor, transformed into diagonal form using rotation matrices, can be written:

$$\mathbf{A}_k = a_k \mathbb{1}_3 + \mathbf{T}_k. \tag{2.58}$$

It is made up of isotropic and anisotropic components: the isotropic component a_k comes once more from the Fermi contact interaction, whereas the (often significant) anisotropic components contained in the traceless tensor $\mathbf{T}_k$ come from the electron–nucleus dipolar interaction [107].

The anisotropic tensor can be characterised by two parameters α and β, which are proportional to the axiality and rhombicity (respectively) of the tensor:

$$\mathbf{T} = \alpha \begin{pmatrix} (1-\beta) & 0 & 0 \\ 0 & (1+\beta) & 0 \\ 0 & 0 & -2 \end{pmatrix}, \tag{2.59}$$

where we have dropped the k subscript for convenience. The hyperfine interaction is described as isotropic if $\alpha = 0$, axial if $\alpha \neq 0$, $\beta = 0$, and rhombic if $\alpha, \beta \neq 0$.

Dipolar interaction

As electron–nucleus dipolar interactions contribute to the anisotropic hyperfine coupling, nucleus–nucleus and electron–electron dipolar coupling can also contribute to the spin Hamiltonian. The dipolar coupling constant gives the strength of these interactions for two spins j and k separated by a distance r_{jk}, with μ_0 the vacuum permeability:

$$b_{jk} = -\frac{\mu_0 \gamma_j \gamma_k \hbar}{4\pi r_{jk}^3}. \tag{2.60}$$

When modelling radical pair systems, electron–electron and nucleus–nucleus interactions are sometimes ignored (although see Section 2.2.3 and the discussion of singlet–triplet dephasing in Section 5.2.2 for examples of cases when electron–electron interactions should not be ignored). However, when considering systems of nuclei without unpaired electrons, the dipolar interaction between two nuclei j and k can be important. In this case the Hamiltonian is given by

$$\hat{\mathcal{H}}_{\mathrm{D}} = \frac{b_{jk}}{r_{jk}^2}\left(3\left(\hat{\mathbf{S}}_j.\mathbf{r}_{jk}\right)\left(\hat{\mathbf{S}}_k.\mathbf{r}_{jk}\right) - r_{jk}^2\left(\hat{\mathbf{S}}_j.\hat{\mathbf{S}}_k\right)\right), \tag{2.61}$$

where $\mathbf{r}_{jk}$ is the vector connecting the positions of the two nuclei such that $|\mathbf{r}_{jk}| = r_{jk}$ [104]. If the internuclear axis is defined as the z-axis then this has the simpler form:

$$\hat{\mathcal{H}}_{\mathrm{D}} = 2b_{jk}\left(\hat{S}_{jz}\hat{S}_{kz} - \frac{1}{2}\hat{S}_{jx}\hat{S}_{kx} - \frac{1}{2}\hat{S}_{jy}\hat{S}_{ky}\right). \tag{2.62}$$

For molecules tumbling isotropically in solution the intramolecular nuclear dipolar couplings average to zero and cannot be seen in the NMR spectrum, unlike the J-couplings. However, the instantaneous value of the dipolar coupling does not disappear. As the molecule tumbles in solution the orientation of the vector $\mathbf{r}_{jk}$ with respect to a fixed axis will change, and this fluctuating magnetic interaction can be a source of spin relaxation. We will model this fluctuation for a system of nuclear spins in Chapter 3.

Further spin interactions 2.2.3

These are not the only interactions that can be of importance when considering interacting systems of spins.

In radical pairs the Zeeman interaction and hyperfine couplings often dominate the spin dynamics, but the dipolar, $D(r)$, and exchange, $J(r)$, coupling between the electron spins can be of similar importance [33, 108]. Both of these depend inversely on r, the inter-radical distance: $D(r) \propto r^{-3}$ and $J(r) \propto \exp(-r)$ [108]. If either (a), the radicals are sufficiently separated that $|D(r)|$ and $|J(r)|$ are both much smaller than the magnitude of the Zeeman interaction and hyperfine couplings, or (b), the effects of the dipolar and exchange interactions are of approximately equal magnitude and opposite sign, then the system is assumed to evolve principally under the influence of the Zeeman and hyperfine interactions only, and electron-coupling interactions can be ignored [108]. If this is not the case then they should be considered.

In radical pair systems we also often ignore any nuclear Zeeman or nucleus–nucleus dipolar interactions, because both of these depend on the gyromagnetic ratio, far smaller for nuclei than for electrons.

As will be seen in Chapter 4, the spin–orbit coupling between the electron spin and the magnetic field generated by the electron's orbital motion can be important. For low-symmetry radicals with no heavy atomic nuclei this coupled orbital angular momentum is not preserved along any axis, and the orbital angular momentum is said to be quenched [109]. This is the case for almost all organic radicals, but when this is not the case anisotropy can be introduced into the electron g-factor, and the spin–orbit coupling can potentially enhance or diminish MFEs [109]. This will be considered in more detail for the linear $CO_2^{\bullet -}$ radical, which has strong unquenched spin–orbit coupling, in Chapter 5.

In closed shell systems of non-quadrupolar nuclei (i.e. without any spins that have $I > 1/2$) the principal nuclear spin interaction that we have not mentioned is chemical shift anisotropy [104]—this can be an important spin interaction at high magnetic field strengths, but is far less important in the low field considered in Chapter 3.

Haberkorn superoperator 2.2.4

If all possible spin states in a system can undergo a first-order reaction with the same rate constant k then the elements of the density matrix will decay with an equal rate. This can be represented by a simple rate equation:

$$\frac{\mathrm{d}}{\mathrm{d}t}\boldsymbol{\rho}_{ij}(t) = -k\boldsymbol{\rho}_{ij}(t) \iff \frac{\mathrm{d}}{\mathrm{d}t}\hat{\rho}(t) = -k\hat{\hat{\mathbb{1}}}\left[\hat{\rho}(t)\right], \tag{2.63}$$

where $\hat{\hat{\mathbb{1}}}$ is simply an identity superoperator. What happens if only a subset of spin states can react? Often, when considering radical pairs, only the singlet subspace (for instance) can undergo a particular reaction.

This can be modelled using a reaction operator. There is some debate over the best form of reaction operator to use when performing spin dynamics calculations [110–112]; in this thesis we will exclusively use the Haberkorn operator [113, 114]. It is a well-established and relatively simple model for spin-selective reactions, and it has recently been rigorously justified using high-order perturbation theory from first principles [112] that the form of reaction operator described here is consistent with the well-established theory of electron transfer reactions. The rationale for the form of the reaction operator is presented below for a simple two-state system, and this form also holds for any larger spin system in the usual $\{|\alpha\rangle, |\beta\rangle\}$ basis.

Consider a system where singlet radical pairs can react with a first order rate constant k_S, and triplets cannot undergo this reaction but instead react with a rate constant k_T, following references [110, 114]. We work in a simple two-level system with basis states $\{|S\rangle, |T\rangle\}$ such that the system state is $|\Psi\rangle = \sqrt{n_S}\,|S\rangle + \sqrt{n_T}\,|T\rangle$ with n_S the fractional population of singlet, n_T the fractional population of triplet, and $n_S + n_T = 1$ such that the wavefunction is correctly normalized. The density matrix for this state is:

$$\boldsymbol{\rho} = \begin{pmatrix} \rho_{SS} & \rho_{ST} \\ \rho_{TS} & \rho_{TT} \end{pmatrix}, \tag{2.64}$$

where $\rho_{SS} = n_S$ and similarly for the triplet fraction.

In this basis, the singlet and triplet projection operators are simply

$$\mathbf{P}^S = \begin{pmatrix} 1 & 0 \\ 0 & 0 \end{pmatrix}, \quad \mathbf{P}^T = \begin{pmatrix} 0 & 0 \\ 0 & 1 \end{pmatrix}, \tag{2.65}$$

and the anticommutators of these operators with the density matrix are

$$\begin{aligned} [\mathbf{P}^S, \boldsymbol{\rho}]_+ &= \begin{pmatrix} 2\rho_{SS} & \rho_{ST} \\ \rho_{TS} & 0 \end{pmatrix}, \\ [\mathbf{P}^T, \boldsymbol{\rho}]_+ &= \begin{pmatrix} 0 & \rho_{ST} \\ \rho_{TS} & 2\rho_{TT} \end{pmatrix}. \end{aligned} \tag{2.66}$$

We define a reaction operator equation

$$\frac{\mathrm{d}}{\mathrm{d}t}\hat{\rho}(t) = -\hat{\hat{\mathcal{K}}}\left[\hat{\rho}(t)\right], \tag{2.67}$$

where $\hat{\hat{\mathcal{K}}}$ is

$$\hat{\hat{\mathcal{K}}}\left[\hat{\rho}(t)\right] = \frac{1}{2}k_{\mathrm{S}}[\hat{P}^{\mathrm{S}}, \hat{\rho}]_{+} + \frac{1}{2}k_{\mathrm{T}}[\hat{P}^{\mathrm{T}}, \hat{\rho}]_{+}. \tag{2.68}$$

We can use Eq. (2.66) to write Eq. (2.67) in Liouville space,

$$\frac{\mathrm{d}}{\mathrm{d}t}\begin{pmatrix}\rho_{\mathrm{SS}}\\ \rho_{\mathrm{ST}}\\ \rho_{\mathrm{TS}}\\ \rho_{\mathrm{TT}}\end{pmatrix} = -\frac{1}{2}\begin{pmatrix}2\rho_{\mathrm{SS}}k_{\mathrm{S}}\\ \rho_{\mathrm{ST}}(k_{\mathrm{S}}+k_{\mathrm{T}})\\ \rho_{\mathrm{TS}}(k_{\mathrm{S}}+k_{\mathrm{T}})\\ 2\rho_{\mathrm{TT}}k_{\mathrm{T}}\end{pmatrix}, \tag{2.69}$$

allowing us to identify the reaction superoperator $\hat{\hat{\mathcal{K}}}$ in matrix form simply as

$$\boldsymbol{\mathcal{K}} = \begin{pmatrix}-k_{\mathrm{S}} & 0 & 0 & 0\\ 0 & -\frac{1}{2}(k_{\mathrm{S}}+k_{\mathrm{T}}) & 0 & 0\\ 0 & 0 & -\frac{1}{2}(k_{\mathrm{S}}+k_{\mathrm{T}}) & 0\\ 0 & 0 & 0 & -k_{\mathrm{T}}\end{pmatrix}. \tag{2.70}$$

The solution to the first order differential equation (2.67) is

$$\hat{\rho}(t) = \exp\left(-\hat{\hat{\mathcal{K}}}t\right)\left[\hat{\rho}(0)\right], \tag{2.71}$$

and since the matrix form of $\hat{\hat{\mathcal{K}}}$ is diagonal in the basis of interest it is now clear that the singlet and triplet states simply decay with rate constants k_{S} and k_{T} as expected, while the coherences in the density matrix decay with the average of these two rate constants. If $k_{\mathrm{S}} = k_{\mathrm{T}}$ then all spin states decay at the same rate, and we regain Eq. (2.63).

Relaxation superoperators 2.2.5

Consider once more the rate of change for an element of the density matrix relaxing to some equilibrium via a first-order process:

$$\frac{\mathrm{d}}{\mathrm{d}t}\rho_{ij}(t) = -k_{ij}\rho_{ij}(t). \tag{2.72}$$

The decay rate constant for this element, k_{ij}, should in general depend on the value of that particular element (the self-relaxation rate) and all the other values in the density matrix (the rate of transfer of populations or coherences).

This would have the form

$$\frac{\mathrm{d}}{\mathrm{d}t}\rho_{ij}(t) = -\sum_{mn} k_{ij,mn}\rho_{mn}(t), \tag{2.73}$$

where the subscripts ij and mn relate to row and column indices for the density matrix, such that $k_{ij,ij}$ gives the self-relaxation rate for $\rho_{ij}(t)$. We have already seen in the Haberkorn operator, Eq. (2.70), an example of a Liouville space operator that includes self-relaxation rates along its diagonal. Relaxation operators extend this idea to include off-diagonal elements $k_{ij,mn}$ that give the rates for transfers of populations or coherences. This would not be possible simply using a Hilbert space formulation of the Liouville-von Neumann equation, where the rate of change of any element of the density matrix depends only on its current value and those with which it is directly linked (i.e. the coherences in its own row or column).

Liouville space allows us to construct a relaxation superoperator where the decay rate for each element of the density matrix depends on all other elements in the density matrix. For instance, for the two level singlet–triplet system used

in Section 2.2.4 we have

$$\frac{\mathrm{d}}{\mathrm{d}t}\begin{pmatrix}\rho_{SS}\\ \rho_{ST}\\ \rho_{TS}\\ \rho_{TT}\end{pmatrix} = -\begin{pmatrix}\Gamma_{SS,SS} & \Gamma_{SS,ST} & \Gamma_{SS,TS} & \Gamma_{SS,TT}\\ \Gamma_{ST,SS} & \Gamma_{ST,ST} & \Gamma_{ST,TS} & \Gamma_{ST,TT}\\ \Gamma_{TS,SS} & \Gamma_{TS,ST} & \Gamma_{TS,TS} & \Gamma_{TS,TT}\\ \Gamma_{TT,SS} & \Gamma_{TT,ST} & \Gamma_{TT,TS} & \Gamma_{TT,TT}\end{pmatrix}\begin{pmatrix}\rho_{SS}\\ \rho_{ST}\\ \rho_{TS}\\ \rho_{TT}\end{pmatrix}, \tag{2.74}$$

where $\Gamma_{SS,SS}$ (for example) is the rate of singlet self-relaxation, while $-\Gamma_{SS,TT}$ is the rate of transfer of triplet population to singlet, and $-\Gamma_{SS,ST}$ is the rate of transfer of singlet–triplet coherence to singlet population. This is more compactly written in terms of the relaxation superoperator $\hat{\hat{\Gamma}}$ as

$$\frac{\mathrm{d}}{\mathrm{d}t}\hat{\rho}(t) = -\hat{\hat{\Gamma}}\hat{\rho}(t). \tag{2.75}$$

Deciding on the form of the relaxation superoperator is not a trivial problem, and will be of concern throughout this thesis. In Chapter 3 we will derive a relaxation superoperator for a system of nuclear spins using Redfield theory. In Chapters 4 and 5 we will consider various phenomenological relaxation superoperators that describe relaxation processes known to occur in radical pair systems.

For many of the relaxation processes we will consider in this thesis, the rate at which small molecules tumble freely in solution will be critical. In these cases the correlation time for Brownian rotational diffusion of a spherical molecule, which is the average time for a molecule to tumble through an angle of one radian, can be estimated using the Stokes–Einstein equation:

$$\tau_c = \frac{4\pi\eta a^3}{3k_B T}, \tag{2.76}$$

where the molecule has radius a in a medium with viscosity η at temperature T [115, 116].

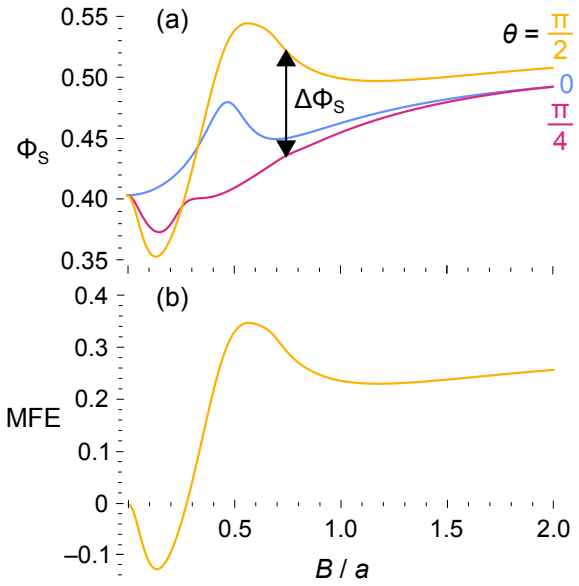

Figure 2.3 Demonstration of MFEs on a toy radical pair system. (a) The singlet yield Φ_S as a function of magnetic field strength for three different relative orientations of the field and the radical pair, described by an angle $\theta = 0$, $\pi/4$, and $\pi/2$ ($\phi = 0$ in all cases). The anisotropy of the singlet yield is the difference between the maximum and minimum values of Φ_S across all relative angles (i.e. more than just the three shown here): $\Delta\Phi_S = \max\left[\Phi_S(\theta,\phi)\right] - \min\left[\Phi_S(\theta,\phi)\right]$. It can be used to quantify the anisotropic response of the radical pair at that particular field strength. (b) The magnetic field effect (MFE) for $\theta = \pi/2$. This MFE is calculated, for a particular orientation of the two radicals, as the difference between the singlet yield at field strength B and at zero field: MFE = $\Phi_S(B) - \Phi_S(0)$. This can be normalized against the value of $\Phi_S(0)$ if desired, as has been done here.

Magnetic field effects 2.3

The effect of an applied magnetic field on a chemical reaction can vary according to, amongst other things, the magnitude of the applied magnetic field, and its orientation with respect to the molecular system. Both of these pieces of information are contained in the vector $\mathbf{B}(\theta,\phi)$, which describes the relative orientation of the molecular axes and the external magnetic field axis.

The singlet yield calculation in Section 2.2.1 involves the Liouvillian operator, which depends on this field vector via the Zeeman interaction in the Hamiltonian and other interactions that we will explore later. The singlet yield calculated with Eq. (2.49) may, therefore, vary as the magnetic field strength B_0 and the polar angles θ and ϕ are varied.

Variation in the singlet yield with both field intensity and orientation, which we call a magnetic field effect (MFE), is shown in Fig. 2.3 for a second model radical pair system.[2] The singlet yield, Φ_S can be calculated for a variety of field strengths and relative orientations, yielding magnetic response curves such as those shown in Fig. 2.3(a). The overall MFE for a given orientation of the field can be defined as the difference between the singlet yield at field strength B and at zero field: MFE $= \Phi_S(B) - \Phi_S(0)$. This value is often normalized against the value of $\Phi_S(0)$, as has been done in Fig. 2.3(b). In Chapter 5 we will be particularly interested in the sign of this change in Φ_S as a field is applied, classifying a field effect as positive if the value of the MFE > 0 at the maximum field strength, or negative if MFE < 0 at this point.

Anisotropic responses 2.3.1

The use of any directional information derived from a radical pair reaction is assumed to be directly related to the difference in magnitude of the product yield achievable from this reaction as the direction of the magnetic field varies with respect to the molecular system.

In this thesis we will use the anisotropy of the singlet yield as a measure of the suitability of a radical pair for detecting field direction, which we quantify as

$$\Delta\Phi_S = \max\left[\Phi_S(\theta,\phi)\right] - \min\left[\Phi_S(\theta,\phi)\right], \tag{2.77}$$

that is the difference between the maximum and minimum values of the singlet yield across all relative orientations of the magnetic field vector and the radical pair. This difference is indicated for a particular value of B in Fig. 2.3(a), but in full calculations the complete range of θ and ϕ are used. Often the anisotropic

[2] In this case the model system is composed of a radical pair in a magnetic field of magnitude B where one of the partner radicals is coupled to a spin-1/2 nucleus (isotropic hyperfine component a, anisotropic components $\alpha = -0.2$, $\beta = 0$, see Section 2.2.2). Relaxation was not included, and both the singlet and triplet forms of the radical pair undergo a reaction with rate constant $k = a/10$. The singlet yield was calculated using a method described in [117].

magnetic response will have inversion symmetry, such that calculations can be sped up by only considering half of the full spherical range of θ and ϕ values [118]. Larger values of $\Delta\Phi_S$ are assumed to provide a more efficient sensor and therefore a more precise compass bearing.

3 Quantum neural processing

Two sets of experiments conducted in the 1970s and 1980s have lent some support to the idea that magnetic spin states may have a biochemical purpose in the brain. As we will see in Chapter 4, quantum effects caused by spin states can, in theory, have biologically relevant effects despite a thermally noisy physiological environment.

The experiments concerned involved lithium, which exists as a mixture of two nuclear isotopes, ^{6}Li and ^{7}Li, in the approximate ratio 8:92 (see Table A.1). Li salts, in their natural isotopic abundance, have commonly been used to treat bipolar disorder in humans, and in a 1979 study the mobility of male rats was shown to be reduced more profoundly by isotopically pure ^{6}Li than by ^{7}Li [119]. In a later study, pregnant rats were treated with isotopically pure Li salts; the ^{6}Li treated mothers groomed and nursed their offspring more than untreated mothers, while those treated with ^{7}Li ignored their offspring and nursed them less frequently [120].

There are two plausible explanations for these experimental results: (1) a kinetic isotope effect (KIE), due to the relatively large ~16% difference in mass between the two isotopes (only reactions involving hydrogen and helium could possibly have larger KIEs), or (2) a magnetic isotope effect (MIE); ^{6}Li has spin quantum number $I = 1$ and a particularly weak quadrupole moment, meaning it behaves more like a spin-$1/2$ than many other nuclei with $I > \frac{1}{2}$, whereas ^{7}Li has $I = \frac{3}{2}$ and a stronger quadrupole moment [121, 122].

A clear interpretation of the, sometimes contradictory, data in references [119] and [120] has been difficult to obtain, in part due to methodological deficiencies. A study published in 2020 aimed to more thoroughly address any isotope-dependent effects of lithium on animal behaviour [45]. Rats were given food containing either natural istopic-abundance Li salts, pure ^{6}Li salts, pure ^{7}Li salts, or NaCl as a control. No difference was found in behaviour after 30 days of this treatment; the animals then continued on this diet but with an added injection of either ketamine (ketamine-induced hyperactivity is a proposed animal model of manic behaviour) or saline (as a control) for eleven further days. On four consecutive days at the end of this regime the hyperlocomotion[1] of the rats was recorded immediately after ketamine injection. It was found that, on the last day alone, the ^{6}Li treated animals exhibited significantly greater and more prolonged reductions in hyperactivity than the other groups. All three Li groups responded similarly on the first three of the four trial days, and it appears that the manic response-attenuating effects of Li strengthened over the four days in all groups, with ^{6}Li eventually producing stronger and longer-lasting effects than either ^{7}Li or natural-abundance Li.

The reason for this apparent differential development of Li responses has yet to be determined. A 2021 study [123] suggests that lithium may influence the recombination dynamics of an oxygen-based radical pair (in fact the [$FADH^{\bullet}$ $O_2^{\bullet -}$] radical pair that is the focus of Chapter 4), using a model of this system to reproduce the observed isotopic dependence in lithium treatment demonstrated in reference [45]. It predicts that the effectiveness of Li treatment should therefore be magnetic-field dependent, providing a potential test of this hypothesis.

Fisher's "quantum cognition" hypothesis 3.1

These lithium results could be taken as an indication that the magnetic properties of nuclei may have an effect on the biochemistry of the brain. This was the

[1] Incessant movement, usually as a result of excessive stimulation of the nervous system.

interpretation of Matthew Fisher when, in 2015, he proposed that ^{31}P nuclear spins might be involved in human neural processing, in a hypothesis that he called "quantum cognition" [42].[2] He envisaged networks of singlet-entangled ^{31}P quantum bits (qubits) contained in $Ca_9(PO_4)_6$ molecules, arguing that when these molecules diffuse into spatially distant neurons they could trigger quantum correlated discharge of Ca^{2+} ions as part of a "quantum-to-biochemical transduction" mechanism [44]. It has been claimed that these molecules would remain entangled for a day "or possibly much longer" [43].

In Fisher's quantum cognition hypothesis, pairs of entangled ^{31}P nuclei are prepared in PO_4^{3-} molecules via an enzymatic process. He argues that hydrolysis of pyrophosphate, $P_2O_7^{4-}$, will have a reaction rate that "depends on the [^{31}P] nuclear spin states, different for singlet and triplet states". In particular, he argues that only $P_2O_7^{4-}$ in which the ^{31}P are singlet-entangled will be successfully hydrolysed, due to a proposed joint rotational-nuclear spin selection rule [124, 125].

These entangled phosphates are then incorporated into separate $Ca_9(PO_4)_6$ molecules to form a network of intermolecularly entangled Posner molecules [42–44, 47]. This process is represented in Fig. 3.1. The entangled $Ca_9(PO_4)_6$ would diffuse into spatially distant neurons, and reactions at one of the entangled molecules may correlate with reactions at the other [42]. For instance, release of Ca^{2+} in a synapse from one Posner molecule may occur alongside a correlated reaction at its entangled partner [42].

Whether this mechanism for singlet state preparation is biochemically plausible *in vivo* is debatable. In particular, there is no clear mechanism to explain how the $Ca_9(PO_4)_6$ molecules would be built up from specific entangled ^{31}P ions, or how the entanglement between ^{31}P ions would persist from $P_2O_7^{4-}$ hydrolysis

[2] Fisher defines *quantum cognition* as a quantum process that modulates "the excitability and signaling of neurons" [42]. Cognition more typically refers to the process of acquiring knowledge and understanding, hence in this thesis we have preferred the term *quantum neural processing*.

to $Ca_9(PO_4)_6$ formation. However unlikely these processes may appear, testing them theoretically would involve speculating further about, and perhaps extending, Fisher's hypothesis. This speculation was not the aim of this work, and since we are specifically interested in rigorously testing the lifetime of the proposed entangled states in order to assess the feasibility of the hypothesis, the details of the preparation mechanism are largely irrelevant to this study. For our purposes, we simply assume that the intermolecular singlet state could be prepared.

A 2020 experimental study aimed to test this model [46], by varying the amount and isotopic composition of calcium in a model organism, which should affect the formation of Posner molecules and therefore (according to Fisher's hypothesis) neural processing. Mice were treated with sevoflurane, an anaesthetic that causes a loss of righting reflex (LORR), used here to simulate a lowering of consciousness or impaired neural processing. An increase in the dose of sevoflurane needed to induce LORR is used as an indicator for an increased consciousness level [126].

It was predicted that mice that were also treated with the calcium chelating octadentate ligand EGTA[3] would require a smaller dose of sevoflurane; according to Fisher's hypothesis, a lower availability of Ca^{2+} ions means less production of Posner molecules and therefore lowered consciousness. However, the study found the opposite: mice treated with EGTA were in fact found to require a significantly increased dose of sevoflurane compared to before treatment with EGTA [46].

Similarly, it was predicted that mice treated with $CaCl_2$ would require an increased dose of sevoflurane to induce LORR, due to increased production of Posner molecules. The opposite was found, with the $CaCl_2$-treated mice requiring a significantly lower dose of sevoflurane compared to before treatment with $CaCl_2$. Furthermore, this result held when the mice were treated with either isotopically pure $^{40}CaCl_2$ or $^{43}CaCl_2$, indicating no Ca isotope effect on consciousness, whereas under Fisher's hypothesis we might expect the introduction of magnetically active

[3] EGTA = ethylene glycol-bis(β-aminoethylether)-N,N,N′,N′-tetraacetic acid.

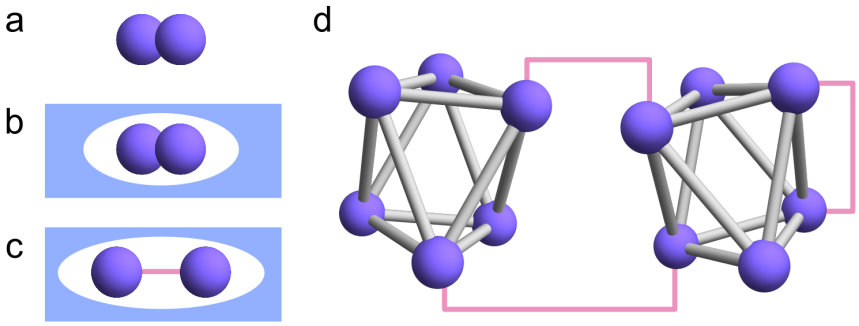

Figure 3.1 A simple diagram showing the formation of singlet-entangled Posner molecules according to Fisher's hypothesis [42]. Only the ^{31}P nuclei are shown. When a $P_2O_7^{4-}$ ion (a) enters an enzyme cavity (b), ions with singlet-entangled nuclei are selectively hydrolysed to produce two entangled PO_4^{2-} ions (c). These are released and incorporated into Posner molecules (d) which are now inter- and intramolecularly singlet-entangled (represented by pink lines).

^{43}Ca ($I = \frac{7}{2}$, as compared to $I = 0$ for ^{40}Ca, see Table A.1) to decohere the ^{31}P nuclear spin entanglement if ^{43}Ca were incorporated into Posner molecules [46].

The experimental results described in references [45, 46] and the theoretical considerations in reference [123] postdate the work described in this chapter (which formed the basis of reference [1]). At the time the work described here was performed there was no published experimental or theoretical consideration of this hypothesis, outside of Fisher's own publications.

Posner molecules 3.2

Posner's cluster was originally identified as a structural unit in hydroxyapatite (HA), the main inorganic constituent of human bones and teeth [127]. The structure of HA, including the Posner molecule region, is shown in Fig. 3.2.

Posner molecules are now thought to be an early intermediate in the formation of amorphous calcium phosphate (the precursor to HA) [129–132], and within Fisher's model they act as carriers for the ^{31}P qubits [42–44, 124]. *Ab initio* structure calculations suggest that an isolated $Ca_9(PO_4)_6$—henceforth referred to as a Posner molecule [47]—in vacuum would have calcium ions at the vertices and centre of

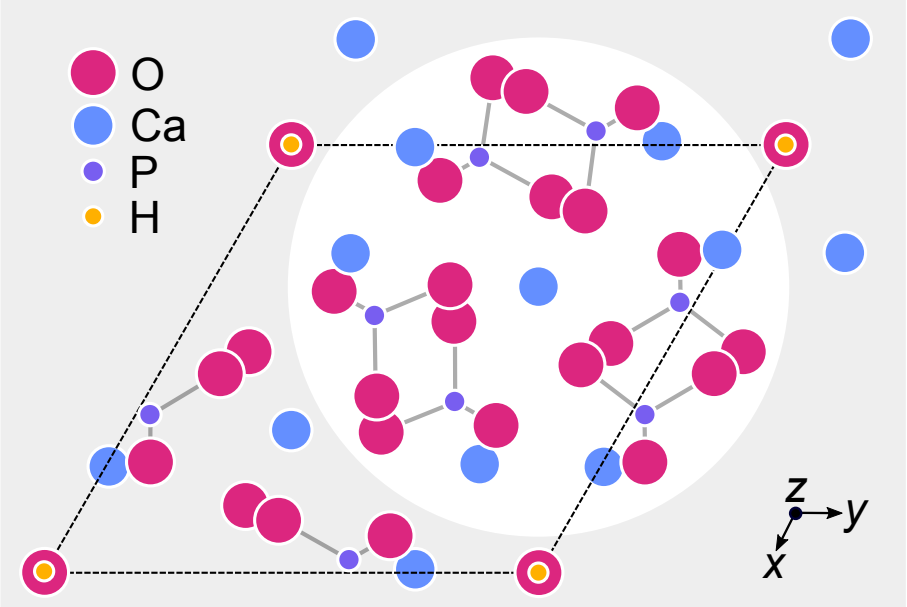

Figure 3.2 The unit cell of hydroxyapatite (extended slightly in the $-x$, y, and z directions), plotted using atomic coordinates from a crystal structure published in reference [128]. The lattice dimensions are $a = b = 9.432$ Å, $c = 6.881$ Å. The structure similar to the Posner molecule, $Ca_9(PO_4)_6$, found in the unit cell of HA is indicated by the circled region.

a distorted cube, with a phosphate ion near the middle of each face [133]. The ^{31}P nuclei have an S_6 arrangement, equivalent to an octahedron that has been stretched along one of its four symmetry axes (see Fig. 3.3). This structure is related to three other degenerate S_6 structures by a slight rearrangement of the atoms. If the energetic barrier to rearrangement is low, and it occurs rapidly on the timescale of spin evolution, then the molecule may have an effective O_h structure in solution (discussed further in later sections). The nearest-neighbour separation between the ^{31}P nuclei is ~0.5 nm, and the diameter of $Ca_9(PO_4)_6$ is ~0.9 nm [130].

Several features of the Posner molecule make it an attractive candidate for slow ^{31}P relaxation in aqueous solution. ^{31}P is the only stable isotope of phosphorus. It has spin-1/2 and therefore no electric quadrupole moment that would be relaxed by local fluctuating electric field gradients. Calcium has five stable isotopes, of which only ^{43}Ca has non-zero spin. Since ^{43}Ca has a natural abundance of 0.135%, we can safely ignore it here. Besides the two mentioned, $Ca_9(PO_4)_6$ contains no other magnetic nuclei, and in particular no ^{1}H nuclei, unlike most

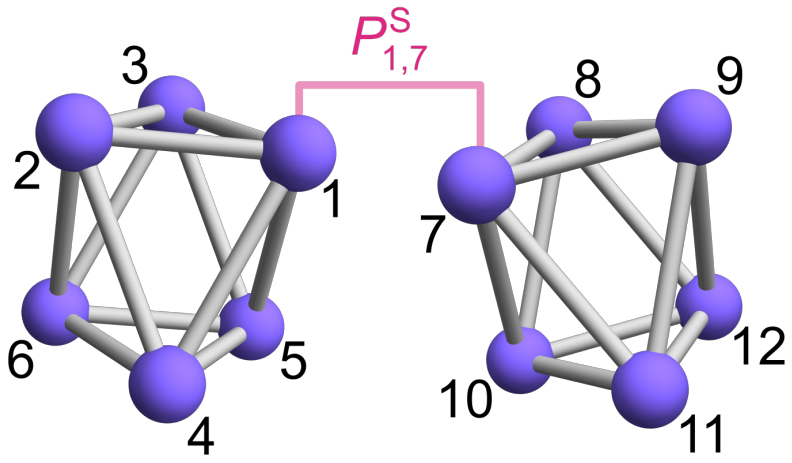

Figure 3.3 Arrangement of ^{31}P nuclei in a pair of entangled Posner molecules, $Ca_9(PO_4)_6$. The pink line indicates the two singlet-entangled spins, 1 and 7. The S_6 arrangement of the ^{31}P nuclei has been exaggeratedly emphasised by a stretch along the symmetry axis. Coupling constants from [47]: nearest neighbours, e.g. $J_{12} = +0.178$ Hz; next-nearest neighbours, e.g. $J_{14} = +0.145$ Hz; furthest neigbours, e.g. $J_{16} = -0.003$ Hz.

organic molecules. Magnetic nuclei such as protons usually lead to efficient dipolar relaxation, since the gyromagnetic ratio of the proton is more than twice that of ^{31}P (see Table A.1). In high-field NMR experiments the spin relaxation of ^{31}P is usually dominated by CSA (chemical shift anisotropy) relaxation. The efficiency of this relaxation depends on the square of the magnetic field strength, such that it will be negligibly slow in the Earth's magnetic field. Finally, since $Ca_9(PO_4)_6$ is a small, roughly spherical molecule, its relatively rapid rotational diffusion will reduce the influence of intermolecular spin–spin interactions.

Long-lived nuclear spin states 3.2.1

The Posner molecule does indeed represent a system of nuclear spins that are particularly magnetically isolated, both from each other and their surroundings. This is fortunate because, in order for the process of nuclear processing Fisher describes to be viable, the entangled states need to persist on long timescales in a noisy biological environment. Fisher calculated that the entangled states

will relax on timescales on the order of one day [42, 43], subsequently revised to 1.8×10^6 s $\simeq$ 21 days or maybe "even longer" [47].

Long-lived nuclear spin states have been an area of increasing interest over the past several years, and are becoming well known in NMR spectroscopy [37, 134–141]. It is well known that the nuclear spin–spin coupling between magnetically equivalent nuclei is often strong but is not seen as a splitting in an NMR spectrum, because transitions between the singlet and triplet states (which are antisymmetric and symmetric, respectively, with respect to exchange of the spin labels) are forbidden. So, for a magnetically equivalent pair of spins we only see a single line at the chemical shift, which comes from transitions between the three triplet states [24].

For near-magnetically equivalent nuclei it is possible, using particular methods that impose and remove symmetry in the nuclear environment at different points in the experiment, to prepare singlet order that persists for many multiples of the usual spin-lattice relaxation time T_1. This is because, similar to the case of magnetic equivalence, coherent singlet–triplet transitions are suppressed in this highly symmetric environment at low magnetic field. T_1 relaxation takes place exclusively in the triplet manifold, and intersystem crossing from singlet to triplet then takes place on a timescale sometimes called T_S. In many cases $T_S \gg T_1$. Therefore, as long as the symmetric nuclear environment is maintained, the singlet order will have a greater lifetime than might otherwise be expected. For an introduction to the field of singlet NMR, see reference [37] and the references therein.

For instance, a relaxation time of $T_S = 50T_1$ has been demonstrated for a pair of ^{13}C nuclei in a specially selected and highly symmetric organic compound [142]. These long-lived states generally depend on (a) protection from the usual routes of spin relaxation due to their particular symmetry/structural properties, and (b)

careful experimental control of their coherent spin dynamics using techniques such as field shuttling, spin-locking, and spin-decoupling [37].

Fisher's proposal involves a ^{31}P molecule with spin relaxation, it is claimed, that is incredibly slow for all nuclear spin states, without any requirements to control any of the coherent spin dynamics. A relaxation time this long for such a molecule would be unprecedented, and ^{31}P relaxation times of small molecules in solution are more typically a few seconds at most [48].

The multiple orders of magnitude difference between these numbers prompted us to use spin dynamics calculations to model the behaviour of entangled states in these molecules. By calculating the spin relaxation properties of the ^{31}P nuclei in $Ca_9(PO_4)_6$ we have been able to derive an upper bound on the entanglement lifetime for a pair of Posner molecules and compare it to Fisher's estimate.

The coherent spin dynamics and time-dependent processes described by Eq. (2.50) together determine the time-dependence of the density operator for a spin system such as the ^{31}P nuclei in a pair of Posner molecules. This time dependence may be calculated, as explained in Section 2.2.1, using a stochastic Liouville master equation (Eq. (2.45)) for the nuclear spin density matrix $\hat{\rho}(t)$. In this case the Liouvillian $\hat{\hat{\mathcal{L}}} = i\hat{\hat{\mathcal{H}}}_0 + \hat{\hat{\Gamma}}$ contains the commutator superoperator corresponding to $\hat{\mathcal{H}}_0$ and the relaxation superoperator $\hat{\hat{\Gamma}}$ (which is related to the time-dependent processes described by $\hat{\mathcal{H}}_1(t)$), both of which are now considered in turn.[4]

Coherent spin dynamics of singlet states 3.3

In Fisher's hypothesis the important state is an intermolecular singlet, i.e. $|S_{a,b}\rangle$, where the two entangled nuclei a and b are in different Posner molecules.[5] This simplest case of intermolecular entanglement—a pair of singlet-entangled ^{31}P nuclei, one contained in each Posner molecule, with all other nuclei maximally

[4] There is no reaction term $\hat{\hat{\mathcal{K}}}$ in this case, unlike the general Eq. (2.45), because we are not considering the effect of formation or reaction of Posner molecules on the spin states.

[5] These entangled molecules may also, for convenience, be labelled a and b.

mixed—will be the one we mainly consider throughout this chapter. One can also imagine states that are in some sense more entangled than this, for instance two or more pairs of entangled nuclei (see Fig. 3.1), which will be discussed in Section 3.5.

The singlet state $|S_{a,b}\rangle$ is represented in Fig. 3.3, where $a = 1$ and $b = 7$ (a case that we will consider for much of this chapter). The density matrix for an initial singlet state is

$$\begin{aligned} \hat{\rho}(0) &= |S_{a,b}\rangle \langle S_{a,b}| \\ &= \frac{1}{Z_a Z_b} \hat{P}^{S}_{a,b}, \end{aligned} \tag{3.1}$$

where $\hat{P}^{S}_{a,b}$ is the singlet projection operator (see Eq. (2.32)) and Z_i are normalization constants to account for the other nuclear spin states in molecules containing a and b. In the case of two Posner molecules $Z_a = Z_b = 32$.

Considering only coherent processes, the time-dependent probability that any two nuclei, labelled j and k, in either molecule will be found in a singlet-entangled pair at time t is given, using Eqs. (2.32) and (2.46), by

$$\begin{aligned} p^{S}_{j,k}(t) = \mathrm{Tr}\left[\hat{\rho}(t)\,\hat{P}^{S}_{j,k}\right] &= \frac{1}{4} - \sum_{\beta=x,y,z} \mathrm{Tr}\left[\hat{\rho}(t)\,\hat{S}_{j\beta}\,\hat{S}_{k\beta}\right] \\ &= \frac{1}{4} - \sum_{\beta=x,y,z} \mathrm{Tr}\left[e^{-i\hat{\mathcal{H}}_0 t}\,\hat{\rho}(0)\,e^{+i\hat{\mathcal{H}}_0 t}\,\hat{S}_{j\beta}\,\hat{S}_{k\beta}\right], \end{aligned} \tag{3.2}$$

where $\hat{\rho}(t) = e^{-i\hat{\mathcal{H}}_0 t}\hat{\rho}(0)e^{+i\hat{\mathcal{H}}_0 t}$ is the density matrix at time t (see Eq. (2.40)).

Since each $Ca_9(PO_4)_6$ contains six spin-1/2 ^{31}P nuclei, the total Hilbert space has dimension $2^{12} = 4096$. This makes the singlet probability time-consuming to calculate; taking the matrix exponentials at each time step in the calculation would involve operations that, for an n-dimensional matrix, have time complexity $\sim O(n^3)$. Therefore, we use a method for calculating this time-dependent singlet probability in the smaller Hilbert space of each individual molecule, as described in [143, 144] and outlined below. This method reduces the time taken for our

particular calculation by a factor of up to $(2^{12})^3/(2^6)^3 = 2^{18} \simeq 2.6 \times 10^5$, making the two-molecule calculation more easily tractable.

We ignore interactions between the two molecules—a reasonable assumption, since Fisher's hypothesis operates when the two $Ca_9(PO_4)_6$ are distant from each other. In this case, the last line in Eq. (3.2) can be rewritten in terms of the Hamiltonian for each molecule (see Eq. (2.52)) using Eq. (3.1) and the fact that $\hat{\mathcal{H}}_0^a$ and $\hat{\mathcal{H}}_0^b$ commute:

$$\begin{aligned}
p^{\mathrm{S}}_{j,k}(t) &= \frac{1}{4} - \frac{1}{Z_a Z_b} \sum_{\beta=x,y,z} \mathrm{Tr}\left[\mathrm{e}^{-\mathrm{i}\hat{\mathcal{H}}_0 t}\, \hat{P}^{\mathrm{S}}_{a,b}\, \mathrm{e}^{+\mathrm{i}\hat{\mathcal{H}}_0 t}\, \hat{S}_{j\beta}\, \hat{S}_{k\beta} \right] \\
&= \frac{1}{4} - \frac{1}{Z_a Z_b} \sum_{\beta=x,y,z} \mathrm{Tr}\left[\mathrm{e}^{-\mathrm{i}\left(\hat{\mathcal{H}}_0^a \oplus \hat{\mathcal{H}}_0^b\right) t} \left(\frac{1}{4}\hat{\mathbb{1}} - \sum_{\alpha=x,y,z} \hat{S}_{a\alpha}\hat{S}_{b\alpha} \right) \mathrm{e}^{+\mathrm{i}\left(\hat{\mathcal{H}}_0^a \oplus \hat{\mathcal{H}}_0^b\right) t}\, \hat{S}_{j\beta}\, \hat{S}_{k\beta} \right] \\
&= \frac{1}{4} + \frac{1}{Z_a Z_b} \sum_{\alpha,\beta=x,y,z} \mathrm{Tr}\left[\left(\mathrm{e}^{-\mathrm{i}\hat{\mathcal{H}}_0^a t} \otimes \mathrm{e}^{-\mathrm{i}\hat{\mathcal{H}}_0^b t} \right) \left(\hat{S}_{a\alpha} \otimes \hat{S}_{b\alpha} \right) \left(\mathrm{e}^{+\mathrm{i}\hat{\mathcal{H}}_0^a t} \otimes \mathrm{e}^{+\mathrm{i}\hat{\mathcal{H}}_0^b t} \right) \left(\hat{S}_{j\beta} \otimes \hat{S}_{k\beta} \right) \right] \\
&= \frac{1}{4} + \frac{1}{Z_a Z_b} \sum_{\alpha,\beta} \mathrm{Tr}\left[\left(\mathrm{e}^{-\mathrm{i}\hat{\mathcal{H}}_0^a t}\, \hat{S}_{a\alpha}\, \mathrm{e}^{+\mathrm{i}\hat{\mathcal{H}}_0^a t}\, \hat{S}_{j\beta} \right) \otimes \left(\mathrm{e}^{-\mathrm{i}\hat{\mathcal{H}}_0^b t}\, \hat{S}_{b\alpha}\, \mathrm{e}^{+\mathrm{i}\hat{\mathcal{H}}_0^b t}\, \hat{S}_{k\beta} \right) \right] \\
&= \frac{1}{4} + \sum_{\alpha,\beta} R^{a,j}_{\alpha\beta}(t) R^{b,k}_{\alpha\beta}(t),
\end{aligned} \tag{3.3}$$

where, after cyclic permutation under the trace,

$$R^{a,j}_{\alpha\beta}(t) = \frac{1}{Z_a}\mathrm{Tr}\left[\hat{S}_{a\alpha}\, \mathrm{e}^{+\mathrm{i}\hat{\mathcal{H}}_0^a t}\, \hat{S}_{j\beta}\, \mathrm{e}^{-\mathrm{i}\hat{\mathcal{H}}_0^a t} \right] = \frac{1}{Z_a}\mathrm{Tr}\left[\hat{S}_{a\alpha}(0)\, \hat{S}_{j\beta}(t) \right] \tag{3.4}$$

is an element of the spin correlation tensor for the chosen nucleus in molecule a. The form of the singlet probability in Eq. (3.3) is much quicker to calculate than that in Eq. (3.2), since the spin correlation tensors are calculated in the Hilbert space of each individual molecule, requiring matrix inversion of a smaller matrix with dimension $2^6 = 64$.

The time-independent spin Hamiltonian for a Posner molecule is

$$\hat{\mathcal{H}}_0 = \omega_0 \sum_k \hat{S}_{kz} + 2\pi \sum_{j<k} \sum_k J_{jk}\, \hat{\mathbf{S}}_j \cdot \hat{\mathbf{S}}_k \tag{3.5}$$

where ω_0 is the Larmor frequency for a ^{31}P nucleus in the Earth's magnetic field, J_{jk} is the scalar coupling constant for nuclei j and k, and the spin operators are as described in Chapter 2.

The first term in Eq. (3.5) describes the Zeeman interaction between the nuclei in the molecule and the Earth's magnetic field (see Eq. (2.55)). Since all the nuclei in a Posner molecule are magnetically equivalent, they will have identical chemical shifts (see Fig. 3.3). The Earth's magnetic field is taken to have flux density $B_0 = 50\,\mu\text{T}$, so that the ^{31}P Larmor frequency is $|\omega_0/2\pi| = \gamma_\text{P} B_0/2\pi = 863\,\text{Hz}$, with $\gamma_\text{P} = 10.84 \times 10^7\,\text{T}^{-1}\,\text{s}^{-1}$ the gyromagnetic ratio of ^{31}P.

The second term in Eq. (3.5) describes the intramolecular J-couplings (see Eq. (2.56)), which are taken from [47] and shown in Fig. 3.3. We consider only intramolecular ^{31}P–^{31}P J-coupling, ignoring the tiny (0.14%) natural abundance of magnetically active ^{43}Ca. It is important in Fisher's hypothesis that the entangled states persist when the Posner molecules are distant from each other, and so we ignore all intermolecular spin interactions, which will generally be far weaker than any intramolecular interactions.

The initial density operator is $\hat{\rho}(0) = \hat{P}^\text{S}_{1,7}/2^{10}$, where we have chosen nuclei 1 and 7 (as labelled in Fig. 3.3) to be the initially singlet-entangled nuclei. This density operator commutes with the Zeeman interaction term in $\hat{\mathcal{H}}_0$ but not with the J-coupling. So, the singlet probability calculated using Eq. (3.3) will oscillate at a variety of frequencies that are determined by the size of the J-coupling constants. Fig. 3.4 shows this singlet probability calculated for the initially entangled state $|\text{S}_{1,7}\rangle$, and Figs. 3.5 and 3.6 show the singlet probability for the nine other

	1	2	3	4	5	6
7	$\|S_{1,7}\rangle$					
8	$\|S_{1,8}\rangle$	$\|S_{2,8}\rangle$				
9						
10	$\|S_{1,10}\rangle$	$\|S_{2,10}\rangle$		$\|S_{4,10}\rangle$		
11						
12	$\|S_{1,12}\rangle$	$\|S_{2,12}\rangle$		$\|S_{4,12}\rangle$		$\|S_{6,12}\rangle$

Table 3.1 There are ten distinct intermolecular singlet states for two Posner molecules, out of 21 possible pairs of nuclei. For instance, $|S_{1,8}\rangle$ and $|S_{1,9}\rangle$ are equivalent via a reflection in the second molecule, and so we need only consider $|S_{1,8}\rangle$. See Fig. 3.3 for numbering of nuclei.

symmetrically distinct intermolecular singlet states in Table 3.1, given an initial state $|S_{1,7}\rangle$.

In Fig. 3.4(a) the singlet probability between spins 1 and 7 drops to the maximally-mixed average of 0.25 within one second, and then oscillates on a timescale of seconds. A singlet probability of 0.25 is the value expected for a maximally mixed pair of spins, since there are three possible triplet states and one singlet. It only occasionally rises above 0.5, as the various oscillations come back into phase. In fact, with the exception of singlet probability between spins 6 and 12 (which are related to spins 1 and 7 by inversion symmetry), all other pairs of spins vary little from 0.25 throughout the time range considered, as can be seen in Fig. 3.5.

The simpler traces in Figs. 3.4(b) and 3.6 are calculated for a reduced coupling pattern, whereby the two largest coupling constants are set equal to their mean, that is $J_{AB} = \frac{1}{2}(J_A + J_B) = 0.162\,\text{Hz}$ where $J_A = 0.178\,\text{Hz}$ and $J_B = 0.145\,\text{Hz}$ [47] (see Fig. 3.3). This would be appropriate if the four degenerate S_6 structures interconvert on a fast timescale compared to these couplings (i.e. $|J_A - J_B|^{-1} \simeq 30\,\text{s}$), leading to an effective O_h symmetry. As would be expected, a simpler coupling

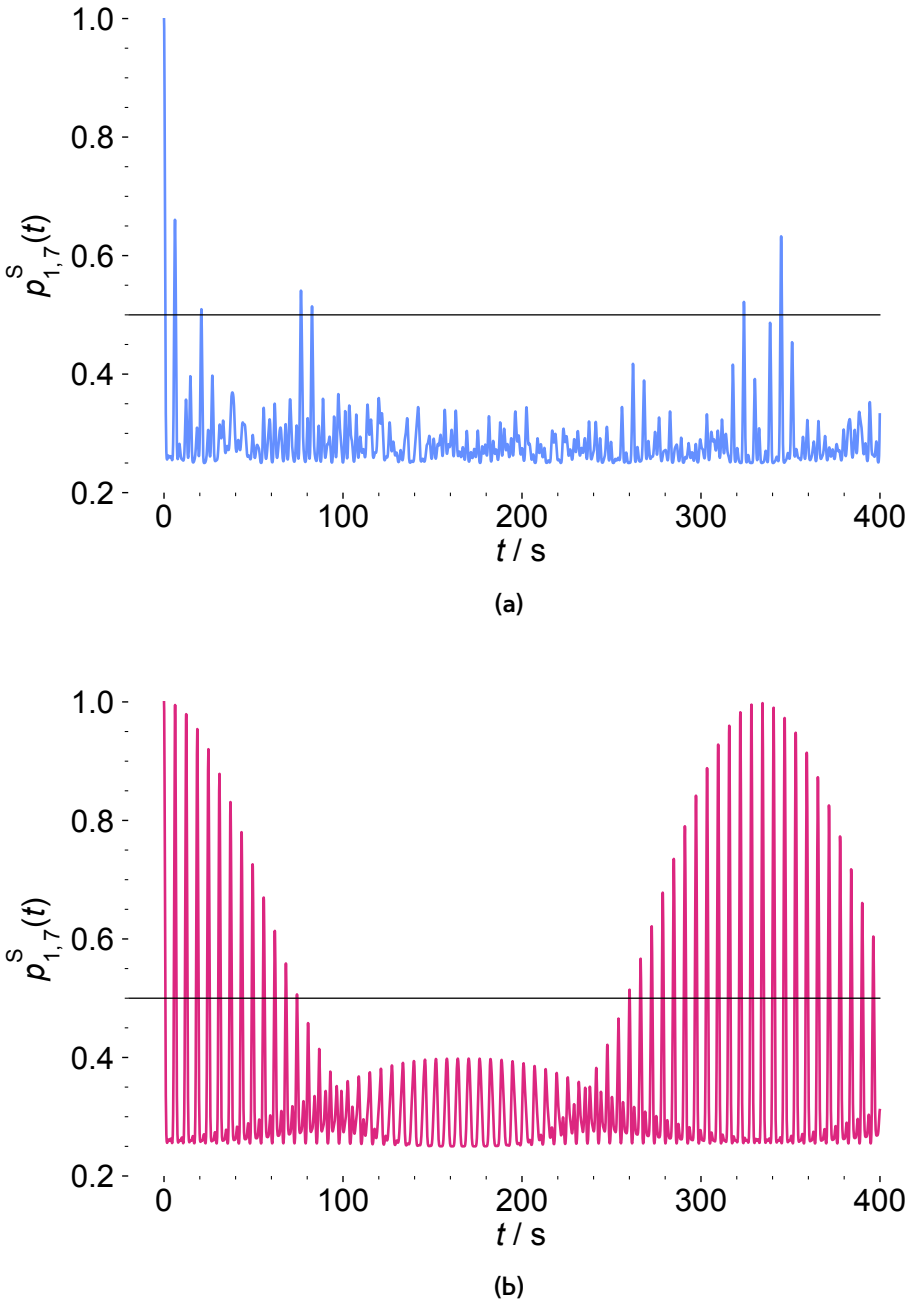

Figure 3.4 The singlet probability $p^{S}_{1,7}(t)$, calculated for a pair of Posner molecules using Eq. (3.3). (a) is calculated assuming S_6 symmetry for the ^{31}P J-coupling constants in $Ca_9(PO_4)_6$, (b) is assuming O_h symmetry. The initial state is a singlet between spins 1 and 7, $|S_{1,7}\rangle$. See Fig. 3.3 for numbering of nuclei. The horizontal lines mark $p^{S}_{1,7}(t) = 0.5$, the threshold for entanglement of a two qubit density matrix describing a linear combination of singlet and triplet [145].

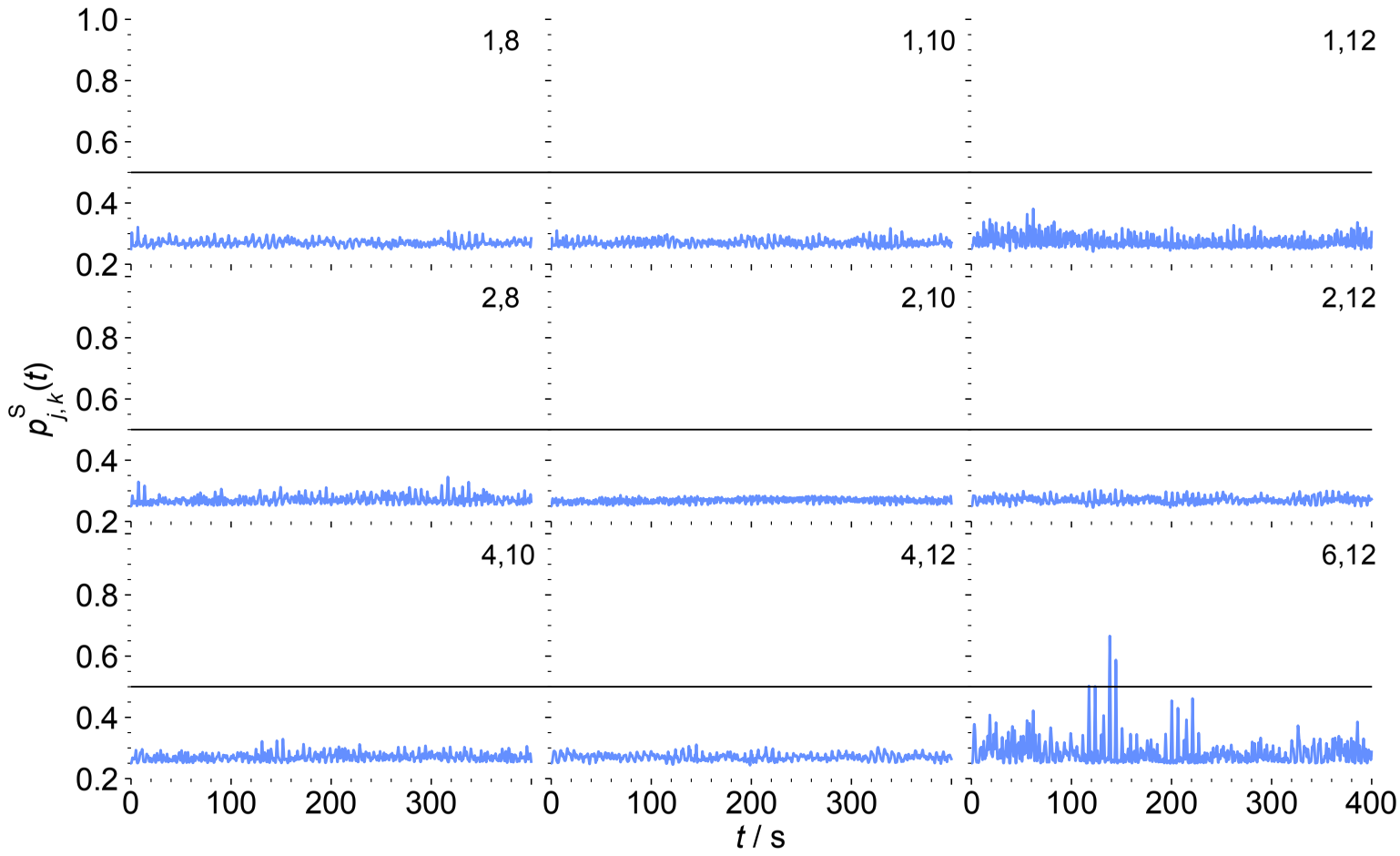

Figure 3.5 The singlet probability $p^{S}_{j,k}(t)$ for all distinct pairs of nuclei j and k in a pair of Posner molecules except (1,7), which is shown in Fig. 3.4a. The singlet probability in each case was calculated using Eq. (3.3), assuming S_6 symmetry for the ^{31}P J-coupling constants in $Ca_9(PO_4)_6$. The initial state is a singlet between spins 1 and 7, $|S_{1,7}\rangle$. See Fig. 3.3 for numbering of nuclei. The horizontal lines mark $p^{S}_{j,k}(t) = 0.5$, the threshold for entanglement of a two qubit density matrix describing a linear combination of singlet and triplet [145].

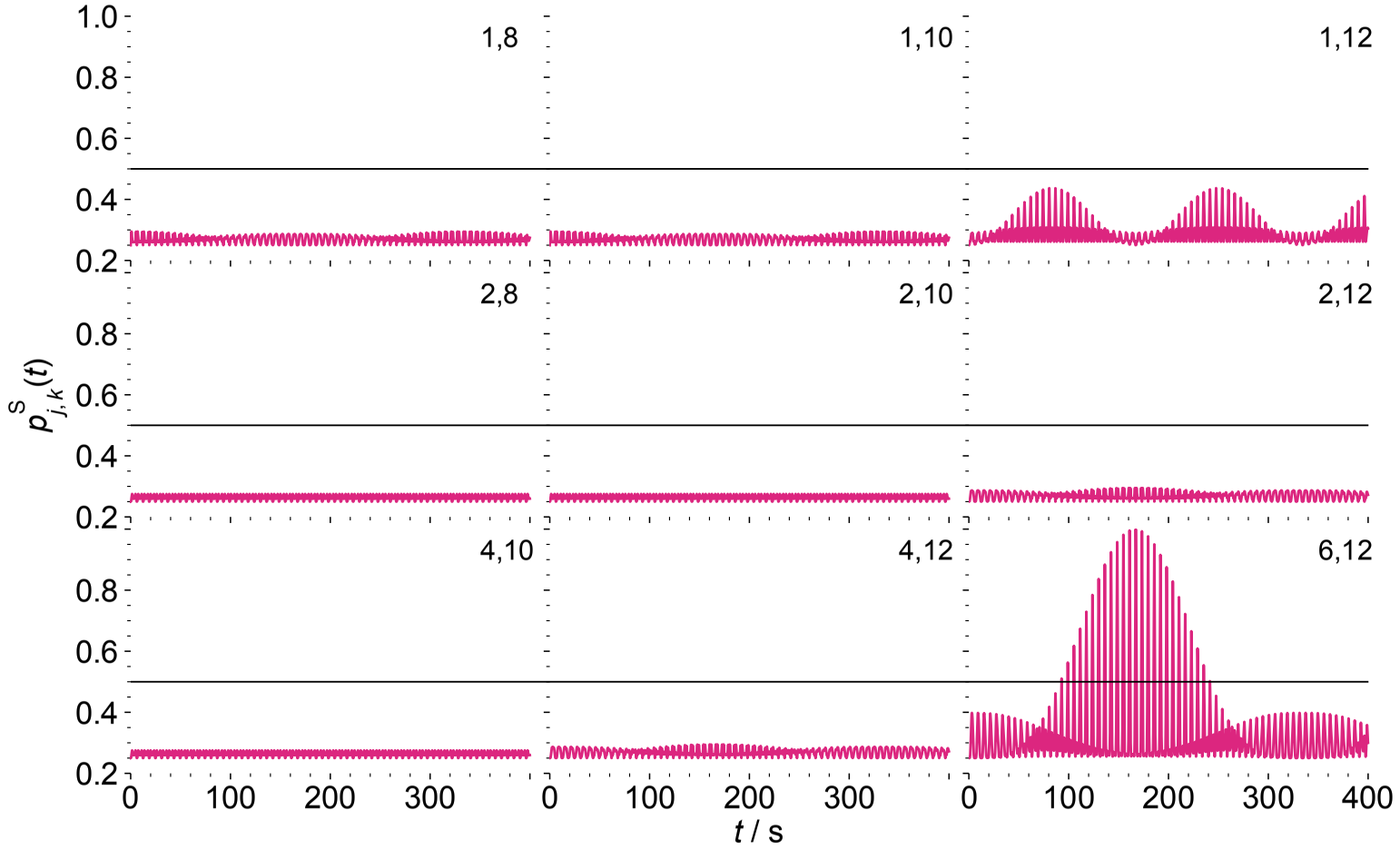

Figure 3.6 The singlet probability $p^{S}_{j,k}(t)$ for all distinct pairs of nuclei j and k in a pair of Posner molecules except (1,7), which is shown in Fig. 3.4b. The singlet probability in each case was calculated using Eq. (3.3), assuming O_h symmetry for the ^{31}P J-coupling constants in $Ca_9(PO_4)_6$. The initial state is a singlet between spins 1 and 7, $|S_{1,7}\rangle$. See Fig. 3.3 for numbering of nuclei. The horizontal lines mark $p^{S}_{j,k}(t) = 0.5$, the threshold for entanglement of a two qubit density matrix describing a linear combination of singlet and triplet [145].

pattern yields a simpler coherent evolution of the singlet probability, but it remains true that most pairs of spins remain around $p^{\mathrm{S}}_{j,k} \simeq 0.25$ at all times.

Measuring entanglement 3.3.1

Since $\hat{\mathcal{H}}_0$ describes a unitary transformation on the Hilbert space, we would not expect it to "destroy" the initial entanglement. The bottom-right panels of Figs. 3.5 and 3.6 show that the singlet probability $p^{\mathrm{S}}_{6,12}(t)$ oscillates in a similar fashion to $p^{\mathrm{S}}_{1,7}(t)$, and indeed all intermolecular pairs have singlet probability greater than 0.25 at some point.

This suggests that the coherent spin dynamics may distribute the initial entanglement across all nuclei in the two molecules. To test this hypothesis, the concurrence—a measure of entanglement between two spins, ranging from 0 (not entangled) to 1 (fully entangled) [99], see Eq. (2.36) in Section 2.1.1—was calculated for all distinct pairs of ^{31}P nuclei in a pair of Posner molecules (see Table 3.1) using a routine from reference [146]. This concurrence, $C_{j,k}(t)$, calculated both for the full set of S_6 couplings and the reduced O_h couplings previously mentioned, can be used directly as a measure of bipartite entanglement and is shown in Fig. 3.7.

For all pairs of nuclei, other than (1,7) and (6,12), the concurrence remains zero throughout the time range in Fig. 3.7. These two pairs are only entangled at times when the corresponding singlet probability (see Figs. 3.4–3.6) rises above 0.5, which is the threshold for entanglement of a two qubit density matrix describing a linear combination of singlet and triplet, $|\mathrm{S}\rangle\langle\mathrm{S}|$ and $\left(\hat{\mathbb{1}} - |\mathrm{S}\rangle\langle\mathrm{S}|\right)/3$ [145]. For most of the time in Fig. 3.7(a) there is no intermolecular two-spin entanglement at all, although it remains possible that intermolecular entanglement between more than two spins may persist at all times. Multipartite entanglement of this kind is more difficult to quantify than bipartite entanglement; there are several potential functions that aim to quantify the amount of entanglement present in a quantum

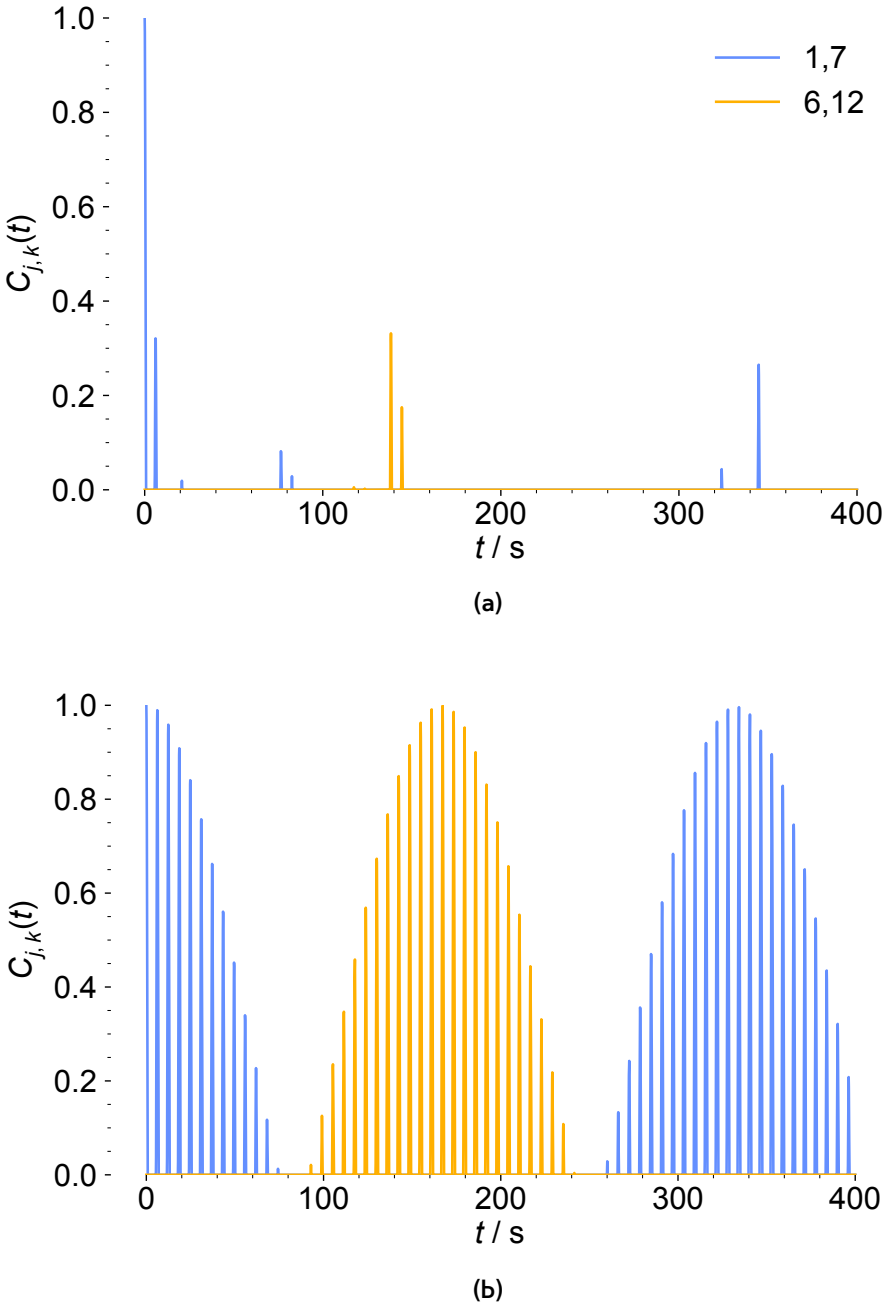

Figure 3.7 The two-qubit concurrence $C_{j,k}(t)$ calculated using Eq. (2.36) for all distinct pairs of spins j and k in a pair of Posner molecules. (a) is calculated assuming S_6 symmetry for the ^{31}P J-coupling constants in $Ca_9(PO_4)_6$, (b) is assuming O_h symmetry. The initial state is a singlet between spins 1 and 7, $|S_{1,7}\rangle$. See Fig. 3.3 for numbering of nuclei. Only pairs (1,7) and (6,12) have non-zero concurrence in the time range considered, and these two pairs only have $C_{j,k}(t) > 0$ when the corresponding singlet probability is greater than 0.5 (see horizontal lines in Figs. 3.4a and 3.5).

state (for a review see reference [98]), with one possibility being a recent extension of concurrence to multiparticle states [147].

Spin relaxation of singlet states 3.4

We have seen examples of spin states containing singlet-entangled pairs of nuclei that will evolve under the scalar couplings in the static Hamiltonian, $\hat{\mathcal{H}}_0$. It is, however, generally possible to find spin states that will not evolve under these kinds of interactions: namely, the eigenstates of $\hat{\mathcal{H}}_0$. It is much harder to engineer spin states that are not eventually relaxed to a thermal equilibrium by $\hat{\mathcal{H}}_1(t)$, the time-dependent part of the spin Hamiltonian (see Eq. (2.50)).

For many molecules containing non-quadrupolar nuclei, such as $Ca_9(PO_4)_6$, the dominant relaxation pathway is dipolar relaxation via the interaction of nuclear magnetic moments in the molecule, particularly in low magnetic fields where CSA effects are weak. Note that this is *intra*molecular dipolar coupling, as opposed to the *inter*molecular dipolar relaxation sometimes considered by Fisher and colleagues [42, 47], although see [148] for a discussion of the intramolecular case. Uncorrelated isotropic Brownian rotational diffusion of the molecule modulates these dipolar couplings and leads to relaxation.

Relaxation superoperator for two entangled molecules 3.4.1

In order to derive the relaxation superoperator, using an approach described in [149–154] and below, we begin by considering the spin Hamiltonian for dipolar coupling between nuclei in the Posner molecule.

Notationally compact dipolar Hamiltonian

If we define the the dipole-dipole axis as the principal axis frame (P) z-axis, then the Hamiltonian for dipolar coupling in a molecule between nuclei j and k is given (from Eq. (2.62)) by

$$\hat{\mathcal{H}}_D^{jk(\mathrm{P})} = \sqrt{6} b_{jk} \hat{T}_{2,0}^{jk}, \tag{3.6}$$

where b_{jk} is the dipole-dipole coupling constant for two spins j and k separated by an intermolecular distance r_{jk} (Eq. (2.60)). In our case $\gamma_j = \gamma_k = \gamma_P$, the gyromagnetic ratio of ^{31}P. In Eq. (3.6), $\hat{T}^{jk}_{2,0}$ is one of the second-order spherical tensors:

$$\begin{aligned} \hat{T}^{jk}_{2,\pm 2} &= \tfrac{1}{2}\hat{S}_{j\pm}\hat{S}_{k\pm}, \quad \hat{T}^{jk}_{2,\pm 1} = \mp\tfrac{1}{2}\left(\hat{S}_{jz}\hat{S}_{k\pm} + \hat{S}_{j\pm}\hat{S}_{kz}\right), \\ \hat{T}^{jk}_{2,0} &= \sqrt{\tfrac{2}{3}}\left(-\tfrac{1}{2}\hat{S}_{jx}\hat{S}_{kx} - \tfrac{1}{2}\hat{S}_{jy}\hat{S}_{ky} + \hat{S}_{jz}\hat{S}_{kz}\right). \end{aligned} \tag{3.7}$$

Any spherical tensor can be transformed under a rotation operator $\hat{\hat{R}}(\alpha,\beta,\gamma)$ through Euler angles (α,β,γ)[6] as

$$\hat{\hat{R}}(\alpha,\beta,\gamma)\,\hat{T}^{jk}_{l,m} = \sum_{m'=-l}^{l} \hat{T}^{jk}_{l,m'}\,\mathfrak{D}^{(l)}_{m',m}(\alpha,\beta,\gamma), \tag{3.8}$$

where $\mathfrak{D}^{(l)}_{m',m}(\alpha,\beta,\gamma)$ are elements of the l^{th} rank Wigner D-matrix [155].

By applying an initial positioning rotation $\hat{\hat{R}}^{j,k}_{\text{pos}}(\alpha,\beta,\gamma)$ from the principal axis frame (P) into the molecular frame through Euler angles (α,β,γ), and then a second molecular rotation $\hat{\hat{R}}_{\text{mol}}(\Omega(t))$ from the molecular frame into the lab frame (L) through time-dependent Euler angles $(\Omega(t))$, we obtain the following expression for the dipolar Hamiltonian in the laboratory frame:

$$\hat{\mathcal{H}}^{jk(\text{L})}_{D}(t) = -\sqrt{6}\,\hbar\,\gamma_P^2\left(\frac{\mu_0}{4\pi}\right)\hat{\hat{R}}_{\text{mol}}(\Omega(t))\;\hat{\hat{R}}^{j,k}_{\text{pos}}(\alpha,\beta,\gamma)\,\hat{T}^{jk}_{2,0}\,/\,r^3_{jk}. \tag{3.9}$$

The time-dependent Hamiltonian for the whole molecule is then given by summing over all pairs of nuclei j and k in the molecule:

$$\hat{\mathcal{H}}_1(t) = -\sqrt{6}\,\hbar\,\gamma_P^2\left(\frac{\mu_0}{4\pi}\right)\hat{\hat{R}}_{\text{mol}}(\Omega(t))\sum_{j<k}\sum_{k}\hat{\hat{R}}^{j,k}_{\text{pos}}(\alpha,\beta,\gamma)\,\hat{T}^{jk}_{2,0}\,/\,r^3_{jk}. \tag{3.10}$$

[6]The convention used throughout this chapter is the z-y'-z'' convention. The first rotation is through an angle α about the rotating object's z axis, then β about the new y' axis, and finally γ about the new z'' axis. This rotation can also be written as $\hat{\hat{R}}(\alpha,\beta,\gamma) = \hat{\hat{R}}_{z''}(\gamma)\hat{\hat{R}}_{y'}(\beta)\hat{\hat{R}}_{z}(\alpha)$ with three separate rotations, which is equivalent to performing all three rotations in the opposite order about the original axes: $\hat{\hat{R}}(\alpha,\beta,\gamma) = \hat{\hat{R}}_{z}(\alpha)\hat{\hat{R}}_{y}(\beta)\hat{\hat{R}}_{z}(\gamma)$ [96].

The atomic coordinates for Posner's cluster, which were obtained by Dr Daniel Kattnig using density function theory (DFT) calculations and used to calculate r_{jk} and $\hat{\hat{R}}^{j,k}_{\text{pos}}$, are given in Appendix B.

We can evaluate the effect of the rotation operators on the spherical tensors using Eq. (3.8). Defining a positioning parameter $\Phi^{jk}_m = \sqrt{6}\, b_{jk}\, \mathfrak{D}^{(2)}_{m,0}(\alpha, \beta, \gamma)$ that is constant for each pair of nuclei in the molecule allows us to write the time-dependent Hamiltonian as

$$\hat{\mathcal{H}}_1(t) = \sum_{j<k} \sum_{k} \sum_{m,m'=-2}^{2} \Phi^{jk}_m \hat{T}^{jk}_{2,m'} \mathfrak{D}^{(2)}_{m',m}(\Omega(t)), \tag{3.11}$$

which can be made notationally more compact by defining a parameter, $\phi^{jk}_{m'}(t)$, containing all time-dependent and positional information about a pair of nuclei:

$$\phi^{jk}_{m'}(t) = \sum_{m=-2}^{2} \Phi^{jk}_m \mathfrak{D}^{(2)}_{m',m}(\Omega(t)). \tag{3.12}$$

This means the time-dependent Hamiltonian can be written as

$$\hat{\mathcal{H}}_1(t) = \sum_{j<k} \sum_{k} \sum_{m'=-2}^{2} \phi^{jk}_{m'}(t) \hat{T}^{jk}_{2,m'}, \tag{3.13}$$

in a form that facilitates simple manipulations and fast calculations.

Applying Redfield theory

Relaxation due to $\hat{\mathcal{H}}_1(t)$ can be described using a well-established theory known as Redfield, or Bloch-Redfield-Wangsness, relaxation theory [151, 153]. This perturbative approach to modelling relaxation is well-established and often used for spin dynamics calculations [34, 96, 149, 151–153, 156–159], although it does suffer from accuracy problems under certain conditions [112], and more generally ap-

plicable perturbative theories of spin relaxation based on the Nakajima–Zwanzig equation have recently been proposed [160].

We will justify that the conditions for the validity of Redfield theory are met throughout this section. In simple terms, we require that the timescale over which the relaxation-causing interaction varies is much longer than the correlation time for the process that modulates that interaction [151].

Therefore, for the Redfield approach to be valid, we firstly require [151, 156] that

$$|b_{jk}|\tau_c \ll 1 \quad \forall \quad j,k, \tag{3.14}$$

where b_{jk} is the dipolar coupling constant defined in Eq. (2.60) and τ_c is the correlation time for the molecular rotational diffusion. Taking 0.5 nm as a rough value for the average separation of the ^{31}P nuclei, we obtain $b \simeq 990$ Hz. The correlation time for Brownian rotation diffusion of a spherical molecule can be estimated by the Stokes–Einstein equation (see Eq. (2.76)). Using the radius $a = 0.44$ nm [130], $T = 310$ K (physiological temperature), and $\eta = 0.69$ mPa s for water we obtain $\tau_c \simeq 58$ ps. Multiplying this value for τ_c by the dipolar coupling constant b calculated above gives a value much less than one—the condition in Eq. (3.14) is easily met, and the Redfield approach is therefore valid.

The Liouville-von Neumann equation (Eq. (2.39)) is used to determine the effect of the total spin Hamiltonian on the system:

$$\frac{\mathrm{d}\hat{\rho}(t)}{\mathrm{d}t} = -\mathrm{i}\left[\hat{\mathcal{H}}_0 + \hat{\mathcal{H}}_1(t), \hat{\rho}(t)\right]. \tag{3.15}$$

It can be shown, for instance in references [151, 153], that, using second order perturbation theory and several valid assumptions, Eq. (3.15) can be rewritten in the interaction representation. This is indicated by a double dagger (‡), whereby

all operators in the laboratory frame are transformed according to

$$\hat{Q}^{\ddagger}(t) = e^{+i\hat{\mathcal{H}}_0 t}\hat{Q}e^{-i\hat{\mathcal{H}}_0 t}. \tag{3.16}$$

In this representation, the time-evolution of the density matrix is given by

$$\frac{d\hat{\rho}^{\ddagger}(t)}{dt} = -\int_0^{\infty} \left\langle \left[\hat{\mathcal{H}}_1^{\ddagger}(t), \left[\hat{\mathcal{H}}_1^{\ddagger}(t-\tau), \hat{\rho}^{\ddagger}(t)\right]\right]\right\rangle d\tau, \tag{3.17}$$

where the angle brackets indicate an ensemble average over the Hamiltonians. Eq. (3.17) is transformed back out of the interaction representation and into the laboratory frame using Eq. (3.16):

$$\frac{d\hat{\rho}(t)}{dt} = -i\left[\hat{\mathcal{H}}_0, \hat{\rho}(t)\right] - \int_0^{\infty} \left\langle \left[\hat{\mathcal{H}}_1(t), \left[e^{-i\hat{\mathcal{H}}_0\tau}\hat{\mathcal{H}}_1(t-\tau)e^{+i\hat{\mathcal{H}}_0\tau}, \hat{\rho}(t)\right]\right]\right\rangle d\tau. \tag{3.18}$$

This is clearly a sum of two terms: the first governs the coherent dynamics of the system, which have already been discussed, and the second is the relaxation term. Eq. (3.18) is a differential equation known as a *master equation* [112].

Extreme narrowing simplification

The master equation in Eq. (3.18) is not analytically soluble in general, and so the extreme narrowing approximation is outlined here, as in [153]. When the random processes (i.e. molecular rotations) take place on a timescale much shorter than all of the eigenvalue differences for the static Hamiltonian (i.e. the transition frequencies), then the conditions for extreme narrowing are met:

$$\omega_{nm}^2\tau_c^2 \ll 1 \quad \forall \quad n, m, \tag{3.19}$$

where $\omega_{nm} = \omega_n - \omega_m$ with $\{\omega_n\}$ the eigenvalues of $\hat{\mathcal{H}}_0$. In the present case, since the J-couplings are small compared to the Earth's magnetic field, the condition in

Eq. (3.19) is equivalent to requiring that

$$6|\omega_0|\tau_c \ll 1, \tag{3.20}$$

where ω_0 is once again the Larmor frequency for ^{31}P nuclei. When $B_0 \simeq 50\,\mu$T, $\omega_0 \simeq 5.4\,$kHz and so $6|\omega_0| \simeq 33\,$kHz. Since $\tau_c^{-1} \simeq 17\,$GHz, the extreme narrowing condition in Eq. (3.20) is clearly satisfied. We also note that the six ^{31}P nuclei in a Posner's molecule would have the same chemical shift since they are magnetically equivalent, and so the ^{31}P NMR spectrum would be a singlet.

By converting into the eigenbasis of $\hat{\mathcal{H}}_0$, the relaxation term in Eq. (3.18), which we label $\hat{T}$, can be written

$$\hat{T} = -\int_0^\infty \left\langle \left[\hat{\mathcal{H}}_1^{(0)}(t), \left[\hat{F}(t,\tau), \hat{\rho}^{(0)}(t)\right]\right]\right\rangle \mathrm{d}\tau, \tag{3.21}$$

where

$$\hat{F}(t,\tau) = \mathrm{e}^{-\mathrm{i}\hat{\mathcal{H}}_0^{(0)}\tau}\hat{\mathcal{H}}_1^{(0)}(t-\tau)\mathrm{e}^{+\mathrm{i}\hat{\mathcal{H}}_0^{(0)}\tau}, \tag{3.22}$$

and the (0) superscript indicates terms transformed into the new basis.

Expanding the commutators, remembering that the ensemble average is taken only over the time-dependent Hamiltonian, means that terms similar to $\hat{K}$ arise:

$$\hat{K} = \int_0^\infty \left\langle \hat{\mathcal{H}}_1^{(0)}(t)\hat{F}(t,\tau)\right\rangle \hat{\rho}^{(0)}(t)\mathrm{d}\tau, \tag{3.23}$$

a single matrix element of which can be written, using the definition of $\hat{F}(t,\tau)$ in Eq. (3.22), as

$$\begin{aligned}\hat{K}_{nm} &= \sum_{p,q}\int_0^\infty \left\langle \left[\hat{\mathcal{H}}_1^{(0)}(t)\right]_{np}\left[\hat{F}(t,\tau)\right]_{pq}\right\rangle \left[\hat{\rho}^{(0)}(t)\right]_{qm}\mathrm{d}\tau \\ &= \sum_{p,q}\int_0^\infty \left\langle \left[\hat{\mathcal{H}}_1^{(0)}(t)\right]_{np}\left[\hat{\mathcal{H}}_1^{(0)}(t-\tau)\right]_{pq}\right\rangle \left[\hat{\rho}^{(0)}(t)\right]_{qm}\mathrm{e}^{-i\omega_{pq}\tau}\mathrm{d}\tau.\end{aligned} \tag{3.24}$$

Using the customary exponentially decaying correlation function

$$\left\langle \hat{\mathcal{H}}_1(t)\hat{\mathcal{H}}_1(t-\tau)\right\rangle = \left\langle \hat{\mathcal{H}}_1(t)\hat{\mathcal{H}}_1(t)\right\rangle \mathrm{e}^{-\frac{|\tau|}{\tau_\mathrm{c}}}, \tag{3.25}$$

in Eq. (3.24) gives:

$$\hat{K}_{nm} = \sum_{p,q}\int_0^\infty \left\langle \left[\hat{\mathcal{H}}_1^{(0)}(t)\right]_{np}\left[\hat{\mathcal{H}}_1^{(0)}(t)\right]_{pq}\right\rangle \left[\hat{\rho}^{(0)}(t)\right]_{qm} \mathrm{e}^{(-i\omega_{pq}-\frac{1}{\tau_\mathrm{c}})\tau}\mathrm{d}\tau. \tag{3.26}$$

This integral is simple to compute, and yields:

$$\hat{K}_{nm} = \sum_{p,q}\left\langle \left[\hat{\mathcal{H}}_1^{(0)}(t)\right]_{np}\left[\hat{\mathcal{H}}_1^{(0)}(t)\right]_{pq}\right\rangle \left[\hat{\rho}^{(0)}(t)\right]_{qm}\left(\frac{\tau_\mathrm{c}}{1+\tau_\mathrm{c}^2\omega_{pq}^2} - i\frac{\omega_{pq}\tau_\mathrm{c}^2}{1+\tau_\mathrm{c}^2\omega_{pq}^2}\right), \tag{3.27}$$

the imaginary component of which is known as the dynamic frequency shift. It corresponds to a shift in energy which is usually small and difficult to measure, and so we ignore it here [156].

Since we are in the extreme narrowing limit (see Eq. (3.19)), $\tau_\mathrm{c}(1+\tau_\mathrm{c}^2\omega_{pq}^2)^{-1} \simeq \tau_\mathrm{c}$, and so:

$$\hat{K}_{nm} \simeq \tau_\mathrm{c}\sum_{p,q}\left\langle \left[\hat{\mathcal{H}}_1^{(0)}(t)\right]_{np}\left[\hat{\mathcal{H}}_1^{(0)}(t)\right]_{pq}\right\rangle \left[\hat{\rho}^{(0)}(t)\right]_{qm}. \tag{3.28}$$

Using a similar argument for all terms in Eq. (3.21) means we obtain the relaxation term $\hat{T}$, Eq. (3.21), now in the extreme narrowing limit:

$$\hat{T} = -\tau_\mathrm{c}\left\langle \left[\hat{\mathcal{H}}_1^{(0)}(t), \left[\hat{\mathcal{H}}_1^{(0)}(t), \hat{\rho}^{(0)}(t)\right]\right]\right\rangle. \tag{3.29}$$

So, by transforming back out of the eigenbasis of $\hat{\mathcal{H}}_0$, we can write the master equation, Eq. (3.18), in the extreme narrowing limit:

$$\frac{\mathrm{d}\hat{\rho}(t)}{\mathrm{d}t} = -i\left[\hat{\mathcal{H}}_0, \hat{\rho}(t)\right] - \tau_\mathrm{c}\left\langle \left[\hat{\mathcal{H}}_1(t), \left[\hat{\mathcal{H}}_1(t), \hat{\rho}(t)\right]\right]\right\rangle. \tag{3.30}$$

Explicit form of the relaxation superoperator

The time-dependence of the density matrix can also be written as in Eq. (2.45):

$$\frac{\mathrm{d}}{\mathrm{d}t}\hat{\rho}(t) = -\hat{\hat{\mathcal{L}}}\left[\hat{\rho}(t)\right], \tag{3.31}$$

where $\hat{\hat{\mathcal{L}}} = \mathrm{i}\hat{\hat{\mathcal{H}}}_0 + \hat{\hat{\Gamma}}$ contains $\hat{\hat{\mathcal{H}}}_0$, the commutation superoperator that corresponds to $\hat{\mathcal{H}}_0$, and $\hat{\hat{\Gamma}}$, the relaxation superoperator. Comparing Eqs. (3.30) and (3.31) allows us to identify that

$$\hat{\hat{\Gamma}} = \left\langle \hat{\hat{\mathcal{H}}}_1(t)\, \hat{\hat{\mathcal{H}}}_1(t) \right\rangle \tau_\mathrm{c}. \tag{3.32}$$

Using Eq. (3.10), the relaxation superoperator may therefore be written:

$$\hat{\hat{\Gamma}} = \tau_\mathrm{c} \left\langle \sum_{j<k} \sum_{k} \sum_{r<s} \sum_{s} \sum_{m',n'=-2}^{2} \phi^{jk}_{m'}(t)\, \phi^{rs}_{n'}(t)\, \hat{\hat{T}}^{jk}_{2,m'}\, \hat{\hat{T}}^{rs}_{2,n'} \right\rangle. \tag{3.33}$$

Since the time-dependence comes from the positioning $\phi(t)$ functions, we consider products of the form:

$$\left\langle \phi^{jk}_{m'}(t)\, \phi^{rs}_{n'}(t) \right\rangle. \tag{3.34}$$

Using Eq. (3.12) and the properties of Wigner functions,[7] products of this type can be expressed as:

$$\begin{aligned} \left\langle \phi^{jk}_{m'}(t)\, \phi^{rs}_{n'}(t) \right\rangle &= \sum_{m,n=-2}^{2} \Phi^{jk}_{m}\, \Phi^{rs}_{n} \left\langle \mathfrak{D}^{(2)}_{m',m}\left(\Omega(t)\right) \mathfrak{D}^{(2)}_{n',n}\left(\Omega(t)\right) \right\rangle \\ &= \sum_{m,n=-2}^{2} \Phi^{jk}_{m}\, \Phi^{rs}_{n} \left\langle \mathfrak{D}^{(2)}_{m',m}\left(\Omega(t)\right) \mathfrak{D}^{*(2)}_{-n',-n}\left(\Omega(t)\right) \right\rangle (-1)^{m'-m}, \end{aligned} \tag{3.35}$$

[7] Specifically, $\mathfrak{D}^{(j)}_{m',m}(\alpha,\beta,\gamma) = (-1)^{m'-m}\mathfrak{D}^{*(j)}_{-m',-m}(\alpha,\beta,\gamma)$.

and, using a result from [153], this can be further evaluated as:

$$\begin{aligned}\left\langle \phi_{m'}^{jk}(t)\,\phi_{n'}^{rs}(t)\right\rangle &= \frac{1}{5}\sum_{m,n=-2}^{2}\Phi_m^{jk}\,\Phi_n^{rs}\,\delta_{m',-n'}\,\delta_{m,-n}\,(-1)^{m'-m}\\ &= \frac{1}{5}\sum_{m=-2}^{2}\Phi_m^{jk}\,\Phi_{-m}^{rs}\,\delta_{m',-n'}\,(-1)^{m'-m}.\end{aligned} \tag{3.36}$$

The relaxation superoperator in the extreme narrowing limit can therefore be calculated directly as:

$$\hat{\hat{\Gamma}} = \frac{\tau_c}{5}\sum_{j<k}\sum_{k}\sum_{r<s}\sum_{s}\sum_{n,m=-2}^{2}(-1)^{n+m}\,\Phi_m^{jk}\,\Phi_{-m}^{rs}\,\hat{\hat{T}}_{2,-n}^{jk}\,\hat{\hat{T}}_{2,n}^{rs}, \tag{3.37}$$

and can be used as in [152] to calculate self-relaxation rate constants Γ_i for a state corresponding to the operator $\hat{P}^i$ (where $\hat{P}^{i\dagger}$ is its Hermitian conjugate):

$$\Gamma_i = \frac{\mathrm{Tr}\left[\hat{\hat{\Gamma}}\left[\hat{P}^i\right]\hat{P}^{i\dagger}\right]}{\mathrm{Tr}\left[\hat{P}^i\hat{P}^{i\dagger}\right]}. \tag{3.38}$$

Effect of relaxation operator on the singlet state

The self-relaxation rate constant Γ_S for the singlet state of interest is given using Eq. (3.38) by

$$\Gamma_S = \frac{\mathrm{Tr}\left[\hat{\hat{\Gamma}}\left[\hat{P}_{a,b}^S\right]\hat{P}_{a,b}^S\right]}{\mathrm{Tr}\left[\hat{P}_{a,b}^S\hat{P}_{a,b}^S\right]}, \tag{3.39}$$

where a and b are the two entangled spins in the singlet state. However, as written the calculation in Eq. (3.39) would be performed in the full Liouville space of two Posner molecules, in which case the Liouville dimension is $4096^2 \simeq 16.8\times10^6$.

This large matrix dimension would make the calculation slow, and therefore we developed a similar approach to that used for the coherent interactions (see

Section 3.3 and in [143, 144]) in order to calculate the relaxation within the Hilbert space of each Posner cluster separately.

Novel method for calculating relaxation of an intermolecular singlet

Using Eqs. (3.30) and (3.32) and the definition of $\hat{P}^{\mathrm{S}}_{a,b}$, the unnormalized initial singlet relaxation rate constant Γ'_{S} (i.e. the numerator of Eq. (3.39)) can be written (in units of τ_{c}) as:

$$\begin{aligned}
\Gamma'_{\mathrm{S}} &= \mathrm{Tr}\left[\left\langle\left[\hat{\mathcal{H}}_1(t),\left[\hat{\mathcal{H}}_1(t),\hat{P}^{\mathrm{S}}_{a,b}\right]\right]\right\rangle\hat{P}^{\mathrm{S}}_{a,b}\right] \\
&= \mathrm{Tr}\left[\left\langle\left[\hat{\mathcal{H}}_1(t),\left[\hat{\mathcal{H}}_1(t),\frac{1}{4}\hat{\mathbb{1}}-\sum_{\alpha}\hat{S}_{a\alpha}\otimes\hat{S}_{b\alpha}\right]\right]\right\rangle\frac{1}{4}\hat{\mathbb{1}}-\sum_{\beta}\hat{S}_{a\beta}\otimes\hat{S}_{b\beta}\right] \\
&= \sum_{\alpha,\beta}\mathrm{Tr}\left[\left\langle\left[\hat{\mathcal{H}}_1(t),\left[\hat{\mathcal{H}}_1(t),\hat{S}_{a\alpha}\otimes\hat{S}_{b\alpha}\right]\right]\right\rangle\hat{S}_{a\beta}\otimes\hat{S}_{b\beta}\right] \\
&= \sum_{\alpha,\beta}\mathrm{Tr}\left[\langle\mathbf{A}\rangle\,\hat{S}_{a\beta}\otimes\hat{S}_{b\beta}\right].
\end{aligned} \tag{3.40}$$

The term labelled **A** can then be written, using Eq. (2.52) for the joint Hamiltonian of two molecules and expanding the commutators, as

$$\begin{aligned}
\mathbf{A} &= \left[\hat{\mathcal{H}}^a_1(t)\oplus\hat{\mathcal{H}}^b_1(t),\left[\hat{\mathcal{H}}^a_1(t)\oplus\hat{\mathcal{H}}^b_1(t),\hat{S}_{a\alpha}\otimes\hat{S}_{b\alpha}\right]\right] \\
&= \left[\hat{\mathcal{H}}^a_1(t),\left[\hat{\mathcal{H}}^a_1(t),\hat{S}_{a\alpha}\right]\right]\otimes\hat{S}_{b\alpha}+\hat{S}_{a\alpha}\otimes\left[\hat{\mathcal{H}}^b_1(t),\left[\hat{\mathcal{H}}^b_1(t),\hat{S}_{b\alpha}\right]\right] \\
&\quad+2\left[\hat{\mathcal{H}}^a_1(t),\hat{S}_{a\alpha}\right]\otimes\left[\hat{\mathcal{H}}^b_1(t),\hat{S}_{b\alpha}\right].
\end{aligned} \tag{3.41}$$

The third term on the last line of Eq. (3.41) will be zero under an ensemble average, since the tumbling of the two molecules is uncorrelated. We note that the commutators in Eq. (3.41) are of the same form as those in Eq. (3.32), and so we define a relaxation superoperator for each separate molecule,

$$\hat{\hat{\Gamma}}^i = \left\langle\hat{\hat{\mathcal{H}}}^i_1(t)\hat{\hat{\mathcal{H}}}^i_1(t)\right\rangle\tau_{\mathrm{c}}, \tag{3.42}$$

such that Eq. (3.40) can now be written as

$$\begin{aligned}\Gamma'_{\mathrm{S}} &= \sum_{\alpha,\beta} \mathrm{Tr}\left[\left(\hat{\hat{\Gamma}}^{a}\left[\hat{S}_{a\alpha}\right]\otimes\hat{S}_{b\alpha}+\hat{S}_{a\alpha}\otimes\hat{\hat{\Gamma}}^{b}\left[\hat{S}_{b\alpha}\right]\right)\left(\hat{S}_{a\beta}\otimes\hat{S}_{b\beta}\right)\right]\\ &= \sum_{\alpha,\beta} \mathrm{Tr}\left[\hat{\hat{\Gamma}}^{a}\left[\hat{S}_{a\alpha}\right]\hat{S}_{a\beta}\otimes\hat{S}_{b\alpha}\hat{S}_{b\beta}+\hat{S}_{a\alpha}\hat{S}_{a\beta}\otimes\hat{\hat{\Gamma}}^{b}\left[\hat{S}_{b\alpha}\right]\hat{S}_{b\beta}\right]\\ &= \sum_{\alpha,\beta} \mathrm{Tr}\left[\hat{\hat{\Gamma}}^{a}\left[\hat{S}_{a\alpha}\right]\hat{S}_{a\beta}\right]\mathrm{Tr}\left[\hat{S}_{b\alpha}\hat{S}_{b\beta}\right]+\mathrm{Tr}\left[\hat{S}_{a\alpha}\hat{S}_{a\beta}\right]\mathrm{Tr}\left[\hat{\hat{\Gamma}}^{b}\left[\hat{S}_{b\alpha}\right]\hat{S}_{b\beta}\right]\\ &= \sum_{\alpha} 2^{N_a-2}\mathrm{Tr}\left[\hat{\hat{\Gamma}}^{a}\left[\hat{S}_{a\alpha}\right]\hat{S}_{a\alpha}\right]+2^{N_b-2}\mathrm{Tr}\left[\hat{\hat{\Gamma}}^{b}\left[\hat{S}_{b\alpha}\right]\hat{S}_{b\alpha}\right],\end{aligned} \tag{3.43}$$

using the fact that $\mathrm{Tr}\left[\hat{S}_{ip}\hat{S}_{iq}\right] = 2^{N_i-2}\delta_{pq}$, where N_i is the number of spins in a molecule, i. Therefore, Eq. (3.43) can be substituted back into Eq. (3.39), allowing us to calculate the singlet relaxation rate constant as

$$\Gamma_{\mathrm{S}} = \sum_{i=a,b} 2^{N_i-2} \sum_{\alpha=x,y,z} \frac{\mathrm{Tr}\left[\hat{\hat{\Gamma}}^{i}\left[\hat{S}_{i\alpha}\right]\hat{S}_{i\alpha}\right]}{\mathrm{Tr}\left[\hat{P}^{\mathrm{S}}_{a,b}\hat{P}^{\mathrm{S}}_{a,b}\right]}, \tag{3.44}$$

with the relaxation superoperators now each in the Liouville space of just one molecule, rather than of the whole system. By comparison with Eq. (3.39), it can be seen that Eq. (3.44) involves a sum of the self relaxation rates for each Cartesian component of the nuclei in the singlet state.

In general $\hat{\hat{\Gamma}}^{1} \neq \hat{\hat{\Gamma}}^{2}$, since the two molecules in the intermolecular singlet state could be different, but in our case the two molecules are identical and so $\hat{\hat{\Gamma}}^{1} = \hat{\hat{\Gamma}}^{2} = \hat{\hat{\Gamma}}^{*}$ where the * indicates that the operator is in the Hilbert space of just one Posner molecule, further simplifying the calculation:

$$\Gamma_{\mathrm{S}} = 2^{N-1} \sum_{\alpha}^{x,y,z} \frac{\mathrm{Tr}\left[\hat{\hat{\Gamma}}^{*}\left[\hat{S}_{a\alpha}\right]\hat{S}_{a\alpha}\right]}{\mathrm{Tr}\left[\hat{P}^{\mathrm{S}}_{a,b}\hat{P}^{\mathrm{S}}_{a,b}\right]}. \tag{3.45}$$

Strict upper limit on lifetime 3.4.2

An intermolecular singlet relaxation rate of $\Gamma_S/s^{-1} = 7.86 \times 10^{-6} \tau_c ps^{-1}$ and a relaxation time (Γ_S^{-1}) of ~37 min were obtained using Eq. (3.45) for Posner molecules dissolved in pure water ($\tau_c = 58$ ps) at 37 °C. For comparison, singlet relaxation times of 51, 43, and 25 min were calculated for the three possible *intra*molecular singlet states $|S_{1,2}\rangle$, $|S_{1,4}\rangle$, and $|S_{1,6}\rangle$ respectively. This is as expected; the intramolecular entanglement ought to be lost on a similar timescale to the intermolecular case because the dipolar field experienced by each ^{31}P is similar.

An estimate of T_1, the spin–lattice relaxation time for one molecule, can also be obtained using the methods described above by calculating the self-relaxation rate constant for the sum z-angular momentum [104], yielding a value of approximately 37 min.[8] This is also as expected; the dipolar coupling between the singlet-entangled nuclei makes no contribution to singlet relaxation because it is symmetric with respect to exchange [135], but does contribute to overall spin–lattice relaxation, so we would expect T_1 for a single Posner molecule to be between the smallest and largest values of Γ_S^{-1} calculated for an intramolecular singlet.

A simple order of magnitude check gives further confidence in these results: the dipolar spin–lattice and spin–spin relaxation rates for a pair of ^{31}P nuclei separated by $r \simeq 0.5$ nm [130] is given in the extreme narrowing limit by [22]

$$T_1^{-1} = T_2^{-2} = \frac{3}{2}\left(\frac{\hbar \gamma_P^2 \mu_0}{4\pi r^3}\right)^2 \tau_c. \tag{3.46}$$

Multiplying this relaxation rate by ten, because each entangled spin is relaxed by five ^{31}P neighbours in its respective molecule, gives a value of approximately $1.5 \times 10^{-5} \tau_c$ ps^{-1}, within a factor of two of Eq. (3.45).

Relaxation rates were also calculated for a variety of other initial states, being a linear combination of up to six shared singlets. For these states the relaxation

[8] It would appear to be a coincidence that this matches, to the nearest minute, the relaxation time for an intermolecular singlet.

times increase with each additional singlet, up to an increase of around a factor of two for six shared singlets. However, the chances of a pair of Posner molecules with more than one or two shared singlets arising biochemically seems unlikely (see also Section 3.5).

Fisher's most conservative initial estimate (one day) for spin relaxation in Posner molecules was obtained by considering the intermolecular dipolar interactions between ^{31}P nuclei in a Posner molecule and the protons in water [42]. One day is far longer than the strict upper limit on relaxation time calculated here (37 min), and so it is clear that intramolecular ^{31}P –^{31}P dipolar relaxation is much more efficient than other mechanisms previously considered for this molecule.

Other relaxation routes 3.4.3

It remains the case that 37 min is still a long relaxation time, when compared to what we might normally expect for ^{31}P nuclei [48]. This can be understood by considering that the model employed here contains reasonably weak interactions that are modulated by rapid tumbling, and so a long coherence time is not surprising. There are many reasons why relaxation times of intermolecular singlets in Posner molecules may be much shorter than the upper bound we have calculated.

Increased correlation time

As can be seen in Eq. (3.32), the relaxation rate depends linearly on the correlation time of the process driving the relaxation. This means that anything that hinders the rotation of the Posner molecule will increase the relaxation rate and decrease the singlet coherence time. In fact there are several processes, all likely to occur in Fisher's hypothesis, that would increase the correlation time: a more viscous solvent than pure water; dimerization, which is essential for the read-out of entanglement [42]; formation of larger oligomeric structures, as are formed during the nucleation of amorphous calcium phosphate [127]; and binding to a larger structure such as a protein or membrane.

Other magnetic processes

Various other magnetic interactions will likely further decrease the coherence time. Dissolved oxygen is ubiquitous *in vivo* and is already known to be an effective relaxation agent in singlet magnetic resonance [140]. Spin–rotation relaxation, caused by the interaction between nuclear spins and the fluctuating magnetic field generated as they rotate, may be significant given weak dipolar interactions and the absence of CSA relaxation (often important in high-field magnetic resonance) in the Earth's magnetic field [134]. Lin and Chiu have used *ab initio* calculations with implicit solvation models to find two structures of $Ca_9(PO_4)_6$ that are more stable than the S_6 form discussed here, which possess very large dipole moments (10 D and 31 D) [161]. These moments mean that the molecule would be strongly solvated, and significant $^{31}P-{}^{1}H$ dipolar relaxation could occur.

Dynamic processes

The study in reference [161] also suggested that $Ca_9(PO_4)_6$ may have multiple structures with similar energy. If so, dynamic processes may lead to other relaxation pathways. For instance, if interconversion of different isomers of the Posner molecule is possible then the assumption of a rigid structure would be invalid, and the accompanying modulation of scalar and dipolar ^{31}P–^{31}P couplings would lead to new relaxation pathways. Furthermore, exchange of phosphate molecules via a mechanism such as

$$Ca_9(PO_4)_6 + H\underline{P}O_4^{2-} \rightleftharpoons Ca_9(PO_4)_5(\underline{P}O_4) + HPO_4^{2-} \qquad 3.47$$

may swap an entangled $Ca_9(PO_4)_6$ spin with one in a random state (underlined). Free phosphate ions in solution have spin relaxation times on the order of seconds [48], and so the scrambling process described above would dramatically accelerate ^{31}P relaxation. Finally, a molecular dynamics study found clusters

related to $Ca_9(PO_4)_6$ but with lower Ca:P ratios that (a) contained protonated phosphate groups, (b) shared phosphate groups between clusters, and (c) had Na^+ partially substituted for Ca^{2+} [132]. The formation and interconversion of all of these structures could further contribute to spin relaxation.

Longer lived states 3.5

Besides relaxation rates for particular states, we can also use the relaxation matrix to directly find long-lived states. The eigenvalues of the relaxation matrix give the relaxation rates of its eigenvector states. For an isolated Posner cluster we found two eigenstates of $\hat{\hat{\Gamma}}$ that have a relaxation eigenvalue of zero (corresponding to infinitely long lifetimes under intramolecular dipolar relaxation). One of these is the trivial identity state, and the second can be written as

$$\left(\frac{1}{2} - \hat{P}^{S}_{1,6}\right)\left(\frac{1}{2} - \hat{P}^{S}_{2,5}\right)\left(\frac{1}{2} - \hat{P}^{S}_{3,4}\right), \tag{3.48}$$

which clearly involves all six ^{31}P nuclei in inversion-related singlet pairs (labelled as in Fig. 3.3). It seems unlikely that this exotic-looking spin state could arise from the enzymatic hydrolysis of pyrophosphate, which may create singlet-entangled pairs but not with the correlation among pairs described by Eq. (3.48).

There are 4094 remaining eigenstates once the two non-relaxing ones have been removed, and of these 553 have self-relaxation times longer than 37 minutes, the longest being around three times longer. So, even if any of the states that relax more slowly than the intermolecular singlet considered throughout this chapter could be prepared in a pair of Posner molecules, and if these states would correspond to intermolecular entanglement (both of which seem unlikely), they would still not last much longer than 37 minutes. Furthermore, the additional factors described in Section 3.4.3 would apply equally well to these slower relaxing states.

Perhaps more importantly, the eigenstates described are for the relaxation superoperator of an *isolated* Posner molecule—the relevant system to consider is in fact the Hilbert (or indeed Liouville) space of a *pair* of Posner molecules, as we have done throughout the rest of this chapter.

Non-relaxing nuclear singlet states occur when fluctuations in local magnetic fields are correlated at the sites of the participating nuclei [37], meaning that the geometrical arrangement of the participating spins should have a centre of inversion [157] as seen for the state in Eq. (3.48). This correlation is not possible for an intermolecular singlet, and so it is certain that all intermolecular nuclear spin states, including those involving singlet states, between two independently rotationally diffusing Posner molecule will experience both the dipolar relaxation modelled in this chapter and any other types of spin relaxation that operate. While there may exist intermolecular states that have slightly longer relaxation times than the singlet state considered throughout this chapter, there will definitely be none that are immune to relaxation, and by analogy to the one molecule case it seems unlikely that their lifetimes could be significantly different to the 37 minutes calculated for the singlet state.

Therefore, in light of the work presented in this chapter it is with some confidence that we can say it is impossible to imagine entangled states for pairs of Posner molecules that exhibit the extraordinarily long lifetimes proposed in Fisher's hypothesis.

Selection rules 3.5.1

One final aspect of Fisher's hypothesis is his "quantum dynamical selection" rules, whereby the C_3 symmetry axis of a Posner molecule would give rise to a "pseudospin" quantum number, $\tau = 0, \pm 1$, based on the indistinguishability of symmetry-related nuclei in small molecules [124]. Fisher predicts this will entangle nuclear spin states with the molecular rotations and remain coherent for

exceedingly long times [42, 124], in an analogous fashion to the coupling between nuclear spin states and rotations that is well known for molecular ortho- and para-hydrogen and causes them to interconvert very slowly.

Under Fisher's proposed selection rule homolytic bond-breaking of ortho-H_2 would be spin-forbidden. Such an argument appears to overlook the inevitability of intramolecular nuclear spin relaxation processes and the interconversion of nuclear spin isomers. In 1933 Wigner[9] showed that ortho- and para-hydrogen can be interconverted when the hydrogen nuclei experience symmetry-breaking local magnetic fields [163]. Hubbard established that the "contribution of spin–rotational interactions to the nuclear magnetic relaxation of identical spin-1/2 nuclei at equivalent positions in spherical liquid molecules" has a much shorter correlation time than that for dipolar interactions [164], and Curl *et al.* showed that "[rapid] conversion from one [spin] isomer to the other must occur since the spin wavefunctions are mixed by spin–rotation interaction" which, alongside the dipolar interactions, can rapidly equilibrate nuclear spin isomers in larger molecules "even in the absence of magnetic collisions" [165]. The reason that these interactions couple states of different nuclear and rotational symmetry is that they have components that are antisymmetric with respect to exchange of the positions and spin states of symmetry-related nuclei [34, 166].

These considerations, alongside the relaxation processes described in this chapter, surely invalidate any selection rules associated with Fisher's "pseudospin" quantum number τ. Recent calculations performed under Fisher's supervision have estimated that the τ pseudospin will have an intramolecular dipolar coupling relaxation time of between 1.7 and 17 hours [148], with a corresponding estimate of the T_1 spin lattice relaxation time due to the same dipolar relaxation

[9] Wigner was an early proponent of the idea that quantum mechanics had something to do with consciousness and the workings of the brain. He reformulated the famous "Schrödinger's cat" thought experiment as "Wigner's friend", proposing that wavefunction collapse is brought about by the influence of the observer's consciousness, outside of any realist interpretation of quantum mechanics [162].

of between 2.5 and 25 hours. In Section 3.4.2 we estimated $T_1 = 37$ min, and the balllistic model for reorienting the dipolar interaction used in [148] presents no clear advantage over the Redfield approach used in this chapter. Indeed, it does not appear to take into account the fact that the $b \simeq 990$ Hz dipolar coupling constant between two ^{31}P nuclei must be scaled up to account for the multiple ^{31}P nuclei in each Posner molecule. Thus the calculated relaxation times in [148] will likely be overestimates of the true value, which is more likely to be reflected by the strict upper limit derived in the work presented here.

Conclusions and further work 3.6

In Section 3.3 it was shown that any initial bipartite entanglement between Posner molecules will persist and reoccur on a timescale of seconds under coherent evolution due to J-coupling. However, it would appear that this coherent evolution means that, for at least half of the time (depending on the level of symmetry in the Posner molecule), there will be no bipartite intermolecular entanglement between nuclei. Whether this is consistent with Fisher's hypothesis will likely depend critically on the chemical details of whatever process will read out the quantum information from entangled molecules.

In Section 3.4 it was shown that the strict upper limit for two-spin singlet entanglement lifetimes in a pair of Posner molecules can be set at 37 minutes. For the reasons outlined in Section 3.4.3, we would suggest that a more realistic lifetime is on the order of a few seconds, as is typical for ^{31}P spin relaxation [48], rather than half an hour. The only conceivable entangled state in the Posner molecule that could possibly have a relaxation time on the order of minutes under physiological conditions would involve *intra*molecular singlets—useless as a source of "spooky action at a distance" [97].

In Section 3.5 it was shown that there are no long-lived intermolecular singlet states that are immune to the coherent or time-dependent parts of the spin Hamil-

tonian. One question that remains unanswered from this work is whether there are intermolecular entangled states involving more than two ^{31}P nuclei that will be immune to coherent or relaxation dynamics. The question of testing whether a particular multinuclear state is entangled is not trivial, and it would be interesting to develop this further. Furthermore, other relaxation mechanisms such as spin–rotation or chemical shift anisotropy could be modelled in order to derive a more accurate upper-bound on the relaxation time.

4 An alternative radical pair for magnetoreception

It is well established that many animal species use a magnetic compass to navigate by the Earth's ~50 μT magnetic field over large distances during their migratory seasons. In particular, it has been shown that migratory songbirds use a light-dependent magnetic compass sense to orient themselves when they make the annual journeys to and from their breeding and feeding grounds [51, 52, 167] with precision better than 5° [168, 169]. Behavioural experiments have shown that this sense relies upon the birds being exposed to light in the $400\,\text{nm} < \lambda < 565\,\text{nm}$ wavelength region of the electromagnetic spectrum [67, 170].

There are two main theories that explain the operation of this compass sense. The first is a magnetite mechanism, whereby directional information is derived from the interaction of the Earth's field with magnetic iron oxide crystals produced in the bird's body [58, 171, 172]. The second, which is the focus of this Chapter, is a radical-pair mechanism, whereby the compass information is derived from the quantum yields of photochemical reactions in the birds' eyes that are affected by the relative orientation of the bird's head and the Earth's field [15, 59, 60].

Radical pair magnetoreception 4.1

Over the past two decades a growing body of evidence has amassed to support cryptochrome proteins as the likely magnetoreceptor for migratory songbirds [15, 60]—that is, the substance that is affected by a magnetic field and provides a signal that will ultimately be interpreted by the bird as a compass bearing [62, 66].

Cryptochromes are a class of blue-light sensitive flavoproteins that can be found in many species of plant and animal [173, 174]. The response of the cryptochrome to a magnetic field relies on a flavin adenine dinucleotide (FAD) cofactor that binds to the protein and, after absorption of a photon in the UV-A or blue regions of the electromagnetic spectrum (from approximately 300 – 500 nm) [175], generates a spin-correlated radical pair with a surface tryptophan (TrpH) residue via a cascade of electron transfers on a timescale of picoseconds [174]. This radical pair is initially in an electronic singlet state, and non-uniform magnetic interactions for the two partner radicals cause this initial state to undergo singlet–triplet mixing, affecting the quantum yields of the products of the photochemical reaction (see also Section 1.2.1). A difference in quantum yields with an applied magnetic field is known as a magnetic field effect (MFE).

The mechanism described above, by which information about the direction of an applied magnetic field is detected by radical species, is known as the radical pair model of magnetoreception. The conventional reaction scheme for cryptochromes is outlined in Fig. 4.1, as well as an extended superoxide mechanism that is the focus of this chapter.

Conventional mechanism (M1) 4.1.1

The generally accepted reaction scheme for magnetic sensitivity in cryptochrome is as shown in Fig. 4.1 (shaded region) and will be referred to here as M1. When cryptochromes are irradiated with blue light the spin-correlated radical pair $\left[\mathrm{FAD}^{\bullet-}\,\mathrm{TrpH}^{\bullet+}\right]$ is formed, which we will call RP1. RP1 is produced via sequential electron transfers along a chain of three or four TrpH residues to the noncovalently bound FAD cofactor [177–179], and is initially in a singlet state. Only the singlet state can return to the ground state, whereas both the singlet and triplet forms can undergo a deprotonation at the $\mathrm{TrpH}^{\bullet+}$ to form the longer lived, magnetically insensitive, species $\mathrm{FAD}^{\bullet-} + \mathrm{Trp}^{\bullet}$ [63, 180].

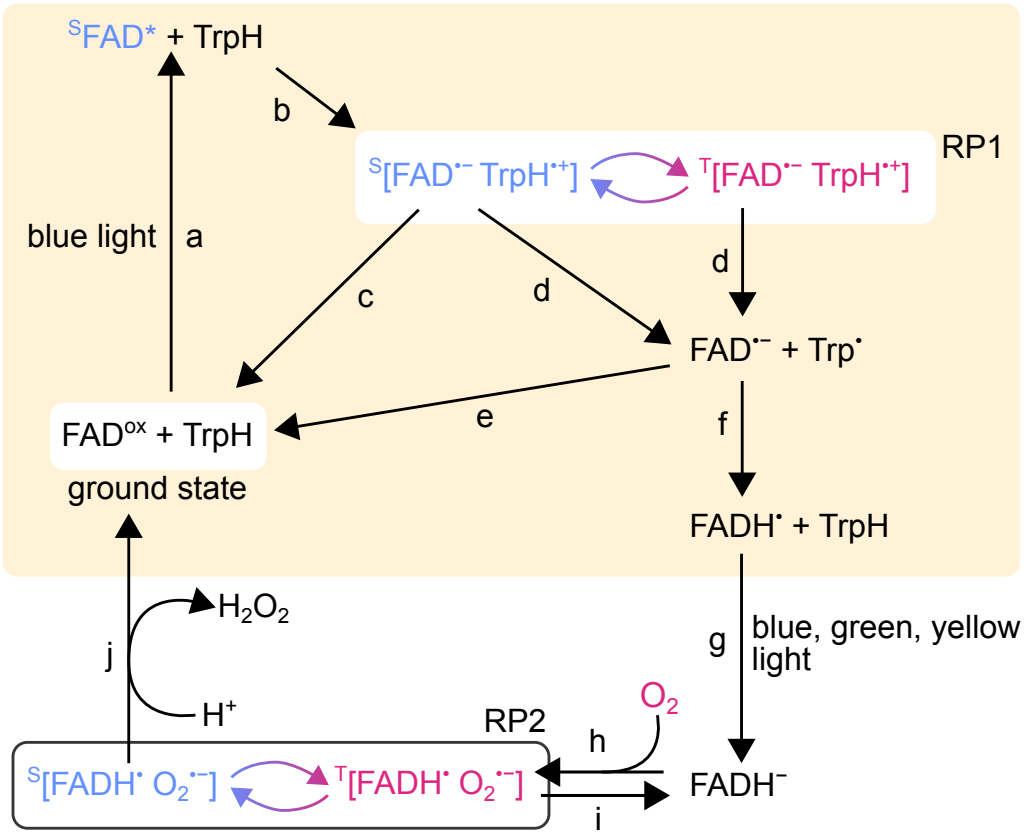

Figure 4.1 The shaded region shows the conventional scheme, M1, which accounts for observed MFEs on the quantum yields of photochemical reactions in purified cryptochromes [63, 176] (a) $^{S}FAD^{*}$, the excited singlet state of FAD, is formed within the protein when the fully oxidized state, FAD^{ox}, is irradiated with blue light ($\lambda < 500\,nm$) (b) A radical pair (RP1) is then formed by sequential electron transfers along a chain of tryptophan (TrpH) residues. RP1 is magnetically sensitive, with the efficiency of its singlet–triplet interconversion (blue/red arrows) depending on its orientation with respect to the Earth's magnetic field. Only singlet RP1 can recombine (c) to form the ground state, while the $TrpH^{\bullet+}$ radical in both the singlet and triplet forms can lose a proton (d) to form a stabilised, magnetically insensitive radical pair. This stabilised radical pair either recombines (e) to regenerate the ground state or reacts further (f) to form the $FADH^{\bullet}$ radical and TrpH. It has been suggested that M1 could be extended to include reoxidation of the reduced flavin by O_2 (this is the superoxide mechanism, M2, which is represented by the whole of this figure). $FADH^{\bullet}$ can absorb a second photon with $\lambda < 650\,nm$ (g), producing the fully reduced flavin anion $FADH^{-}$ after a further electron transfer. Reversible, spin-selective oxidation of FADH by (electronic triplet) O_2 (h, i) forms a $[FADH^{\bullet}\ O_2^{\bullet-}]$ radical pair, RP2, initially in a triplet state. RP2, like RP1, can also undergo triplet–singlet interconversion, with only the singlet state able to be oxidized back to the ground state (j). In principle, RP2 can be magnetically sensitive [15, 85–87, 176]. A version of this figure has been published in reference [2].

It is believed that the extent and timing of singlet–triplet interconversion in radical pairs such as RP1 is influenced by the direction of the Earth's magnetic field relative to the two radical species. This is because there are anisotropic magnetic interactions in RP1, and the direction of the bird's head relative to the magnetic field vector will modulate these anisotropic interactions and therefore the quantum yields of the $FADH^{\bullet}$ radical and any downstream signalling states. It is presumed that the changes in these yields are the source of directional information that is sent from the receptors in the eyes to the brain and used as a navigational tool [15, 181].

Superoxide mechanism (M2) 4.1.2

Despite a considerable amount of evidence that has built up around M1 [15], several aspects of the reaction scheme have either (a) relatively circumstantial evidence in support of them, or (b) potential alternative explanations. In recent years there has been debate over alternative radical pairs that may be more suitable than RP1 as a magnetosensor [182].

In 2009, a behavioural study reported that European robins were disoriented when exposed to low-intensity (tens of nT) magnetic fields that oscillated at the Larmor frequency for a free electron in the Earth's magnetic field ($\nu_{\mathrm{L}} = \gamma_{\mathrm{e}} B_0 / 2\pi \simeq 1.3\,\mathrm{MHz}$) [183]. The Larmor frequency is proportional to the magnetic field strength, and when this was artificially doubled from $B_0 = 46\,\mu\mathrm{T}$ (the local geomagnetic field strength) to $92\,\mu\mathrm{T}$ and the birds were pre-exposed to the stronger field for 3 hours, they were similarly disoriented by a low-intensity field oscillating at $\nu \simeq 2.6\,\mathrm{MHz}$.

Such a resonant response from a radical pair compass sensor would only be expected if one of the radicals were devoid of hyperfine interactions, such that its energy level splitting depends solely on the Zeeman interaction between the applied field and the electron spin [183].

This condition is evidently not met by RP1, in which both radicals contain several magnetically active nuclei (i.e. ^{1}H, ^{14}N, see Fig. 4.3) with which the electrons have significant hyperfine interactions [182]. The condition will also not be met by most other small organic radicals [32]. The only reasonable molecule that has been suggested that meets this criterion is the superoxide radical $O_2^{\bullet -}$ [85–87, 182, 183], suitable because it has no hyperfine interactions (^{16}O has no nuclear spin and is more than 99.7% abundant, see Table A.1). It must be noted, however, that later experiments performed under more rigorous conditions have failed to reproduce the response to Larmor frequency fields that was described in reference [183], and in fact showed that birds are more disoriented by weak broadband electromagnetic fields than narrow-band fields at the Larmor frequency [184]. A survey of the results of disorientation experiments of this type can be found in references [185, 186].

Although the involvement of superoxide in the magnetoreception mechanism is in no way established, it cannot be immediately dismissed. In Fig. 4.1 a mechanism M2 is outlined, which includes a [FADH$^{\bullet}$ $O_2^{\bullet -}$] radical pair (RP2) that could arise in cryptochrome and potentially generate MFEs.

The flavin in RP1 may be protonated and the tryptophan residue reduced, such that a second light-activation and electron transfer step could occur, forming the fully reduced flavin anion FADH^{-}. This can then be oxidized by molecular oxygen, forming the superoxide-containing radical-pair [FADH$^{\bullet}$ $O_2^{\bullet -}$] known as RP2. It has been shown both *in vitro* and *in vivo* that O_2 efficiently oxidizes reduced flavins [87, 187, 188]. RP2 will initially be in a triplet state (due to oxygen's $^{3}\Sigma_g^{-}$ electronic ground state), but can undergo triplet–singlet interconversion in a field-dependent fashion much like RP1, with only the singlet RP2 able to regenerate the resting state via a second electron transfer [86]. Therefore, it could function as a magnetoreceptor in much the same way as RP1 does in M1.

The processes described for M2 require light-dependent steps that produce $FADH^-$. Firstly, $FADH^\bullet$ is produced from FAD^{ox}, exactly the same as in the M1 scheme, requiring blue light ($\lambda < 500\,\text{nm}$). Secondly, $FADH^-$ is produced, which requires either blue, green, or yellow light with $\lambda < 650\,\text{nm}$. The critical argument in favour of the M2 mechanism is that wavelengths longer than 500 nm are not strongly absorbed by the ground state oxidized flavin. So, light with wavelengths in the range $500\,\text{nm} < \lambda < 650\,\text{nm}$ cannot on its own lead to either $FADH^\bullet$ or $FADH^-$. Certain other experimental and theoretical results, which mainly rely on the difference in the absorption spectra of FAD^{ox} and $FADH^\bullet$, support the M2 mechanism's flavin-superoxide radical pair.

Immunohistochemical experiments suggest that activated cryptochrome 1a (Cry1a) where the FAD has been fully or partially reduced can occur in chicken retinæ if they are illuminated by light with $\lambda \leq 565\,\text{nm}$, conditions under which birds can use their magnetic compass to orient [69]. Activated (reduced) cryptochrome and well-oriented behaviour were both observed under green light with $\lambda > 500\,\text{nm}$, which is not absorbed by the resting (oxidized) state of FAD, and the authors suggested this means that RP1 is not the crucial radical pair for magnetoreception. However, further experiments performed alongside those described in [69, 189] have indicated no (or little) activated Cry1a when the chickens were exposed to light with $\lambda \geq 500\,\text{nm}$ [190].

When the chickens were kept in the dark before the experiment, there was no activated cryptochrome found under green light, whereas there was staining under UV-A or blue light where the complete photocycle can occur [189]. This indicates that the key radical pair for magnetoreception may actually be formed in a reoxidation reaction "in the dark", i.e. a reaction that is not light-dependent, between the fully reduced flavin $FADH^-$ (which cannot be formed by green light alone) and another molecule such as oxygen.

So-called "flickering" experiments have shown that robins can successfully orient when a 50 μT magnetic field is supplied only during periods of darkness lasting around 100 ms, alternated with either green ($\lambda \simeq 565$ nm) or turquoise ($\lambda \simeq 500$ nm) light [191]. Since RP1 would have a lifetime of microseconds at most, it was argued that these results indicate that the key step for magnetoreception occurs without light activation and therefore that RP1 could not be the magnetic sensor [64].

Experiments on *Arabidopsis* (plant) cryptochrome have shown that there is a magnetic response to plant growth, even when the magnetic field is only present during periods of darkness [192]. It has been claimed that this means the reoxidation of $FADH^-$ in the dark must be the critical reaction for magnetosensing, although it is unclear why there would be a biological parallel to migratory birds.

Theoretical considerations support the idea that $O_2^{\bullet -}$ could be produced when oxygen reoxidizes fully reduced flavin, or involved in reoxidizing partially reduced flavin [86]. These processes seem more chemically feasible than the suggestion in [85] that superoxide reduces $FADH^\bullet$ to $FADH^-$.

The flavin radical has several anisotropic hyperfine interactions [182], whereas we have already established that $O_2^{\bullet -}$ has none. It is this asymmetry in the distribution of hyperfine interactions that makes RP2 attractive for magnetoreception [182, 183]. It has been shown that a radical pair $[FAD^{\bullet -}\, Z^\bullet]$, where $Z^\bullet$ has no hyperfine interactions and can be positively or negatively charged, or neutral, can have anisotropic magnetic responses 100 times more sensitive than RP1 [182].

Although there does not appear to be hard experimental evidence of a binding site for $O_2^{\bullet -}$ or O_2 in a cryptochrome protein, which would be a necessary condition for formation of RP2, a study that used molecular dynamics simulations and electronic structure calculations suggests that $O_2^{\bullet -}$ (and its protonated form $HO_2^\bullet$) can be stabilised via hydrogen bonding to reduced forms of FAD in

Drosophila melanogaster cryptochrome [88]. Within this study the active site was defined as a sphere with a radius of 0.5 nm around the flavin, and an oxygen molecule was placed in this active site, with the stability of the results assessed by performing molecular dynamics simulations on several random initial conditions of the flavin–oxygen complex. The cryptochrome–oxygen system was neutralized with 13 Na^+ atoms and solvated in a cubic water box with side length 10.5 nm. Both $O_2^{\bullet -}$ and $HO_2^{\bullet}$ radicals were found ~0.3 nm from the flavin group, with a ~40 meV singlet–triplet splitting calculated for the radical pair [$FAD^{\bullet -}$ $HO_2^{\bullet}$]. Although the calculations suggested that hydrogen bonding would hold the radicals close to the flavin, the motion of the two radicals did not appear to be constrained by this bonding in either amplitude or frequency. Such a large singlet–triplet splitting (40 meV $\simeq$ 345 T in magnetic field units, i.e. 7×10^6 times stronger than the Earth's magnetic field and 10^5 times stronger than the hyperfine interactions in the flavin, as will be described in Section 4.2) would prevent the MFE from developing, making this arrangement of the flavin and oxygen radicals unsuitable as a geomagnetic sensor.[1]

Taken together, the experimental and theoretical considerations outlined above build a picture of the possible alternative reaction mechanism M2 (Fig. 4.1). A reasonable test for the suitability of RP2 as a magnetoreceptor is the anisotropy of the singlet product yield, which we will calculate (see Section 4.2.2).

Spin relaxation in the superoxide radical 4.1.3

Spin relaxation is a term for the set of processes by which all spin coherence is returned to an equilibrium state, as described in Section 2.2.5.

If spin relaxation occurs on a significantly faster timescale than the singlet–triplet interconversion caused by the Earth's 50 μT magnetic field then there can be no MFE. Several theoretical studies have assessed the spin relaxation of RP1, mainly focusing on modulation of the hyperfine interactions via motional fluctu-

[1] This conclusion is contrary to the conclusion of [88].

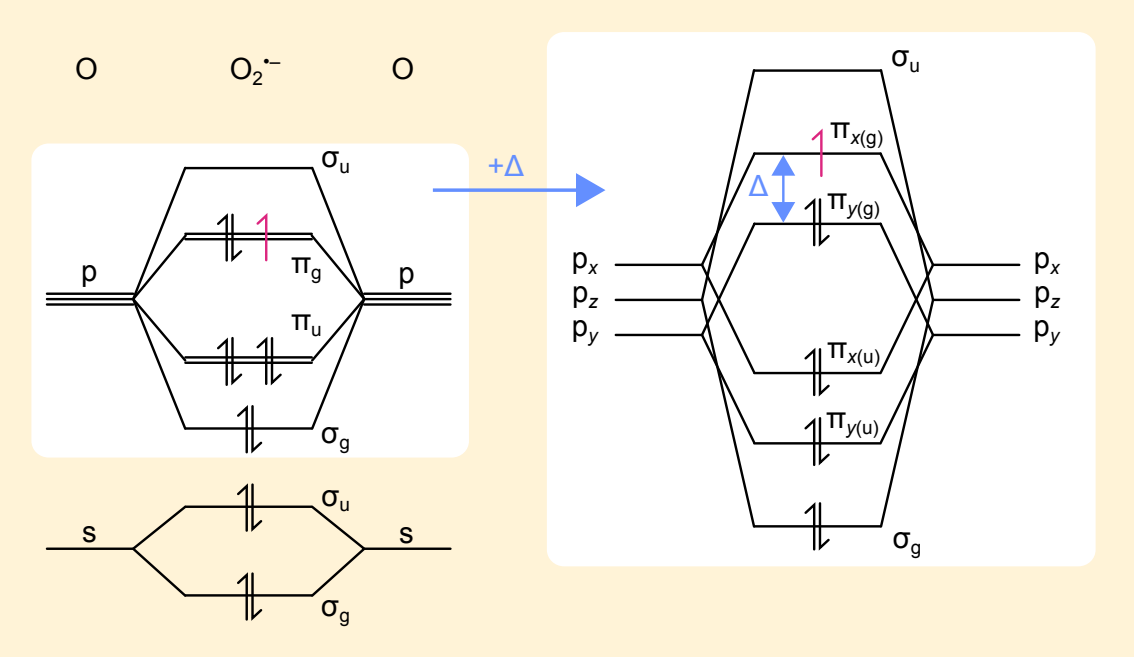

Figure 4.2 Molecular orbital diagram for $O_2^{\bullet -}$ radical, showing an unpaired electron (pink) in a π_g antibonding orbital. Upon application of a ligand field an energy gap of magnitude Δ is introduced between the p_x and p_y orbitals, lifting the degeneracy of the corresponding π_g orbitals. Note that this diagram is not drawn to any accurate energy scale.

ations [154, 159, 193]. These studies conclude that the $TrpH^{\bullet +}$ radical is likely to undergo more rapid spin relaxation than $FAD^{\bullet -}$ (and therefore less likely to be compatible with geomagnetic sensing), and that if the dominant relaxation processes are due to fluctuations in hyperfine interactions then a radical with fewer hyperfine interactions than $TrpH^{\bullet +}$, and ideally one with none at all, would be a more suitable magnetosensor. On a superficial level, these two conclusions could support a [$FADH^{\bullet}$ $O_2^{\bullet -}$] geomagnetic sensor.

A necessary condition that has been derived for any geomagnetic sensor is that the radical pair should not undergo electron spin relaxation much faster than 1 μs [61, 86]. Spin equilibration is in fact expected to be unusually fast for the $O_2^{\bullet -}$ radical, when compared to other organic radicals [86, 194]. This is because of the orbitally degenerate electronic ground state in $O_2^{\bullet -}$ and its significant spin–orbit coupling.

$O_2^{\bullet-}$ has cylindrical symmetry and an unpaired electron in its orbitally degenerate $^2\Pi_g$ ground state (see Fig. 4.2). The energies of the π_x and π_y orbitals are degenerate (setting z as the intermolecular axis, see Figs. 4.2 and 4.3), so the electron is free to move between these orbitals. This is equivalent to an orbital current about the internuclear axis and therefore generates a magnetic field that interacts with the spin magnetic moment [109]. In $O_2^{\bullet-}$ the spin–orbit coupling constant $\lambda = -160\,\mathrm{cm}^{-1}$ [195], equivalent to 170 T or 0.74 $k_B T$ at 310 K.

Spin–orbit coupling is usually quenched by low symmetry for organic radicals [109]. For radicals such as $O_2^{\bullet-}$, with high symmetry and strong spin–orbit coupling, the total spin–orbital angular momentum can be treated as an effective spin [196], and spin–rotational relaxation of the electron spin coherence occurs on the timescale that the quantization axis (i.e. the internuclear axis) tumbles in solution [197].

This means that, as long as the orbital angular momentum remains unquenched, as may be the case if the molecule is free to tumble in solution, the electron spin will be quantized along the molecular axis [86]. In this case spin relaxation will occur on a timescale of picoseconds to nanoseconds as the molecule tumbles, negating any significant response to an Earth's strength field (~50 μT) and rendering it unsuitable for magnetoreception [198]. In papers proposing or discussing the M2 mechanism, the rapid spin relaxation of $O_2^{\bullet-}$ has mainly been ignored or dismissed [85, 189–191, 199, 200].

A potential way that the problem of rapid spin relaxation in $O_2^{\bullet-}$ may be avoided is if Kattnig's radical-scavenging mechanism—whereby one of the two radicals reacts with a paramagnetic scavenger—occurs in cryptochrome [198, 201]. Within this model the "influence of radical scavengers" removes the "restrictions related to fast spin relaxation of superoxide" [198]. However, there is currently no experimental evidence that supports the radical-scavenging mechanism, and

it will not be considered further in this thesis where we focus on the simpler two-radical model.

Rapid spin relaxation explains why the aqueous solution ESR spectrum of $O_2^{\bullet -}$ appears to have never been recorded. It also explains why unambiguous MFEs on superoxide-containing radical pairs have only been observed for magnetic field strengths orders of magnitude stronger than the Earth's [194, 202]. It appears that superoxide could only be involved in magnetoreception if "the radical is complexed tightly enough to quench the majority of its orbital angular momentum and to prevent rapid re-orientation" but in such a way that hyperfine interactions are small [86]. Such inhibition of spin relaxation via the removal of the degeneracy for the highest occupied orbitals (see Fig. 4.2) has allowed the ESR spectrum of $O_2^{\bullet -}$ to be observed in frozen solutions [203] and in crystals of alkali halides [204].

We consider a superoxide molecule that has been immobilised in some way such that it experiences a ligand field splitting of magnitude Δ and the orbital angular momentum is partially quenched. This may happen if $O_2^{\bullet -}$ is bound to a suitable protein, reducing the spin relaxation rate and potentially allowing a significant magnetic response. Our aim is to define a regime under which superoxide based radical pairs, such as RP2, could give significant anisotropic singlet yield responses. We will then be able to discuss the biological viability of this regime.

Modelling RP2 4.2

The coherent spin Hamiltonian used for the flavin radical (indicated by a superscript F) can be written, in angular frequency units of $\hbar$, as

$$\begin{aligned} \hat{\mathcal{H}}_0^{\mathrm{F}}(\theta,\phi) &= \hat{\mathcal{H}}_{\mathrm{Z}}^{\mathrm{F}}(\theta,\phi) + \hat{\mathcal{H}}_{\mathrm{HF}}^{\mathrm{F}}, \\ \hat{\mathcal{H}}_{\mathrm{Z}}^{\mathrm{F}}(\theta,\phi) &= -\mu_{\mathrm{B}}\, g_{\mathrm{F}}\, \mathbf{B}(\theta,\phi)\cdot\hat{\mathbf{S}}_{\mathrm{F}} = \boldsymbol{\omega}(\theta,\phi)\cdot\hat{\mathbf{S}}_{\mathrm{F}}, \\ \hat{\mathcal{H}}_{\mathrm{HF}}^{\mathrm{F}} &= \mu_{\mathrm{B}}\, g_{\mathrm{F}} \sum_{i=1,2} \hat{\mathbf{S}}_{\mathrm{F}}\cdot\mathbf{A}^{(i)}\cdot\hat{\mathbf{I}}^{(i)}, \end{aligned} \tag{4.1}$$

where $\hat{\mathcal{H}}_{\mathrm{Z}}^{\mathrm{F}}(\theta,\phi)$ describes the isotropic Zeeman interaction between the unpaired electron and the magnetic field, $\hat{\mathcal{H}}_{\mathrm{HF}}^{\mathrm{F}}$ contains the hyperfine interactions, $\hat{\mathbf{S}}_{\mathrm{F}}$ is a vector containing the spin operators $\hat{S}_{\mathrm{F}x}$, $\hat{S}_{\mathrm{F}y}$, and $\hat{S}_{\mathrm{F}z}$ for the electron in $\mathrm{FADH}^{\bullet}$, $\hat{\mathbf{I}}^{(i)}$ is a similar nuclear spin operator, $g_{\mathrm{F}} = 2$ is the g-value for the flavin radical (ignoring the small anisotropic component), $\mathbf{A}^{(i)}$ is the diagonal hyperfine coupling tensor for nucleus i, and $\boldsymbol{\omega}(\theta,\phi) = -\mu_{\mathrm{B}}\, g_{\mathrm{F}}\, \mathbf{B}(\theta,\phi)$ is the Larmor frequency vector. The vector $\mathbf{B}(\theta,\phi)$ serves to orient the radical system with respect to the external magnetic field axis, and varies with the polar angles θ and ϕ:

$$\mathbf{B}(\theta,\phi) = B_0 \begin{pmatrix} \sin\theta\cos\phi \\ \sin\theta\sin\phi \\ \cos\theta \end{pmatrix}, \tag{4.2}$$

where B_0 is the magnitude of the external field.

In Eq. (4.1) we consider only two nuclei: nitrogen N5 ($i = 1$) and N10 ($i = 2$), with positions in the flavin molecule as labelled in Fig. 4.3. These nuclei have the largest hyperfine interactions with the electron in the flavin radical [182]. There are several other hyperfine interactions with magnetically active nuclei in the flavin, which were ignored in this work since they are either smaller than those for N5 and N10, or more isotropic and therefore less likely to cause an anisotropic magnetic response [182]. Furthermore, it has previously been shown that the two nitrogen hyperfine interactions considered here are mainly responsible for any anisotropic magnetic response of a flavin radical to a magnetic field [182, 205].

These two hyperfine interactions are approximately axially symmetric about the flavin z-axis (which is the normal to the molecular plane, as shown in Fig. 4.3), and in this work the small rhombic parts of these interactions were ignored such

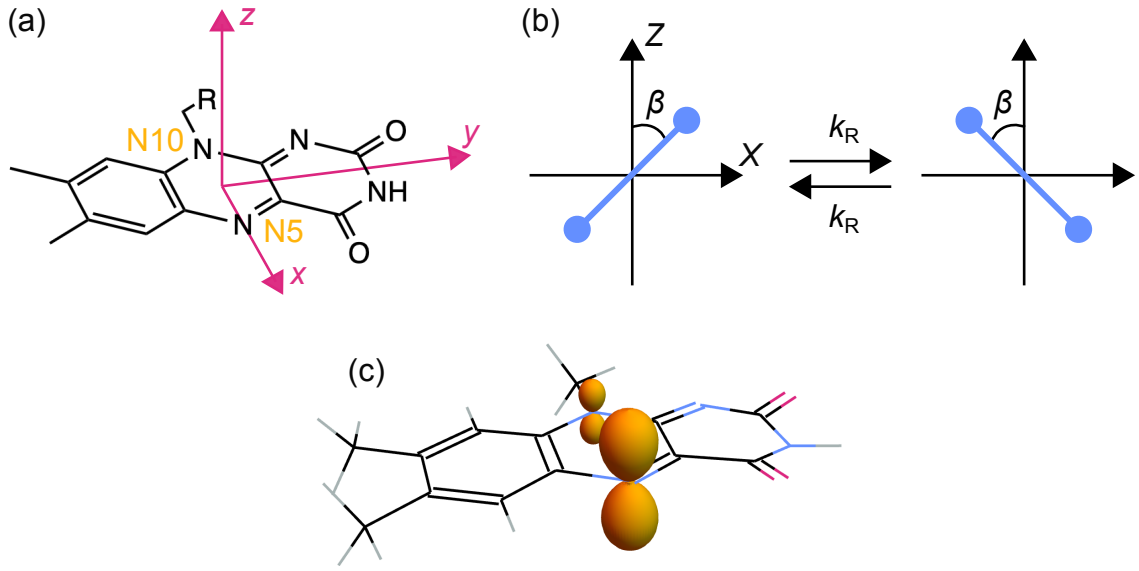

Figure 4.3 Axis systems used in this work. (a) Structure of FAD and the molecular axis system of the $FADH^{\bullet}$ radical, with z normal to the molecular plane. (b) Representation of the two-site rocking motion of the $O_2^{\bullet-}$ radical (blue) in the space-fixed XZ-plane. The superoxide is oriented such that, in its average position, the molecular axis of $O_2^{\bullet-}$ is parallel to the Z-direction. For the three relative orientations of the two radicals considered in this work the $FADH^{\bullet}$ is rotated such that its z-axis is parallel to the X-, Y-, or Z-axis. These three cases are referred to as the X-, Y- and Z- orientations respectively, the case shown here being Z. (c) The two principal hyperfine interactions in $FADH^{\bullet}$, which are both approximately axial and perpendicular to the xy-plane of the flavin [182], are those of the nitrogens N5 and N10 as labelled in (a). In this work the two hyperfine interactions have been slightly simplified to remove small rhombic components (see Eq. (4.3)). In (c) the radial distance from the nucleus to the 3D surface plotted is proportional to the strength of the hyperfine interaction, as described in [182], and the R group from the FAD structure in (a) has been omitted.

that the principal components of the two hyperfine tensors are:

$$A_{jj}^{(i)} \,/\, \mathrm{mT} \quad \begin{array}{c|cc} & \mathrm{N5}\ (i=1) & \mathrm{N10}\ (i=2) \\ A_{xx}^{(i)} & -0.0914 & -0.00255 \\ A_{yy}^{(i)} & -0.0914 & -0.00255 \\ A_{zz}^{(i)} & +1.4767 & +0.74670 \end{array} \tag{4.3}$$

where $A_{jj}^{(i)}$ are the diagonal elements of the hyperfine tensor $\mathbf{A}^{(i)}$ for the interaction between the electron and nuclear spin numbered i. These hyperfine tensors are slightly simplified versions of those in [182], where the small xx and yy components have been set equal to their average. This means that the anisotropy results calculated will be a best-case scenario, since removing any small rhombic components only serves to make the hyperfine interaction more isotropic, and therefore the magnetic response less anisotropic.

The coherent spin Hamiltonian used for the superoxide radical (indicated by a superscript S) can be written as

$$\begin{aligned} \hat{\mathcal{H}}_0^{\mathrm{S}}(\theta,\phi) &= \hat{\mathcal{H}}_{\mathrm{Z}}^{\mathrm{S}}(\theta,\phi) + \hat{\mathcal{H}}_{\mathrm{HF}}^{\mathrm{S}}, \\ \hat{\mathcal{H}}_{\mathrm{Z}}^{\mathrm{S}}(\theta,\phi) &= -\mu_{\mathrm{B}}\, g_{\mathrm{S}}\, \mathbf{B}(\theta,\phi)\cdot\hat{\mathbf{S}}_{\mathrm{S}} - 2\mu_{\mathrm{B}}\, g_{\mathrm{L}}\, \mathbf{B}(\theta,\phi)\cdot\hat{\mathbf{L}} \\ &= \boldsymbol{\omega}(\theta,\phi)\cdot\left(\hat{\mathbf{S}}_{\mathrm{S}} + \hat{\mathbf{L}}\right), \end{aligned} \tag{4.4}$$

where $\hat{\mathbf{L}}$ is a fictitious spin-1/2 operator that represents the orbital angular momentum of $O_2^{\bullet-}$, the factor of two in the second term of $\hat{\mathcal{H}}_{\mathrm{Z}}^{\mathrm{F}}(\theta,\phi)$ accounts for the fact that the orbital angular moment quantum number, $l = 1$, is twice that of a spin-1/2, and $\hat{\mathbf{S}}_{\mathrm{S}}$ is the electron spin operator vector for $O_2^{\bullet-}$. The g-values used were $g_{\mathrm{S}} = 2$ and $g_{\mathrm{L}} = 1$, and all other symbols are as defined in Eq. (4.1). For most of the calculations presented in this chapter, $\hat{\mathcal{H}}_{\mathrm{HF}}^{\mathrm{S}}$ was taken to be equal to a zero operator, since ^{16}O has no nuclear spin (see Table A.1). In Section 4.5 potential isotope effects on RP2 are discussed; if ^{17}O is substituted for ^{16}O then hyperfine

couplings are introduced between the electron and the two spins-5/2 in $^{17}O_2^{\bullet-}$, as in Eq. (4.4) for N5 and N10. The components of the (diagonal) anisotropic hyperfine tensors for both ^{17}O atoms are $A_{xx} = +1.6292\,\text{mT}$, $A_{yy} = +1.4935\,\text{mT}$, and $A_{zz} = -7.6467\,\text{mT}$.[2]

The orientation of the $O_2^{\bullet-}$ and $FADH^{\bullet}$ radicals relative to each other, and to the magnetic field $\mathbf{B}$, are in principle free to vary. The form of Eqs. (4.1) and (4.4) means that a simple repositioning of the flavin radical relative to the superoxide radical involves a trivial cyclic relabelling of the x, y, and z spin operators for the flavin (i.e. $x, y, z \rightarrow z, x, y \rightarrow y, z, x$). This allows us to consider three relative orientations of the two radicals, whereby the flavin z-axis is aligned with either the X, Y, or Z-axis as described in Fig. 4.3, without the need to consider more complicated rotations (similar to those performed in Section 3.4.1 for the Posner molecule). We will refer to these three arrangements simply as the X-, Y-, or Z-orientations respectively.

The relative orientation of the magnetic field vector $\mathbf{B}\,(\theta, \phi)$ and the Z-axis, described by polar angles θ (between $\mathbf{B}$ and the Z-axis) and ϕ (between the component of $\mathbf{B}$ in the XY-plane and the X-axis), is free to vary. It is assumed that the radicals are distant enough from each other that they do not interact, and so electron spin coupling between the two radicals was ignored. The spin relaxation in the flavin was assumed to be negligibly slow, as compared with the superoxide relaxation, to which we now turn.

Two-site exchange model 4.2.1

We model the superoxide located in a binding site and undergoing librational (rocking) motion about an axis perpendicular to the internuclear axis, as described for other radicals in [158] and shown in Fig. 4.3. The $O_2^{\bullet-}$ rotates through a small

[2]The hyperfine tensors were calculated using Gaussian 09 with B3LYP/6-311++G(d,p) for geometry optimization and B3LYP/EPR-III for the hyperfine interactions. Implicit solvation (water) was included via the polarizable continuum model. The calculation was performed by Dr Thomas Fay. Initial calculations of MFEs on RP2 that included $^{17}O_2^{\bullet-}$ were performed by Jiwang Chen.

angle of $\pm\beta^\circ$ with a rate constant k_R. This modulates both the spin–orbit coupling and ligand field experienced by the $O_2^{\bullet-}$, and will be a stochastic source of spin relaxation. The $FADH^\bullet$ is assumed to be stationary.

The Hamiltonians describing the spin–orbit coupling ($\hat{\mathcal{H}}^\mathrm{S}_\mathrm{SO}$) and ligand field splitting ($\hat{\mathcal{H}}^\mathrm{S}_\mathrm{LF}$) in superoxide have the following non-zero elements:

$$\begin{aligned}\left\langle m_\mathrm{s},\pi_\pm\middle|\hat{\mathcal{H}}^\mathrm{S}_\mathrm{SO}\middle|m_\mathrm{s},\pi_\pm\right\rangle &= \pm m_\mathrm{s}\lambda,\\ \left\langle m_\mathrm{s},\pi_x\middle|\hat{\mathcal{H}}^\mathrm{S}_\mathrm{LF}\middle|m_\mathrm{s},\pi_x\right\rangle &= -\left\langle m_\mathrm{s},\pi_y\middle|\hat{\mathcal{H}}^\mathrm{S}_\mathrm{LF}\middle|m_\mathrm{s},\pi_y\right\rangle = \frac{1}{2}\Delta,\end{aligned} \tag{4.5}$$

where $|\pi_\pm\rangle = \left(\left|\pi_{x(\mathrm{g})}\right\rangle \pm \mathrm{i}\left|\pi_{y(\mathrm{g})}\right\rangle\right)/\sqrt{2}$ are linear combinations of the two antibonding π_g orbitals, $m_\mathrm{s} = \pm 1/2$ is the magnetic quantum number for the electron spin, λ is the strength of the spin–orbit coupling, and Δ is the strength of the ligand field splitting (see Fig. 4.2).

The form of Eq. (4.5) means that these interactions can be more conveniently recast in terms of the fictitious spin-1/2 operator $\hat{\mathbf{L}}$ that represents the $O_2^{\bullet-}$ orbital angular momentum (see Eq. (4.4)). With the molecular axis of $O_2^{\bullet-}$ parallel to the Z-axis (see Fig. 4.3) the sum of the two interactions in Eq. (4.5) can therefore be written as

$$\hat{\mathcal{H}}^\mathrm{S}_\mathrm{SO} + \hat{\mathcal{H}}^\mathrm{S}_\mathrm{LF} = 2\lambda\hat{L}_Z\hat{S}_\mathrm{SZ} + \Delta\hat{L}_X, \tag{4.6}$$

where $\hat{S}_\mathrm{SZ}$ is an element of $\hat{\mathbf{S}}_\mathrm{S}$, and a factor of two has once more been included in both terms to account for the orbital angular momentum quantum number.

Spin relaxation is then introduced by allowing the $O_2^{\bullet-}$ radical to jump between two orientations, rotating about the Y-axis through an angle of $\pm\beta^\circ$ as shown in Fig. 4.3. A symmetric two-site exchange model was used for this rocking, with a first-order rate constant k_R, such that the total spin Hamiltonian for

$O_2^{\bullet-}$ (combining Eqs. (4.4) and (4.6)) becomes

$$\begin{aligned}\hat{\mathcal{H}}^{S}_{\pm}(\theta,\phi) =& \hat{\mathcal{H}}^{S}_{0}(\theta,\phi) + \hat{\mathcal{H}}^{S}_{SO}(\pm\beta) + \hat{\mathcal{H}}^{S}_{LF}(\pm\beta)\\ =& \boldsymbol{\omega}(\theta,\phi)\cdot\left(\hat{\mathbf{S}}_S + \hat{\mathbf{L}}\right)\\ &+ 2\lambda\left(\hat{L}_Z\cos\beta \pm \hat{L}_X\sin\beta\right)\left(\hat{S}_{SZ}\cos\beta \pm \hat{S}_{SX}\sin\beta\right)\\ &+ \Delta\left(\hat{L}_X\cos\beta \mp \hat{L}_Z\sin\beta\right).\end{aligned} \tag{4.7}$$

Calculating the singlet yield 4.2.2

Singlet and triplet radical pairs are assumed to react separately (as shown in Fig. 4.1) and at equal rates, as is typical in many comparable studies [145, 158, 182, 185, 193]. This rate is chosen to be $k = 10^6 s^{-1}$, which is probably near optimal for an Earth strength magnetic field $B_0 = 50\,\mu T$ [89]. This reactivity was modelled using a trivial Haberkorn superoperator [114] $\hat{\hat{\mathcal{K}}} = k\hat{\hat{\mathbb{1}}}$.

The two-site exchange model is implemented by introducing a stochastic Liouvillian matrix operator $\mathcal{L}(\theta,\phi)$, as in [158], which will introduce spin relaxation [103] as the radical hops between the two sites:

$$\mathcal{L}(\theta,\phi) = \begin{pmatrix}\mathcal{L}_+(\theta,\phi) + k_R\mathbb{1} & -k_R\mathbb{1}\\ -k_R\mathbb{1} & \mathcal{L}_-(\theta,\phi) + k_R\mathbb{1}\end{pmatrix} \tag{4.8}$$

where k_R is the rocking rate constant and $\mathbb{1}$ are identity matrices. This matrix $\mathcal{L}(\theta,\phi)$ acts on a state vector that represents the two orientations of the $O_2^{\bullet-}$ radical:

$$|\rho\rangle = \begin{pmatrix}|\rho_+\rangle\\ |\rho_-\rangle\end{pmatrix}, \tag{4.9}$$

where $|\rho_\pm\rangle$ are state vectors formed from the corresponding density matrices. At $t = 0$ both orientations are equally populated by the triplet state, reflecting the ${}^3\Sigma_g^-$ ground state of O_2. This means that $\hat{\rho}_+ = \hat{\rho}_- = \frac{1}{Z}\hat{P}^T$, where $\hat{P}^T = \frac{1}{3}\left(\hat{\mathbb{1}} - \hat{P}^S\right)$

is the triplet projection operator, $\hat{P}^{\mathrm{S}}$ is the singlet projection operator, and Z is the number of nuclear spin states.

The superoperators $\hat{\hat{\mathcal{L}}}_{\pm}(\theta,\phi)$ in Eq. (4.8) are

$$\hat{\hat{\mathcal{L}}}_{\pm}(\theta,\phi) = \mathrm{i}\hat{\hat{\mathcal{H}}}_{\pm}(\theta,\phi) + \hat{\hat{\mathcal{K}}}, \tag{4.10}$$

where $\hat{\mathcal{H}}_{\pm}(\theta,\phi) = \hat{\mathcal{H}}_0^{\mathrm{F}}(\theta,\phi) + \hat{\mathcal{H}}_{\pm}^{\mathrm{S}}(\theta,\phi)$ (Eqs. (4.1) and (4.7)).

The fractional quantum yield of singlet reaction product for a given orientation of the radical pair with respect to the magnetic field vector, $\Phi_{\mathrm{S}}(\theta,\phi)$, can be calculated as described in Section 2.2.1, where in this case $k_{\mathrm{S}} = k = 10^6\,\mathrm{s}^{-1}$. We use this to quantify the anisotropic magnetic response across all possible relative orientations of the magnetic field and the radical pair, as described in Section 2.3.1, with $\Delta\Phi_{\mathrm{S}}$ the anisotropy of the singlet yield (see Eq. (2.77)).

Anisotropy results 4.3

We have used the methods outlined above to calculate the anisotropy of the singlet yield for a range of combinations of the $O_2^{\bullet-}$ rocking rate constant (k_{R}), the angle through which $O_2^{\bullet-}$ rocks (β), and the strength of the ligand field splitting relative to the spin–orbit coupling (Δ/λ). A further variable is the relative orientation of the two radicals, and as was described in Section 4.2 we will consider three relative orientations labelled X, Y, and Z.

Figs. 4.4, 4.5, and 4.6 show the anisotropy of the singlet yield for values of k_{R} spanning the range $10^6\,\mathrm{s}^{-1}$ to $10^{12}\,\mathrm{s}^{-1}$ (inclusive), three values of the ratio $\Delta/\lambda = 0.1$, 1, and 10, and two values of the angle $\beta = 2°$ and 5°. Wider ranges for k_{R}, Δ/λ, and β were also considered, and in the case of Δ/λ and β these are presented and discussed with later figures. Faster and slower motion than

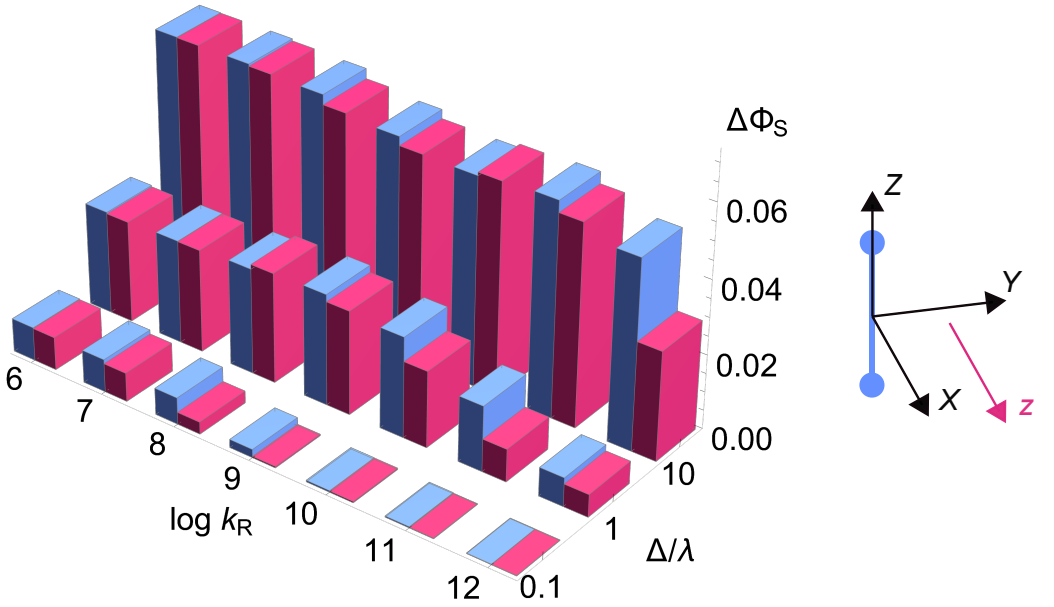

Figure 4.4 X-orientation. The singlet yield anisotropy $\Delta\Phi_S$, plotted as a function of the rocking rate constant, k_R, and the ratio of the ligand field splitting, Δ, to the spin–orbit coupling, λ, for a [$FADH^\bullet$ $O_2{}^{\bullet-}$] radical pair. The $FADH^\bullet$ radical is oriented such that its z-axis is aligned with the X-axis (see Fig. 4.3). The angle through which the superoxide rocks was set at either $\beta = 2°$ (blue) or $\beta = 5°$ (pink).

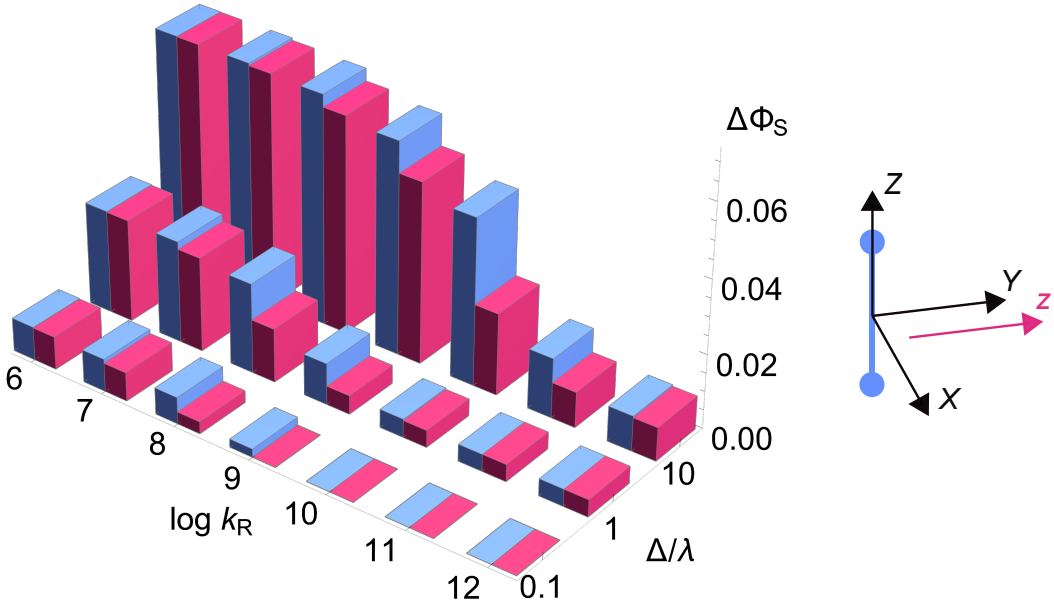

Figure 4.5 Y-orientation. The singlet yield anisotropy $\Delta\Phi_S$, plotted as a function of the rocking rate constant, k_R, and the ratio of the ligand field splitting, Δ, to the spin–orbit coupling, λ, for a [$FADH^\bullet$ $O_2{}^{\bullet-}$] radical pair. The $FADH^\bullet$ radical is oriented such that its z-axis is aligned with the Y-axis (see Fig. 4.3). The angle through which the superoxide rocks was set at either $\beta = 2°$ (blue) or $\beta = 5°$ (pink).

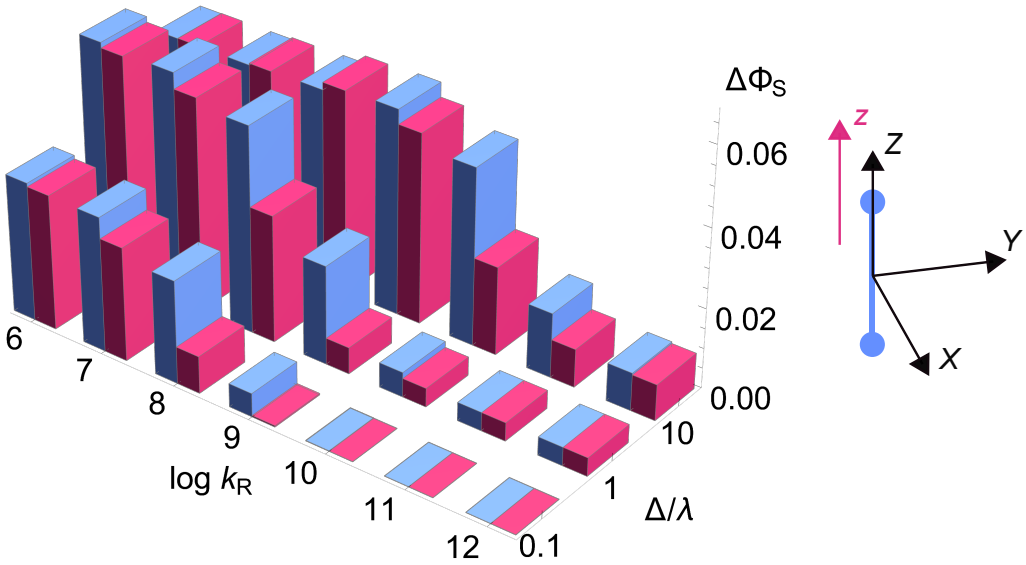

Figure 4.6 Z-orientation. The singlet yield anisotropy $\Delta\Phi_S$, plotted as a function of the rocking rate constant, k_R, and the ratio of the ligand field splitting, Δ, to the spin–orbit coupling, λ, for a [$FADH^\bullet$ $O_2^{\bullet-}$] radical pair. The $FADH^\bullet$ radical is oriented such that its z-axis is aligned with the Z-axis (see Fig. 4.3). The angle through which the superoxide rocks was set at either $\beta = 2°$ (blue) or $\beta = 5°$ (pink).

is covered by the range $10^6\,s^{-1} \leq k_R \leq 10^{12}\,s^{-1}$ is discussed in Section 4.4. All calculations assume that $\Delta < 0$ such that $\Delta/\lambda > 0$.[3]

For all three relative orientations of the two radicals there is a strong dependence on magnetic field direction when the ligand field splitting is larger than the spin–orbit coupling (i.e. when $\Delta/\lambda > 1$, the back row of each figure) and when the rocking motion is slower (the left hand side of each figure). These trends are visible for all three relative orientations in Figs. 4.4–4.6, with additional observations that (a) $\Delta\Phi_S$ is least sensitive to Δ/λ for the Z orientation (Fig. 4.6), and (b) $\Delta\Phi_S$ is least sensitive to k_R for the X orientation (Fig. 4.4). Almost identical responses are found if the hyperfine values appropriate for $FAD^{\bullet-}$ are used instead of those for $FADH^\bullet$ [182], as would be expected (see Figs. C.1, C.2, and C.3 in Appendix C). The main difference is that the magnitude of $\Delta\Phi_S$ is slightly larger for $FAD^{\bullet-}$ than for $FADH^\bullet$.

[3] As far as we have seen, the sign of Δ does not affect any of the results presented here—the choice that $\Delta/\lambda > 0$ is only one of convenience.

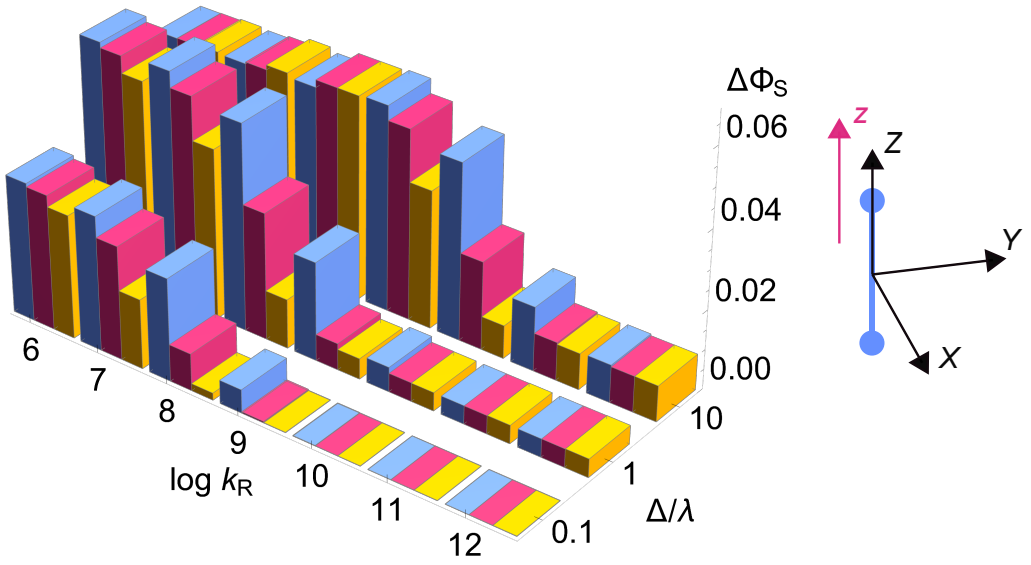

Figure 4.7 The singlet yield anisotropy $\Delta\Phi_S$, plotted as a function of the rocking rate constant, k_R, and the ratio of the ligand field splitting, Δ, to the spin–orbit coupling, λ, for a [$FADH^\bullet\ O_2^{\bullet-}$] radical pair. The $FADH^\bullet$ radical is oriented such that its z-axis is aligned with the Z-axis (see Fig. 4.3). The angle through which the superoxide rocks was set at either $\beta = 2°$ (blue), $\beta = 5°$ (pink), or $\beta = 10°$ (yellow).

In general, a larger rocking angle gives a smaller singlet anisotropy, as can be seen by comparing pink bars ($\beta = 5°$) to blue ($\beta = 2°$). The trend continues if we consider a larger value of $\beta = 10°$, shown in yellow in Fig. 4.7 for the Z-orientation. However, as the angle is increased the two-site exchange model used for the superoxide rocking becomes less suitable. It models instantaneous random hopping from one orientation to the other, and although this is an acceptable model for smaller angles, for larger rocking angles the molecule would sample intermediate sites for longer time periods and an extension of the model to include extra sites would be preferable [96]. This calculation would be significantly more intensive, since the size of the Liouvillian operator would increase with the addition of each site, and so in this thesis only small angles using the two-site model were considered.

The range of Δ/λ considered in Figs. 4.4–4.6 appears to cover the broadest range of anisotropy values accessible for the [$FADH^\bullet\ O_2^{\bullet-}$] system. A sample set

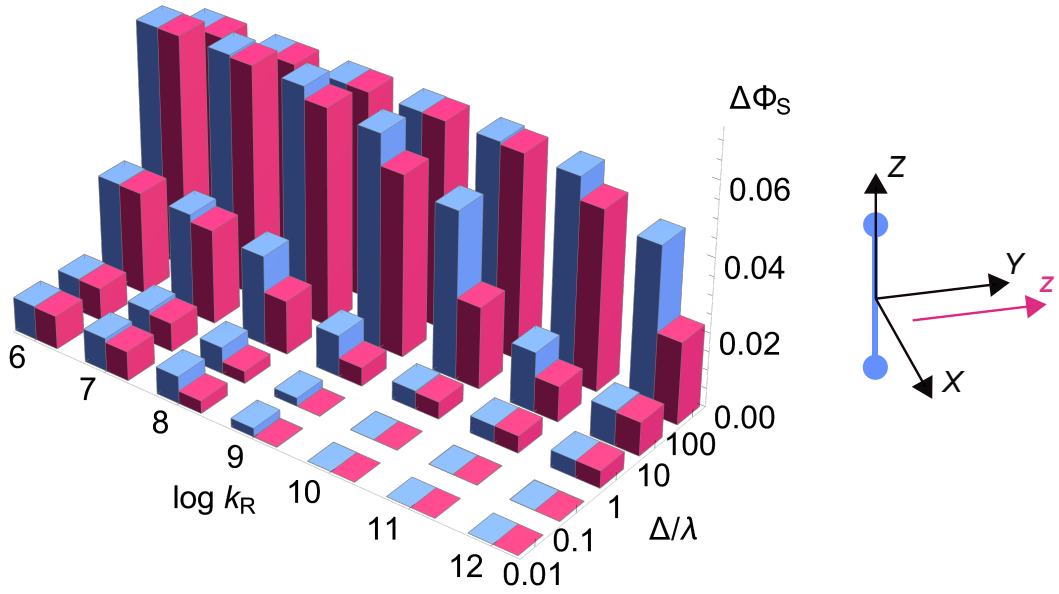

Figure 4.8 The singlet yield anisotropy $\Delta\Phi_S$, plotted as a function of the rocking rate constant, k_R, and a broad range of the ratio of the ligand field splitting, Δ, to the spin–orbit coupling, λ, for a [$FADH^\bullet\ O_2^{\bullet-}$] radical pair. The $FADH^\bullet$ radical is oriented such that its z-axis is aligned with the Y-axis (see Fig. 4.3). The angle through which the superoxide rocks was set at either $\beta = 2°$ (blue) or $\beta = 5°$ (pink).

of anisotropy results for a wider range of Δ/λ values is shown in Fig. 4.8. When Δ/λ is decreased to 0.01 (the front row of Fig. 4.8) the anisotropy does not become smaller, instead appearing to have plateaued by around $\Delta/\lambda \simeq 0.1$. When Δ/λ is increased to 100 (the back row of Fig. 4.8) the maximum anisotropy found does not increase past the maximum found for the range $0.1 \leq \Delta/\lambda \leq 10$. In some cases the anisotropy for a particular value of k_R does increase when Δ/λ is increased from 10 to 100, in particular for the faster values of the rocking rate constant, for instance $k_R \geq 10^9\ s^{-1}$ in Fig. 4.8.

Feasibility of derived conditions 4.4

To put the results of these simulations in context, we consider two extreme cases. For an [$FADH^{\bullet-}\ Z^\bullet$] radical pair, as described in Section 4.1.2, in which the $Z^\bullet$ radical has no orbital angular momentum and (critically) no hyperfine couplings, we separately calculated the singlet yield anisotropy (using our sim-

plified model of the hyperfine couplings in the flavin, and beginning in the triplet state) as $\Delta\Phi_S = 0.0564$. As would be expected, the same value is found for the $[FADH^\bullet\ O_2^{\bullet-}]$ radical pair when $O_2^{\bullet-}$ is stationary ($k_R = \beta = 0$) and the orbital angular momentum is quenched ($\Delta/\lambda \gg 1$). The closest Figs. 4.4–4.6 come to this regime is when $k_R = 10^6\,s^{-1}$ and $\Delta/\lambda = 10$, which indeed give values of $\Delta\Phi_S$ close to 0.0564. In Fig. 4.8, when $\Delta/\lambda = 100$ and $k_R = 10^6\,s^{-1}$, the value of $\Delta\Phi_S = 0.0565$.

At the other extreme is a $O_2^{\bullet-}$ radical that is not restricted by a ligand field, tumbling with a rotational correlation time τ_c appropriate for $O_2^{\bullet-}$ in water at physiological temperature. This correlation time can be estimated from the Stokes–Einstein equation, Eq. (2.76). Using $a = 150\,pm$ for the hydrodynamic radius, $T = 310\,K$ (physiological temperature), and $\eta = 0.69\,mPa\,s$ for the viscosity of water at 310 K [206], we obtain $\tau_c \simeq 2.3\,ps$. This is close to the value of 2.5 ps that has previously been used by Karogodina *et al.* [194]. The nearest that the data in Figs. 4.4–4.6 come to this regime is when $k_R = 10^{12}\,s^{-1}$ and $\Delta/\lambda = 0.1$, or in Fig. 4.8 when $\Delta/\lambda = 0.01$, and in all these cases $\Delta\Phi_S \simeq 0$, which would render it unsuitable as a geomagnetic sensor as predicted.

A final comparison worth making is to the $\left[FAD^{\bullet-}\ TrpH^{\bullet+}\right]$ radical pair that is often cited as the critical magnetosensor in the M1 mechanism. A typical value of $\Delta\Phi_S$ has previously been calculated for this radical pair (beginning in the singlet state) as 0.00138, which is around 50 times smaller than the largest values of $\Delta\Phi_S$ calculated here for $[FADH^\bullet\ O_2^{\bullet-}]$.

Conclusions and further work 4.5

In order to function effectively as a geomagnetic compass sensor, the anisotropy of the singlet yield must be sufficiently large to provide directional information. When the radical pair involved in magnetic sensing is $[FADH^\bullet\ O_2^{\bullet-}]$, we have shown that strongly anisotropic product yields can in principle occur, but only if the $O_2^{\bullet-}$ is constrained by a relatively strong ligand field ($\Delta/\lambda \geq 1$, i.e. $|\Delta| \gtrsim$

200 cm^{-1} $\simeq$ k_BT) and any rotational motion is slow ($k_R \lesssim 10^9\,s^{-1}$, i.e. rotating at least 1000 times less rapidly than it does in aqueous solution). Rotations end-over-end would not be acceptable, since the electron spin is quantized along the molecular axis and random rotations of this kind would rapidly relax the spin coherence on the timescale of the tumbling.

Furthermore, reactions of any geomagnetic sensor, spin-selective or not, must occur on a ~1 μs timescale (for example steps c, d, i, and j in Fig. 4.1). If reactions occur much faster than this then there is no time for a ~50 μT field to affect the spin motion, and if reactions are much slower then spin relaxation will destroy any spin coherence [61]. Also, electron coupling interactions (either exchange or dipolar) should not be much stronger than the Zeeman (~50 μT) or hyperfine (~1 mT) interactions in the two radicals; if this is not true then there will be no singlet–triplet interconversion [108]. This latter consideration would mean the radicals should be separated by > ~3.5 nm, although it is possible that partial cancelling of exchange and dipolar interactions (see Section 2.2.3) may allow the radicals to be as close as 2.0 ± 0.2 nm [108]. In practice, all of these considerations mean that any radical pair magnetoreceptor, including one based on [$FADH^\bullet\ O_2^{\bullet-}$], must have the radicals no closer together than ~1.5 nm, to avoid electron coupling destroying the MFE, and probably no further than ~2.0 nm, such that recombination can compete with the formation of stabilised radicals [61, 108, 176, 178, 207].

The case for M2 having a role in magnetic sensing *in vivo* would be stronger if it could be shown, potentially *in vitro*, that the rate of oxidation of $FADH^-$ in cryptochromes is altered by an applied magnetic field in an oxygen-dependent manner. It would also be improved if a binding site for $O_2^{\bullet-}$ could be found in cryptochrome that is more than 1.5 nm away from the flavin, and with an electronic exchange interaction weaker than the hyperfine interactions (i.e. < 100 neV). There is as yet no experimental evidence to support such a binding site, and as was discussed in Section 4.1.2, any calculated binding sites are unsuitable for

	Δ/λ		
	0.1	1.0	10.0
X	1.00	3.84	10.11
Y	1.00	3.78	8.49
Z	2.31	3.73	3.54

Table 4.1 Ratio of the reaction yield anisotropies, $\Delta\Phi_S$, for $\left[\text{FADH}^\bullet\ {}^{16}\text{O}_2{}^{\bullet-}\right]$ and $\left[\text{FADH}^\bullet\ {}^{17}\text{O}_2{}^{\bullet-}\right]$.

geomagnetic sensing because the oxygen radical would be too close to the flavin, making the exchange interaction too strong [88].

Finally, M2 would be further supported by the demonstration of a strong magnetic isotope effect on the rate of oxidation. If $^{16}O_2$ could be substituted for $^{17}O_2$ then hyperfine interactions would be introduced into the $O_2{}^{\bullet-}$ radical that should reduce any magnetic field effect and also accelerate the formation of ground state (oxidized) flavin. We have calculated, by introducing the hyperfine couplings described in Section 4.2 for $^{17}O_2{}^{\bullet-}$ into Eq. (4.4) and without including rocking motion (i.e. $k_R = \beta = 0$) that the reaction yield anisotropy for $\left[\text{FADH}^\bullet {}^{17}\text{O}_2{}^{\bullet-}\right]$ is always comparable to or smaller than that for $\left[\text{FADH}^\bullet {}^{16}\text{O}_2{}^{\bullet-}\right]$. Values of the ratio of $\Delta\Phi_S$ for the ^{16}O radical pair to that for the ^{17}O radical pair are given in Table 4.1, where it can be seen that inclusion of the ^{17}O hyperfine couplings causes a 4- to 10-fold reduction in the anisotropy of the MFE for the larger values of $\Delta/\lambda = 1.0$ and 10.0, which give the largest MFEs. When $\Delta/\lambda = 0.1$ the change is less pronounced, but for this ratio the MFE itself is much smaller.

As it is currently, and given the stringent conditions calculated and described above, the involvement of the superoxide radical in avian magnetoreception must remain highly speculative until and unless further experimental evidence arises.

5 Magnetic field effects on a reaction of CO_2

In 2020 it was reported that the yield of formic acid (HCO_2H) formed via electrocatalytic reduction of CO_2 can be increased by up to ~100% upon application of a 0.9 T magnetic field [76]. This effect appeared similar to apparent magnetic field effects (MFEs) reported in other systems by the same group, Pan *et al.* [208, 209]. It appears that the CO_2 results in reference [76] have not been reproduced, and in a more recent paper on CO_2 electroreduction using a different catalyst the same group do not mention any magnetic field effects [210].

Magnetic field effects on electrochemical reactions are often unrelated to spin–selectivity, instead occurring due to thermal effects, magnetoconvection [70], or other effects on the electrochemical setup, which would all be difficult to control. In reference [76] the authors discuss their efforts to control for convection effects, which involved applying the magnetic field parallel to the charge transport direction, and argue that this means the Lorentz force is negligible and magnetoconvection effects can be ignored. They make no mention of any potential effects of the magnetic field on their experimental setup that are unrelated to convection, and go on to attribute the observed increased yield to a change in the efficiency of interconversion of the electronic singlet and triplet states of a radical pair [$H^{\bullet}\ CO_2^{\bullet -}$] [76].

It was suggested that the two radicals involved are formed by electroreduction at a tin nanoparticle electrode:

$$\begin{aligned} CO_2 + e^- &\rightarrow CO_2^{\bullet -}, \\ HCO_3^- + e^- &\rightarrow H^\bullet + CO_3^{2-}. \end{aligned} \tag{5.1}$$

The proposed reaction scheme for radical pair reactivity after the electroreduction process is shown in Fig. 5.1. In this scheme the radical pairs are formed in a statistical mixture: 75% triplet, 25% singlet. The rationale for spin-selective reactivity of such freely diffusing pairs (or "F-pairs", as opposed to geminate "G-pairs" in which the two radicals are formed concurrently [211]) is well established, and similar to that discussed in Chapter 4 for the radical pair model of magnetoreception.

The reaction of the triplet pair to combine and produce the diamagnetic formate ion HCO_2^- is spin forbidden, whereas the singlet pair can undergo this reaction: ${}^S[H^\bullet CO_2^{\bullet -}] \rightarrow HCO_2^-$. At the same time, both radical pairs can diffuse apart without reacting, and it is this asymmetric reactivity that produces spin coherence for such F-pairs, despite the lack of the pure singlet or triplet coherence that can be formed in photochemical reactions such as those discussed in Chapter 4. The rate of interconversion between these two forms of the radical pair may be dependent on an external magnetic field, which is how the proposed MFE would arise.

Fig. 5.2 shows the change in the measured electrocatalytic current for the reduction of CO_2 (henceforth referred to as the magnetocurrent), which was measured by varying the strength of an applied magnetic field between 0 T and ~0.9 T in a sawtooth pattern with a period of 55 s [76]. The normalized trace shown in Fig. 5.2 is for the average of the three different field-dependence traces reported in [76]. The three reported traces were essentially identical in shape and differed only in magnitude based on the strength of a CO_2-saturated aqueous solution

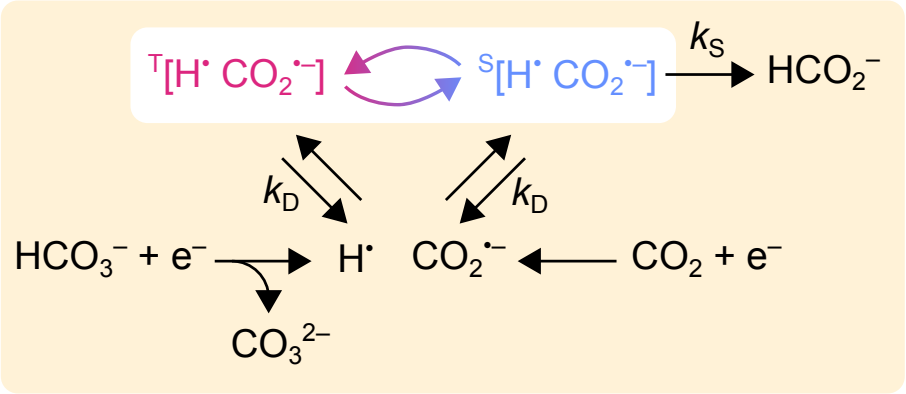

Figure 5.1 Proposed reaction scheme for electrocatalytic reduction of carbon dioxide to produce formic acid. $H^{\bullet}$ and $CO_2^{\bullet-}$ radicals are formed at the electrode by reduction of HCO_3^- and CO_2 respectively. These two radicals can encounter one another to form a radical pair $[H^{\bullet}\ CO_2^{\bullet-}]$, which has a 75% chance of being in a triplet state and 25% chance of being singlet. The interconversion of these two forms, indicated by the red/blue arrows, can in theory be affected by an applied magnetic field. Both forms of the radical pair can diffuse apart with a rate constant k_D, whereas only the singlet can react further to form formate HCO_2^- with rate constant k_S. The scheme is adapted from [3] and based on the one described in [76].

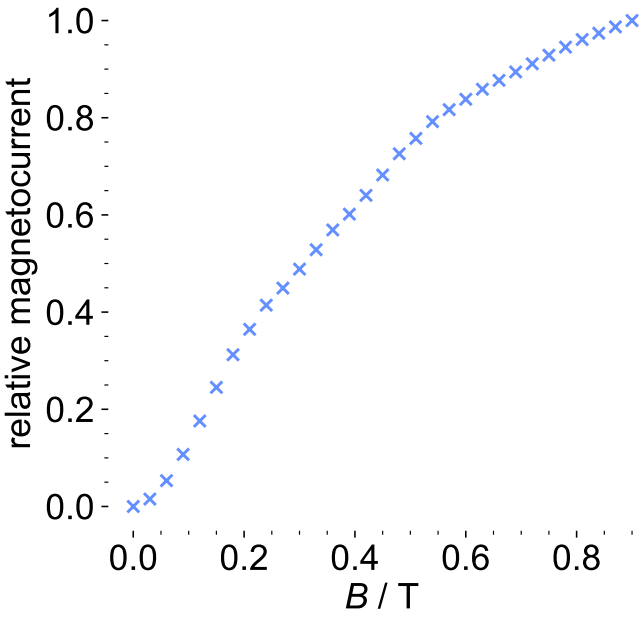

Figure 5.2 The dependence of magnetocurrent on an applied magnetic field, constructed from the time-dependence of these two quantities as shown in Fig. 2(b) of Pan *et al.* [76]. In [76] there were three field-dependence traces reported for differing strengths of $KHCO_3$ solution; the trace shown here is the average of the three, rescaled to 1.0 at 0.9 T, since all three had essentially identical shapes.

$[KHCO_3]$ / mol dm^{-3}	0.1	0.2	0.3
Peak magnetocurrent (%)	42	58	90
Increase in yield of $KHCO_3$ (%)	40	57	100

Table 5.1 Peak magnetocurrents, and corresponding increases in the yield of formic acid, reported in [76] as an MFE on the electrocatalytic reduction of CO_2.

of $KHCO_3$.[1] Peak magnetocurrents, and corresponding increases in the yield of formic acid, for the three concentrations mentioned are given in Table 5.1. The sigmoidal shape of the curve in Fig. 5.2 is consistent with a radical pair reaction where the MFE tends to saturate at higher field [34, 63, 212].

This rise in the magnetocurrent and product yield as the field is applied would be consistent with increased efficiency of triplet → singlet conversion, which would increase the amount of singlet pairs present and therefore the number of radical pairs that can react onwards to form HCO_2^-. There are many mechanisms that may cause this interconversion, with Pan *et al.* arguing that it can be attributed to a combination of two well-established mechanisms for singlet–triplet interconversion: the Δg mechanism and the hyperfine mechanism (i.e. coherent evolution under a hyperfine interaction) [76].

The Δg mechanism relies on the difference in the electronic Zeeman interaction between the two radicals, whereas the hyperfine mechanism is due to the magnetic coupling of the electron and nucleus in the hydrogen radical [35, 89]. The Δg mechanism, it was argued, would dominate, because it becomes more efficient at high field, whereas the hyperfine mechanism becomes less efficient [76].

However, besides these two interactions, there are several others that could critically affect how the $[H^\bullet\, CO_2^{\bullet -}]$ radical pair interacts with an applied magnetic field. In particular, rotational modulation of the anisotropic Zeeman interaction of CO_2^- [107, 194, 213], spin–rotation relaxation in CO_2^- [194, 214, 215], and translational modulation of the exchange interaction of the two radicals [63, 216],

[1] The concentration was either 0.1 mol dm^{-3}, 0.2 mol dm^{-3}, or 0.3 mol dm^{-3}.

may all lead to spin relaxation that will affect the magnetic field response of the two radicals. The radical pair mechanism is the ideal theoretical framework to quantitatively examine the quantum spin dynamics [15, 34, 89, 144, 217, 218] associated with all of these magnetic interactions, and elucidate the true cause of the MFEs reported by Pan *et al.* in [76]. We will consider whether the Δg mechanism favoured by Pan *et al.* can fully explain their measured results, and what impact spin relaxation would have on the system.

Modelling the radical pair 5.1

The proportion of $[H^{\bullet}\,CO_2{}^{\bullet-}]$ radical pairs that combine to produce HCO_2H was calculated using the method described in Section 2.2.1 by solving a stochastic Liouville master equation (Eq. (2.45)) for the radical pair density matrix. In this case the density matrix describes a spin system containing the electron and proton in $H^{\bullet}$ and the unpaired electron in $CO_2{}^{\bullet-}$, and the Liouvillian superoperator $\hat{\hat{\mathcal{L}}} = i\hat{\hat{\mathcal{H}}}_0 + \hat{\hat{\mathcal{K}}} + \hat{\hat{\Gamma}}_k$ is composed of three terms responsible for coherent interactions, reactivity of the radicals, and relaxation[2] respectively, which are more fully explained in Sections 5.1.1–5.1.3.

The fractional yield of formate, once all radical pairs have disappeared, is given by the singlet yield, since only singlet radical pairs can go on to produce formate. The singlet yield was calculated for an initial state $\hat{\rho}(0) = \hat{\mathbb{1}}/4Z$ reflecting a statistical 1:3 mixture of singlet and triplet states (i.e. a maximally mixed state), where Z is the number of nuclear spin states.

[2]The superscript label k will denote which type of relaxation is being considered (see Section 5.1.3).

Coherent interactions 5.1.1

The coherent spin Hamiltonian used for the [$H^\bullet$ $CO_2^{\bullet-}$] radical pair can be written, in angular frequency units of $\hbar$, as

$$\begin{aligned}\hat{\mathcal{H}}_0 &= \hat{\mathcal{H}}_Z + \hat{\mathcal{H}}_{HF},\\ \hat{\mathcal{H}}_Z &= \mu_B B \left(g_H \hat{S}_{Hz} + g_{CO_2} \hat{S}_{Cz}\right),\\ \hat{\mathcal{H}}_{HF} &= \mu_B a_H g_e \hat{\mathbf{S}}_H \cdot \hat{\mathbf{I}}_H,\end{aligned} \tag{5.2}$$

where $\hat{\mathcal{H}}_Z$ describes the isotropic Zeeman interactions of the $H^\bullet$ and $CO_2^{\bullet-}$ electrons with the applied magnetic field, and $\hat{\mathcal{H}}_{HF}$ describes the isotropic hyperfine interaction in $H^\bullet$ between the electron and the nucleus. In Eq. (5.2) $\hat{\mathbf{S}}_i$ is a column vector containing the electron spin operators $\hat{S}_{ix}$, $\hat{S}_{iy}$, and $\hat{S}_{iz}$ for $H^\bullet$ (i = H) and $CO_2^{\bullet-}$ (i = C), $\hat{\mathbf{I}}_H$ is a similar nuclear spin operator for $H^\bullet$, g_H = 2.0114 [219] and g_{CO_2} = 2.0007 [220] are the isotropic g-values for the two radicals, g_e is the g-factor for the electron, a_H = 50.74 mT is the hyperfine coupling constant for the proton [221], and B is the applied magnetic field strength. The coherent Hamiltonian superoperator $\hat{\hat{\mathcal{H}}}_0$ can be formed from Eq. (5.2) as described in Eq. (2.44)

Using the spin Hamiltonian as stated above involves assuming that the $CO_2^{\bullet-}$ tumbles sufficiently rapidly that any coherent evolution due to the anisotropic components of its g-tensor will average out. This assumption may break down if the $CO_2^{\bullet-}$ radical remains firmly bound to the catalyst for relatively long periods of time. We also assume that (1) the two diffusing radicals are sufficiently separated that there is no net effect of electron spin coupling on the coherent spin dynamics, i.e. any exchange and dipolar interactions can be ignored as in Chapter 4, (2) that the nuclear Zeeman interaction in $H^\bullet$ will be much smaller than any electronic Zeeman interactions and can be ignored, since the proton has a much smaller magnetic moment than the electron, and (3) that the natural abundance of ^{13}C in the carbon dioxide radical (1.1%) can be ignored, as can the far smaller (~0.038%)

proportion of magnetically active ^{17}O, such that the only nucleus we need consider is that of the hydrogen radical (see Table A.1).

Some calculations also involved isotopic substitution (see Section 5.3), and appropriate changes were made to the spin Hamiltonian and operators to reflect this. For calculations involving $^2H^\bullet$, $\hat{\mathcal{H}}_{HF}$ in Eq. (5.2) was replaced by $\mu_B\, a_D\, g_e \hat{\mathbf{S}}_D \cdot \hat{\mathbf{I}}_D$ where the hyperfine coupling constant for deuterium ($^2H = D$) is smaller than that for ^1H by the ratio of their gyromagnetic ratios γ_i: $a_D = \frac{\gamma_D}{\gamma_H} a_H = 7.79\,\text{mT}$. For calculations involving $^{13}CO_2^{\bullet-}$, a term $\mu_B a_C g_e \hat{\mathbf{S}}_C \cdot \hat{\mathbf{I}}_C$ was added to $\hat{\mathcal{H}}_{HF}$ in Eq. (5.2). The isotropic ^{13}C hyperfine coupling constant for $^{13}CO_2^{\bullet-}$ is $a_C = 19.93\,\text{mT}$ [222]. Since ^2H has $I = 1$ and ^{13}C has $I = 1/2$, the number of nuclear spin states in all four isotopologous radical pairs are: $Z = 2$ for $\left[^1H^\bullet\ ^{12}CO_2^{\bullet-}\right]$; $Z = 3$ for $\left[^2H^\bullet\ ^{12}CO_2^{\bullet-}\right]$; $Z = 4$ for $\left[^1H^\bullet\ ^{13}CO_2^{\bullet-}\right]$; $Z = 6$ for $\left[^2H^\bullet\ ^{13}CO_2^{\bullet-}\right]$.

Reaction operator 5.1.2

The reactivity shown in Fig. 5.1 was modelled using a Haberkorn superoperator $\hat{\hat{\mathcal{K}}}$ (see Section 2.2.4):

$$\hat{\hat{\mathcal{K}}} = \frac{1}{2} k_S \left(\hat{P}^S \otimes \hat{\mathbb{1}} + \hat{\mathbb{1}} \otimes \left(\hat{P}^S \right)^T \right) + k_D \hat{\mathbb{1}} \otimes \hat{\mathbb{1}} \tag{5.3}$$

in which $\hat{P}^S$ is the usual singlet projection operator, the superscript ^{T} is the transpose, k_S is the first-order rate constant describing spin-selective formation of formic acid from the singlet radical pair, and k_D is the first-order rate constant describing the rate at which both singlet and triplet radicals diffuse apart (see Fig 5.1). Eq. (5.3) is equivalent to

$$\hat{\hat{\mathcal{K}}} \left[\hat{\rho}(t) \right] = \frac{1}{2} k_S \left[\hat{P}^S, \hat{\rho}(t) \right]_+ + k_D \hat{\rho}(t). \tag{5.4}$$

Spin relaxation 5.1.3

Electron spin relaxation can have profound effects on the sensitivity of radical pair reactions, such as the one proposed in [76], to magnetic fields [223–226]. This effect was not discussed by Pan *et al.* when explaining their observed MFE, and some form of spin relaxation should certainly be considered as a potential explanation for the effect. In this work we consider sources of spin relaxation mainly focused on the $CO_2^{\bullet -}$ radical, assuming that spin relaxation for the $H^\bullet$ radical would be slower than for $CO_2^{\bullet -}$. Many of the common mechanisms of spin relaxation rely on rotational diffusion and conformational changes of the radical modulating anisotropic couplings and g-tensors, and none of this is possible for the completely isotropic $H^\bullet$ radical. In each case either a phenomenological relaxation rate constant k_i or an appropriate correlation time τ_c will be the variable parameter used to fit the experimental data, with the forms of the relaxation superoperators given in Section 5.2.2 as the types of relaxation modelled are introduced.

Fitting the experimental results 5.2

In order to elucidate the mechanism that would explain the MFE observed by Pan *et al.* in [76], we consider each of the coherent and relaxation interactions outlined in Sections 5.1.1–5.1.3 and calculate the field-dependence of the singlet yield. In the experimental results Pan *et al.* reported an increase in formate yield as the applied field was increased from 0 to 900 mT, which we call a positive MFE. This was attributed to the Δg mechanism, and so a first check is whether this particular mechanism, or any of the others mentioned above, could produce the observed qualitative result (positive MFE) rather than a negative MFE, or no MFE. The second aim is to use this mechanism, or combination of mechanisms, to fit the experimental data. The physical feasibility of the fitted parameters can then be used to assess whether the mechanisms indicated are reasonable.

Many of the simulations in our study predicted a pronounced "low field effect" [227–229], which is a sharp rise in the singlet yield for weak magnetic fields (on the order of a few mT). The data presented by Pan *et al.* did not include this feature (see reference [76] or Fig. 5.2), and indeed it may have been overlooked or not present. This is because the sharp rise in singlet yield occurs at the very start of the range of applied field strengths, and so the small rise may be mistaken for the "zero-field" condition. In this work we exclude any fields weaker than 30 mT from the attempts to match simulations to the experimental data, and define the MFE as either positive or negative according to whether the singlet yield is larger or smaller at 900 mT than at 30 mT, i.e. whether $\Delta\Phi_S(900\,\mathrm{mT})$ is positive or negative where

$$\Delta\Phi_S(B) = \Phi_S(B) - \Phi_S(B = 30\,\mathrm{mT}). \tag{5.5}$$

As we will see later in Section 5.2.3, some of the more physically feasible fitted parameters do, upon inspection of the region $B < 30\,\mathrm{mT}$, predict a sharp low field effect. This could be sought more carefully experimentally, as a test of the modelling described here.

In the following calculations the rate constants k_S and k_D (see Eq. (5.3) and Fig. 5.1) are varied over a wide range from $10^3\,\mathrm{s}^{-1}$ to $10^{11}\,\mathrm{s}^{-1}$, chosen for the following reasons.

For there to be a significant MFE on the reaction of $H^\bullet$ and $CO_2^{\bullet-}$, the exchange interaction between the radicals must not greatly exceed the hyperfine coupling [108], meaning that the diffusing radicals must on average be more than 1.0–1.5 nm apart. We can estimate the time required, t_D, for one or both of the radicals to diffuse through a distance $\Delta r \simeq 1\,\mathrm{nm}$ from this average separation to the contact distance at which they can combine and produce HCO_2^-. The translational diffusion coefficients of small molecules in water at room temperature are $D < \sim 10^{-9}\,\mathrm{m^2\,s^{-1}}$ such that $t_D = \Delta r^2/D > \sim 10^{-9}\,\mathrm{s}$. An upper limit on k_S is therefore the reciprocal of this time, such that $k_S < \sim 10^9\,\mathrm{s}^{-1}$.

The MFE would also be very small if the diffusion rate constant, k_D, were much greater than the frequency of singlet–triplet interconversion, i.e. if the radicals diffuse apart before any significant singlet–triplet interconversion can occur. This frequency is approximately given by $\gamma_e a_H \simeq 9 \times 10^9\,\mathrm{s}^{-1}$ [221]. Therefore an upper limit on k_D can be set at around $\sim 10^{10}\,\mathrm{s}^{-1}$. Bearing both of these estimates in mind, a generous upper limit on both rate constants was set at $10^{11}\,\mathrm{s}^{-1}$.

A generous lower limit for both rate constants was set at $10^3\,\mathrm{s}^{-1}$; processes that happen on such a timescale, i.e. on the order of milliseconds, will only affect radical pairs with lifetimes that are somewhat longer, which would be remarkably long-lived (typically, radical pair lifetimes are on the order of ns to μs [153]). So, these upper and lower limits give confidence that we will uncover any behaviour of the spin system that is of potential physical relevance.

Hyperfine and Δg mechanisms 5.2.1

Initially we consider only coherent interactions and chemical reactivity, i.e. ignoring spin relaxation, such that $\hat{\hat{\mathcal{L}}} = \mathrm{i}\hat{\hat{\mathcal{H}}}_0 + \hat{\hat{\mathcal{K}}}$.

When both the Δg and hyperfine mechanisms operate simultaneously (i.e. $a_H = 50.74\,\mathrm{mT}$ and $\Delta g = 0.0107$), the MFE is negative over the whole range of rate constant values. Example MFEs can be seen in Fig. 5.3 for $k_D = 10^4\,\mathrm{s}^{-1}$ and $10^3\,\mathrm{s}^{-1} \leq k_S \leq 10^9\,\mathrm{s}^{-1}$, with further examples in Fig. D.1 (Appendix D). The source of this negative MFE can be investigated by modifying the simulation, artificially switching the hyperfine and Δg mechanisms on and off.

When the hyperfine interaction is omitted ($a_H = 0$) such that the Δg mechanism arising from the difference in g-values for the two electrons ($\Delta g = 0.0107$ [219, 220]) is the only source of singlet–triplet interconversion, the MFE is consistently positive for all combinations of rate constants k_S and k_D in the stated ranges. Plots of the singlet yield against applied field in this case can be seen in Fig. D.2, where the positive MFE is clearly visible in many cases.

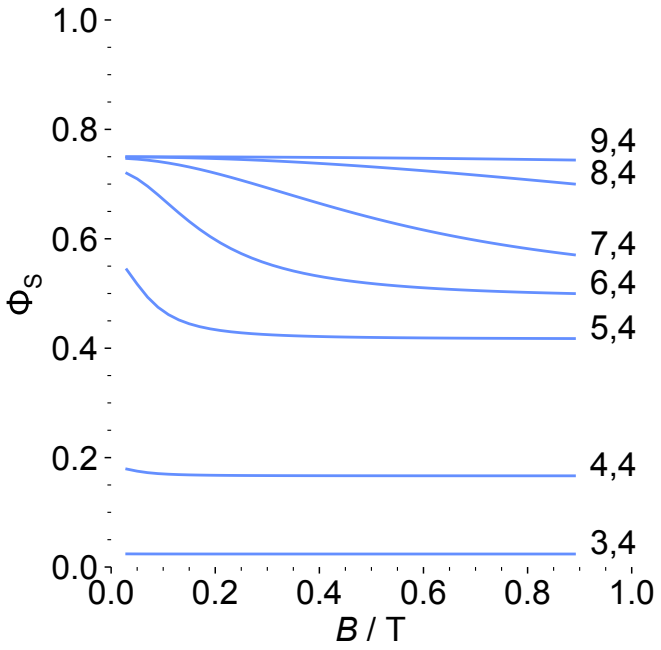

Figure 5.3 Calculated MFEs on the $H^{\bullet} + CO_2^{\bullet-}$ reaction showing Φ_S as a function of B for $0.03\,\mathrm{T} < B < 0.9\,\mathrm{T}$. No spin relaxation is included, $\Delta g = 0.0107$, and $a_H = 50.74\,\mathrm{mT}$. Each line is labelled with the values of the two rate constants: $\log_{10} k_S$, $\log_{10} k_D$.

On the other hand, when the hyperfine interaction is reinstated ($a_H = 50.74\,\mathrm{mT}$) and the Δg mechanism is omitted by setting the two g-values equal to their mean (such that $\Delta g = 0$), the MFE is consistently negative. Plots of the singlet yield against applied field can be seen in Fig. D.3, which closely resembles Fig. D.1. In some of the cases shown in Figs. D.2 and D.3 the calculated MFE is of a very small magnitude that is not visible on the scale of the plot and may not be experimentally observable.

In fact, it is true across all modelling techniques used in this chapter that combinations of rate constants where $k_S \leq k_D$ gave small or negligible magnetic field effects, when compared to $k_S > k_D$. This can be understood in reference to the reaction scheme shown in Fig. 5.1; if the rate at which radicals diffuse apart is much faster than the rate at which singlet radical pairs can react then no MFE will be able to build up, since no appreciable singlet–triplet mixing can occur before the radicals are separated.

So, despite the suggestion of Pan *et al.* that the Δg mechanism explains their observed positive MFE [76], it is entirely outweighed by the hyperfine coupling in the hydrogen atom. The two acting together cannot account for the observed change in magnetocurrent observed by Pan *et al.*

The hyperfine mechanism causes singlet–triplet mixing at a frequency of $g_e \mu_B a_H / 2\pi \simeq 1420\,\text{MHz}$, whereas the mixing due to the Δg mechanism occurs at a frequency of $\Delta g \mu_B B / h \simeq 135\,\text{MHz}$ if $B = 0.9\,\text{T}$, and less otherwise. So, the ~10 times faster singlet–triplet mixing caused by the hyperfine mechanism means that it dominates, and the MFE is negative. Using this model there are no other time-independent magnetic interactions in either of the radicals that could outweigh the hyperfine mechanism, and so the suggestion by Pan *et al.* that the Δg mechanism explains their observed MFE cannot be supported.

Relaxation processes 5.2.2

It seems likely that spin relaxation may have an important role to play, supported by the observed magnetocurrent still increasing at 900 mT (see Fig. 5.2 and reference [76]). If spin relaxation were not important, any MFE due to the hyperfine interaction should start to saturate as soon as the applied field exceeds the hyperfine interaction (~50 mT) [63, 230]. As was mentioned at the start of this section, many simulations in this study predicted a pronounced, and sometimes sharp, low-field effect when $B < 30\,\text{mT}$, which may indeed be due to saturation of an MFE caused by the hydrogen atom's ~50 mT hyperfine interaction.

Random fields

A first test of spin relaxation is to include a simple model of random time-dependent local fields. This generic mechanism relaxes the three Cartesian components of the electron spin with the same phenomenological rate constant k_{RF}, with the relaxation superoperator [193] given by

$$\hat{\hat{\Gamma}}_{\mathrm{RF}} = k_{\mathrm{RF}} \left[\frac{3}{4} \hat{\mathbb{1}} \otimes \hat{\mathbb{1}} - \hat{S}_{\mathrm{C}x} \otimes \hat{S}^{\mathrm{T}}_{\mathrm{C}x} - \hat{S}_{\mathrm{C}y} \otimes \hat{S}^{\mathrm{T}}_{\mathrm{C}y} - \hat{S}_{\mathrm{C}z} \otimes \hat{S}^{\mathrm{T}}_{\mathrm{C}z} \right], \tag{5.6}$$

where $\hat{S}_{\mathrm{C}i}$ is the i-component of the electron spin operator for $CO_2^{\bullet -}$. The singlet product yield was simulated for rate constants k_{RF} between $10^6\,\mathrm{s}^{-1}$ and $10^{12}\,\mathrm{s}^{-1}$, with k_{S} and k_{D} in the previously mentioned ranges, $a_{\mathrm{H}} = 50.74\,\mathrm{mT}$, and $\Delta g = 0.0107$. The form of the calculated MFEs, which can be seen in Fig. D.4, will be discussed after introducing a second relaxation mechanism.

Singlet–triplet dephasing

Singlet–triplet dephasing is a spin relaxation mechanism that would arise from diffusional modulation of the electron exchange interaction [216]. The singlet and triplet electronic eigenstates of a radical pair with a large exchange interaction are energetically separated and cannot interconvert—if the radicals diffuse apart such that the exchange interaction is decreased for a time then coherences between singlet and triplet states can arise. When the radicals diffuse together again, each radical pair must collapse into either a singlet or triplet state, of which the singlets can go on to react and form products [231]. This introduction and removal of coherence between singlets and triplets can cause strong spin relaxation, and moreover any such modulation of the electron exchange interaction can be modelled using a superoperator of the form

$$\hat{\hat{\Gamma}}_{\mathrm{ST}} = k_{\mathrm{ST}} \left[\hat{P}^{\mathrm{S}} \otimes \hat{P}^{\mathrm{T}} + \hat{P}^{\mathrm{T}} \otimes \hat{P}^{\mathrm{S}} \right], \tag{5.7}$$

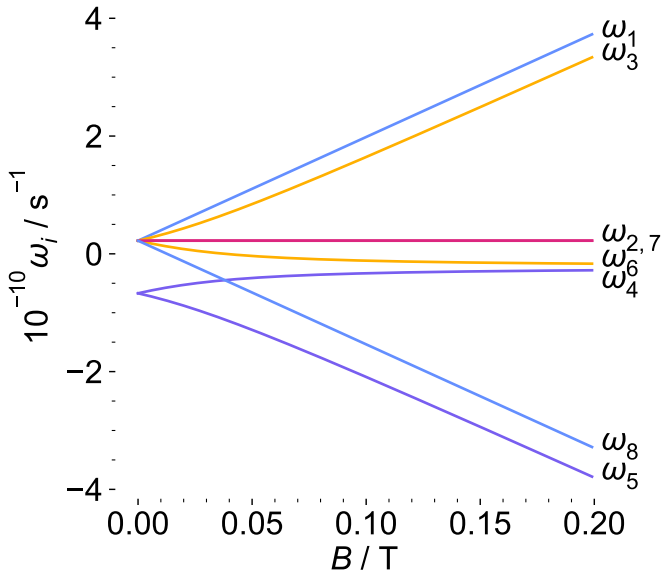

Figure 5.4 Energy eigenvalues ω_i of $\hat{\mathcal{H}}_0$ as a function of the applied field strength for the $\left[{}^1\mathrm{H}^\bullet\,{}^{12}\mathrm{CO}_2{}^{\bullet-}\right]$ system (see Fig. 5.1). The eigenstates are labelled i = 1–8, after reference [232]. At high magnetic field, states 1 and 3 correspond to T_{+1}, states 5 and 8 correspond to T_{-1}, and states 2, 4, 6, and 7 correspond to linear combinations of T_0 and S.

where k_{ST} is a phenomenological singlet–triplet dephasing rate constant, and $\hat{P}^{\mathrm{S}}$ and $\hat{P}^{\mathrm{T}}$ are the singlet and triplet projection operators. The singlet product yield was simulated for this mechanism of spin relaxation with rate constant k_{ST} varying between $10^6\,\mathrm{s}^{-1}$ and $10^{12}\,\mathrm{s}^{-1}$ and k_{S} and k_{D} as before. These MFEs can be seen in Fig. D.5.

Including either random fields relaxation or singlet–triplet dephasing did change the shape of the field dependence when compared to Fig. 5.3 or Figs. D.1–D.2, but in all cases the MFEs were very small, or larger but strictly negative, throughout the range of field strengths considered.[3] This result is not surprising, and can be explained by considering the energetic separation of the T_{+1} and T_{-1} states from the T_0 and S states at high magnetic fields, as is shown in Fig. 5.4, which plots the eigenstates of $\hat{\mathcal{H}}_0$ (see Eq. (5.1.1), where in this case we have ignored the small difference in g-values) as a function of the applied field strength.

[3]Examples of calculated MFEs including random fields relaxation or singlet–triplet dephasing can be seen in Figs. D.4 and D.5.

When the magnetic field is comparable to the hyperfine interaction (~50 mT), the singlet–triplet interconversion caused by spin relaxation is more efficient than at higher magnetic fields, where the T_{+1} and T_{-1} are energetically isolated from the singlet state and therefore much slower to convert to S and react to give the product. The two relaxation mechanisms introduced here do not change those dynamics, since they do not depend explicitly on the strength of the applied field. However, we can speculate that a relaxation process that becomes more efficient as the strength of an applied magnetic field increases may indeed give rise to a positive MFE. If the relaxation of T_{+1} and T_{-1} to T_0, and therefore to S, is more efficient at high fields than at low fields, then we may see more singlet product formed at high fields and therefore a positive MFE.

As an initial test of this possibility, we simply allowed the rate constant for the random fields relaxation superoperator (see Eq. (5.6)) to vary quadratically with the strength of the applied magnetic field: $k_{RF} = qB^2$ where q is a proportionality constant that varies between $10^6\,T^{-2}\,s^{-1}$ and $10^{12}\,T^{-2}\,s^{-1}$. Several relaxation mechanisms increase quadratically in their efficiency with an applied magnetic field, which is the rationale behind this simple model [107, 213–215]. With all other rate constants and variables in the ranges previously mentioned there are indeed combinations of parameters that give positive MFEs similar in appearance to Fig. 5.2, with examples shown in Fig. D.6. Encouraged by this result, we can move to modelling field-dependent spin relaxation in a more realistic manner.

g-tensor anisotropy

The g-anisotropy mechanism arises from rotational modulation of the anisotropic electron Zeeman interaction for the carbon dioxide radical [213]. The appropriate

relaxation superoperator is

$$\hat{\hat{\Gamma}}_{\mathrm{GA}} = \frac{1}{15}\sum_{j=x,y,z}\left(\frac{g_{jj}-g_{\mathrm{iso}}}{g_{\mathrm{iso}}}\right)^2\omega_0^2\left[3J(\omega_0)\left(\frac{1}{2}\hat{\mathbb{1}}\otimes\hat{\mathbb{1}}-\hat{S}_{\mathrm{C}x}\otimes\hat{S}^{\mathrm{T}}_{\mathrm{C}x}-\hat{S}_{\mathrm{C}y}\otimes\hat{S}^{\mathrm{T}}_{\mathrm{C}y}\right)\right. \\ \left.+2J(0)\left(\frac{1}{2}\hat{\mathbb{1}}\otimes\hat{\mathbb{1}}-2\hat{S}_{\mathrm{C}z}\otimes\hat{S}^{\mathrm{T}}_{\mathrm{C}z}\right)\right], \tag{5.8}$$

where $g_{\mathrm{iso}} = (g_{xx} + g_{yy} + g_{zz})/3$ is the isotropic g-value for $CO_2^{\bullet-}$, g_{ii} are the principal components of the $CO_2^{\bullet-}$ g-tensor: $g_{xx} = 2.0032$, $g_{yy} = 1.9975$, $g_{zz} = 2.0014$ [220], $J(\omega) = \tau_{\mathrm{c}}/(1+\omega^2\tau_{\mathrm{c}}{}^2)$ is taken as the spectral density function, τ_{c} is the rotational correlation time for the radical, and ω_0 is the electron Larmor frequency. This relaxation mechanism depends explicitly on the applied magnetic field via the field-dependent Larmor frequency, with relaxation expected to be faster at higher fields. It is possible to obtain positive MFEs using this mechanism, with several positive MFEs calculated for integer values of $\log_{10}\tau_{\mathrm{c}}$ (the rotational correlation time, which appears in the spectral density function in Eq. (5.8)), $\log_{10} k_{\mathrm{S}}$, and $\log_{10} k_{\mathrm{D}}$. Some example MFEs with τ_{c} between 1 ps and 1 μs and k_{S} and k_{D} in the usual ranges are shown in Fig. D.7.

Having established that positive MFEs could be obtained, we were able to fit the experimental data [76]. Treating τ_{c} as a variable parameter, its value was optimized, given integer values of $\log_{10} k_{\mathrm{S}}$ and $\log_{10} k_{\mathrm{D}}$ between 3 and 11, using a least-squares fitting procedure to match the experimental data. The simulations of

$$\Delta\Phi_{\mathrm{S}}(B) = \frac{\Phi_{\mathrm{S}}(B) - \Phi_{\mathrm{S}}(B = 30\,\mathrm{mT})}{|\Phi_{\mathrm{S}}(B = 900\,\mathrm{mT}) - \Phi_{\mathrm{S}}(B = 30\,\mathrm{mT})|} \tag{5.9}$$

were optimized against the normalized experimental data shown in Fig. 5.2. Satisfactory agreement was found for the 17 sets of parameters, summarised in Table 5.2, which are discussed in Section 5.2.3.

$\log_{10} k_D$ \ $\log_{10} k_S$	6	7	8	9	10	11
3	1.25	0.61	0.61	0.64	0.65	0.65
4		**8.9**	**4.6**	**5.4**	5.7	5.7
5					12.4	14.2
6						
7						
8						
9						1.0*
10					10.3*	9.1*
11						65*

Table 5.2 Optimized values of the rotational correlation time τ_c for given integer combinations of $\log_{10} k_S$ and $\log_{10} k_D$ (both k_S and k_D are in s^{-1}). The values shown give calculated MFEs that are in agreement with the experimental result measured by Pan *et al.* [76] when spin relaxation is modelled using the g-tensor anisotropy mechanism. The units of τ_c in the top part of the table are ps, whereas the four asterisked values in the bottom right of the table are in μs. Greyed out entries in the table indicated combinations of k_S and k_D for which an acceptable fit to the experimental data could not be found. The criterion for an acceptable fit was relatively loose, partly because of a lack of data on the uncertainty in the experimentally recorded values. This means the parameters giving an acceptable fit cover a broad range of values, which is discussed and narrowed down in the main text. The three entries in bold indicate the most credible values of k_S, k_D, and τ_c according to this analysis, and are discussed in the main text.

Spin–rotation

The anisotropy of the g-tensor also plays a role in spin–rotation relaxation, caused by the interaction of the electron spin with the rotational angular momentum of the radical. The superoperator for this spin–rotation relaxation has the same form as that for random fields relaxation:

$$\hat{\hat{\Gamma}}_{\mathrm{SR}} = k_{\mathrm{SR}} \left[\frac{3}{4} \hat{\mathbb{1}} \otimes \hat{\mathbb{1}} - \hat{S}_{\mathrm{C}x} \otimes \hat{S}^{\mathrm{T}}_{\mathrm{C}x} - \hat{S}_{\mathrm{C}y} \otimes \hat{S}^{\mathrm{T}}_{\mathrm{C}y} - \hat{S}_{\mathrm{C}z} \otimes \hat{S}^{\mathrm{T}}_{\mathrm{C}z} \right], \tag{5.10}$$

which is the same as Eq. (5.6) but with the relaxation rate constant k_{RF} replaced by k_{SR}, a relaxation rate constant depending on the rotational correlation time and the components of the anisotropic g-tensor:

$$k_{\mathrm{SR}} = \frac{1}{9\tau_{\mathrm{c}}} \sum_{j=x,y,z} \left(g_{jj} - g_{\mathrm{e}} \right)^2, \tag{5.11}$$

where $g_{\mathrm{e}} \simeq 2.0023$ is the g-value for a free electron [214, 215].

Allowing the rotational correlation time to take values between 1 ps and 1 μs, which is a similar range to the values found in Table 5.2, modelling spin–rotation relaxation gave MFEs that were uniformly negative (examples are shown in Fig. D.8). When including both spin–rotation and g-tensor anisotropy mechanisms the MFE was either negative, or in a couple of cases positive but very small ($< 1\%$) (examples are shown in Fig. D.9).

In summary, we were able to model the magnetocurrent MFE satisfactorily using the coherent Hamiltonian and Haberkorn reaction operator alongside a g-tensor anisotropy relaxation superoperator, but not with any of the other types of relaxation processes mentioned (spin–rotation, singlet–triplet dephasing, or random fields).

Discussion of fitted parameters 5.2.3

Table 5.2 summarises the sets of parameters $\log_{10} k_S$, $\log_{10} k_D$, and τ_c that successfully account for the MFE observed by Pan *et al.* [76]. This modelling includes hyperfine and Δg mechanisms of singlet–triplet interconversion in the radical pair $[H^\bullet\, CO_2{}^{\bullet-}]$, with good agreement with experimental data provided that rotational modulation of the anisotropic Zeeman interaction (g-tensor anisotropy) is the dominant relaxation pathway for this radical pair.

Fig. 5.5 shows the calculated MFE on the radical pair $\left[{}^1H^\bullet\, {}^{12}CO_2{}^{\bullet-}\right]$ (and its isotopologues, see Section 5.3), calculated for two example sets of parameters from Table 5.2, and in each case they show excellent agreement with the (normalized) magnetocurrent from Fig. 5.2, which is also shown. Fig. 5.6 shows the MFE calculated for the same parameters as in Fig. 5.5 but now including the field range $0 \leq B/\mathrm{T} \leq 0.03$. A pronounced and sharp low field effect can be seen in Fig. 5.6(a), which is not present for the combination of parameters shown in Fig. 5.6(b).

Since the fitted parameters in Table 5.2 cover such a broad range of values, the question remains: which of these parameter combinations, if any, is physically reasonable? We can discount some of them using simple physical arguments. The Stokes–Einstein equation (2.76) can be used to estimate the rotational diffusion correlation time τ_c. If we take $a \simeq 150\,\mathrm{pm}$ for CO_2, with $\eta \simeq 10^{-3}\,\mathrm{kg\,m^{-1}\,s^{-1}}$ for water at $T = 298\,\mathrm{K}$, then we get $\tau_c \simeq 3.4\,\mathrm{ps}$. This is a reasonable lower bound on the rotational correlation time, which will be higher in (for instance) a more viscous medium, therefore we can discount the top row of Table 5.2 ($k_D = 10^3\,\mathrm{s^{-1}}$), in which the optimized value of $\tau_c \simeq 1\,\mathrm{ps}$.

The two right hand columns of Table 5.2 have values of k_S ($10^{10}\,\mathrm{s^{-1}}$ and $10^{11}\,\mathrm{s^{-1}}$) that exceed the upper limit on the rate constant for the production of formate of $\sim 10^9\,\mathrm{s^{-1}}$ estimated in Section 5.2. Therefore, we can probably exclude these two columns.

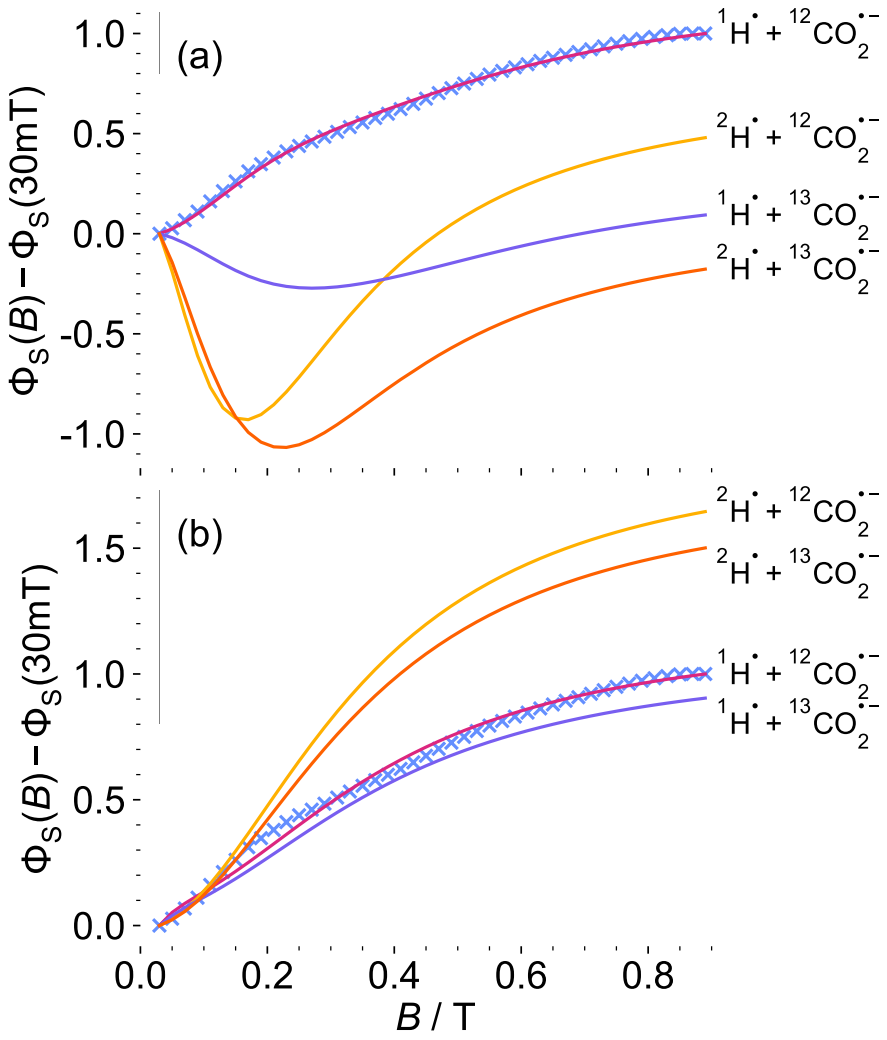

Figure 5.5 Calculated MFE on the $H^\bullet + CO_2^{\bullet-}$ reaction, including spin relaxation from the g-tensor anisotropy mechanism. The pink line has been fitted to the experimental data from Pan *et al.* [76], which is shown in blue crosses. In (a) the fitted parameters are $k_S = 10^7\,s^{-1}$, $k_D = 10^4\,s^{-1}$, $\tau_c = 8.9\,ps$, in (b) they are $k_S = 10^{11}\,s^{-1}$, $k_D = 10^9\,s^{-1}$, $\tau_c = 1.0\,\mu s$. The plots show the difference between the singlet yield at field B and the yield at $B = 30\,mT$, scaled to 1.0 at 0.9 T for the pink lines ($^1H^\bullet + {}^{12}CO_2^{\bullet-}$). In each panel the same scaling factor as for the pink line is used for the other three isotopologues. As discussed in the main text, the parameters used in (b) are relatively unrealistic compared to the more physically reasonable ones in (a).

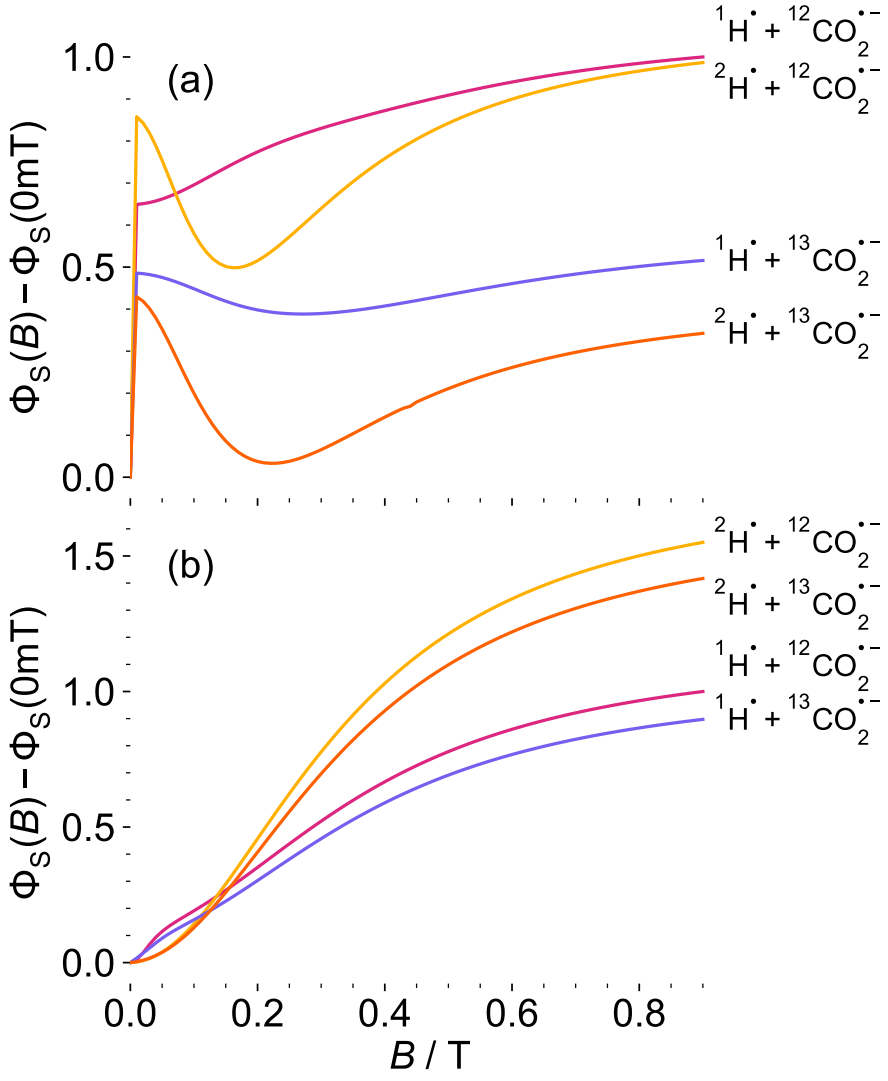

Figure 5.6 Calculated MFE on the $H^\bullet + CO_2^{\bullet-}$ reaction, including spin relaxation from the g-tensor anisotropy mechanism. The pink line has been fitted to the experimental data from Pan *et al.* [76]. In (a) the fitted parameters are $k_S = 10^7\,s^{-1}$, $k_D = 10^4\,s^{-1}$, $\tau_c = 8.9\,ps$, in (b) they are $k_S = 10^{11}\,s^{-1}$, $k_D = 10^9\,s^{-1}$, $\tau_c = 1.0\,\mu s$. The plots show the difference between the singlet yield at field B and the yield at zero-field, scaled to 1.0 at 0.9 T for the pink lines ($^1H^\bullet + {}^{12}CO_2^{\bullet-}$). In each panel the same scaling factor as for the pink line is used for the other three isotopologues. As discussed in the main text, the parameters used in (b) are relatively unrealistic compared to the more physically reasonable ones in (a), which also show a pronounced low field effect, visible here.

A further argument can be made to explain why all four asterisked entries in the bottom right of Table 5.2 can be discounted. These have rotational correlation times as long as 1 μs, or even longer, and it is unlikely that the expression used for the relaxation superoperator in Eq. (5.8) is valid for rotational correlation times as long as this. A condition for Eq. (5.8) to hold is that $\omega^2\tau_c^2 \ll 1$, where ω are the eigenvalues of $\hat{\mathcal{H}}_0$. This is known as the motional narrowing regime [213], as was seen in a slightly different setting in Chapter 3. As is shown in Fig. 5.4, ω will be on the order of $10^{10}\,\mathrm{s}^{-1}$, and if $\tau_c \simeq 1\,\mu\mathrm{s}$ then the motional narrowing condition is clearly not met. We can therefore discount all the asterisked entries in Table 5.2.

This leaves the three bold values in Table 5.2, i.e.

$$\begin{aligned} 5 \lesssim \tau_c/\mathrm{ps} \lesssim 10, \\ 10^7 \lesssim k_S/\mathrm{s}^{-1} \lesssim 10^9, \\ k_D/\mathrm{s}^{-1} \simeq 10^4. \end{aligned} \tag{5.12}$$

These conditions are the most physically realistic of the optimized conditions found. Furthermore, they do predict a pronounced low field effect in the region $B < 30\,\mathrm{mT}$, as can be seen in Fig. 5.6(b), which could be sought experimentally as a test of this model.

This analysis predicts that $k_S \ll k_D$, which can be understood by considering how the spin–lattice relaxation rate Γ for $CO_2^{\bullet-}$, as predicted by the g-tensor anisotropy mechanism [107], depends on the strength of the magnetic field:

$$\Gamma = \frac{1}{5}\sum_{j=x,y,z}\left(\frac{g_{jj}-g_{\mathrm{iso}}}{g_{\mathrm{iso}}}\right)^2\left(\frac{\omega_0^2\tau_c}{1+\omega_0^2{\tau_c}^2}\right), \tag{5.13}$$

where ω_0 is the Larmor frequency, which is linearly dependent on the magnetic field strength.

Fig. 5.7 shows Eq. (5.13) plotted for four values of the rotational correlation time: $\tau_c = 1\,\mathrm{ps}$, 4 ps, 16 ps, and 64 ps. For all of the correlation times shown the

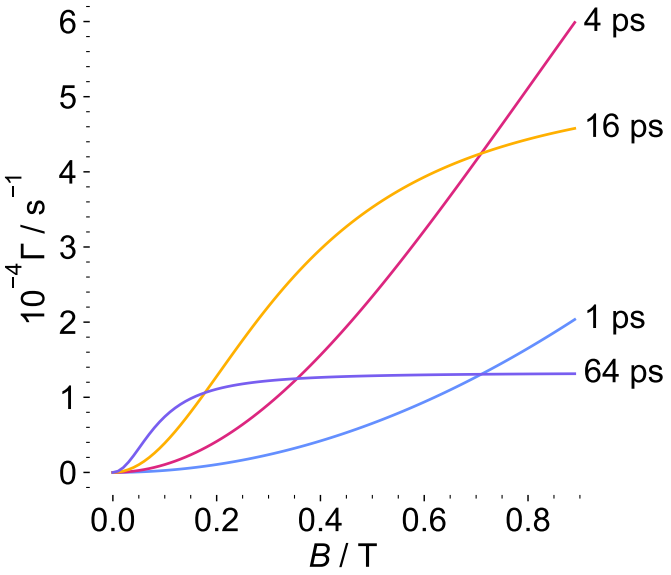

Figure 5.7 Calculated spin–lattice relaxation rate of $CO_2^{\bullet-}$ (g-tensor anisotropy mechanism, Eq. (5.13)) plotted as a function of magnetic field strength for four values of τ_c = 1 ps (blue), 4 ps (pink), 16 ps (yellow), and 64 ps (purple).

relaxation is faster at higher field. This is as required for a positive MFE; without efficient spin–lattice relaxation at high field the radical pairs that are initially in the T_{+1} and T_{-1} states (which make up 50% of the total for F-pairs of the type we consider here) can never react to produce formate. This is because at high field the transition from $T_{\pm1}$ to S is energetically forbidden (see Fig. 5.4). Spin relaxation that is strongly field-dependent, as in Fig. 5.7, can transfer population from the unreactive $T_{\pm1}$ states to T_0, which can mix coherently with the singlet state and go on to form HCO_2^-.

This process is most efficient when $\omega_0\tau_c \simeq 1$, which for $B = 0.9\,\mathrm{T}$ is when $\tau_c \simeq 6.3\,\mathrm{ps}$ and $\Gamma_{max} \simeq 6.7 \times 10^4\,\mathrm{s}^{-1}$. Unsurprisingly, this value of τ_c falls within the range of τ_c values predicted in the bold region of Table 5.2. The slow value of $k_D \simeq 10^4\,\mathrm{s}^{-1}$ can also be understood when we consider that if k_D were not smaller than Γ_{max} then the $T_\pm$ states would not have time to relax to T_0 before the radicals diffuse apart.

The bold values predicted in Table 5.2 also allow us to comment on the dynamic behaviour of the radicals at the electrode, albeit speculatively in the absence of further experimental data to test our model. The small value of k_D implies that the radicals may be loosely adsorbed on the surface of the catalyst; if they were freely diffusing in solution they would separate at a rate much faster than $10^4\,s^{-1}$. Furthermore, the fact that τ_c is only a little higher than the Stokes–Einstein estimate of 3.4 ps implies that the rotational motion of the carbon dioxide radical is not strongly constrained by this adsorption.

Isotopologous reaction 5.3

Isotopic substitution can influence a chemical reaction either by affecting the mass of the reactants (a mass isotope effect) or by the introduction/removal/adjustment of the hyperfine field. For radical pair reactions the latter, associated with the different magnetic moments of the isotopes, is the principal effect [233]. In particular, for the reaction $H^\bullet + CO_2^{\bullet-} \rightarrow HCO_2^-$, a covalent bond is formed in a reaction that will have little-to-no activation energy, and so any mass isotope effects should be negligible compared to the magnetic isotope effects.

The MFE associated with the optimized sets of parameters in Table 5.2 can be calculated for radical pairs $[H^\bullet\,CO_2^{\bullet-}]$ where the hydrogen has been replaced by deuterium, or the ^{12}C replaced by ^{13}C, or both. As described in Section 5.1.1, deuterium has a hyperfine coupling that is around ~6.5 times smaller than hydrogen, and ^{13}C substitution introduces a hyperfine coupling of 19.93 mT [222]. Examples of these isotopologue MFEs for two of the optimized sets of parameters from Table 5.2 are shown in Fig. 5.5 and 5.6.

In Fig. 5.5(a)[4] the isotopic substitutions change the MFE from monotonically increasing to biphasic, initially decreasing and then increasing once $B \gtrsim 200\,mT$. For the (less physically reasonable) parameters in Fig. 5.5(b)[5] the MFE remains

[4] $k_S = 10^7\,s^{-1}$, $k_D = 10^4\,s^{-1}$, and $\tau_c = 8.9\,ps$.
[5] $k_S = 10^{11}\,s^{-1}$, $k_D = 10^9\,s^{-1}$, and $\tau_c = 1.0\,\mu s$.

monophasic throughout the range of field strengths. It is significantly larger for $^2H^\bullet$ than for $^1H^\bullet$, and introduction of ^{13}C slightly decreases the size of the MFE, all other things being equal.

Therefore, the magnetic isotope effects predicted in Figs. 5.5 and 5.6, and in particular the pronounced qualitative change for the physically reasonable parameters used in Figs. 5.5(a) and 5.6(a), could provide the basis for an experimental test both of the reaction mechanism provided by Pan *et al.* [76] and of the model used in this chapter to interpret their results.

Conclusions and further work 5.4

In this chapter the tools of radical pair spin dynamics have been used to simulate the effects of applied magnetic fields on the electrocatalytic reduction of CO_2 to HCO_2^-, as reported by Pan *et al.* [76]. The Δg mechanism favoured by the authors of this study has been shown to be insufficient to explain the positive MFE that they observed, whereas a combination of coherent singlet–triplet mixing from the same Δg mechanism and hyperfine interactions, alongside relaxation resulting from the anisotropic g-tensor in the $CO_2^{\bullet-}$ radical, has been shown to be sufficient to fit the experimental results. The analysis presented in this chapter puts strong constraints on the parameters used in this model, suggesting (1) a relatively fast reaction rate for formation of formate ions from singlet radical pairs, (2) a relatively slow translational diffusion rate, and (3) a fairly typical rotational correlation time for a small molecule in solution. Taken together, conditions (1)–(3) indicate loose adsorption of the reactants at the electrode. Furthermore, some of the fitted parameters found predict a pronounced low field effect, which could be sought experimentally as a test of the model used. Finally, it has been shown that isotopic substitution of ^2H for ^1H and/or $^{13}CO_2$ for $^{12}CO_2$ would disrupt the spin dynamics sufficiently to provide a qualitative test of the proposed reaction scheme in [76], and the model we have used to fit the experimental data.

6 Oscillating reactions and magnetic fields

Chemical processes in which the concentrations of the reactants and products vary periodically are known as *oscillating reactions*. They were first described in the 19th century, and met with much scepticism. Although discussion of the theory behind chemical oscillators dates back to the early 20th century, they were not systematically studied, as part of the broader field of non-linear chemical dynamics, until the mid-1970s [234]. The speculative potential of oscillating reactions to amplify small changes in applied magnetic fields will be explored, within a relatively abstract theoretical framework, in this chapter.

During a chemical reaction (at constant temperature and pressure) the change in Gibbs free energy should always be negative—this is equivalent to the Second Law of Thermodynamics, i.e. that the total entropy of a closed system must increase over time [21]. At first glance, an oscillatory reaction appears to break this requirement because it moves through the same position in concentration space multiple times. This behaviour is shown in Fig. 6.1 for a simple oscillating system.

So, for many years scientists doubted the existence of true oscillating reactions, convinced that they broke the Second Law of Thermodynamics in a similar way to proposed perpetual motion machines. However, these types of reactions are in fact (and of course) entirely consistent with the laws of thermodynamics. This is because they are examples of reactions that are far from equilibrium [235]. The concentrations of the reaction intermediates never move through an equilibrium

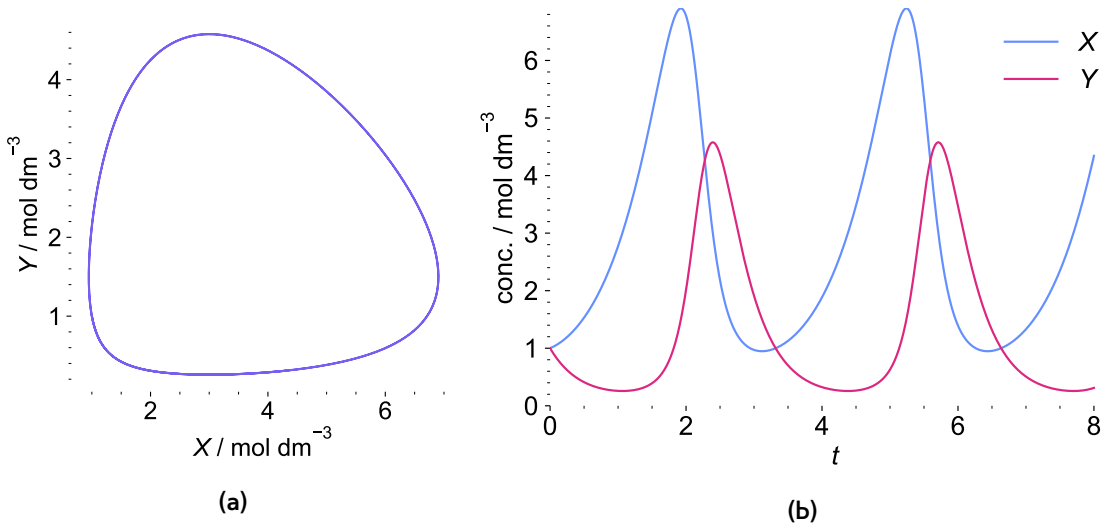

Figure 6.1 Oscillating concentration plots for a reaction that follows the Lotka–Volterra equations (see Eq. (6.3), a numerical solution to which is shown in these plots). (a) Concentration phase space plot, i.e. a parametric plot of $X(t)$ and $Y(t)$. (b) The same data as (a), but as a plot against time. The parameters are $k_1 = 0.3\,\mathrm{dm^3\,mol^{-1}\,s^{-1}}$, $k_2 = 1\,\mathrm{dm^3\,mol^{-1}\,s^{-1}}$, $k_3 = 3\,\mathrm{s^{-1}}$, $X(0) = Y(0) = 1\,\mathrm{mol\,dm^{-3}}$, and $A = 5\,\mathrm{mol\,dm^{-3}}$.

point, and thus any oscillations observed are entirely consistent with the Second Law.

Oscillating reactions 6.1

A requirement for an oscillating reaction system is that one of the reactants must catalyse its own production. The simplest example of such an autocatalytic reaction is:

$$\mathrm{A} + \mathrm{X} \underset{k_{-1}}{\overset{k_1}{\rightleftharpoons}} 2\mathrm{X}, \tag{6.1}$$

but this reaction will not exhibit oscillatory behaviour. Instead, the concentration of X will increase monotonically until an equilibrium has been reached. So, although autocatalysis is necessary for oscillations, it is clearly not sufficient.

For oscillations to occur the autocatalytic reaction must be coupled to an inhibiting reaction that depletes the concentration of X, for instance by including a

second reaction of X with a species Y.

$$\begin{aligned} \mathrm{A} + \mathrm{X} &\xrightarrow{k_1} 2\mathrm{X} \\ \mathrm{X} + \mathrm{Y} &\xrightarrow{k_2} 2\mathrm{Y} \\ \mathrm{Y} &\xrightarrow{k_3} \mathrm{E} \end{aligned} \tag{6.2}$$

In Eq. (6.2) we have assumed that A is in large excess, such that the first reaction is essentially irreversible. We have also added a third reaction that depletes the concentration of Y, without which we would once more see no oscillations, this time because the concentration of Y rather than X would increase monotonically.

This system of reactions is known as the Lotka–Volterra equations. They are the simplest set of oscillating reactions, well known in ecology where they are sometimes called the predator–prey equations. The rate equations for Eq. (6.2) are

$$\begin{aligned} \frac{\mathrm{d}X(t)}{\mathrm{d}t} &= k_1 AX - k_2 XY, \\ \frac{\mathrm{d}Y(t)}{\mathrm{d}t} &= k_2 XY - k_3 Y, \end{aligned} \tag{6.3}$$

where we have used $X(t)$ to represent the concentration of X at time t, and similarly for Y. A is assumed to be in a large constant excess. If we plot the numerical solution to these equations we can see that the concentrations of X and Y both oscillate periodically with time, which is what was shown in Fig. 6.1.

In order to understand the driving force for this oscillatory behaviour, it is worth considering the ecological application of these equations to predator–prey systems. If A is in large excess then we can think of it as an abundant food resource, such as grass. As the number of X, a prey species such as rabbits or hares, increases then so does the number of Y, a predator such as foxes or lynxes. At some point there are so many predators that the prey population begins to decrease, eventually to such low levels that a large predator population cannot be supported and so that population also decreases. The cycle then repeats.

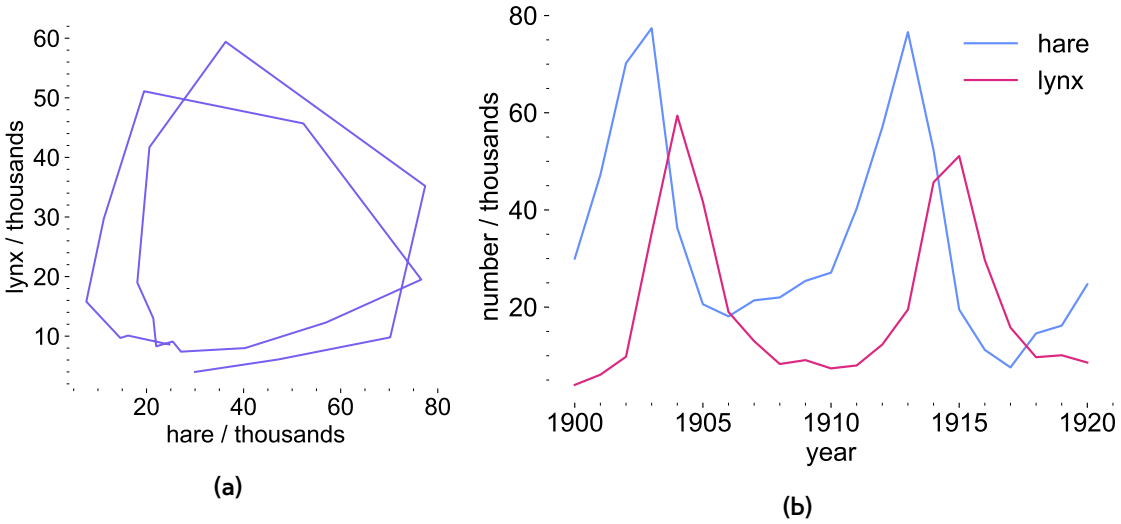

Figure 6.2 Oscillations in the numbers of pelts collected by the Hudson Bay Company in the period 1900–1920 [236]. The lynx preys on the hare. In (a) the parametric plot begins at the bottom point and then spirals anti-clockwise, and the form of the oscillations in (b) corresponds nicely to that shown in Fig. 6.1(b).

Fig. 6.2 shows some example data from an ecological system that exhibits Lotka–Volterra behaviour, where the number of lynx and hare pelts collected by a trapping company in Canada directly correspond to this Lotka–Volterra dynamics. We can keep this ecological argument in mind when considering chemical systems that follow the Lotka–Volterra equations, or other oscillating systems, whereby the prey can be thought of as an activating chemical species, and predator as an inhibitor. For instance, it explains why the third equation in Eq. (6.2) is needed to see oscillations—in the ecological model it represents predators dying, and without this process we would just see an explosion in predator population and no oscillations.

Brusselator 6.1.1

Another example of an autocatalytic oscillating reaction system is the Brusselator, so named because it was first proposed in 1968 at the Université Libre de Bruxelles by Prigogine and Lefever [90]. The equations that describe the Brusselator system are given below.

$$\begin{aligned} \mathrm{A} &\xrightarrow{k_1} \mathrm{X} \\ \mathrm{Y} + 2\mathrm{X} &\xrightarrow{k_2} 3\mathrm{X} \\ \mathrm{X} + \mathrm{B} &\xrightarrow{k_3} \mathrm{D} + \mathrm{Y} \\ \mathrm{X} &\xrightarrow{k_4} \mathrm{E} \end{aligned} \tag{6.4}$$

It differs from the Lotka–Volterra system because the only autocatalytic step is the second reaction, which is third order, and also because there is a second reactant in large excess (B).

It is clear that the concentrations of X and Y for the Brusselator system are confined: if all $k_i \neq 0$ then the total amount of X or Y cannot increase *ad infinitum*. Since this is the case, there are two asymptotic solutions. Either the concentrations of X and Y reach a stable steady state, or they oscillate periodically in a limit cycle [234, 237]. This result, known as the Poincaré–Bendixson theorem, shows that a system thus confined (in this case by stoichiometry and mass conservation) cannot move arbitrarily through the concentration phase space on a random walk [234].

Consider the rate equations[1] for the concentrations of X and Y:

$$\begin{aligned} \frac{\mathrm{d}X}{\mathrm{d}\tau} &= k_1 A + k_2 X^2 Y - k_3 X B - k_4 X, \\ \frac{\mathrm{d}Y}{\mathrm{d}\tau} &= -k_2 X^2 Y + k_3 X B. \end{aligned} \tag{6.5}$$

[1] In Eq. (6.5) time is denoted by τ, so as to distinguish it from the dimensionless t in the transformed Eq. (6.6) and all further equations in this chapter.

These can be rewritten as

$$\begin{aligned}\frac{\mathrm{d}x}{\mathrm{d}t} &= a - bx + x^2y - x,\\ \frac{\mathrm{d}y}{\mathrm{d}t} &= bx - x^2y,\end{aligned} \tag{6.6}$$

where

$$\begin{aligned} a &= \tfrac{k_1}{k_4}\sqrt{\tfrac{k_2}{k_4}}A, \quad b = \tfrac{k_3}{k_4}B,\\ x &= \sqrt{\tfrac{k_2}{k_4}}X, \qquad y = \sqrt{\tfrac{k_2}{k_4}}Y,\\ t &= k_4\tau. \end{aligned} \tag{6.7}$$

The dimensionless parameters x, y, a, and b are directly proportional to the concentrations of X, Y, A, and B respectively, with proportionality constants that depend on the rate constants in Eq. (6.4). A steady state for Eq. (6.6) exists when $\frac{\mathrm{d}x}{\mathrm{d}t} = \frac{\mathrm{d}y}{\mathrm{d}t} = 0$, a pair of simultaneous equations that when solved give the steady state concentrations $x_{\mathrm{ss}} = a$ and $y_{\mathrm{ss}} = b/a$.

Limit cycles and Hopf bifurcation 6.1.2

Whether an oscillating system will attain a steady state or undergo limit cycle oscillations [234, 237] can be ascertained by analysing the Jacobian matrix:

$$\mathbf{J} = \begin{pmatrix} \frac{\partial \dot{x}}{\partial x} & \frac{\partial \dot{x}}{\partial y} \\ \frac{\partial \dot{y}}{\partial x} & \frac{\partial \dot{y}}{\partial y} \end{pmatrix}_{\mathrm{ss}}, \tag{6.8}$$

where $\dot{x}$ and $\dot{y}$ are the time derivatives as in Eq. (6.6) and the partial derivatives are evaluated at $x = x_{\mathrm{ss}}$ and $y = y_{\mathrm{ss}}$. Thus, for the Brusselator as expressed in Eq. (6.6), the Jacobian is

$$\mathbf{J} = \begin{pmatrix} -b + 2xy - 1 & x^2 \\ b - 2xy & -x^2 \end{pmatrix}_{\mathrm{ss}} = \begin{pmatrix} b - 1 & a^2 \\ -b & -a^2 \end{pmatrix}. \tag{6.9}$$

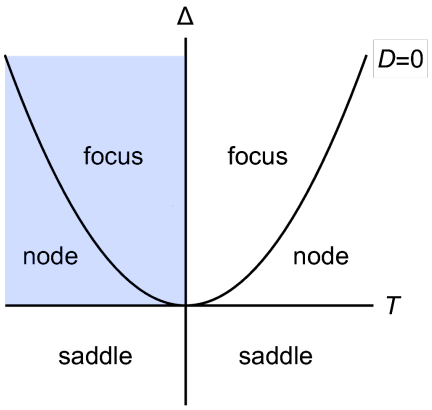

Figure 6.3 Classification of solutions as focus, node, or saddle point, in terms of the trace, T, determinant, Δ, and discriminant, D of the Jacobian matrix $\mathbf{J}$ (see Eq. (6.10)). The shading indicates the stable nodes and foci. The Hopf bifurcation is the line $T = 0$ for $\Delta > 0$.

The eigenvalues of this matrix can be used to classify the nature of any stationary points, and can be written in terms of the the trace, $\mathrm{Tr}\,\mathbf{J} = T$, and determinant, $|\mathbf{J}| = \Delta$ of the matrix [238] . We find these eigenvalues by solving the characteristic polynomial:

$$\begin{aligned} |\mathbf{J} - \lambda \mathbb{1}| &= \lambda^2 - T\lambda + \Delta = 0 \\ \implies \lambda_\pm &= \frac{1}{2}\left(T \pm \sqrt{T^2 - 4\Delta}\right) \\ &= \frac{1}{2}\left(T \pm \sqrt{D}\right), \end{aligned} \tag{6.10}$$

where we have defined the discriminant, $D = T^2 - 4\Delta$, in the last line. As described in [238], these eigenvalues can be divided into three distinct classes, outlined below and summarised in Fig. 6.3.

1. $\lambda_\pm$ are real, distinct, and have the same sign. This is the case when both $D > 0$ and $\Delta > 0$. This is classed as a *node*; it is stable if both eigenvalues are negative, and unstable if both are positive.

2. $\lambda_\pm$ are real, distinct, and opposite in sign. This is the case when $D > 0$ but $\Delta < 0$. It is classed as a *saddle point*.

3. $\lambda_\pm$ are complex conjugate (complex roots of real matrices always come in conjugate pairs). This is the case when $D < 0$ and $T \neq 0$. This is classed as a *focus*, or *spiral*; it is stable if the real parts of the eigenvalues are both negative, and unstable if they are positive.

For the Brusselator system as defined in Eq. (6.6) we have $T = b - 1 - a^2$ and $\Delta = a^2$. Since a is real and positive, there will be no saddle points as Δ will never be negative. In this work, the distinction between a node and focus is less critical, and it will suffice to say that they are simply attractive points if stable, or repulsive points if unstable. It is sometimes helpful to think of a node as a point to which all points in concentration space will be attracted directly, whereas a focus is one into which points tend to spiral, like water down a drain.

It is clear from considering $\Delta > 0$ in Fig. 6.3 that, whether a node or a focus, an equilibrium point is stable if $T < 0$ and unstable if $T > 0$. Using $T = b - 1 - a^2$ we can therefore say that a stationary point in the Brusselator will be stable if $a^2 + 1 > b$, and unstable if $a^2 + 1 < b$.

If the steady state is stable then the system will reach those concentrations of x_{ss} and y_{ss} at arbitrarily long times. For an unstable steady state, by the Poincaré–Bendixson theorem, a closed system such as the Brusselator must exhibit oscillations [234]. Dividing these two regions of stability and instability is the *Hopf bifurcation*, the line $T = 0$ with $\Delta > 0$ in Fig. 6.3. A bifurcation is a division of a solution into two branches or parts.

Canard cycles 6.1.3

We have established that the Brusselator will either attain a steady state if $a^2+1 > b$, or exhibit oscillations if $a^2 + 1 < b$. These oscillations will approach a limit cycle—that is to say that after some time they will repeatedly traverse the same closed path in the phase space as in Fig. 6.1. In general, finding these limit cycles can be a difficult problem [239].

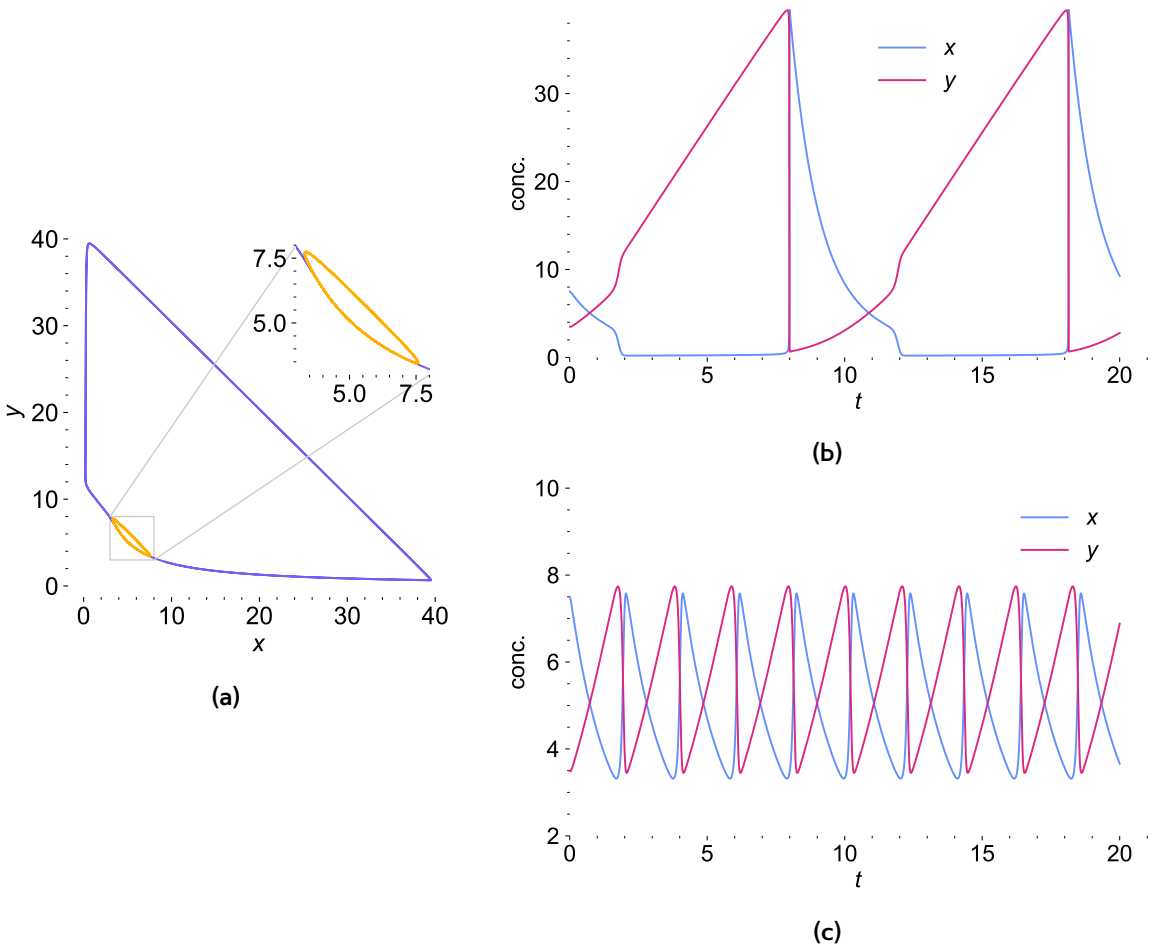

Figure 6.4 Solutions to the Brusselator equations with $b = 26$ and $a = 4.970$ (large purple cycle in (a) and both lines in (b)) or $a = 4.971$ (small yellow cycle in (a) and both lines in (c)). The initial condition is $x(0) = 7.5$, $y(0) = 3.5$ (used throughout this work). In (a) the two cycles touch in the bottom left corner, as shown in the inset box.

An interesting property of the Brusselator is that, for certain values of a and b near the Hopf bifurcation ($a^2 + 1 = b$), the limit cycles undergo a sharp transition in size. To demonstrate this, consider the numerical solution to Eq. (6.6) when $b = 26$ and $a \lesssim \sqrt{b-1}$, shown in Fig. 6.4. When $a = 4.970$ the closed limit cycle that $x(t)$ and $y(t)$ follow varies between ~0.4 and ~39.5 for both x and y, as can be seen in Fig. 6.4(a) ((purple) cycle) and 6.4(b). When $a < 4.970$ the limit cycle is of a similarly large magnitude. However, when a is increased past 4.970 such that $4.971 \leq a \leq 5.000$ there is a dramatic decrease in the extent of the limit cycle, now oscillating periodically between ~3.4 and ~7.7 as can be seen in Fig. 6.4(a)

(yellow cycle) and 6.4(c). Both limit cycles intersect (see inset in Fig. 6.4(a)) in the region of the stationary-state solution, which in each case is when $x_{ss} = a \simeq 4.97$ and $y_{ss} = b/a \simeq 5.23$. As can be seen in Figs. 6.4(b) and 6.4(c), the larger limit cycle also has a slower frequency, while the smaller limit cycle is faster.[2]

So, a decrease of less than 0.02% in a from 4.971 to 4.970 causes an ~800% increase in the amplitude of the limit cycle from ~4.3 concentration units to ~39.1. In fact the change in a that can trigger a large change in oscillation extent can be even smaller still; if a is changed from 4.97087 and 4.97086, the corresponding change in $x_{max} - x_{min}$ is 5.2 to 39.3. In this case a 2 ppm reduction in a has caused an ~8-fold increase in the oscillation extent.

This step change in the size of the limit cycle is known as a *false bifurcation*—the qualitative behaviour of the system (limit cycle as opposed to a steady state) remains the same, but the quantitative extent of this limit cycle changes abruptly [241]. This false bifurcation is in contrast to the true (Hopf) bifurcation at $a^2+1 = b$ that has already been discussed, or the saddle–node bifurcation that many other systems exhibit [242]. This particularly sharp change in the size of a limit cycle is known as a *canard*, or a *canard explosion* [91, 241, 243, 244].

Review of literature on the Brusselator and canards 6.1.4

Canard explosions can be seen in many oscillating reactions, for instance see references [245–247]. They can be described as the transition from a small amplitude limit state to a large amplitude relaxation oscillatory state within a small range of a control parameter [247]. Chemical examples of canards can be found in [241, 247].

The original work on canards is by Benoit *et al.* [91]. This paper describes a canard[3] in an oscillating system as "an abrupt change in the behaviour of the

[2] In fact both the large and small limit cycles exhibit distinct slow and fast changes in concentrations at different stages of their cycles (with the fast changes particularly noticeable as near-vertical lines). This type of behaviour is sometimes described as *slow-fast*, and an analysis of the Brusselator in these terms can be found in reference [240].

[3] Canard means duck in French—in some systems these limit cycles look somewhat like the outline of a cartoon duck.

solutions", or more formally as "a trajectory of $\mathcal{U}_a$ [an attracting manifold] where at least one segment follows a portion of slow curve made up of both attractive and repulsive points" [91].[4]

This is restated, perhaps more clearly, by Szmolyan and Wechselberger in [243] as: "A canard solution is a solution of a singularly perturbed system which follows an attracting slow manifold, passes close to a bifurcation point of the critical manifold and then follows, rather surprisingly, a repelling slow manifold for a considerable amount of time".

After an extensive literature review we have concluded that the canard behaviour near the Hopf bifurcation in the Brusselator is as yet unpublished.[5] It first came to light over twenty years ago when Sarah Allatt described it in a Part II thesis [248]. Later more fully characterised by Edward Baxter [249], it appears to have remained unexplored in the intervening two decades. In Baxter's thesis he lists a number of systems in which these "curiously duck shaped" transitions have been observed, and suggests that this was "the first time that this particular canard transition [in the Brusselator] has been reported".

In the early 2000s, computing power was a somewhat limiting resource when studying these types of differential equations. While this certainly remains true for many systems, the relatively simple Brusselator equations are now far more easily tractable than they were twenty years ago. However, in an extensive search of the literature only three papers published since 2001 mention both "canard" and "Brusselator".

In Matzinger's 2006 paper he explains that "the Brusselator is an example of a singularly perturbed differential equation with an additional parameter" [250], i.e. one of the form

$$\epsilon \frac{\mathrm{d}x}{\mathrm{d}t} = F(x, y, \epsilon, a), \tag{6.11}$$

[4] Translated from the French: "Nous appellerons canard une trajectoire de $\mathcal{U}_a$ dont un segment au moins a pour ombre une portion de courbe lente comportant à la fois des points attractifs et des points répulsifs".

[5] A manuscript based on the work presented in this chapter has recently been published [4].

that cannot be fully approximated by setting the perturbing parameter ϵ equal to zero. The Brusselator as expressed in the first line of Eq. (6.6) can be written in this form if we define $\epsilon = 1/b$:

$$\epsilon \frac{\mathrm{d}x}{\mathrm{d}t} = \epsilon(a + x^2 y - x) - x. \tag{6.12}$$

Matzinger suggests that these types of differential equations will exhibit canard solutions under certain conditions, citing the Brusselator as an example, but it is unclear how the form of the Brusselator used in his work relates to the form we consider here.

In Erneux's 2018 paper he describes a "canard explosion" as a "transition from a small-amplitude limit cycle to canard cycles as we approach a critical value of the bifurcation parameter" and states that both the Turing and Sel'kov models exhibit such features [244]. The Turing model is an oscillatory system unrelated to the Brusselator, whereas the Sel'kov is a reduced form of the Brusselator:

$$\begin{aligned} \mathrm{Y} + 2\mathrm{X} &\xrightarrow{k_2} 3\mathrm{X} \\ \mathrm{B} &\xrightarrow{k_3} \mathrm{Y} \\ \mathrm{X} &\xrightarrow{k_4} \mathrm{E} \end{aligned} \tag{6.13}$$

which, although clearly related (compare to Eq. (6.4)), exhibits key differences such as unbounded solutions. So, the authors conclude that "the Brusselator is the first minimal two-variable model explaining the onset of chemical oscillations in a way fully compatible with thermodynamics and the laws of mass action" [244]. However, they make no mention of canard oscillations in the Brusselator itself.

Qin and co-authors, in their 2020 paper [251], consider an earlier study of Baer and Erneux into "the transition between a singular Hopf bifurcation and relaxation oscillations" in the Brusselator [245, 252]. They say that in this study the "authors [Baer and Erneux] were specifically interested in the analytical prediction of the

canard explosion that occurs when $A \ll 1$". Their A is our a—clearly we are not looking at the regime $a \ll 1$. In [251] they also list many other studies into systems that exhibit canards, none of which appears to be the canard explosion that we describe in the Brusselator when $a > 1$.

Besides these three papers [244, 250, 251] that specifically mention "Brusselator" alongside "canard", a few other references are noteworthy at this point. Desroches *et al.* review mixed mode chemical oscillations (MMOs), describing canards as occurring in "slow-fast systems after a singular Hopf bifurcation" [253]. They list many systems that exhibit MMOs and/or canards, but do not mention the Brusselator. Nicolis describes the bifurcation of the Brusselator in some detail, but does not note the existence of a canard [254].

So, although the bifurcation of the Brusselator near $a^2 + 1 = b$ is well known and described, it would appear that its particularly sharp canard transition at $a^2 + 1 \lesssim b$ either remains undescribed, or is well known but considered completely unnoteworthy. Given the fact that canard transitions have been described in detail for many oscillating systems (see, for instance, the list in reference [251]) it seems unlikely that the latter is true, and so we must assume the former.

Modelling the canard explosion 6.2

It has been established that the Brusselator system has a Hopf bifurcation from a stable steady state to an unstable one at $a^2 + 1 = b$. We have also asserted that the Brusselator system exhibits a canard explosion at $a^2 + 1 \lesssim b$. Both of these features can be explored by numerically integrating Eq. (6.6) and inspecting the resulting solutions.

Location and magnitude of the canard 6.2.1

The form of the oscillations for various values of a and b can be used to establish the position and size of the canard explosion. We have already seen this in Fig. 6.4 for the case when $b = 26$. Fig. 6.5 shows this transition more fully explored for

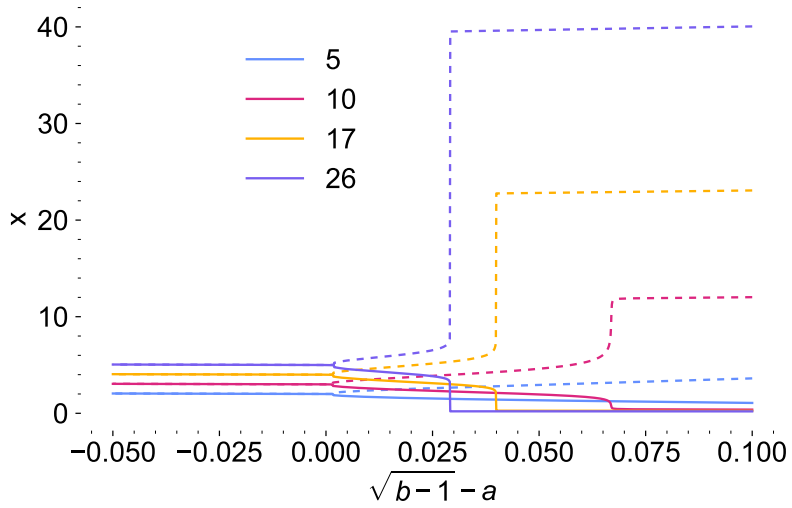

Figure 6.5 Maximum and minimum concentrations of x as a function of $\sqrt{b-1}-a$ for given values of b (indicated by coloured lines). When $a > \sqrt{b-1}$ (i.e. the left hand part of the plot) then there are no oscillations since the system is past the Hopf bifurcation. For larger values of b the canard explosion can be seen as a sharp decrease in oscillation size as a is increased.

$b = 26$ and three other values of b. The different traces show the maximum and minimum concentration values for x (y shows corresponding behaviour) as a function of a for a given value of b. The difference between these two lines is an indication of the size of any oscillations that occur in the solution. The solutions shown ignore oscillatory behaviour that either decays or builds in, such that we consider only the size of the stable oscillations.

As a is decreased (moving left to right on the plot) there is a transition from steady state behaviour (i.e. $x = x_{ss} = a$ when $a > \sqrt{b-1}$) through the Hopf bifurcation at $a = \sqrt{b-1}$ that leads to small limit cycles when $a \lesssim \sqrt{b-1}$, followed by a canard explosion to large cycles. As b is decreased both the size and sharpness of the canard explosion decreases. For $b = 5$ there is no sharp canard explosion, and the size of the oscillations in x grow relatively smoothly as a is decreased.

The canard explosion can also be seen as a sharp change in the frequency of the oscillations—as was previously mentioned, the large limit cycle has a lower frequency than the small one. This will be discussed later, and is shown in Fig. 6.8.

Magnetic fields and oscillating reactions 6.3

The canard explosion in the Brusselator occurs because of a very small change in the system parameters—how could such a change arise? One possible explanation would be an applied magnetic field. We have already seen in previous chapters how relatively weak magnetic fields can influence chemical reactions. One can imagine a situation where a weak applied magnetic field, either constant or time-dependent, may change one of the system parameters and in doing so force the system through the canard explosion.

This type of magnetic field effect (MFE) can in fact be introduced to the Brusselator system by supposing that one of the reactions proceeds via a radical pair, which we label RP. If the first reaction in Eq. (6.4) proceeds via this radical pair then we have:

$$\mathrm{A} \underset{k'_{-1}}{\overset{k'_1}{\rightleftharpoons}} \mathrm{RP} \xrightarrow{k_\mathrm{X}} \mathrm{X}. \tag{6.14}$$

It is assumed that the first step with rate constant k'_1, and its reverse reaction with rate constant k'_{-1}, occur exclusively via electronic singlet states, while both singlet and triplet radical pairs can form X with the same rate constant k_X. If a magnetic field is applied to this system then the probability Φ_X that the radical pair RP reacts to form X rather than returning to A will be affected, because this magnetic field modulates the extent and timing of the singlet–triplet interconversion in the RP [15, 89, 255].

The spin dynamics of the radical pair will follow the master equation:

$$\frac{\mathrm{d}}{\mathrm{d}t}\hat{\rho}(t) = -\hat{\hat{\mathcal{L}}}\left[\hat{\rho}(t)\right] + k'_1 \frac{\hat{P}^\mathrm{S}}{Z}, \tag{6.15}$$

where the density matrix is defined such that its trace is equal to the concentration of radical pairs divided by the concentration of A, assumed to be constant: $\mathrm{Tr}\left[\hat{\rho}\right] = [\mathrm{RP}]/[\mathrm{A}]$. In Eq. (6.15) the first term accounts for the coherent spin dynamics of RP

and the reactions that remove radical pairs, the second for the ongoing formation of singlet-state radical pairs from A, and Z is the number of nuclear spin states.

The Liouvillian is given (ignoring relaxation effects) as in Section 2.2.1 by $\hat{\hat{\mathcal{L}}} = \mathrm{i}\hat{\hat{\mathcal{H}}} + \hat{\hat{\mathcal{K}}}$. The spin Hamiltonian $\hat{\mathcal{H}}$ will, in general, contain terms for the Zeeman, hyperfine, exchange, and dipolar interactions for RP, and by considering the processes in Eq. (6.14) we can identify the reaction superoperator as

$$\hat{\hat{\mathcal{K}}} = \frac{k'_{-1}}{2}\left[\hat{P}^{\mathrm{S}}, \hat{\rho}(t)\right]_{+} + k_{\mathrm{X}}\hat{\rho}(t) \tag{6.16}$$

where the first term accounts for the reaction RP $\xrightarrow{k'_1}$ A (singlets only), and the second term accounts for the reaction RP $\xrightarrow{k_{\mathrm{X}}}$ X (both singlets and triplets).

If we treat RP as a short-lived intermediate present at low concentration (i.e. the reactions that deplete the concentration of RP are much faster than those that form it, $k'_{-1} + k_{\mathrm{X}} \gg k'_1$) then we can set Eq. (6.15) equal to zero, finding the steady state solution:

$$\hat{\rho} = \frac{k'_1}{Z}\hat{\hat{\mathcal{L}}}^{-1}\left[\hat{P}^{\mathrm{S}}\right]. \tag{6.17}$$

Substituting Eq. (6.17) into an expression for the rate of change in the concentration of X gives

$$\begin{aligned}\frac{\mathrm{d}[\mathrm{X}]}{\mathrm{d}t} = k_{\mathrm{X}}[\mathrm{RP}] &= k_{\mathrm{X}}\mathrm{Tr}\left[\hat{\rho}\right][\mathrm{A}] \\ &= \frac{k_{\mathrm{X}}k'_1}{Z}\mathrm{Tr}\left[\hat{\hat{\mathcal{L}}}^{-1}\left[\hat{P}^{\mathrm{S}}\right]\right][\mathrm{A}] \\ &= k'_1\Phi_{\mathrm{X}}[\mathrm{A}] \\ &= k_1[\mathrm{A}],\end{aligned} \tag{6.18}$$

where $\Phi_{\mathrm{X}} = \frac{k_{\mathrm{X}}}{Z}\mathrm{Tr}\left[\hat{\hat{\mathcal{L}}}^{-1}\left[\hat{P}^{\mathrm{S}}\right]\right]$ is the fraction of radical pairs that go on to form X, which can be affected by a magnetic field (as described for Eq. (6.14)).

So, we have shown that the effect of an applied magnetic field on the kinetics of the A $\xrightarrow{k_1}$ X reaction step in Eq. (6.5) can be modelled simply by modifying the rate constant k_1, and hence the parameter a (see Eq. (6.7)).

So, can a small change in an applied magnetic field, modelled by varying the constant a in Eq. (6.6), switch the system from the large to the small limit cycle? This type of amplification effect would be interesting chemically, since it is well established that magnetic fields can alter the kinetics and product yields for certain chemical reactions, despite being far outweighed energetically by the thermal energy $k_B T$ [34, 89, 217, 255, 256]. For instance, systems that follow the radical pair model are often predicted or observed to exhibit changes in reaction rates and/or product yields that are around, or much smaller than, tens of percent. Naturally this leads to speculation about potential chemical amplification effects [198, 201, 257–259], particularly for the weak geomagnetic fields that are involved in avian magnetoreception [15, 51, 52, 64] or for weaker still anthropogenic electromagnetic fields that are sometimes claimed to have adverse implications for human health [12, 260–263].

Therefore, we aimed to systematically investigate the potential effects of weak magnetic fields on systems that can be modelled using the Brusselator, in order to know whether a small magnetically-induced change in one of the rate constants in a multi-step chemical reaction could result in a far larger change in the concentrations of the reaction intermediates or the overall rate of reaction. We focused on the effect of either a step-change in a static field, or an oscillating field, considering both random and single frequency oscillations.

To model this variation in the applied field over time, the same differential equations as in Eq. (6.6) were once more solved numerically, but this time allowing

the parameter a to vary with time:

$$\begin{aligned} \frac{\mathrm{d}x}{\mathrm{d}t} &= a(t) - bx + x^2y - x, \\ \frac{\mathrm{d}y}{\mathrm{d}t} &= bx - x^2y. \end{aligned} \tag{6.19}$$

Throughout the calculations that follow we will mainly present results relating to the $b = 26$ system that is, by now, familiar. As b is increased past 26 there is no appreciable change in the sharpness of the canard explosion, since it is already essentially vertical. Furthermore, $b = 26$ exhibits a particularly sharp canard explosion compared to smaller values of b. Where relevant we mention how the results for $b = 26$ compare to those for smaller values of b.

Static fields 6.3.1

The application of a static field that changes the value of a by a small amount can be modelled by switching the value of a at a given time t_{on}:

$$a(t) = \begin{cases} a_1, & \text{if } t \leq t_{\mathrm{on}} \\ a_2, & \text{if } t > t_{\mathrm{on}} \end{cases} \tag{6.20}$$

For the $b = 26$ system the effect of switching a field "on" at various times t_{on}, and thereby pushing a from one side of the canard to the other, is shown in Fig. 6.6. This is a way of modelling the change in k_1 that might be caused either by switching a weak static magnetic field on/off, or by making a small change in the magnitude of an existing static field. In Fig. 6.6(a) and (b) $a_1 = 4.970$ and $a_2 = 4.971$, so that switching the field on changes the parameters from those appropriate for a large cycle to a small cycle. As can be seen, the system does indeed switch from the larger cycle to the smaller, but not instantly, instead completing a circuit round the large cycle before switching to the small cycle. Conversely, in Fig. 6.6(c) and (d) $a_1 = 4.971$ and $a_2 = 4.970$, such that the switch is from small to large cycle. In this case the system is more responsive. In both cases the switch between cycles only occurs when the concentrations are near to the intersection point for

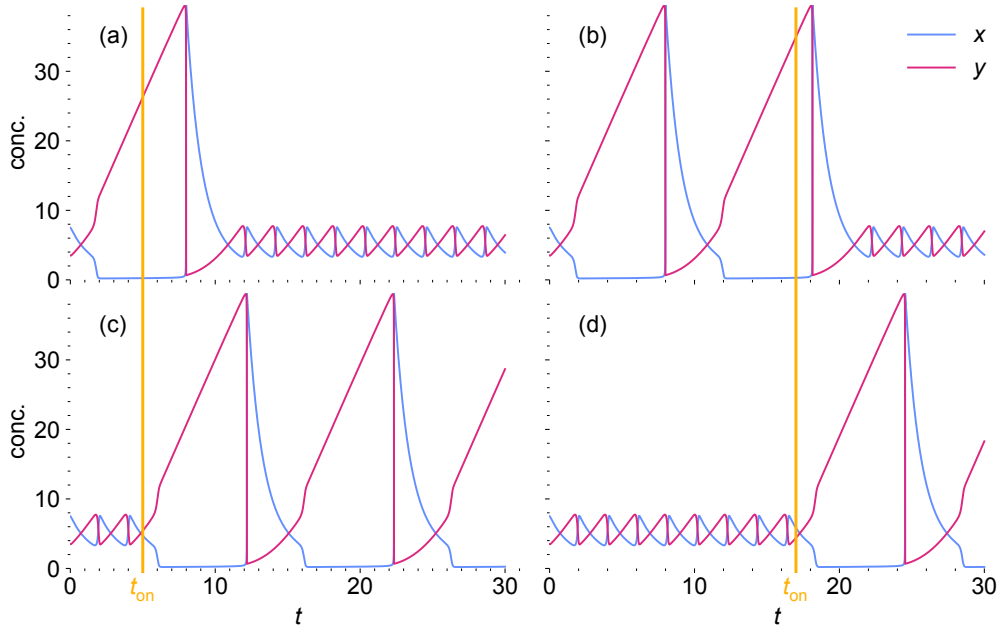

Figure 6.6 Concentrations of x (blue) and y (pink) for $b = 26$. In (a) and (b) $a_1 = 4.970$ and $a_2 = 4.971$, in (c) and (d) they are reversed so that $a_1 = 4.971$ and $a_2 = 4.970$ (see Eq. (6.20)). The time at which a changes is $t_{on} = 5$ in (a) and (c), and $t_{on} = 17$ in (b) and (d), indicated by the yellow vertical lines.

the two limit cycles, when $x \simeq y \simeq 5$, see Fig. 6.4(a). For systems with smaller b, the switch between cycle sizes can be smoother, exhibiting intermediate limit cycles. Presumably this is because the canard explosion itself is smoother, as seen in Fig. 6.5.

This has demonstrated that a small (here ±0.02%) constant change in one of the system parameters is sufficient to reliably switch the oscillations from small to large or vice versa.

Oscillating fields 6.3.2

It has been shown that oscillating magnetic fields, as well as randomly oscillating magnetic fields (sometimes called electromagnetic noise), can have effects on biochemical systems [200, 264], and oscillating magnetic fields have been implicated as potential disruptors for avian magnetoreception [86, 183] (although, these results are not uncontroversial—see for instance reference [184] and the discussion

in Chapter 4). Bearing this in mind, we next considered the effect of both single-component oscillating fields and randomly oscillating fields on the Brusselator system.

Single-component

An oscillating component in the parameter $a(t)$ can be modelled as

$$a(t) = a_c + A\sin(\omega t), \tag{6.21}$$

where a_c is the central value about which $a(t)$ oscillates, A is the amplitude of the oscillations, and ω the angular frequency of the oscillations, such that the period of oscillation is $p = 2\pi/\omega$. In the work presented here a_c is generally 4.97086 (appropriate for a large limit cycle) unless otherwise stated, chosen because it is within 10^{-5} of the value of a that corresponds to the canard explosion.

Arbitrary frequencies

Initially we considered arbitrary values of ω, and found that it is possible to push the system between the large and small limit cycle with these oscillating fields. Some representative results can be seen in Fig. 6.7. The oscillating field can switch the system between the large and small limit cycles, and vice versa, but only if the value of a happens to be sufficiently large (in the case of switching from large to small cycles) or sufficiently small (in the case of switching from small to large cycles) when the system is at the end of an oscillation and near the intersection of the two limit cycles. For the $b = 26$ case this intersection point is around $x \simeq 4.97$, as seen previously in Fig. 6.4. In Fig. 6.7 we only see the large and small cycles—in systems with smaller b, the oscillating field can allow the system to traverse intermediate limit cycles.

For faster oscillations the switch between large and small cycles rarely happens, as demonstrated in Fig. 6.7(a) and (b). It seems that a changes too rapidly to allow

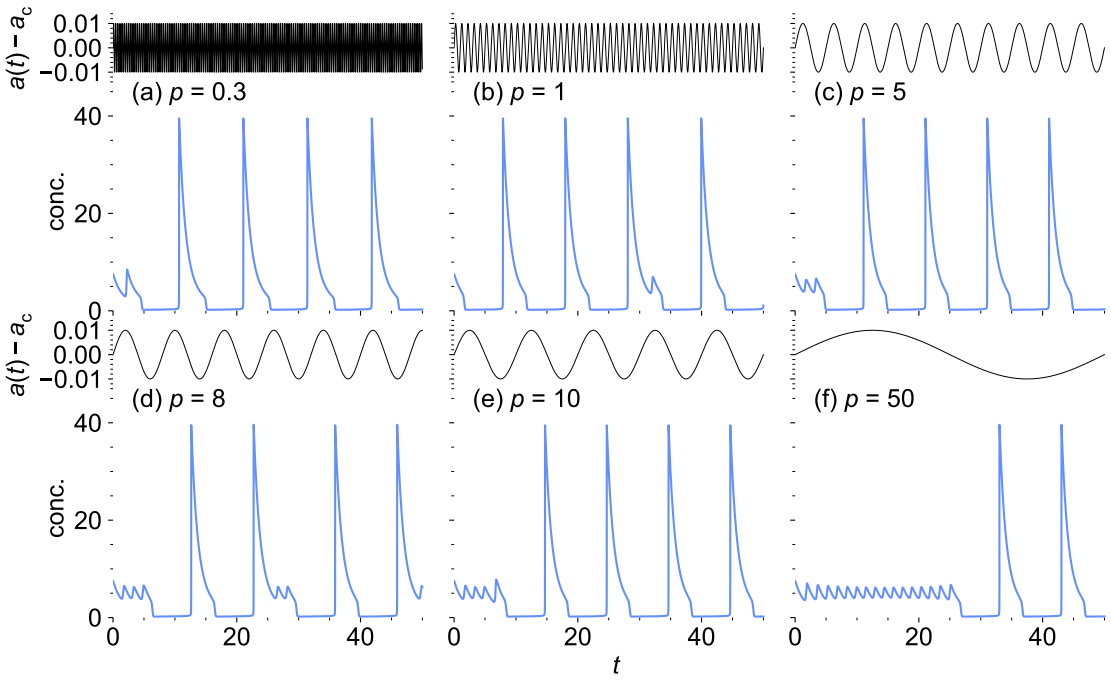

Figure 6.7 Concentration of x (blue) as a function of time, with $b = 26$ and an applied field causing $a(t)$ to oscillate about $a_c = 4.97086$ with $A = 0.01$ (see Eq. (6.21)). In plots (a–f) the applied field is oscillating with a period given by the plot label, and the corresponding oscillation in $a(t) - a_c$ is shown as a black trace above each plot (note the different vertical scales for $a(t) - a_c$ and concentration).

the transition to take place, and the system instead experiences an average value of $a = 4.97086$ and mainly stays in the appropriate large oscillation.

For intermediate or slower oscillations the lower and higher values of $a(t)$ are experienced for sufficiently long times that the crossover can happen, and so the system switches back and forth between large and small limit cycles, for instance in Fig. 6.7(d) and (f). In (f) it is particularly clear that the large limit cycle corresponds to lower values of $a(t)$ and the small limit cycle to higher $a(t)$, a trend that continues for larger values of t.

Furthermore, if the period of oscillations roughly matches the period of the large limit cycle (~10 time units for $b = 26$) then, once the system attains the large limit cycle, it appears to be locked into it. This can be seen in Fig. 6.7(e), where the period of oscillation is approximately equal to that of the large cycle, or in (c), where the period is roughly half that of the large cycle. In these two cases the large limit cycle continues for values of t that are somewhat larger than those plotted in Fig. 6.7, but at very large times a switch is sometimes seen.

Matching limit cycle frequencies

The limit cycles themselves clearly have a characteristic frequency, and so we next considered what would happen if the frequency of the applied field exactly matches that of the limit cycle.

The period of the limit cycle oscillations, for a given combination of a and b, can be found by measuring the gaps between peaks in the concentration of x as a function of time. Such analysis was performed for the same values of b as in Fig. 6.5, considering only values of $a \leq \sqrt{b-1}$. The periods of oscillation are shown as a function of a for various values of b in Fig. 6.8. It is clear by comparison with Fig. 6.5 that the large decrease in oscillation magnitude at the canard coincides with a decrease in period of the oscillations; small oscillations are fast oscillations, and large ones are slow.

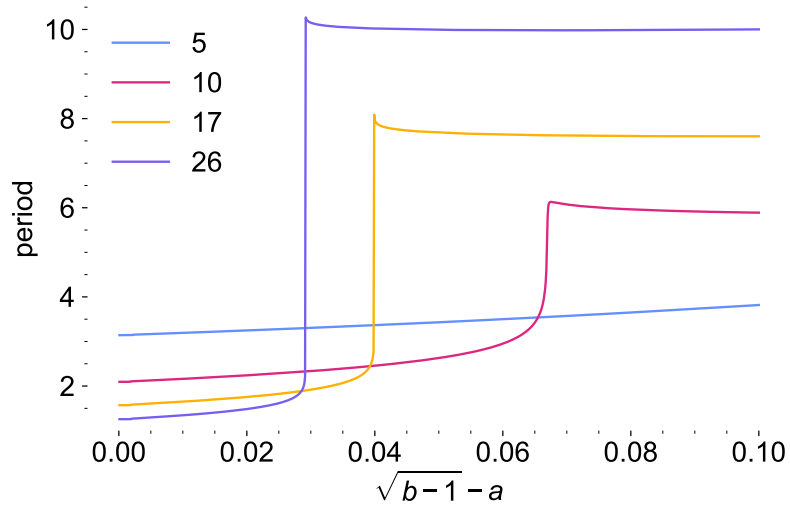

Figure 6.8 Oscillation period as a function of $\sqrt{b-1}-a$ for given values of b (indicated by coloured lines). We have not plotted any values where $a > \sqrt{b-1}$ since this is past the Hopf bifurcation, and thus there are no oscillations at arbitrarily long times. The canard explosion can be seen for the larger values of b as a sharp decrease in oscillation period as a is increased.

Having calculated the oscillation periods, we were able use the corresponding frequencies to simulate fields oscillating appropriately for both the large and small limit cycle (see Eq. (6.21)). The effect of a field oscillating at the frequency of the large limit cycle's oscillations, and at the frequency of the small limit cycle's, are shown in Fig. 6.9. For the slower oscillating field (Fig. 6.9(b) and (e)) the system quickly locks into the large limit cycle, even if $a(t)$ is oscillating about a value of a_c that is appropriate for the small limit cycle, as is the case in (e). This pattern is not seen for the faster oscillating field (Fig. 6.9(c) and (f)), where the system does not simply remain in the small limit cycle, but occasionally traverses the large one.

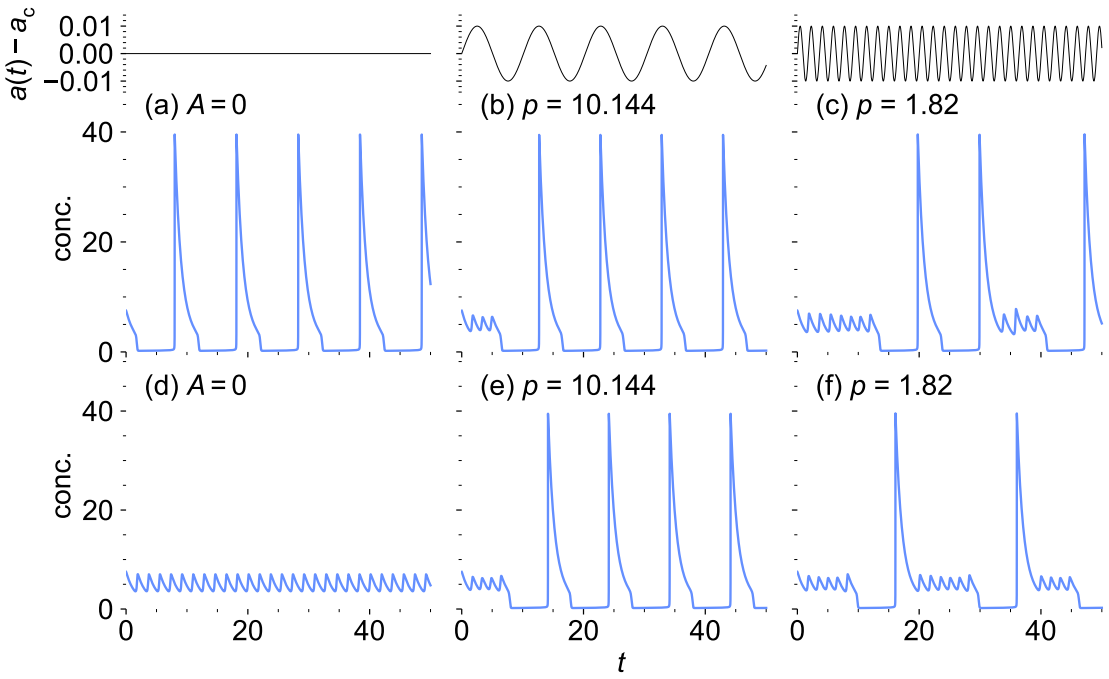

Figure 6.9 Concentration of $x(t)$ (blue), with $b = 26$ and an applied field causing $a(t)$ to oscillate about either $a_c = 4.96986$ (a–c) or $a_c = 4.97186$ (d–f). The amplitude of the oscillation is zero in (a) and (c) (i.e. no oscillations in a), and $A = 0.01$ in all other cases (see Eq. (6.21)). In plots (a) and (d) the applied field is static, in (b) and (e) it oscillates with a period $p = 10.144$, as measured for $b = 26$, $a = 4.96986$, and in (c) and (f) it oscillates with a period $p = 1.82$, as measured for $b = 26$, $a = 4.97186$. The oscillation in $a(t) - a_c$ is shown as a black trace above each column (note the different vertical scales for $a(t) - a_c$ and concentration).

Random fields

A simple model of random noise was used to investigate the effect it may have on the Brusselator. The random fields were modelled by treating $a(t)$ as a sum of randomly oscillating components:

$$a(t) = a_c + A \sum_{i=1}^{N} \sin(\omega_i t + c_i), \tag{6.22}$$

where each ω_i is a random frequency in the range $0 \leq \omega_i \leq 30$, each c_i is a random phase in the range $0 \leq c_i \leq 2\pi$, N is the number of oscillating components (100 unless otherwise stated), and $A = 0.001$, with the parameters chosen such that the random oscillations have a similar standard deviation (~0.0071) to $a(t)$ in Figs. 6.7 and 6.9.

Clearly each time this simulation is run then the behaviour will be different, since each $a(t)$ will have different random components. The solutions for six different realisations of this model ($a_c = 4.97$, $b = 26$), can be seen in Fig. 6.10, often causing the system to switch back and forth between limit cycles, similar to the behaviour seen in Figs. 6.7 and 6.9. It is worth noting that in the simple method used here the oscillating components have infinite lifetimes, whereas instantaneously random noise, such as Gaussian noise, would not.

Discussion of effects of oscillating parameters 6.3.3

It has been shown in this chapter that the effect of a weak magnetic field on an oscillating system that follows Eq. (6.4) can be modelled by varying the parameter a in Eq. (6.6), corresponding to a field-dependence in one of the reaction rate constants. This modelling can be done without the need to explicitly evaluate the spin dynamics for the system. This relatively simple model has allowed us to explore whether the autocatalysis in the Brusselator system could lead to amplification of weak MFEs.

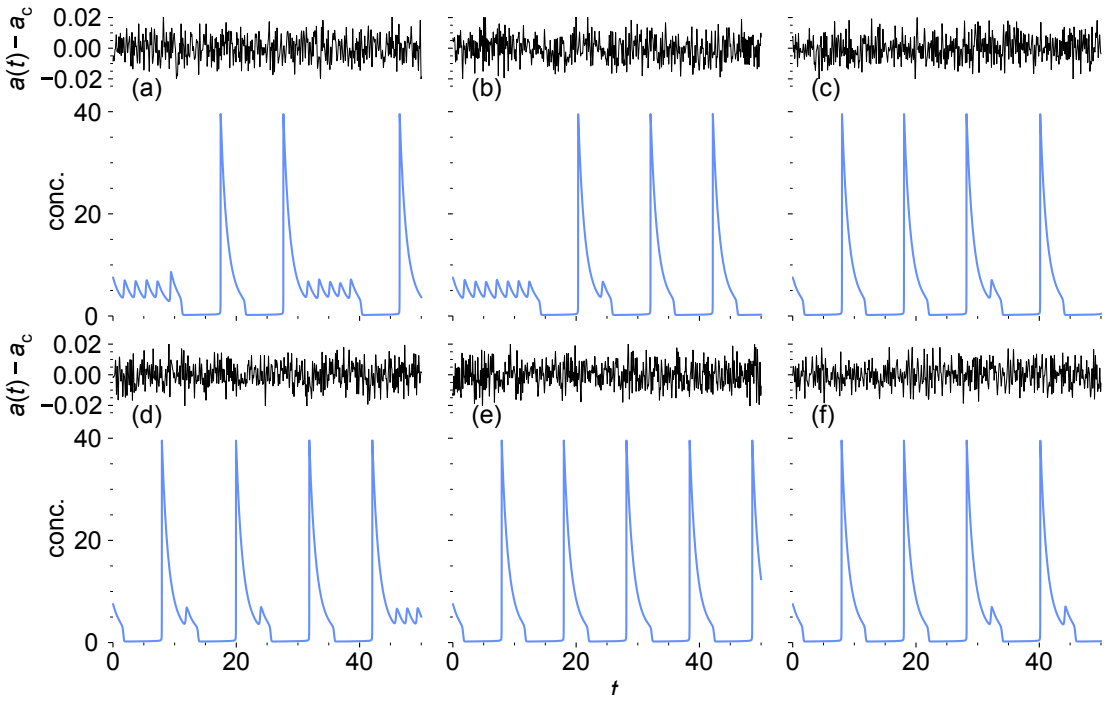

Figure 6.10 Concentration of x (blue) with $b = 26$ and an applied field causing $a(t)$ to vary randomly about $a_c = 4.97086$. The variation in $a(t) - a_c$ is shown as a black trace above each plot (note the different vertical scales for $a(t) - a_c$ and concentration).

Within this oscillating system we have shown that dramatic changes in the extent of oscillations can be brought about by small magnetically-induced changes in the rate constant for the initiation step in Eq. (6.4). It is likely that similar effects could equally well be observed if other steps in the Brusselator system of equations were magnetically sensitive, but a magnetically-sensitive initiation step seems a likely option; many photochemical reactions generate a magnetically sensitive radical pair in their initiation step, not least the magnetically sensitive flavin-tryptophan radical pair implicated in avian magnetoreception [15].

In particular, an especially large change in oscillation extent, known as a canard explosion, in the Brusselator for $1 < a \lesssim \sqrt{b-1}$ has been explored and reported here for the first time. In this canard region, we have shown that a small change in a can cause a dramatic change in oscillation extent. This change can be caused by a step-change in a static value of a (Fig. 6.5) or via an oscillation (Figs. 6.7, 6.9, and 6.10). One could imagine that oscillating fields may present better amplification

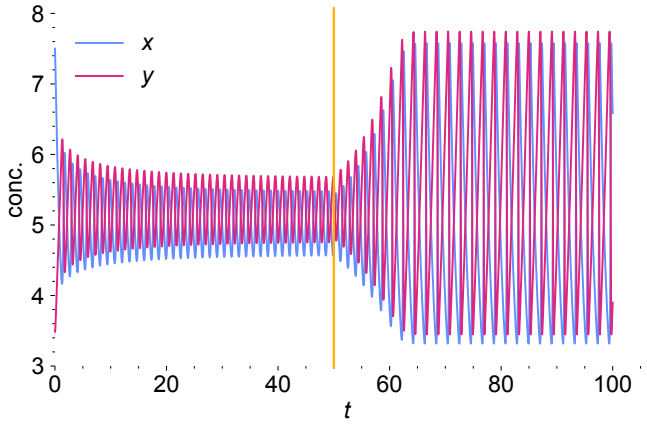

Figure 6.11 Concentrations of x (blue) and y (pink) with $b = 26$. Initially $a = 4.995$, and at $t = 50$ (indicated by the vertical line) the value of a is decreased to 4.971.

than a static jump due to (for instance) resonant modulation of a at the frequency of the chemical oscillation selectively driving this oscillation to a higher amplitude. This has not been observed for the Brusselator—sinusoidally oscillating fields exhibit similar magnitude amplification to a change in a static value of a—but could in principle be sought out in other chemical oscillator models [265, 266].

Even if the change in a does not span the canard we can still see substantial amplification effects, for instance the purple line corresponding to $b = 26$ in Fig. 6.5 still shows a strong non-linear increase in the size of oscillation extent even when a is decreased outside of the canard region. In the region $0.005 < \sqrt{b-1} - a < 0.029$, a decreases by 0.48% from 4.995 to 4.971 whereas the oscillation amplitude increases by ~230% (from ~1.2 units to ~4 units). This is shown more clearly in Fig. 6.11, which shows a marked increase in the size of the oscillations in x and y as a is decreased from 4.995 to 4.971. This amplification is in contrast to the behaviour when a is decreased by 0.48% from 5.050 to 5.026 (i.e. outside of the canard region), producing a corresponding 0.48% change in x (since $x = x_{ss} = a$ in this region).

No matter whether we are in the canard region or not, we have demonstrated that small relative changes in the magnetically sensitive rate constant can produce

far greater relative changes in the concentrations of the reaction intermediates. Within the framework we describe, tiny MFEs can indeed be amplified by this chemical oscillator.

Conclusions and further work 6.4

Could the theoretical work presented in this chapter be tested experimentally? It is not clear from the literature whether (bio)chemical oscillators exist that could show the amplification we have outlined. Strong magnetic field effects, with applied fields of ~100 mT, have been observed on the oscillating peroxide-oxidase reaction, which is made up of a minimum of between 10 and 15 elementary reactions, several of which produce or consume radicals—hence, the observed effects were attributed to a radical pair mechanism [267–269]. The effects of a magnetic field ($1\,\mathrm{mT} \leq B \leq 100\,\mathrm{mT}$) on two coupled[6] enzyme reactions, where one reaction step involves radical pair intermediates, have been modelled, showing some frequency-dependent effects [270].

The Belousov–Zhabotinsky (BZ) reaction is a well known chemical oscillator that involves multiple reaction steps, some of which may involve radicals of the form $BrO_x^{\bullet}$ [271], and which can also include paramagnetic metal ions. In the stirred BZ reaction the mixture changes colour on a timescale of seconds, and over time spots of different coloured reaction solution appear that develop into concentric circles/waves, resulting from coupling between autocatalysis and diffusion [234]. Changes in the velocity of this wavefront, when subjected to magnetic field gradient, have been attributed to magnetic convection [272–276], and similar effects have been observed in the reaction of a Co^{2+} complex with hydrogen peroxide [277–280]. In one study it was reported that low frequency electromagnetic fields (field strength between 5 μT and 30 μT with frequency up to 120 Hz) can change the oscillation frequency of the BZ reaction, with the effect attributed to an

[6] The product of each enzyme-catalysed reaction is the substrate of the other.

MFE on an electron transfer rate [281]. A second study over a wider range of field strengths and frequencies found no statistically significant effects [282]. Similarly, no statistically significant magnetic field effect was observed in a separate study of BZ oscillations catalysed by ferroin and cerium when a static field of 0.14 T was applied [283]. In none of these studies on, or related to, the BZ reaction has it been suggested that radical pairs are responsible for an observed MFE.

If a suitable oscillating (bio)chemical system with the potential for radical pair-dependent oscillations could be found then it may be possible to test whether an applied magnetic field affects the concentrations of reaction intermediates, especially if (a) the optical absorbance of the intermediates in solution differs considerably in a spectroscopically accessible region of the electromagnetic spectrum, and/or (b) the intermediates exhibit distinguishable fluorescence behaviour. Further, a simple initial test could be to use a permanent magnet to introduce a step-change in the applied magnetic field, in a similar fashion to Section 6.3.1 [283]. Given the results in the literature reported above, we would suggest that the peroxidase–oxidase oscillator in references [267–269] would be the most appropriate system in which the kind of MFE we have discussed may be sought.

In this chapter we have demonstrated that small changes in a magnetically-sensitive rate constant can introduce dramatically larger changes in the reaction intermediate concentrations in a model of oscillating chemical reactions. Specifically considering the Brusselator system of equations for an oscillating set of reactions, we have modelled this magnetic sensitivity using a simple set of coupled differential equations with a varying parameter, and thus explored the size of this amplification effect as the parameter varies by step-changes, sinusoidal oscillation, or randomly. We have shown that the canard explosion in the Brusselator system facilitates particularly large amplification, but that other less restrictive regions of parameter space can also exhibit strong amplification effects.

7 Conclusion

In this thesis, quantum mechanical calculations have been used to explore the nuclear and electronic spin dynamics of molecular processes that may be of biological importance [1–4]. There are several software packages that have been developed for simulating spin systems such as those considered here, some of which have been relatively recently introduced [284–286]. Many of the tools in these kinds of packages focus on simulating NMR and ESR spectra (although not all, see references [33, 286] for instance), whereas a theme throughout this thesis has been taking a broad view of the possible interactions within a system, evaluating which of these will most critically affect the dynamic behaviour of interest, and deriving conditions on the corresponding molecular environment and behaviour that could potentially be probed experimentally. Here we summarise the main conclusions of this work, wherein all of the contributions mentioned below were performed by the author unless otherwise stated or cited.

In Chapter 3 we showed that entanglement between the ^{31}P nuclei in two spatially separated $Ca_9(PO_4)_6$ molecules will oscillate on a timescale of seconds due to the J-coupling between the nuclei in each molecule. This type of entanglement is suggested to be important in a theory of neural processing [42–44], and these oscillations mean that for much of the time there is no bipartite entanglement between the two nuclei, although it may be possible that entanglement between more than two nuclei develops. By using Redfield theory [149, 152] to model the intramolecular dipolar coupling for a pair of Posner molecules we were able to set a strict upper lifetime for singlet entanglement of 37 minutes [1]. We were

able to take advantage of the lack of interactions between the two molecules (each of which contains six spin-1/2 nuclei) to modify the method of calculating the relaxation superoperator, developing a technique that uses correlation tensors similar to those in references [143, 144] to calculate relaxation rate constants for the entangled singlet state of interest. This method could potentially be used to calculate the spin dynamics of other similar two-molecule entangled states, or singlet-entangled states that may arise in certain NMR experiments [37]. We outlined other relaxation routes that may operate for a pair of Posner molecules, suggesting that the relaxation lifetime of these entangled states *in vivo*, if it were possible to prepare them, would likely be shorter yet than our strict upper limit.

In Chapter 4 we modelled the spin dynamics of a flavin-superoxide radical pair more thoroughly than has previously been done when considering it as part of a potential geomagnetic sensor in migratory birds [85–87, 182, 183]. By calculating the anisotropy of the singlet yield, which we took to be indicative of compass precision, we were able to derive a strict set of conditions that must be met for a flavin-superoxide radical pair to operate *in vivo* [2]. In particular, the strong spin–orbit coupling in this radical [195] must be at least partially quenched, with slow rotational motion of the superoxide radical constrained by a relatively strong ligand field. Therefore, we suggested that the flavin-superoxide radical pair must remain speculative until and unless a binding site for superoxide radicals in a cryptochrome can be found that satisfies these criteria; or oxygen-dependent MFEs are demonstrated in cryptochromes; or a magnetic isotope effect on the rate of flavin oxidation by $^{16}O_2/^{17}O_2$ is demonstrated. In the absence of results such as these, the flavin-tryptophan radical pair more commonly cited remains the most likely candidate for an avian magnetoreceptor [15].

In Chapter 5 we considered the magnetic field-dependent reduction of CO_2 in an electrocatalytic system [76], and were able to demonstrate that the Δg mechanism of singlet–triplet interconversion that the experimental study's authors

suggested was responsible for the MFE cannot, in fact, account for it. By modelling a variety of relaxation mechanisms, we showed that the Δg and hyperfine interactions of the radicals, alongside relaxation resulting from the anisotropic g-tensor in $CO_2^{\bullet -}$, can account qualitatively for the experimental MFE [3]. As in Chapter 4, we were able to put a strong set of constraints on the rate constants associated with the reaction scheme proposed in [76], suggesting that the rate of formation of formate ions from singlet radical pairs should be significantly faster than the translational diffusion rate of the reactants, and that the rotational correlation time for the $CO_2^{\bullet -}$ radical should be of a fairly typical magnitude for an aqueous solution. This indicates that the reactants must be relatively loosely adsorbed at the electrode. We have suggested that an isotopic substitution of either ^{2}H for ^{1}H or ^{13}C for ^{12}C could be used to test the proposed reaction scheme and our modelling of it.

In Chapter 6 we explored a theoretical model of a chemical oscillator [90], using it to demonstrate that small changes in a magnetically-sensitive rate constant for the initiation step in this system of reactions can introduce dramatically larger changes in the extent of reaction-intermediate concentration oscillations. The step-change in these oscillations that occurs as a result of a small change in one of the system parameters is known as a canard [91, 243]. Following the initial discovery of a canard in the Brusselator system of equations around twenty years ago [248, 249], we have gone on to fully explore and characterise it for the first time [4]. We explored the size of this potential amplification effect by varying the system parameter representing the magnetic field via step-changes, sinusoidal oscillations, and random changes, and showed that all three can cause strong amplification effects. We also noted that large amplification effects can be seen outside of the canard explosion regime. Finally, we have suggested a biological system where this amplification could potentially be found experimentally [267–269].

Bibliography

[1] T. C. Player and P. J. Hore. Posner qubits: spin dynamics of entangled $Ca_9(PO_4)_6$ molecules and their role in neural processing. *Journal of The Royal Society Interface*, **15** (147) 20180494, 2018.

[2] T. C. Player and P. J. Hore. Viability of superoxide-containing radical pairs as magnetoreceptors. *Journal of Chemical Physics*, **151** (22) 225101, 2019.

[3] T. C. Player and P. J. Hore. Source of magnetic field effects on the electrocatalytic reduction of CO_2. *Journal of Chemical Physics*, **153** (8) 084303, 2020.

[4] T. C. Player, E. D. Baxter, S. Allatt, and P. J. Hore. Amplification of weak magnetic field effects on oscillating reactions. *Scientific Reports*, **11** (1) 1–9, 2021.

[5] J. R. R. Tolkien. *The Fellowship of the Ring*. George Allen & Unwin, London, 1954.

[6] E. Schrödinger. *What is life? The Physical Aspect of the Living Cell*. Cambridge University Press, Cambridge, 1945.

[7] F. H. Crick and J. D. Watson. Molecular structure of nucleic acids. *Nature*, **171** 737–738, 1953.

[8] B. Maddox. The double helix and the "wronged heroine". *Nature*, **421** (6921) 407–408, 2003.

[9] P. Fatt and B. Katz. Spontaneous subthreshold activity at motor nerve endings. *The Journal of Physiology*, **117** (1) 109–128, 1952.

[10] W. Gilbert. *De Magnete, Magneticisque Corporibus, et de Magno Magnete Tellure (On the Magnet and Magnetic Bodies, and on That Great Magnet the Earth)*. Peter Short, London, 1600.

[11] J. McFadden and J. Al-Khalili. The origins of quantum biology. *Proceedings of the Royal Society A: Mathematical, Physical and Engineering Sciences*, **474** (2220) , 2018.

[12] Y. Kim, F. Bertagna, E. M. D'Souza, D. J. Heyes, L. O. Johannissen, E. T. Nery, A. Pantelias, A. Sanchez-Pedreño Jimenez, L. Slocombe, M. G. Spencer, J. Al-Khalili, G. S. Engel, S. Hay, S. M. Hingley-Wilson, K. Jeevaratnam, A. R. Jones, D. R. Kattnig, R. Lewis, M. Sacchi, N. S. Scrutton, S. R. P. Silva, and J. McFadden. Quantum Biology: An Update and Perspective. *Quantum Reports*, **3** (1) 1–48, 2021.

[13] F. Caruso, A. W. Chin, A. Datta, S. F. Huelga, and M. B. Plenio. Highly efficient energy excitation transfer in light-harvesting complexes: The fundamental role of noise-assisted transport. *Journal of Chemical Physics*, **131** (10) 105106, 2009.

[14] G. Wald, P. K. Brown, and I. R. Gibbons. The problem of visual excitation. *Journal of the Optical Society of America*, **53** (1) 20–35, 1963.

[15] P. J. Hore and H. Mouritsen. The radical-pair mechanism of magnetoreception. *Annual Review of Biophysics*, **45** 299–344, 2016.

[16] L. Turin. A spectroscopic mechanism for primary olfactory reception. *Chemical Senses*, **21** (6) 773–791, 1996.

[17] W. Pauli. Über den Einfluß der Geschwindigkeitsabhängigkeit der Elektronenmasse auf den Zeemaneffekt. *Zeitschrift für Physik*, **31** (1) 373–385, 1925.

[18] W. Gerlach and O. Stern. Der experimentelle Nachweis der Richtungsquantelung im Magnetfeld. *Zeitschrift für Physik*, **9** (1) 349–352, 1922.

[19] G. E. Uhlenbeck and S. Goudsmit. Ersetzung der Hypothese vom unmechanischen Zwang durch eine Forderung bezüglich des inneren Verhaltens jedes einzelnen Elektrons. *Die Naturwissenschaften*, **13** (47) 953–954, 1925.

[20] S. A. Goudsmit. De ontdekking van de electronenrotatie (translated by J. H. van der Waals). *Nederlands Tijdschrift voor Natuurkunde*, **37** 386, 1971.

[21] P. W. Atkins, J. de Paula, and J. Keeler. *Atkins' Physical Chemistry*. Oxford University Press, Oxford, 2017.

[22] R. K. Harris. *Nuclear magnetic resonance spectroscopy: a physicochemical view*. Pitman, London, 1983.

[23] G. B. Field, W. B. Somerville, and K. Dressler. Hydrogen molecules in astronomy. *Annual Review of Astronomy and Astrophysics*, **4** (1) 207–244, 1966.

[24] P. J. Hore. *Nuclear Magnetic Resonance*. Oxford University Press, Oxford, 1995.

[25] R. F. Butler. *Paleomagnetism: Magnetic Domains to Geologic Terranes*. Blackwell Scientific Publications, Boston, 1992.

[26] P. Alken, E. Thébault, C. D. Beggan, H. Amit, J. Aubert, J. Baerenzung, T. N. Bondar, W. J. Brown, S. Califf, A. Chambodut, A. Chulliat, G. A. Cox, C. C. Finlay, A. Fournier, N. Gillet, A. Grayver, M. D. Hammer, M. Holschneider, L. Huder, G. Hulot, T. Jager, C. Kloss, M. Korte, W. Kuang, A. Kuvshinov, B. Langlais, J.-M. Léger, V. Lesur, P. W. Livermore, F. J. Lowes, S. Macmillan, W. Magnes, M. Mandea, S. Marsal, J. Matzka, M. C. Metman, T. Minami, A. Morschhauser, J. E. Mound, M. Nair, S. Nakano, N. Olsen, F. J. Pavón-Carrasco, V. G. Petrov, G. Ropp, M. Rother, T. J. Sabaka, S. Sanchez, D. Saturnino, N. R. Schnepf, X. Shen, C. Stolle, A. Tangborn, L. Tøffner-Clausen, H. Toh, J. M. Torta, J. Varner, F. Vervelidou, P. Vigneron, I. Wardinski, J. Wicht, A. Woods, Y. Yang, Z. Zeren, and B. Zhou. International Geomagnetic Reference Field: the thirteenth generation. *Earth, Planets and Space*, **73** 49, 2021.

[27] R. E. Gill, T. L. Tibbitts, D. C. Douglas, C. M. Handel, D. M. Mulcahy, J. C. Gottschalck, N. Warnock, B. J. McCaffery, P. F. Battley, and T. Piersma. Extreme endurance flights by landbirds crossing the Pacific Ocean: Ecological corridor rather than barrier? *Proceedings of the Royal Society B: Biological Sciences*, **276** (1656) 447–457, 2009.

[28] S. A. Shaffer, Y. Tremblay, H. Weimerskirch, D. Scott, D. R. Thompson, P. M. Sagar, H. Moller, G. A. Taylor, D. G. Foley, B. A. Block, and D. P. Costa. Migratory shearwaters integrate oceanic resources across the Pacific Ocean in an endless summer. *Proceedings of the National Academy of Sciences of the United States of America*, **103** (34) 12799–12802, 2006.

[29] N. Chernetsov, A. Pakhomov, D. Kobylkov, D. Kishkinev, R. A. Holland, and H. Mouritsen. Migratory Eurasian reed warblers can use magnetic declination to solve the longitude problem. *Current Biology*, **27** (17) 2647–2651, 2017.

[30] P. Berthold, W. V. Bossche, W. Fiedler, E. Gorney, M. Kaatz, Y. Leshem, E. Nowak, and U. Querner. Der Zug des Weißstorchs (Ciconia ciconia): eine besondere Zugform auf Grund neuer Ergebnisse. *Journal für Ornithologie*, **142** (1) 73, 2001.

[31] Wikimedia Commons. Creative Commons Licence, 2021.

[32] M. J. Perkins. *Radical Chemistry*. Ellis Horwood series in organic chemistry. Ellis Horwood, New York, London, 1994.

[33] P. J. Hore, K. L. Ivanov, and M. R. Wasielewski. Spin chemistry. *Journal of Chemical Physics*, **152** (12) 120401, 2020.

[34] U. E. Steiner and T. Ulrich. Magnetic field effects in chemical kinetics and related phenomena. *Chemical Reviews*, **89** (1) 51–147, 1989.

[35] K. A. McLauchlan and U. E. Steiner. The spin-correlated radical pair as a reaction intermediate. *Molecular Physics*, **73** (2) 241–263, 1991.

[36] H. Hayashi. *Introduction to Dynamic Spin Chemistry*. World Scientific Publisher, Singapore, 2004.

[37] M. H. Levitt. Singlet nuclear magnetic resonance. *Annual Review of Physical Chemistry*, **63** 89–105, 2012.

[38] S. Hameroff and R. Penrose. Consciousness in the universe: A review of the 'Orch OR' theory. *Physics of Life Reviews*, **11** (1) 39–78, 2014.

[39] M. Tegmark. Importance of quantum decoherence in brain processes. *Physical Review E - Statistical Physics, Plasmas, Fluids, and Related Interdisciplinary Topics*, **61** (4) 4194–4206, 2000.

[40] C. Koch and K. Hepp. Quantum mechanics in the brain. *Nature*, **440** (7084) 611–612, 2006.

[41] K. Hepp. Coherence and decoherence in the brain. *Journal of Mathematical Physics*, **53** (9) 095222, 2012.

[42] M. P. Fisher. Quantum cognition: The possibility of processing with nuclear spins in the brain. *Annals of Physics*, **362** 593–602, 2015.

[43] C. P. Weingarten, P. M. Doraiswamy, and M. P. Fisher. A new spin on neural processing: Quantum cognition. *Frontiers in Human Neuroscience*, **10** 541, 2016.

[44] M. P. Fisher. Are we quantum computers, or merely clever robots? *International Journal of Modern Physics B*, **31** 7, 2017.

[45] A. Ettenberg, K. Ayala, J. T. Krug, L. Collins, M. S. Mayes, and M. P. Fisher. Differential effects of lithium isotopes in a ketamine-induced hyperactivity model of mania. *Pharmacology Biochemistry and Behavior*, **190** 172875, 2020.

[46] R. Chen, N. Li, H. Qian, R. H. Zhao, and S. H. Zhang. Experimental evidence refuting the assumption of phosphorus-31 nuclear-spin entanglement-mediated consciousness. *Journal of Integrative Neuroscience*, **19** (4) 595–600, 2020.

[47] M. W. Swift, C. G. Van De Walle, and M. P. Fisher. Posner molecules: From atomic structure to nuclear spins. *Physical Chemistry Chemical Physics*, **20** (18) 12373–12380, 2018.

[48] D. G. Gorenstein. *Phosphorous-31 NMR: Principles and Applications*. Elsevier Inc., Orlando, 2012.

[49] T. P. Harrison. Birds in the Moon. *Isis*, **45** (4) 323–330, 1954.

[50] A. Lee. The Great Migration Mystery. *History Today*, 2020.

[51] G. C. Nordmann, T. Hochstoeger, and D. A. Keays. Unsolved mysteries: Magnetoreception—A sense without a receptor. *PLoS Biology*, **15** (10) e2003234, 2017.

[52] H. Mouritsen. Long-distance navigation and magnetoreception in migratory animals. *Nature*, **558** (7708) 50–59, 2018.

[53] K. J. Lohmann, J. T. Hester, and C. M. Lohmann. Long-distance navigation in sea turtles. *Ethology Ecology and Evolution*, **11** (1) 1–23, 1999.

[54] M. J. Freake, R. Muheim, and J. B. Phillips. Magnetic maps in animals: A theory comes of age? *Quarterly Review of Biology*, **81** (4) 327–347, 2006.

[55] K. J. Lohmann, C. M. Lohmann, and C. S. Endres. The sensory ecology of ocean navigation. *Journal of Experimental Biology*, **211** (11) 1719–1728, 2008.

[56] R. A. Holland. True navigation in birds: From quantum physics to global migration. *Journal of Zoology*, **293** (1) 1–15, 2014.

[57] S. M. Reppert and J. C. de Roode. Demystifying Monarch Butterfly Migration. *Current Biology*, **28** (17) R1009–R1022, 2018.

[58] J. L. Kirschvink, M. M. Walker, and C. E. Diebel. Magnetite-based magnetoreception. *Current Opinion in Neurobiology*, **11** (4) 462–467, 2001.

[59] K. Schulten, C. E. Swenberg, and A. Weller. A biomagnetic sensory mechanism based on magnetic field modulated coherent electron spin motion. *Zeitschrift fur Physikalische Chemie*, **111** (1) 1–5, 1978.

[60] T. Ritz, S. Adem, and K. Schulten. A model for photoreceptor-based magnetoreception in birds. *Biophysical Journal*, **78** (2) 707–718, 2000.

[61] C. T. Rodgers and P. J. Hore. Chemical magnetoreception in birds: The radical pair mechanism. *Proceedings of the National Academy of Sciences of the United States of America*, **106** (2) 353–360, 2009.

[62] M. Liedvogel and H. Mouritsen. Cryptochromes—A potential magnetoreceptor: what do we know and what do we want to know? *Journal of the Royal Society Interface*, **7** S147–S162, 2010.

[63] K. Maeda, A. J. Robinson, K. B. Henbest, H. J. Hogben, T. Biskup, M. Ahmad, E. Schleicher, S. Weber, C. R. Timmel, and P. J. Hore. Magnetically sensitive light-induced reactions in cryptochrome are consistent with its proposed role as a magnetoreceptor. *Proceedings of the National Academy of Sciences of the United States of America*, **109** (13) 4774–4779, 2012.

[64] R. Wiltschko and W. Wiltschko. Magnetoreception in birds. *Journal of the Royal Society Interface*, **16** 20190295, 2019.

[65] J. Xu, L. E. Jarocha, T. Zollitsch, M. Konowalczyk, K. B. Henbest, S. Richert, M. J. Golesworthy, J. Schmidt, V. Déjean, D. J. C. Sowood, M. Bassetto, J. Luo, J. R. Walton, J. Fleming, Y. Wei, T. L. Pitcher, G. Moise, M. Herrmann, H. Yin, H. Wu, R. Bartölke, S. J. Käsehagen, S. Horst, G. Dautaj, P. D. F. Murton, A. S. Gehrckens, Y. Chelliah, J. S. Takahashi, K.-W. Koch, S. Weber, I. A. Solov'yov, C. Xie, S. R. Mackenzie, C. R. Timmel, H. Mouritsen, and P. J. Hore. Magnetic sensitivity of cryptochrome 4 from a migratory songbird. *Nature*, **594** (7864) 535–540, 2021.

[66] H. Mouritsen and P. J. Hore. The magnetic retina: Light-dependent and trigeminal magnetoreception in migratory birds. *Current Opinion in Neurobiology*, **22** (2) 343–352, 2012.

[67] W. Wiltschko, U. Munro, H. Ford, and R. Wiltschko. Red light disrupts magnetic orientation of migratory birds. *Nature*, **364** (6437) 525–527, 1993.

[68] W. Wiltschko and R. Wiltschko. The effect of yellow and blue light on magnetic compass orientation in European robins, Erithacus rubecula. *Journal of Comparative Physiology - A Sensory, Neural, and Behavioral Physiology*, **184** (3) 295–299, 1999.

[69] C. Nießner, S. Denzau, K. Stapput, M. Ahmad, L. Peichl, W. Wiltschko, and R. Wiltschko. Magnetoreception: Activated cryptochrome 1a concurs with magnetic orientation in birds. *Journal of the Royal Society Interface*, **10** 20130638, 2013.

[70] Y. Zhang, C. Liang, J. Wu, H. Liu, B. Zhang, Z. Jiang, S. Li, and P. Xu. Recent advances in magnetic field-enhanced electrocatalysis. *ACS Applied Energy Materials*, **3** (11) 10303–10316, 2020.

[71] L. M. Monzon and J. M. Coey. Magnetic fields in electrochemistry: The Lorentz force. A mini-review. *Electrochemistry Communications*, **42** 38–41, 2014.

[72] K. T. Nam and S. Park. Electrochemical cell in the brain. *Nature Nanotechnology*, **15** (8) 625–626, 2020.

[73] J. Park, K. Jin, A. Sahasrabudhe, P. H. Chiang, J. H. Maalouf, F. Koehler, D. Rosenfeld, S. Rao, T. Tanaka, T. Khudiyev, Z. J. Schiffer, Y. Fink, O. Yizhar, K. Manthiram, and P. Anikeeva. In situ electrochemical generation of nitric oxide for neuronal modulation. *Nature Nanotechnology*, **15** (8) 690–697, 2020.

[74] M. S. George and J. J. Taylor. Theoretical Basis for Transcranial Magnetic Stimulation. In *A Clinical Guide to Transcranial Magnetic Stimulation*, pages 1–7. Oxford University Press, 2014.

[75] B. Li, J. P. Virtanen, A. Oeltermann, C. Schwarz, M. A. Giese, U. Ziemann, and A. Benali. Lifting the veil on the dynamics of neuronal activities evoked by transcranial magnetic stimulation. *eLife*, **6** e30552, 2017.

[76] H. Pan, X. Jiang, X. Wang, Q. Wang, M. Wang, and Y. Shen. Effective magnetic field regulation of the radical pair spin states in electrocatalytic CO_2 reduction. *Journal of Physical Chemistry Letters*, **11** (1) 48–53, 2020.

[77] S. Solomon, G. K. Plattner, R. Knutti, and P. Friedlingstein. Irreversible climate change due to carbon dioxide emissions. *Proceedings of the National Academy of Sciences of the United States of America*, **106** (6) 1704–1709, 2009.

[78] W. Wang, S. Wang, X. Ma, and J. Gong. Recent advances in catalytic hydrogenation of carbon dioxide. *Chemical Society Reviews*, **40** (7) 3703–3727, 2011.

[79] E. V. Kondratenko, G. Mul, J. Baltrusaitis, G. O. Larrazábal, and J. Pérez-Ramírez. Status and perspectives of CO_2 conversion into fuels and chemicals by catalytic, photocatalytic and electrocatalytic processes. *Energy and Environmental Science*, **6** (11) 3112–3135, 2013.

[80] A. M. Appel, J. E. Bercaw, A. B. Bocarsly, H. Dobbek, D. L. Dubois, M. Dupuis, J. G. Ferry, E. Fujita, R. Hille, P. J. Kenis, C. A. Kerfeld, R. H. Morris, C. H. Peden, A. R. Portis, S. W. Ragsdale, T. B. Rauchfuss, J. N. Reek, L. C. Seefeldt, R. K. Thauer, and G. L. Waldrop. Frontiers, opportunities, and challenges in biochemical and chemical catalysis of CO_2 fixation. *Chemical Reviews*, **113** (8) 6621–6658, 2013.

[81] S. N. Habisreutinger, L. Schmidt-Mende, and J. K. Stolarczyk. Photocatalytic reduction of CO_2 on TiO_2 and other semiconductors. *Angewandte Chemie - International Edition*, **52** (29) 7372–7408, 2013.

[82] M. Aresta, A. Dibenedetto, and A. Angelini. Catalysis for the valorization of exhaust carbon: from CO_2 to chemicals, materials, and fuels. Technological use of CO_2. *Chemical Reviews*, **114** (3) 1709–1742, 2014.

[83] G. A. Ozin. Throwing new light on the reduction of CO_2. *Advanced Materials*, **27** (11) 1957–1963, 2015.

[84] D. D. Zhu, J. L. Liu, and S. Z. Qiao. Recent advances in inorganic heterogeneous electrocatalysts for reduction of carbon dioxide. *Advanced Materials*, **28** (18) 3423–3452, 2016.

[85] I. A. Solov'yov and K. Schulten. Magnetoreception through cryptochrome may involve superoxide. *Biophysical Journal*, **96** (12) 4804–4813, 2009.

[86] H. J. Hogben, O. Efimova, N. Wagner-Rundell, C. R. Timmel, and P. J. Hore. Possible involvement of superoxide and dioxygen with cryptochrome in avian magnetoreception: Origin of Zeeman resonances observed by in vivo EPR spectroscopy. *Chemical Physics Letters*, **480** (1-3) 118–122, 2009.

[87] P. Müller and M. Ahmad. Light-activated cryptochrome reacts with molecular oxygen to form a flavin-superoxide radical pair consistent with magnetoreception. *Journal of Biological Chemistry*, **286** (24) 21033–21040, 2011.

[88] P. Mondal and M. Huix-Rotllant. Theoretical insights into the formation and stability of radical oxygen species in cryptochromes. *Physical Chemistry Chemical Physics*, **21** (17) 8874–8882, 2019.

[89] C. T. Rodgers. Magnetic field effects in chemical systems. *Pure and Applied Chemistry*, **81** (1) 19–43, 2009.

[90] I. Prigogine and R. Lefever. Symmetry breaking instabilities in dissipative systems. II. *Journal of Chemical Physics*, **48** (4) 1695–1700, 1968.

[91] E. Benoit, J. L. Callot, F. Diener, and M. Diener. Chasse au canard (première partie). *Collectanea Mathematica*, **32** 37–119, 1981.

[92] S. Sondheim, G. Furth, and R. H. Noeltner. Company: A Musical Comedy, 1970.

[93] P. A. Dirac. A new notation for quantum mechanics. *Mathematical Proceedings of the Cambridge Philosophical Society*, **35** (3) 416–418, 1939.

[94] R. P. Feynman, R. B. Leighton, and M. L. Sands. *Feynman Lectures on Physics. Vol. II: Mainly Electromagnetism and Matter*. Addison-Wesley, Reading, 1964.

[95] P. J. Hore, J. A. Jones, and S. Wimperis. *NMR: The Toolkit*. Oxford University Press, Oxford, 2000.

[96] S. Worster. *Order, Motion and Relaxation in Radical Pair Compass Magnetoreception*. PhD thesis, University of Oxford, 2018.

[97] A. Einstein, B. Podolsky, and N. Rosen. Can quantum-mechanical description of physical reality be considered complete? *Physical Review*, **47** (10) 777–780, 1935.

[98] R. Horodecki, P. Horodecki, M. Horodecki, and K. Horodecki. Quantum entanglement. *Reviews of Modern Physics*, **81** (2) 865–942, 2009.

[99] W. K. Wootters. Entanglement of formation of an arbitrary state of two qubits. *Physical Review Letters*, **80** (10) 2245–2248, 1998.

[100] R. Kubo. A stochastic theory of line shape. *Advances in Chemical Physics*, **15** 101–127, 1969.

[101] R. Kubo. Statistical physics of random systems. *Journal of the Physical Society of Japan*, **26** (S) 1–5, 1969.

[102] J. H. Freed, G. V. Bruno, and C. F. Polnaszek. Electron spin resonance line shapes and saturation in the slow motional tegime. *Journal of Physical Chemistry*, **75** (22) 3385–3398, 1989.

[103] J. C. Lau, N. Wagner-Rundell, C. T. Rodgers, N. J. Green, and P. J. Hore. Effects of disorder and motion in a radical pair magnetoreceptor. *Journal of the Royal Society Interface*, **7** S257–S264, 2010.

[104] M. H. Levitt. *Spin Dynamics*. Wiley, Chichester, 2001.

[105] A. D. Buckingham and I. Love. Theory of the anisotropy of nuclear spin coupling. *Journal of Magnetic Resonance (1969)*, **2** (3) 338–351, 1970.

[106] D. L. Bryce and R. E. Wasylishen. Evaluation of the influence of anisotropic indirect nuclear spin-spin coupling tensors on effective residual dipolar couplings for model peptides, 2003.

[107] N. M. Atherton. *Principles of Electron Spin Resonance*. Ellis Horwood, Chichester, 1993.

[108] O. Efimova and P. J. Hore. Role of exchange and dipolar interactions in the radical pair model of the avian magnetic compass. *Biophysical Journal*, **94** (5) 1565–1574, 2008.

[109] I. V. Khudyakov, Y. A. Serebrennikov, and N. J. Turro. Spin–orbit coupling in free-radical reactions: On the way to heavy elements. *Chemical Reviews*, **93** (1) 537–570, 1993.

[110] J. A. Jones and P. J. Hore. Spin-selective reactions of radical pairs act as quantum measurements. *Chemical Physics Letters*, **488** (1-3) 90–93, 2010.

[111] I. K. Kominis. Quantum Zeno effect explains magnetic-sensitive radical-ion-pair reactions. *Physical Review E – Statistical, Nonlinear, and Soft Matter Physics*, **80** (5) 056115, 2009.

[112] T. P. Fay. *Quantum Master Equations for Spin Chemistry*. PhD thesis, University of Oxford, 2020.

[113] R. C. Johnson and R. E. Merrifield. Effects of magnetic fields on the mutual annihilation of triplet excitons in anthracene crystals. *Physical Review B*, **1** (2) 896–902, 1970.

[114] R. Haberkorn. Density matrix description of spin-selective radical pair reactions. *Molecular Physics*, **32** (5) 1491–1493, 1976.

[115] D. Lavalette, C. Tétreau, M. Tourbez, and Y. Blouquit. Microscopic viscosity and rotational diffusion of proteins in a macromolecular environment. *Biophysical Journal*, **76** (5) 2744–2751, 1999.

[116] A. D. McNaught, A. Wilkinson, and S. Chalk. *IUPAC. Compendium of Chemical Terminology, 2nd ed. (the "Gold Book")*. Blackwell Scientific Publications, Oxford, 1997.

[117] C. R. Timmel, F. Cintolesi, B. Brocklehurst, and P. J. Hore. Model calculations of magnetic field effects on the recombination reactions of radicals with anisotropic hyperfine interactions. *Chemical Physics Letters*, **334** (4-6) 387–395, 2001.

[118] J. Luo and P. J. Hore. Chiral-induced spin selectivity in the formation and recombination of radical pairs: cryptochrome magnetoreception and EPR detection. *New Journal of Physics*, **23** 043032, 2021.

[119] K. W. Lieberman, G. J. Alexander, and P. Stokes. Dissimilar effects of lithium isotopes on motility in rats. *Pharmacology, Biochemistry and Behavior*, **10** (6) 933–935, 1979.

[120] J. A. Sechzer, K. W. Lieberman, G. J. Alexander, D. Weidman, and P. E. Stokes. Aberrant parenting and delayed offspring development in rats exposed to lithium. *Biological Psychiatry*, **21** (13) 1258–1266, 1986.

[121] F. W. Wehrli. Temperature-dependent spin-lattice relaxation of ^{6}Li in aqueous lithium chloride. *Journal of Magnetic Resonance (1969)*, **23** (3) 527–532, 1976.

[122] D. Sundholm, P. Pyykkö, L. Laaksonen, and A. J. Sadlej. Nuclear quadrupole moment of lithium from combined fully numerical and discrete basis-set calculations on LiH. *Chemical Physics Letters*, **112** (1) 1–9, 1984.

[123] H. Zadeh-Haghighi and C. Simon. Entangled radicals may explain lithium effects on hyperactivity. *arXiv*, page 2103.11057, 2021.

[124] M. P. Fisher and L. Radzihovsky. Quantum indistinguishability in chemical reactions. *Proceedings of the National Academy of Sciences of the United States of America*, **115** (20) E4551–E4558, 2018.

[125] N. Yunger Halpern and E. Crosson. Quantum information in the Posner model of quantum cognition. *Annals of Physics*, **407** 92–147, 2019.

[126] N. P. Franks. General anaesthesia: From molecular targets to neuronal pathways of sleep and arousal. *Nature Reviews Neuroscience*, **9** (5) 370–386, 2008.

[127] A. S. Posner and F. Betts. Synthetic amorphous calcium phosphate and its relation to bone mineral structure. *Accounts of Chemical Research*, **8** 273–281, 1975.

[128] M. I. Kay, R. A. Young, and A. S. Posner. Crystal structure of hydroxyapatite. *Nature*, **204** (4963) 1050–1052, 1964.

[129] X. Yin and M. J. Stott. Biological calcium phosphates and Posner's cluster. *Journal of Chemical Physics*, **118** (8) 3717–3723, 2003.

[130] A. Dey, P. H. Bomans, F. A. Müller, J. Will, P. M. Frederik, G. De With, and N. A. Sommerdijk. The role of prenucleation clusters in surface-induced calcium phosphate crystallization. *Nature Materials*, **9** (12) 1010–1014, 2010.

[131] L. Wang, S. Li, E. Ruiz-Agudo, C. V. Putnis, and A. Putnis. Posner's cluster revisited: Direct imaging of nucleation and growth of nanoscale calcium phosphate clusters at the calcite-water interface. *CrystEngComm*, **14** (19) 6252–6256, 2012.

[132] G. Mancardi, C. E. Hernandez Tamargo, D. Di Tommaso, and N. H. De Leeuw. Detection of Posner's clusters during calcium phosphate nucleation: A molecular dynamics study. *Journal of Materials Chemistry B*, **5** (35) 7274–7284, 2017.

[133] G. Treboux, P. Layrolle, N. Kanzaki, K. Onuma, and A. Ito. Existence of posner's cluster in vacuum. *Journal of Physical Chemistry A*, **104** (21) 5111–5114, 2000.

[134] G. Pileio. Relaxation theory of nuclear singlet states in two spin-½ systems. *Progress in Nuclear Magnetic Resonance Spectroscopy*, **56** (3) 217–231, 2010.

[135] M. Carravetta, O. G. Johannessen, and M. H. Levitt. Beyond the T_1 limit: Singlet nuclear spin states in low magnetic fields. *Physical Review Letters*, **92** 153003, 2004.

[136] M. Carravetta and M. H. Levitt. Theory of long-lived nuclear spin states in solution nuclear magnetic resonance. I. Singlet states in low magnetic field. *The Journal of Chemical Physics*, **122** (21) 214505, 2005.

[137] G. Pileio, M. Carravetta, E. Hughes, and M. H. Levitt. The long-lived nuclear singlet state of ^{15}N-nitrous oxide in solution. *Journal of the American Chemical Society*, **130** (38) 12582–12583, 2008.

[138] P. R. Vasos, A. Comment, R. Sarkar, P. Ahuja, S. Jannin, J. P. Ansermet, J. A. Konter, P. Hautle, B. Van Den Brandt, and G. Bodenhausen. Long-lived states to sustain hyperpolarized magnetization. *Proceedings of the National Academy of Sciences of the United States of America*, **106** (44) 18469–18473, 2009.

[139] G. Pileio, M. Carravetta, and M. H. Levitt. Storage of nuclear magnetization as long-lived singlet order in low magnetic field. *Proceedings of the National Academy of Sciences of the United States of America*, **107** (40) 17135–17139, 2010.

[140] M. C. Tayler and M. H. Levitt. Singlet nuclear magnetic resonance of nearly-equivalent spins. *Physical Chemistry Chemical Physics*, **13** (13) 5556–5560, 2011.

[141] Y. Feng, R. M. Davis, and W. S. Warren. Accessing long-lived nuclear singlet states between chemically equivalent spins without breaking symmetry. *Nature Physics*, **8** (11) 831–837, 2012.

[142] G. Stevanato, J. T. Hill-Cousins, S. S. Roy, L. J. Brown, R. C. Brown, G. Pileio, and M. H. Levitt. A nuclear singlet lifetime of more than one hour in room-temperature solution. *Angewandte Chemie – International Edition*, **54** (12) 3740–3743, 2015.

[143] K. Schulten and P. G. Wolynes. Semiclassical description of electron spin motion in radicals including the effect of electron hopping. *Journal of Chemical Physics*, **68** (7) 3292–3297, 1978.

[144] D. E. Manolopoulos and P. J. Hore. An improved semiclassical theory of radical pair recombination reactions. *Journal of Chemical Physics*, **139** (12) 124106, 2013.

[145] H. J. Hogben, T. Biskup, and P. J. Hore. Entanglement and sources of magnetic anisotropy in radical pair-based avian magnetoreceptors. *Physical Review Letters*, **109** 220501, 2012.

[146] T. Cubitt. Matlab Code – Partial Trace, 2013.

[147] V. S. Bhaskara and P. K. Panigrahi. Generalized concurrence measure for faithful quantification of multiparticle pure state entanglement using Lagrange's identity and wedge product. *Quantum Information Processing*, **16** (5) 118, 2017.

[148] V. Hou. Spin-dynamics and relaxation in Posner molecules. Master's thesis, University of California, Santa Barbara, 2020.

[149] A. G. Redfield. The theory of relaxation processes. *Advances in Magnetic and Optical Resonance*, **1** 1–32, 1965.

[150] C. P. Slichter. *Principles of Magnetic Resonance*. Springer-Verlag, Berlin, New York, 1978.

[151] M. Goldman. Advances in magnetic resonance: Formal theory of spin-lattice relaxation. *Journal of Magnetic Resonance*, **149** (2) 160–187, 2001.

[152] I. Kuprov, N. Wagner-Rundell, and P. J. Hore. Bloch-Redfield-Wangsness theory engine implementation using symbolic processing software. *Journal of Magnetic Resonance*, **184** (2) 196–206, 2007.

[153] N. Wagner-Rundell. *Electron Spin Relaxation Effects on Radical Recombination Reactions in Weak Magnetic Fields*. PhD thesis, University of Oxford, 2008.

[154] S. Worster, D. R. Kattnig, and P. J. Hore. Spin relaxation of radicals in cryptochrome and its role in avian magnetoreception. *Journal of Chemical Physics*, **145** 035104, 2016.

[155] D. A. Varshalovich, A. Moskalev, and V. K. Khersonskii. *Quantum Theory of Angular Momentum*. World Scientific Publishing, 1988.

[156] J. H. Freed and G. K. Fraenkel. Theory of linewidths in electron spin resonance spectra. *Journal of Chemical Physics*, **39** (2) 326–348, 1963.

[157] H. J. Hogben, P. J. Hore, and I. Kuprov. Multiple decoherence-free states in multi-spin systems. *Journal of Magnetic Resonance*, **211** (2) 217–220, 2011.

[158] H. G. Hiscock, S. Worster, D. R. Kattnig, C. Steers, Y. Jin, D. E. Manolopoulos, H. Mouritsen, and P. J. Hore. The quantum needle of the avian magnetic compass. *Proceedings of the National Academy of Sciences of the United States of America*, **113** (17) 4634–4639, 2016.

[159] D. R. Kattnig, I. A. Solov'yov, and P. J. Hore. Electron spin relaxation in cryptochrome-based magnetoreception. *Physical Chemistry Chemical Physics*, **18** (18) 12443–12456, 2016.

[160] T. P. Fay, L. P. Lindoy, and D. E. Manolopoulos. Electron spin relaxation in radical pairs: Beyond the Redfield approximation. *Journal of Chemical Physics*, **151** (15) 154117, 2019.

[161] T. J. Lin and C. C. Chiu. Structures and infrared spectra of calcium phosphate clusters by ab initio methods with implicit solvation models. *Physical Chemistry Chemical Physics*, **20** (1) 345–356, 2017.

[162] E. Wigner. *Symmetries and Reflections – Scientific Essays of Eugene P. Wigner*. M.I.T. Press, Cambridge, Massachusetts, 1967.

[163] E. P. Wigner. Über die paramagnetische Umwandlung von Para-Orthowasserstoff. III. *Zeitschrift fur Physikalische Chemie B*, **23** 28–32, 1933.

[164] P. S. Hubbard. Theory of nuclear magnetic relaxation by spin-rotational interactions in liquids. *Physical Review*, **131** (3) 1155–1165, 1963.

[165] R. F. Curl, J. V. Kasper, and K. S. Pitzer. Nuclear spin state equilibration through nonmagnetic collisions. *Journal of Chemical Physics*, **46** (8) 3220–3228, 1967.

[166] K. G. Petzinger and D. J. Scalapino. Para- to ortho-hydrogen conversion on magnetic surfaces. *Physical Review B*, **8** (1) 266–279, 1973.

[167] W. Wiltschko and R. Wiltschko. Magnetic compass of European robins. *Science*, **176** (4030) 62–64, 1972.

[168] S. Åkesson, J. Morin, R. Muheim, and U. Ottosson. Avian orientation at steep angles of inclination: Experiments with migratory white-crowned sparrows at the magnetic North Pole. *Proceedings of the Royal Society B: Biological Sciences*, **268** (1479) 1907–1913, 2001.

[169] N. Lefeldt, D. Dreyer, N. L. Schneider, F. Steenken, and H. Mouritsen. Migratory blackcaps tested in Emlen funnels can orient at 85 degrees but not at 88 degrees magnetic inclination. *Journal of Experimental Biology*, **218** (2) 206–211, 2015.

[170] R. Wiltschko, K. Stapput, P. Thalau, and W. Wiltschko. Directional orientation of birds by the magnetic field under different light conditions. *Journal of the Royal Society Interface*, **7** S163–S177, 2010.

[171] J. L. Kirschvink and J. L. Gould. Biogenic magnetite as a basis for magnetic field detection in animals. *BioSystems*, **13** (3) 181–201, 1981.

[172] M. Winklhofer. Magnetoreception. *Journal of the Royal Society Interface*, **7** S131–S134, 2010.

[173] M. Ahmad and A. R. Cashmore. HY4 gene of A. thaliana encodes a protein with characteristics of a blue-light photoreceptor. *Nature*, **366** (6451) 162–166, 1993.

[174] C. A. Dodson, P. J. Hore, and M. I. Wallace. A radical sense of direction: Signalling and mechanism in cryptochrome magnetoreception. *Trends in Biochemical Sciences*, **38** (9) 435–446, 2013.

[175] B. Liu, H. Liu, D. Zhong, and C. Lin. Searching for a photocycle of the cryptochrome photoreceptors. *Current Opinion in Plant Biology*, **13** (5) 578–586, 2010.

[176] D. M. Sheppard, J. Li, K. B. Henbest, S. R. Neil, K. Maeda, J. Storey, E. Schleicher, T. Biskup, R. Rodriguez, S. Weber, P. J. Hore, C. R. Timmel, and S. R. Mackenzie. Millitesla magnetic field effects on the photocycle of an animal cryptochrome. *Scientific Reports*, **7**, 2017.

[177] Y. T. Kao, C. Tan, S. H. Song, N. Öztürk, J. Li, L. Wang, A. Sancar, and D. Zhong. Ultrafast dynamics and anionic active states of the flavin cofactor in cryptochrome and photolyase. *Journal of the American Chemical Society*, **130** (24) 7695–7701, 2008.

[178] P. Müller, J. Yamamoto, R. Martin, S. Iwai, and K. Brettel. Discovery and functional analysis of a 4th electron-transferring tryptophan conserved exclusively in animal cryptochromes and (6-4) photolyases. *Chemical Communications*, **51** (85) 15502–15505, 2015.

[179] D. Nohr, S. Franz, R. Rodriguez, B. Paulus, L. O. Essen, S. Weber, and E. Schleicher. Extended electron-transfer in animal cryptochromes mediated by a tetrad of aromatic amino acids. *Biophysical Journal*, **111** (2) 301–311, 2016.

[180] K. B. Henbest, K. Maeda, P. J. Hore, M. Joshi, A. Bacher, R. Bittl, S. Weber, C. R. Timmel, and E. Schleicher. Magnetic-field effect on the photoactivation reaction of Escherichia coli DNA photolyase. *Proceedings of the National Academy of Sciences of the United States of America*, **105** (38) 14395–14399, 2008.

[181] H. Mouritsen, D. Heyers, and O. Güntürkün. The Neural Basis of Long-Distance Navigation in Birds. *Annual Review of Physiology*, **78** 133–154, 2016.

[182] A. A. Lee, J. C. Lau, H. J. Hogben, T. Biskup, D. R. Kattnig, and P. J. Hore. Alternative radical pairs for cryptochrome-based magnetoreception. *Journal of the Royal Society Interface*, **11** (95) , 2014.

[183] T. Ritz, R. Wiltschko, P. J. Hore, C. T. Rodgers, K. Stapput, P. Thalau, C. R. Timmel, and W. Wiltschko. Magnetic compass of birds is based on a molecule with optimal directional sensitivity. *Biophysical Journal*, **96** (8) 3451–3457, 2009.

[184] S. Schwarze, N. L. Schneider, T. Reichl, D. Dreyer, N. Lefeldt, S. Engels, N. Baker, P. J. Hore, and H. Mouritsen. Weak broadband electromagnetic fields are more disruptive to magnetic compass orientation in a night-migratory songbird (Erithacus rubecula) than strong narrow-band fields. *Frontiers in Behavioral Neuroscience*, **10** 55, 2016.

[185] H. G. Hiscock, H. Mouritsen, D. E. Manolopoulos, and P. J. Hore. Disruption of magnetic compass orientation in migratory birds by radiofrequency electromagnetic fields. *Biophysical Journal*, **113** (7) 1475–1484, 2017.

[186] H. Hiscock. *Long-lived Spin Coherence in Radical Pair Compass Magnetoreception*. PhD thesis, University of Oxford, 2018.

[187] V. Massey. Activation of molecular oxygen by flavins and flavoproteins. *Journal of Biological Chemistry*, **269** (36) 22459–22462, 1994.

[188] L. J. van Wilderen, G. Silkstone, M. Mason, J. J. van Thor, and M. T. Wilson. Kinetic studies on the oxidation of semiquinone and hydroquinone forms of Arabidopsis cryptochrome by molecular oxygen. *FEBS Open Bio*, **5** (1) 885–892, 2015.

[189] C. Nießner, S. Denzau, L. Peichl, W. Wiltschko, and R. Wiltschko. Magnetoreception in birds: I. Immunohistochemical studies concerning the cryptochrome cycle. *Journal of Experimental Biology*, **217** (23) 4221–4224, 2014.

[190] C. Nießner, S. Denzau, L. Peichl, W. Wiltschko, and R. Wiltschko. Magnetoreception: activation of avian cryptochrome 1a in various light conditions. *Journal of Comparative Physiology A: Neuroethology, Sensory, Neural, and Behavioral Physiology*, **204** (12) 977–984, 2018.

[191] R. Wiltschko, M. Ahmad, C. Nießner, D. Gehring, and W. Wiltschko. Light-dependent magnetoreception in birds: The crucial step occurs in the dark. *Journal of the Royal Society Interface*, **13** (118) , 2016.

[192] M. Pooam, L. D. Arthaut, D. Burdick, J. Link, C. F. Martino, and M. Ahmad. Magnetic sensitivity mediated by the Arabidopsis blue-light receptor cryptochrome occurs during flavin reoxidation in the dark. *Planta*, **249** (2) 319–332, 2019.

[193] D. R. Kattnig, J. K. Sowa, I. A. Solov'Yov, and P. J. Hore. Electron spin relaxation can enhance the performance of a cryptochrome-based magnetic compass sensor. *New Journal of Physics*, **18** 063007, 2016.

[194] T. Y. Karogodina, I. G. Dranov, S. V. Sergeeva, D. V. Stass, and U. E. Steiner. Kinetic magnetic-field effect involving the small biologically relevant inorganic radicals NO and $O_2^{\cdot -}$. *ChemPhysChem*, **12** (9) 1714–1728, 2011.

[195] K. Huber and G. Herzberg. *Molecular Spectra and Molecular Structure*. Van Nostrand Reinhold, New York, 1979.

[196] U. E. Steiner and Y. A. Serebrennikov. Adiabatic rotation of effective spin. I. New insight into spin–rotational interaction. *Journal of Chemical Physics*, **100** (10) 7503–7507, 1994.

[197] Y. A. Serebrennikov and U. E. Steiner. Adiabatic rotation of effective spin. II. Spin–rotational relaxation. *Journal of Chemical Physics*, **100** (10) 7508–7514, 1994.

[198] D. R. Kattnig. Radical-pair-based magnetoreception amplified by radical scavenging: Resilience to spin relaxation. *Journal of Physical Chemistry B*, **121** (44) 10215–10227, 2017.

[199] R. J. Usselman, I. Hill, D. J. Singel, and C. F. Martino. Spin biochemistry modulates reactive oxygen species (ROS) production by radio frequency magnetic fields. *PLoS ONE*, **9** (3) e93065, 2014.

[200] R. J. Usselman, C. Chavarriaga, P. R. Castello, M. Procopio, T. Ritz, E. A. Dratz, D. J. Singel, and C. F. Martino. The Quantum Biology of Reactive Oxygen Species Partitioning Impacts Cellular Bioenergetics. *Scientific Reports*, **6** 38543, 2016.

[201] D. R. Kattnig and P. J. Hore. The sensitivity of a radical pair compass magnetoreceptor can be significantly amplified by radical scavengers. *Scientific Reports*, **7** 11640, 2017.

[202] T. Y. Karogodina, S. V. Sergeeva, and D. V. Stass. Magnetic field effect in the reaction of recombination of nitric oxide and superoxide anion. *Applied Magnetic Resonance*, **36** (2-4) 195–208, 2009.

[203] M. C. R. Symons, G. W. Eastland, and L. R. Denny. Effect of solvation on the electron spin resonance spectrum of the superoxide ion. *Journal of the Chemical Society, Faraday Transactions 1: Physical Chemistry in Condensed Phases*, **76** 1868–1874, 1980.

[204] W. Känzig and M. H. Cohen. Paramagnetic resonance of oxygen in alkali halides. *Physical Review Letters*, **3** (11) 509–510, 1959.

[205] F. Cintolesi, T. Ritz, C. W. Kay, C. R. Timmel, and P. J. Hore. Anisotropic recombination of an immobilized photoinduced radical pair in a 50-μT magnetic field: A model avian photomagnetoreceptor. *Chemical Physics*, **294** (3) 385–399, 2003.

[206] L. Korson, W. Drost-Hansen, and F. J. Millero. Viscosity of water at various temperatures. *Journal of Physical Chemistry*, **73** (1) 34–39, 1969.

[207] T. M. Zollitsch, L. E. Jarocha, C. Bialas, K. B. Henbest, G. Kodali, P. L. Dutton, C. C. Moser, C. R. Timmel, P. J. Hore, and S. R. Mackenzie. Magnetically Sensitive Radical Photochemistry of Non-natural Flavoproteins. *Journal of the American Chemical Society*, **140** (28) 8705–8713, 2018.

[208] H. Pan, X. Xiao, B. Hu, Y. Shen, and M. Wang. Generating huge magnetocurrent by using spin-dependent dehydrogenation based on electrochemical system. *Journal of Physical Chemistry C*, **121** (51) 28420–28424, 2017.

[209] H. Pan, M. Wang, Y. Shen, and B. Hu. Large magnetocurrent effect in the electrochemical detection of oxalate in aqueous solution. *Journal of Physical Chemistry C*, **122** (34) 19880–19885, 2018.

[210] X. Jiang, X. Wang, Q. Wang, X. Xiao, J. Chen, M. Wang, and Y. Shen. Efficient Activation and Electroreduction of Carbon Dioxide on an Electrocatalyst Cadmium Carbonate. *ACS Applied Energy Materials*, **4** (3) 2073–2080, 2021.

[211] J. R. Woodward. Radical pairs in solution. *Progress in Reaction Kinetics and Mechanism*, **27** 165–207, 2002.

[212] K. M. Salikhov, Y. N. Molin, R. Z. Sagdeev, and A. L. Buchachenko. *Spin Polarization and Magnetic Field Effects in Radical Reactions*. Elsevier, New York, 1984.

[213] D. Kivelson. Theory of ESR linewidths of free radicals. *Journal of Chemical Physics*, **33** (4) 1094–1106, 1960.

[214] G. Nyberg. Spin–rotational relaxation in solution E.S.R. *Molecular Physics*, **12** (1) 69–81, 1967.

[215] P. W. Atkins and D. Kivelson. ESR linewidths in solution. II. Analysis of spin–rotational relaxation data. *Journal of Chemical Physics*, **44** (1) 169–174, 1966.

[216] A. I. Shushin. The effect of the spin exchange interaction on SNP and RYDMR spectra of geminate radical pairs. *Chemical Physics Letters*, **181** (2-3) 274–278, 1991.

[217] B. Brocklehurst. Magnetic fields and radical reactions: Recent developments and their role in nature. *Chemical Society Reviews*, **31** (5) 301–311, 2002.

[218] A. Lewis. *Spin Dynamics in Radical Pairs*. Springer International Publishing, Cham, 2018.

[219] K. Ishikawa, N. Sumi, A. Kono, H. Horibe, K. Takeda, H. Kondo, M. Sekine, and M. Hori. Synergistic formation of radicals by irradiation with both vacuum ultraviolet and atomic hydrogen: A real-time in situ electron spin resonance study. *Journal of Physical Chemistry Letters*, **2** (11) 1278–1281, 2011.

[220] D. W. Ovenall and D. H. Whiffen. Electron spin resonance and structure of the CO_2^- radical ion. *Molecular Physics*, **4** (2) 135–144, 1961.

[221] A. Carrington and A. D. McLachlan. *Introduction to Magnetic Resonance*. Harper & Row, New York, 1967.

[222] J. H. Lunsford and J. P. Jayne. Formation of CO_2^- radical ions when CO_2 is adsorbed on irradiated magnesium oxide. *Journal of Physical Chemistry*, **69** (7) 2182–2184, 1965.

[223] H. Hayashi and S. Nagakura. Theoretical study of relaxation mechanism in magnetic field effects on chemical reactions. *Bulletin of the Chemical Society of Japan*, **57** (2) 322–328, 1984.

[224] R. Nakagaki, M. Yamaoka, O. Takahira, K. I. Hiruta, Y. Fujiwara, and Y. Tanimoto. Magnetic field and isotope effects on photochemistry of chain-linked compounds containing benzophenone and hydrogen-donor moieties. *Journal of Physical Chemistry A*, **101** (4) 556–560, 1997.

[225] T. Klumpp, M. Linsenmann, S. L. Larson, B. R. Limoges, D. Bürssner, E. B. Krissinel, C. M. Elliott, and U. E. Steiner. Spin chemical control of photoinduced electron-transfer processes in ruthenium(II)-trisbipyridine-based supramolecular triads. *Journal of the American Chemical Society*, **121** (5) 1076–1087, 1999.

[226] H. Hayashi, Y. Sakaguchi, and M. Wakasa. Magnetic field effects and spin dynamics of radical reactions in solution. *Bulletin of the Chemical Society of Japan*, **74** (5) 773–783, 2001.

[227] B. Brocklehurst. Spin correlation in the geminate recombination of radical ions in hydrocarbons. Part 1.—Theory of the magnetic field effect. *J. Chem. Soc., Faraday Trans. 2*, **72** 1869–1884, 1976.

[228] U. Till, C. R. Timmel, B. Brocklehurst, and P. J. Hore. The influence of very small magnetic fields on radical recombination reactions in the limit of slow recombination. *Chemical Physics Letters*, **298** (1-3) 7–14, 1998.

[229] C. R. Timmel, U. Till, B. Brocklehurst, K. A. McLauchlan, and P. J. Hore. Effects of weak magnetic fields on free radical recombination reactions. *Molecular Physics*, **95** (1) 71–89, 1998.

[230] T. Miura, K. Maeda, and T. Arai. The spin mixing process of a radical pair in low magnetic field observed by transient absorption detected nanosecond pulsed magnetic field effect. *Journal of Physical Chemistry A*, **110** (12) 4151–4156, 2006.

[231] H. J. Hogben. *Coherent Spin Dynamics of Radical Pairs in Weak Magnetic Fields*. PhD thesis, University of Oxford, 2011.

[232] A. M. Lewis, T. P. Fay, D. E. Manolopoulos, C. Kerpal, S. Richert, and C. R. Timmel. On the low magnetic field effect in radical pair reactions. *Journal of Chemical Physics*, **149** 034103, 2018.

[233] K. M. Salikhov. *Magnetic Isotope Effect in Radical Reactions*. Springer-Verlag, Vienna, 1996.

[234] I. R. Epstein and J. A. Pojman. *An Introduction to Nonlinear Chemical Dynamics*. Oxford University Press, New York, 1988.

[235] S. de Groot and P. Mazur. *Non-Equilibrium Thermodynamics*. North-Holland, Amsterdam, 1984.

[236] P. Howard. *Modeling Basics*. Texas A&M University, Lecture Notes for Math 442, 2009.

[237] P. Gray and S. K. Scott. *Chemical Oscillations and Instabilities*. Clarendon Press, Oxford, 1990.

[238] D. W. Jordan and P. Smith. *Nonlinear Ordinary Differential Equations – An Introduction for Scientists and Engineers*. Oxford University Press, Oxford, 2007.

[239] D. Hilbert. Mathematical problems. *Bulletin of the American Mathematical Society*, **8** (10) 437–480, 1902.

[240] X. Li, J. Hou, and Y. Shen. Slow-fast effect and generation mechanism of Brusselator based on coordinate transformation. *Open Physics*, **14** (1) 261–268, 2016.

[241] B. Peng, V. Gáspár, and K. Showalter. False bifurcations in chemical systems: canards. *Philosophical Transactions of the Royal Society of London. Series A: Physical and Engineering Sciences*, **337** (1646) 275–289, 1991.

[242] Y. A. Kuznetsov. *Elements of Applied Bifurcation Theory*. Springer, New York, 1998.

[243] P. Szmolyan and M. Wechselberger. Canards in $\mathbb{R}3$. *Journal of Differential Equations*, **177** (2) 419–453, 2001.

[244] T. Erneux. Early models of chemical oscillations failed to provide bounded solutions. *Philosophical Transactions of the Royal Society A: Mathematical, Physical and Engineering Sciences*, **376** (2124) 20170380, 2018.

[245] S. M. Baer and T. Erneux. Singular Hopf bifurcation to relaxation oscillations. *SIAM Journal on Applied Mathematics*, **46** (5) , 1986.

[246] S. K. Scott and A. S. Tomlin. Period doubling and other complex bifurcations in non-isothermal chemical systems. *Philosophical Transactions of the Royal Society of London. Series A: Physical and Engineering Sciences*, **332** (1624) 51–68, 1990.

[247] M. Brøns and K. Bar-Eli. Canard explosion and excitation in a model of the Belousov-Zhabotinsky reaction. *Journal of Physical Chemistry*, **95** (22) 8706–8713, 1991.

[248] S. Allatt. Magnetic Field Effects and Chemical Feedback. Part II thesis, University of Oxford, 2000.

[249] E. D. A. Baxter. Magnetic Field Effects on Oscillating Reactions. Part II thesis, University of Oxford, 2001.

[250] É. Matzinger. Asymptotic behaviour of solutions near a turning point: The example of the Brusselator equation. *Journal of Differential Equations*, **220** (2) 478–510, 2006.

[251] B. W. Qin, K. W. Chung, A. Algaba, and A. J. Rodríguez-Luis. High-order analysis of canard explosion in the brusselator equations. *International Journal of Bifurcation and Chaos*, **30** (5) 2050078, 2020.

[252] S. M. Baer and T. Erneux. Singular Hopf Bifurcation to Relaxation Oscillations. II. *SIAM Journal on Applied Mathematics*, **52** (6) 1651–1664, 1992.

[253] M. Desroches, J. Guckenheimer, B. Krauskop, C. Kuehn, H. M. Osinga, and M. Wechselberger. Mixed-mode oscillations with multiple time scales. *SIAM Review*, **54** (2) 211–288, 2012.

[254] G. Nicolis. *Introduction to Nonlinear Science*. Cambridge University Press, Cambridge, 1995.

[255] A. R. Jones. Magnetic field effects in proteins. *Molecular Physics*, **114** (11) 1691–1702, 2016.

[256] P. J. Hore. Are biochemical reactions affected by weak magnetic fields? *Proceedings of the National Academy of Sciences of the United States of America*, **109** (5) 1357–1358, 2012.

[257] D. R. Kattnig, E. W. Evans, V. Déjean, C. A. Dodson, M. I. Wallace, S. R. Mackenzie, C. R. Timmel, and P. J. Hore. Chemical amplification of magnetic field effects relevant to avian magnetoreception. *Nature Chemistry*, **8** (4) 384–391, 2016.

[258] J. Juutilainen, M. Herrala, J. Luukkonen, J. Naarala, and P. J. Hore. Magnetocarcinogenesis: Is there a mechanism for carcinogenic effects of weak magnetic fields? *Proceedings of the Royal Society B: Biological Sciences*, **285** 20180590, 2018.

[259] P. Hore. Upper bound on the biological effects of 50/60 Hz magnetic fields mediated by radical pairs. *eLife*, **8** e44179, 2019.

[260] B. Brocklehurst and K. A. McLauchlan. Free radical mechanism for the effects of environmental electromagnetic fields on biological systems. *International Journal of Radiation Biology*, **69** (1) 3–24, 1996.

[261] J. Swanson and L. Kheifets. Biophysical mechanisms: a component in the weight of evidence for health effects of power-frequency electric and magnetic fields. *Radiation Research*, **165** (4) 470–478, 2006.

[262] M. J. Crumpton and A. R. Collins. Are environmental electromagnetic fields genotoxic? *DNA Repair*, **3** (10) 1385–1387, 2004.

[263] M. J. Crumpton. The Bernal Lecture 2004: Are low-frequency electromagnetic fields a health hazard? *Philosophical Transactions of the Royal Society B: Biological Sciences*, **360** (1458) 1223–1230, 2005.

[264] C. Eichwald and J. Walleczek. Low-frequency-dependent effects of oscillating magnetic fields on radical pair recombination in enzyme kinetics. *Journal of Chemical Physics*, **107** (13) 4943–4950, 1997.

[265] D. S. Simakov and J. Pérez-Mercader. Noise induced oscillations and coherence resonance in a generic model of the nonisothermal chemical oscillator. *Scientific Reports*, **3** 2404, 2013.

[266] H. S. Lawson, G. Holló, R. Horvath, H. Kitahata, and I. Lagzi. Chemical resonance, beats, and frequency locking in forced chemical oscillatory systems. *Journal of Physical Chemistry Letters*, **11** (8) 3014–3019, 2020.

[267] A. C. Møller and L. F. Olsen. Effect of magnetic fields on an oscillating enzyme reaction. *Journal of the American Chemical Society*, **121** (27) 6351–6354, 1999.

[268] A. C. Møller, A. Lunding, and L. F. Olsen. Further studies of the effect of magnetic fields on the oscillating peroxidase-oxidase reaction. *Physical Chemistry Chemical Physics*, **2** (15) 3443–3446, 2000.

[269] A. C. Møller and L. F. Olsen. Perturbations of simple oscillations and complex dynamics in the peroxidase-oxidase reaction using magnetic fields. *Journal of Physical Chemistry B*, **104** 140–146, 2000.

[270] C. Eichwald and J. Walleczek. Magnetic field perturbations as a tool for controlling enzyme-regulated and oscillatory biochemical reactions. *Biophysical Chemistry*, **74** (3) 209–224, 1998.

[271] R. Glaser and M. Jost. Disproportionation of bromous acid HOBrO by direct o-tOansfer and via anhydrides $O(BrO)_2$ and $BrO–BrO_2$. An ab initio study of the mechanism of a key step of the Belousov–Zhabotinsky oscillating reaction. *Journal of Physical Chemistry A*, **116** (32) 8352–8365, 2012.

[272] H. Okano, H. Kitahata, D. Akai, and N. Tomita. The influence of a gradient static magnetic field on an unstirred Belousov–Zhabotinsky reaction. *Bioelectromagnetics*, **29** (8) 598–604, 2008.

[273] H. Okano, H. Kitahata, and D. Akai. Effect of a gradient static magnetic field on an unstirred Belousov–Zhabotinsky reaction by changing the thickness of the medium. *Journal of Physical Chemistry A*, **113** (13) 3061–3067, 2009.

[274] H. Okano and H. Kitahata. Modulation of the shape and speed of a chemical wave in an unstirred Belousov–Zhabotinsky reaction by a rotating magnet. *Bioelectromagnetics*, **34** (3) 220–230, 2013.

[275] R. Nishikiori, S. Morimoto, Y. Fujiwara, and Y. Tanimoto. Effect of vertical magnetic field on the chemical wave propagation speed in Belousov–Zhabotinsky reaction. *Chemistry Letters*, **39** 394–395, 2010.

[276] R. Nishikiori, S. Morimoto, Y. Fujiwara, A. Katsuki, R. Morgunov, and Y. Tanimoto. Magnetic field effect on chemical wave propagation from the Belousov–Zhabotinsky reaction. *Journal of Physical Chemistry A*, **115** (18) 4592–4597, 2011.

[277] E. Boga, S. Kádár, G. Peintler, and I. Nagypál. Effect of magnetic fields on a propagating reaction front. *Nature*, **347** (6295) 749–751, 1990.

[278] H. Xiaoying, K. Kustin, I. Nagypál, and G. Peintler. A family of magnetic field dependent chemical waves. *Inorganic Chemistry*, **33** (10) 2077–2078, 1994.

[279] R. Evans, C. R. Timmel, P. J. Hore, and M. M. Britton. Magnetic resonance imaging of a magnetic field-dependent chemical wave. *Chemical Physics Letters*, **397** 67–72, 2004.

[280] R. Evans, C. R. Timmel, P. J. Hore, and M. M. Britton. Magnetic resonance imaging of the manipulation of a chemical wave using an inhomogeneous magnetic field. *Journal of the American Chemical Society*, **128** (22) 7309–7314, 2006.

[281] M. Blank and L. Soo. Electromagnetic acceleration of the Belousov-Zhabotinski reaction. *Bioelectrochemistry*, **61** 93–97, 2003.

[282] W. Sontag. Low frequency electromagnetic fields and the Belousov–Zhabotinsky reaction. *Bioelectromagnetics*, **27** (4) 314–319, 2006.

[283] R. Evans. *The Effect of Magnetic Fields on Autocatalytic Chemical Reactions*. PhD thesis, University of Oxford, 2007.

[284] H. J. Hogben, M. Krzystyniak, G. T. Charnock, P. J. Hore, and I. Kuprov. Spinach – A software library for simulation of spin dynamics in large spin systems. *Journal of Magnetic Resonance*, **208** (2) 179–194, 2011.

[285] C. Bengs and M. H. Levitt. SpinDynamica: Symbolic and numerical magnetic resonance in a Mathematica environment. *Magnetic Resonance in Chemistry*, **56** (6) 374–414, 2018.

[286] C. Nielsen and I. A. Solov'yov. MolSpin – Flexible and extensible general spin dynamics software. *Journal of Chemical Physics*, **151** (19) 194105, 2019.

[287] EasySpin. Nuclear isotope database, 2021.

[288] M. J. Frisch, G. W. Trucks, H. B. Schlegel, G. E. Scuseria, M. A. Robb, J. R. Cheeseman, G. Scalmani, V. Barone, B. Mennucci, G. A. Petersson, H. Nakatsuji, M. Caricato, X. Li, H. P. Hratchian, A. F. Izmaylov, J. Bloino, G. Zheng, J. L. Sonnenberg, M. Hada, M. Ehara, K. Toyota, R. Fukuda, J. Hasegawa, M. Ishida, T. Nakajima, Y. Honda, O. Kitao, H. Nakai, T. Vreven, J. Montgomery, J. A., J. E. Peralta, F. Ogliaro, M. Bearpark, J. J. Heyd, E. Brothers, K. N. Kudin, V. N. Staroverov, R. Kobayashi, J. Normand, K. Raghavachari, A. Rendell, J. C. Burant, S. S. Iyengar, J. Tomasi, M. Cossi, N. Rega, J. M. Millam, M. Klene, J. E. Knox, J. B. Cross, V. Bakken, C. Adamo, J. Jaramillo, R. Gomperts, R. E. Stratmann, O. Yazyev, A. J. Austin, R. Cammi, C. Pomelli, J. W. Ochterski, R. L. Martin, K. Morokuma, V. G. Zakrzewski, G. A. Voth, P. Salvador, J. J. Dannenberg, S. Dapprich, A. D. Daniels, Ö. Farkas, J. B. Foresman, J. V. Ortiz, J. Cioslowski, and D. J. Fox. Gaussian 09, 2016.

A Selected nuclear isotopes

	I	Z	g_N	abundance / %
^{1}H	1/2	2	+5.586	99.99
^{2}H	1	3	+0.857	0.0115
^{6}Li	1	3	+0.822	7.59
^{7}Li	3/2	4	+2.171	92.41
^{12}C	0	1	0.0	98.93
^{13}C	1/2	2	+1.405	1.07
^{14}N	1	3	+0.404	99.63
^{15}N	1/2	2	−0.566	0.37
^{16}O	0	1	0.0	99.76
^{17}O	5/2	6	−0.758	0.038
^{31}P	1/2	2	+2.263	100.0
^{40}Ca	0	1	0.0	96.94
^{43}Ca	7/2	8	−0.376	0.14

Table A.1 Selected nuclear isotopes with their spin quantum number, degeneracy, nuclear g-factor, and natural abundance [287].

B Atomic coordinates for Posner's cluster

Table B.1 shows the DFT optimized atomic coordinates of an S_6 Posner molecule. These were obtained by optimizing the geometry for a Posner molecule with S_6 symmetry from [133] in Gaussian 09 [288] using density functional theory (DFT). The Ahlrich triple-zeta basis set def2-TZVPP was used in combination with the BP86 functional. The DFT work was performed by Daniel Kattnig (now at the Living Systems Institute, University of Exeter, UK).

Table B.1 DFT optimized atomic coordinates, in Å, for Posner's molecule with S_6 symmetry. Numbering of the phosphorus nuclei is as in Fig. 3.3.

		x	y	z
1	O	−0.9344	+3.8163	+1.4609
2	Ca	−2.7835	+2.0443	+0.7842
3	O	−1.7198	+2.5381	−1.1499
4	Ca	+0.3786	+3.4328	−0.7842
5	O	−3.7722	+1.0989	−1.4609
6	P(1)	+0.0000	+2.6944	+2.0654
7	P(5)	−2.3334	+1.3472	−2.0654
8	O	−1.9765	+1.4995	−3.5593
9	O	+0.3104	+2.4615	+3.5593
10	O	+1.3382	+2.7585	+1.1499
11	O	−0.8317	+1.3528	+1.6409
12	O	+2.8378	+2.7174	−1.4609
13	O	−3.0580	−0.2203	+1.1499
14	O	+0.7557	+1.3966	−1.6409
15	O	−1.5874	−0.0439	−1.6409
16	P(4)	+2.3334	+1.3472	−2.0654
17	Ca	−3.1622	−1.3885	−0.7842
18	O	−2.2869	−0.9619	+3.5593
19	Ca	+0.0000	+0.0000	−3.4214
20	Ca	+0.0000	+0.0000	+0.0000
21	Ca	+0.0000	+0.0000	+3.4214
22	O	+2.2869	+0.9619	−3.5593
23	Ca	+3.1622	+1.3885	+0.7842
24	P(3)	−2.3334	−1.3472	+2.0654
25	O	+1.5874	+0.0439	+1.6409
26	O	−0.7557	−1.3966	+1.6409
27	O	+3.0580	+0.2203	−1.1499
28	O	−2.8378	−2.7174	+1.4609
29	O	+0.8317	−1.3528	−1.6409
30	O	−1.3382	−2.7585	−1.1499
31	O	−0.3104	−2.4615	−3.5593
32	O	+1.9765	−1.4995	+3.5593
33	P(2)	+2.3334	−1.3472	+2.0654
34	P(6)	+0.0000	−2.6944	−2.0654
35	O	+3.7722	−1.0989	+1.4609
36	Ca	−0.3786	−3.4328	+0.7842
37	O	+1.7198	−2.5381	+1.1499
38	Ca	+2.7835	−2.0443	−0.7842
39	O	+0.9344	−3.8163	−1.4609

C Additional singlet yield anisotropy plots for $O_2^{\bullet -}$ radical pair

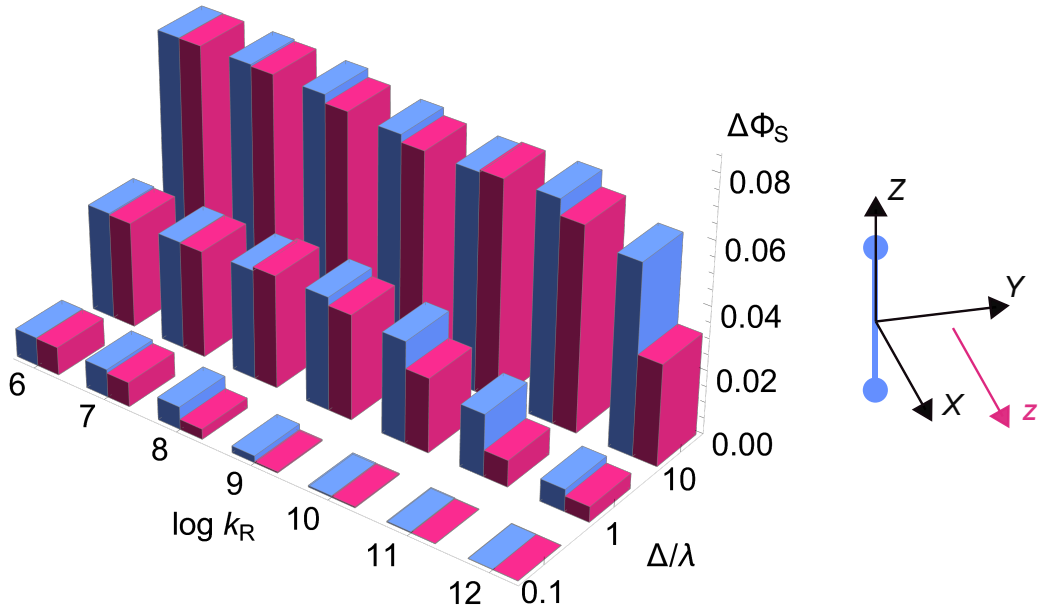

Figure C.1 X-orientation. The singlet yield anisotropy $\Delta\Phi_S$, plotted as a function of the rocking rate constant, k_R, and the ratio of the ligand field splitting, Δ, to the spin–orbit coupling, λ, for a [$FAD^{\bullet -}O_2^{\bullet -}$] radical pair. The $FAD^{\bullet -}$ radical is oriented such that its z-axis is aligned with the X-axis (see Fig. 4.3). The angle through which the superoxide rocks was set at either $\beta = 2°$ (blue) or $\beta = 5°$ (pink).

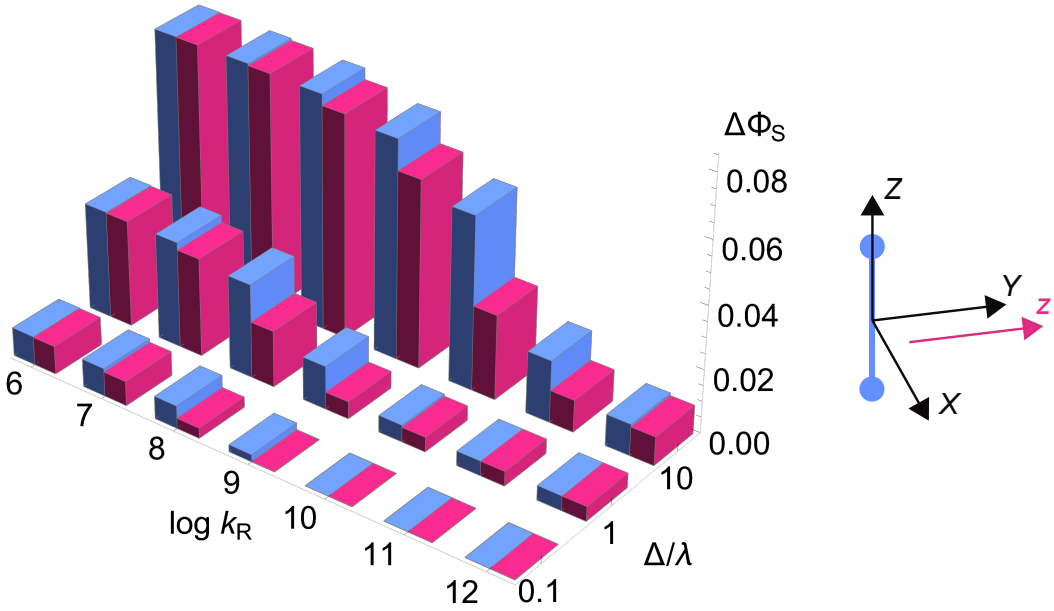

Figure C.2 Y-orientation. The singlet yield anisotropy $\Delta\Phi_S$, plotted as a function of the rocking rate constant, k_R, and the ratio of the ligand field splitting, Δ, to the spin–orbit coupling, λ, for a [$FAD^{\bullet-}O_2^{\bullet-}$] radical pair. The $FAD^{\bullet-}$ radical is oriented such that its z-axis is aligned with the Y-axis (see Fig. 4.3). The angle through which the superoxide rocks was set at either $\beta = 2°$ (blue) or $\beta = 5°$ (pink).

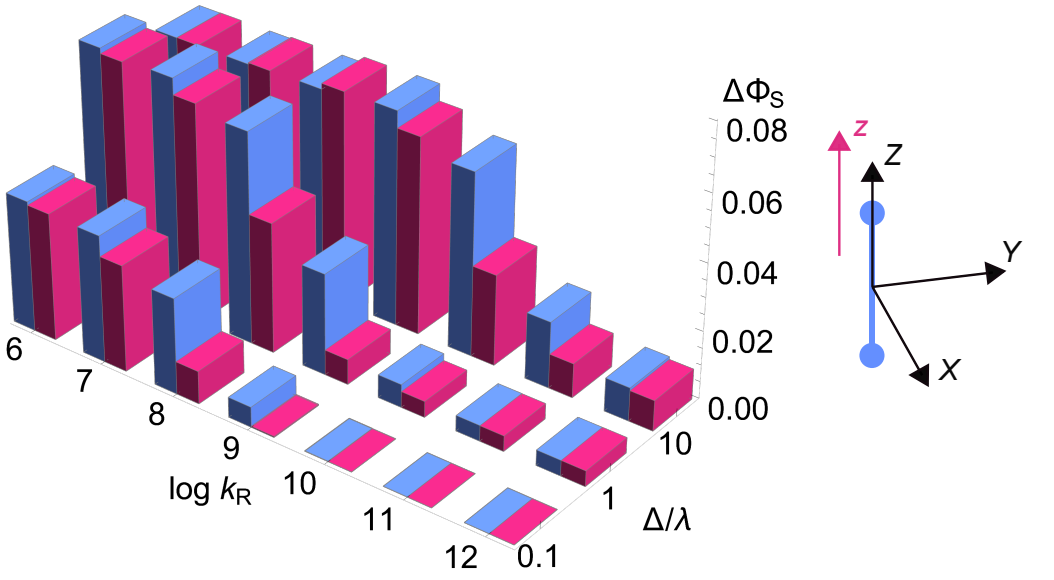

Figure C.3 Z-orientation. The singlet yield anisotropy $\Delta\Phi_S$, plotted as a function of the rocking rate constant, k_R, and the ratio of the ligand field splitting, Δ, to the spin–orbit coupling, λ, for a [$FAD^{\bullet-}O_2^{\bullet-}$] radical pair. The $FAD^{\bullet-}$ radical is oriented such that its z-axis is aligned with the Z-axis (see Fig. 4.3). The angle through which the superoxide rocks was set at either $\beta = 2°$ (blue) or $\beta = 5°$ (pink).

D Additional MFE curves for CO_2 radical pair

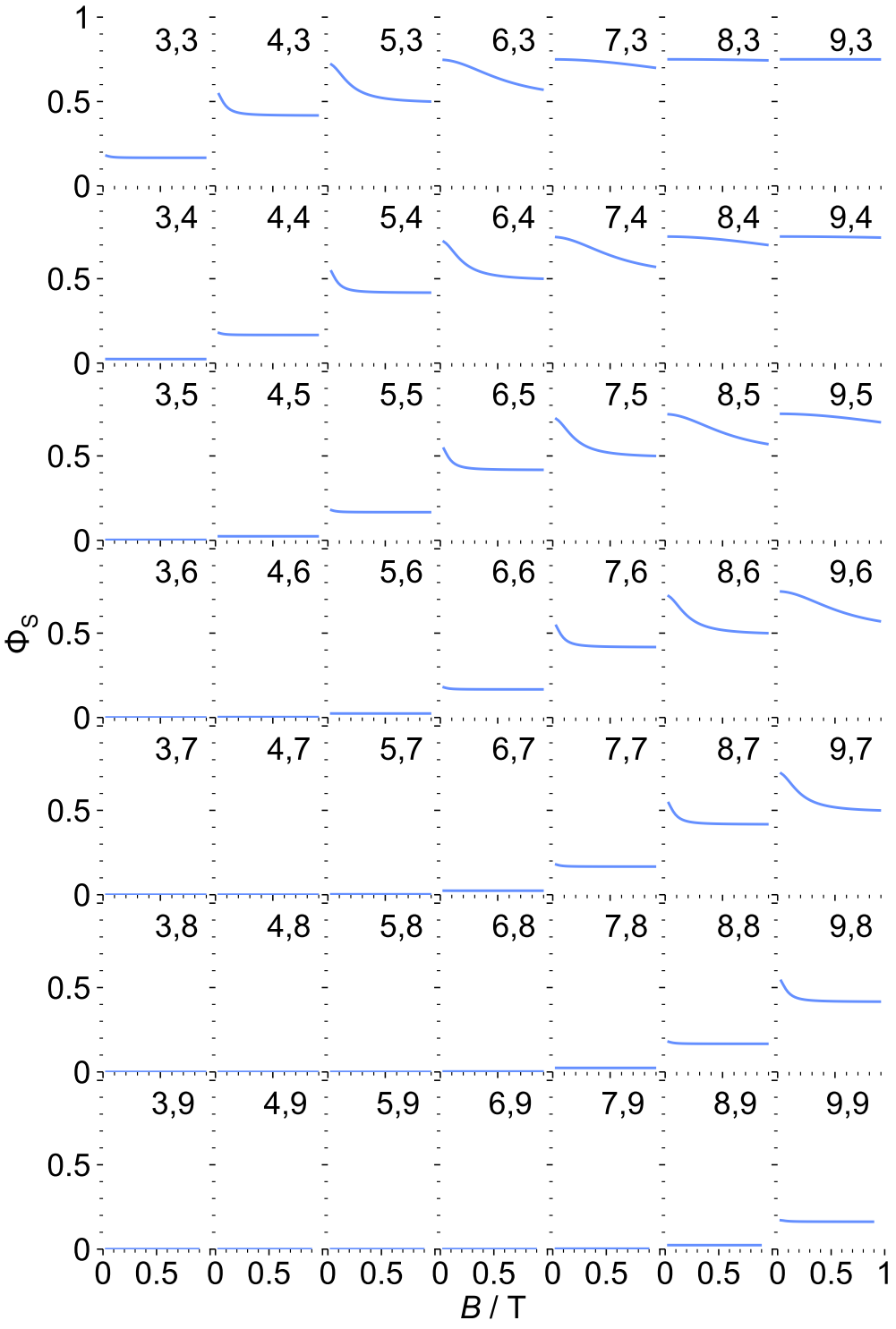

Figure D.1 Δg and hyperfine mechanisms together. Calculated MFEs on the $H^{\bullet} + CO_2^{\bullet-}$ reaction showing Φ_S as a function of B for $0.03\,\mathrm{T} < B < 0.9\,\mathrm{T}$. $\Delta g = 0.0107$, $a_H = 50.74\,\mathrm{mT}$, and no spin relaxation. Each panel is labelled with the values of the two rate constants: $\log_{10} k_S, \log_{10} k_D$.

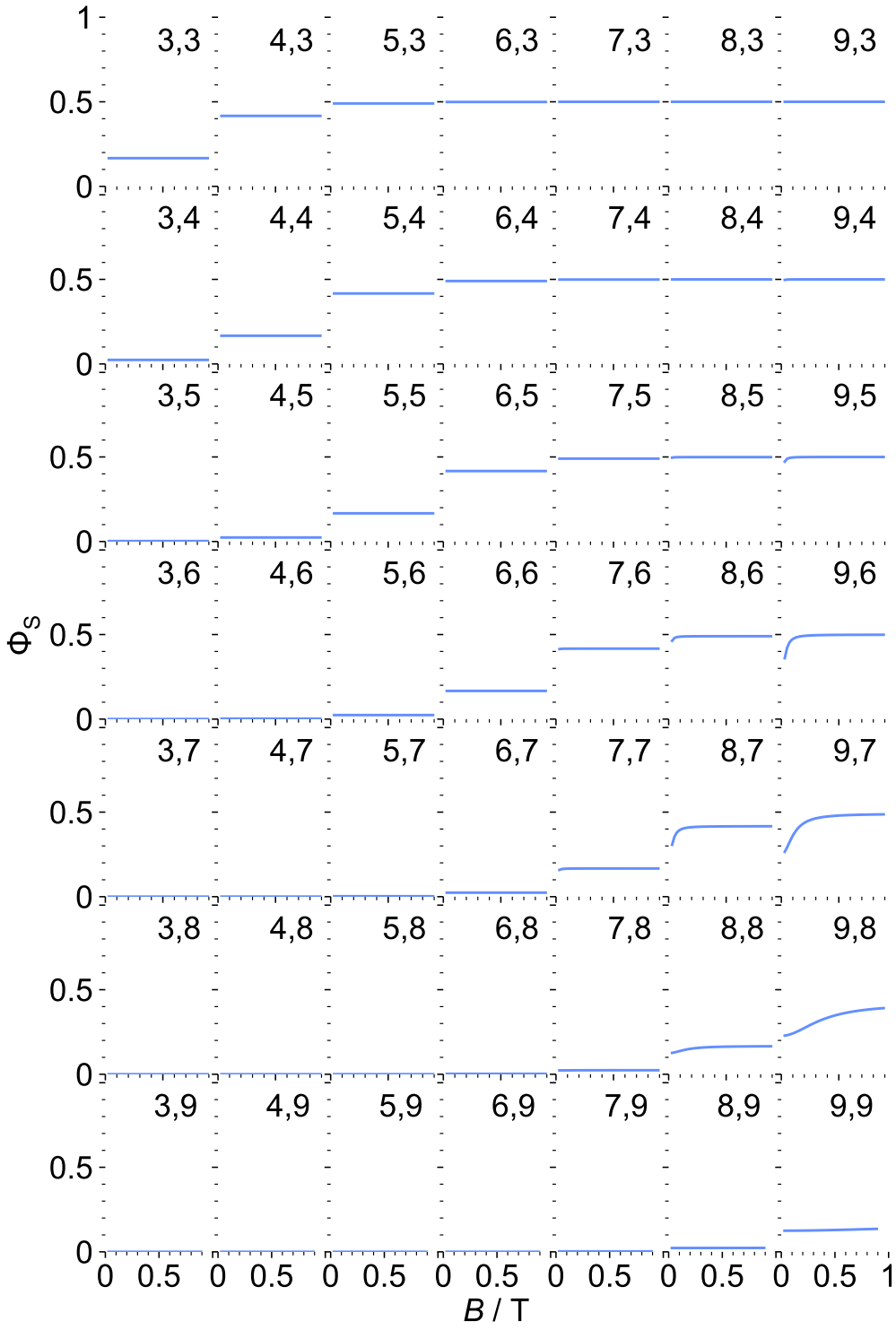

Figure D.2 Δg mechanism alone. Calculated MFEs on the $H^{\bullet} + CO_2^{\bullet -}$ reaction showing Φ_S as a function of B for $0.03\,\mathrm{T} < B < 0.9\,\mathrm{T}$. $\Delta g = 0.0107$, $a_H = 0$, and no spin relaxation. Each panel is labelled with the values of the two rate constants: $\log_{10} k_S$, $\log_{10} k_D$.

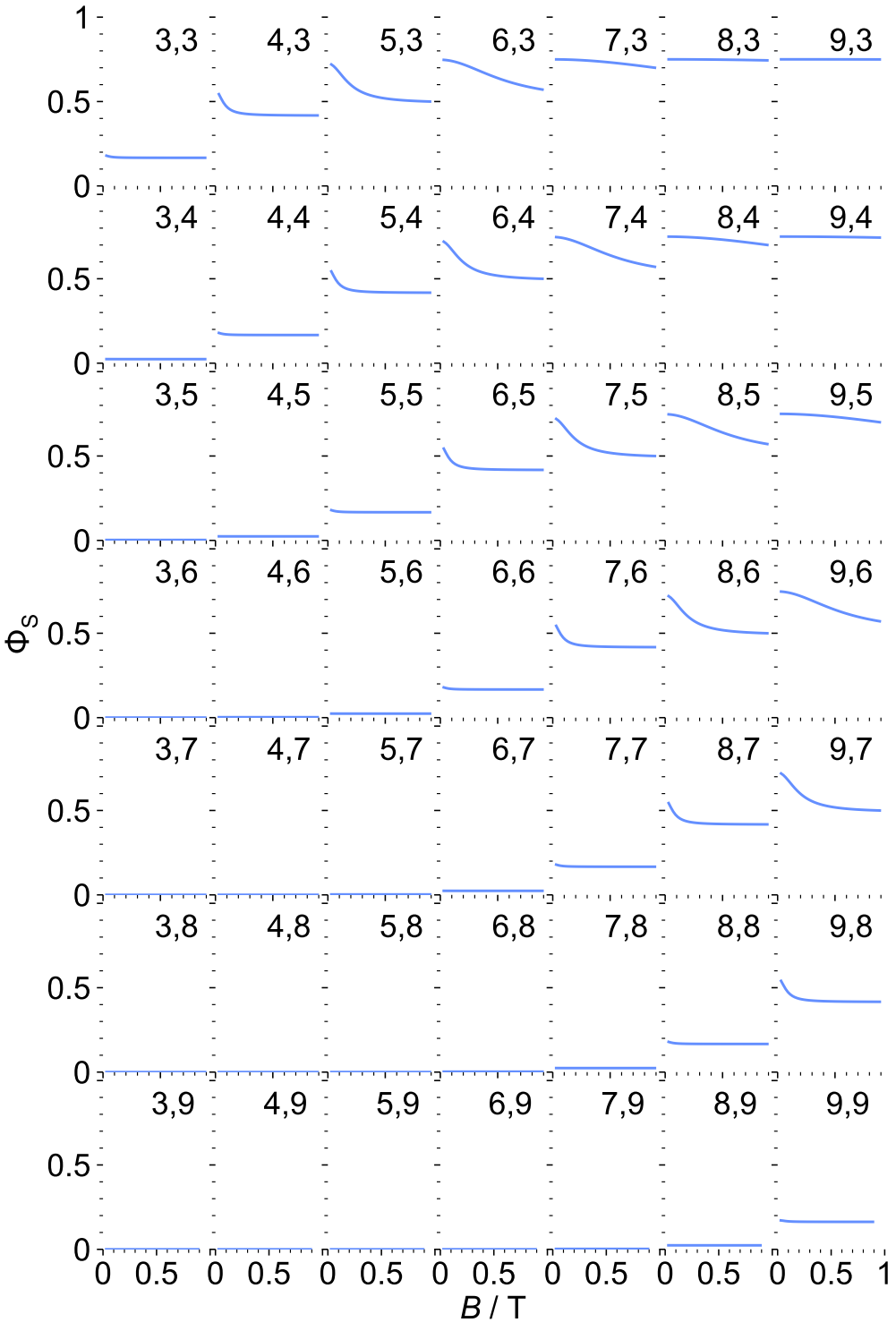

Figure D.3 Hyperfine mechanism alone. Calculated MFEs on the $H^{\bullet}$ + $CO_2^{\bullet-}$ reaction showing Φ_S as a function of B for $0.03\,\mathrm{T} < B < 0.9\,\mathrm{T}$. $\Delta g = 0$, $a_H = 50.74\,\mathrm{mT}$, and no spin relaxation. Each panel is labelled with the values of the two rate constants: $\log_{10} k_S, \log_{10} k_D$.

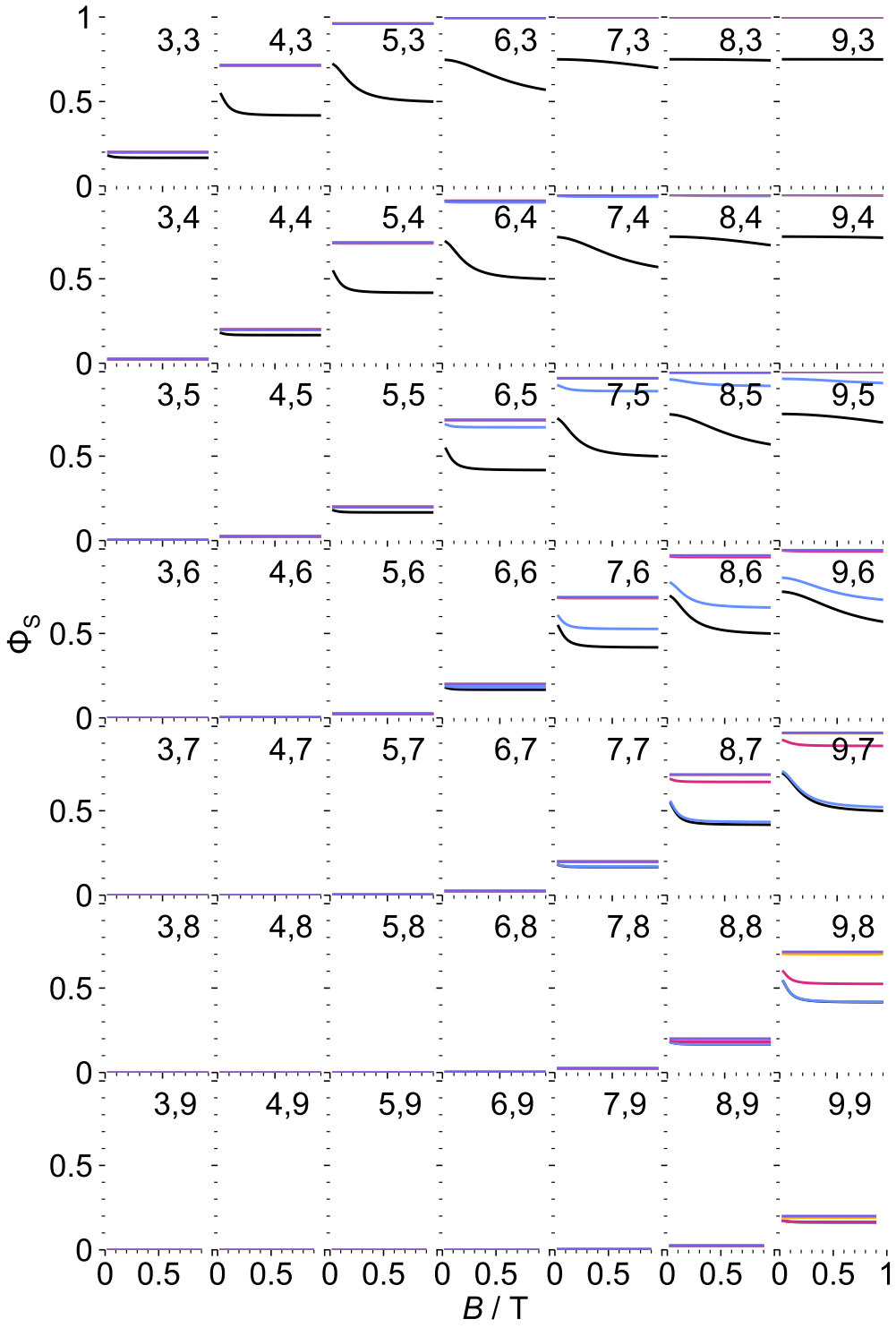

Figure D.4 Random fields relaxation mechanism. Calculated MFEs on the $H^{\bullet}$ + $CO_2^{\bullet-}$ reaction showing Φ_S as a function of B for 0.03 T < B < 0.9 T. Δg = 0.0107, a_H = 50.74 mT, and including random fields spin relaxation. The relaxation rate constants k_{RF} are 0 (black line), 10^6 s^{-1} (blue), 10^8 s^{-1} (pink), 10^{10} s^{-1} (yellow), and 10^{12} s^{-1} (purple), and each panel is labelled with the values of the two rate constants: $\log_{10} k_S$, $\log_{10} k_D$.

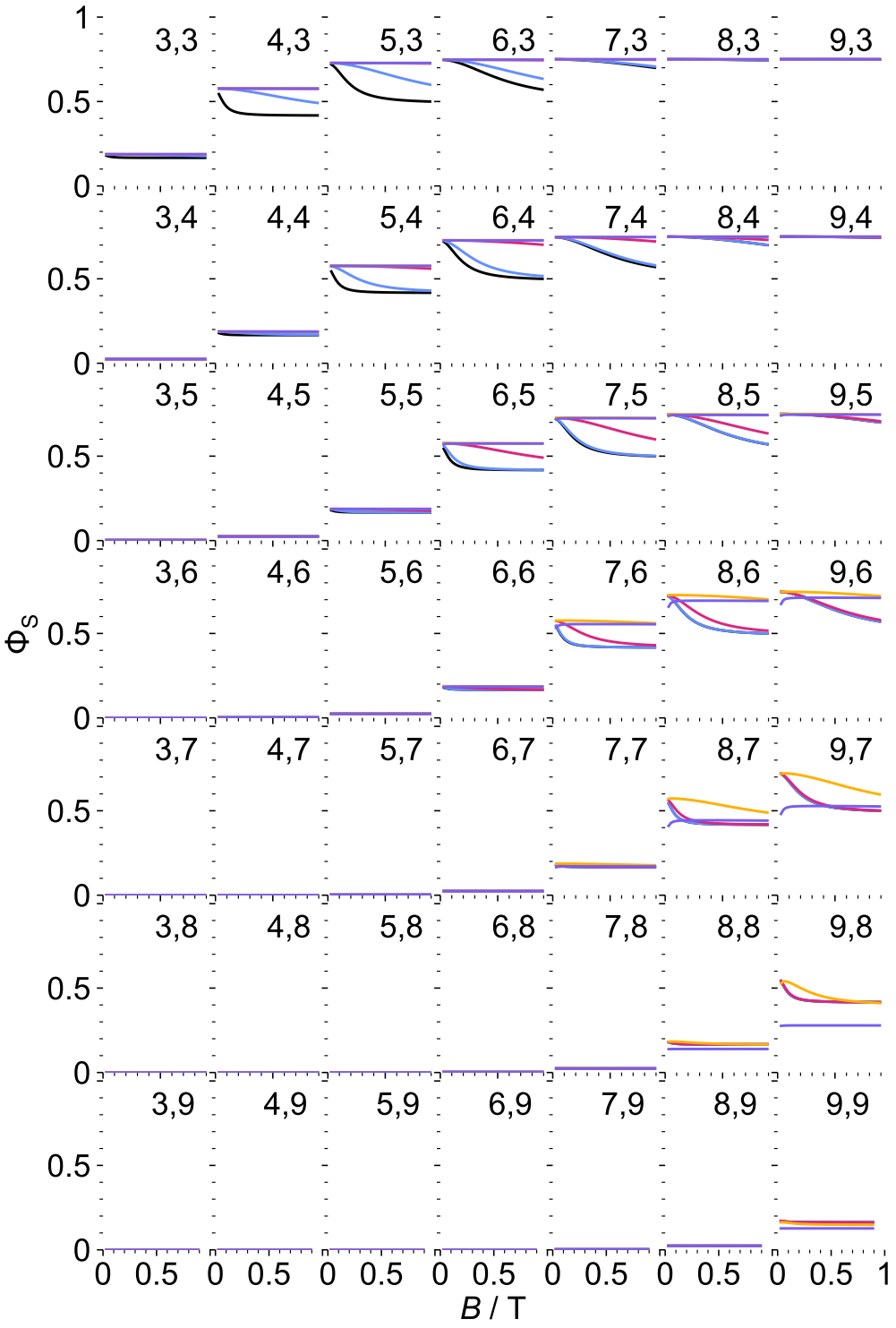

Figure D.5 Singlet–triplet dephasing relaxation mechanism. Calculated MFEs on the $H^\bullet + CO_2^{\bullet-}$ reaction showing Φ_S as a function of B for 0.03 T < B < 0.9 T. $\Delta g = 0.0107$, a_H = 50.74 mT, and including Singlet–triplet dephasing. The relaxation rate constants k_{ST} are 0 (black line), $10^6\,s^{-1}$ (blue), $10^8\,s^{-1}$ (pink), $10^{10}\,s^{-1}$ (yellow), and $10^{12}\,s^{-1}$ (purple), and each panel is labelled with the values of the two rate constants: $\log_{10} k_S, \log_{10} k_D$.

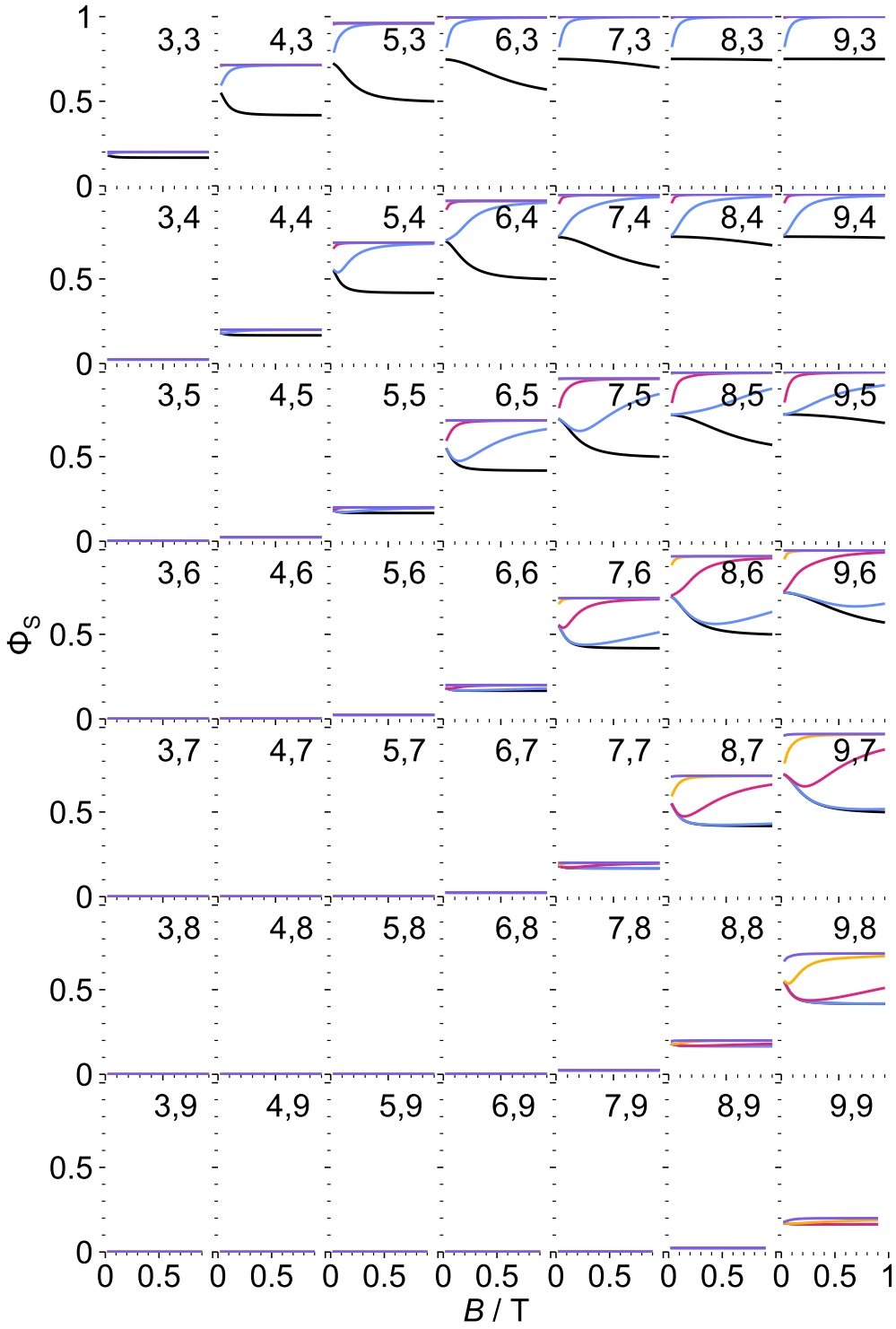

Figure D.6 Field-dependent random fields relaxation mechanism. Calculated MFEs on the $H^{\bullet}$ + $CO_2^{\bullet-}$ reaction showing Φ_S as a function of B for $0.03\,T < B < 0.9\,T$. Δg = 0.0107, a_H = 50.74 mT, and including random fields spin relaxation. The relaxation rate constants $k_{RF} = qB^2$ where q is a proportionality constant that we allowed to vary between $10^6\,T^{-2}\,s^{-1}$ and $10^{12}\,T^{-2}\,s^{-1}$. The values of q shown are 0 (i.e. no relaxation, black line), $10^6\,T^{-2}\,s^{-1}$ (blue), $10^8\,T^{-2}\,s^{-1}$ (pink), $10^{10}\,T^{-2}\,s^{-1}$ (yellow), and $10^{12}\,T^{-2}\,s^{-1}$ (purple), and each panel is labelled with the values of the two rate constants: $\log_{10} k_S, \log_{10} k_D$.

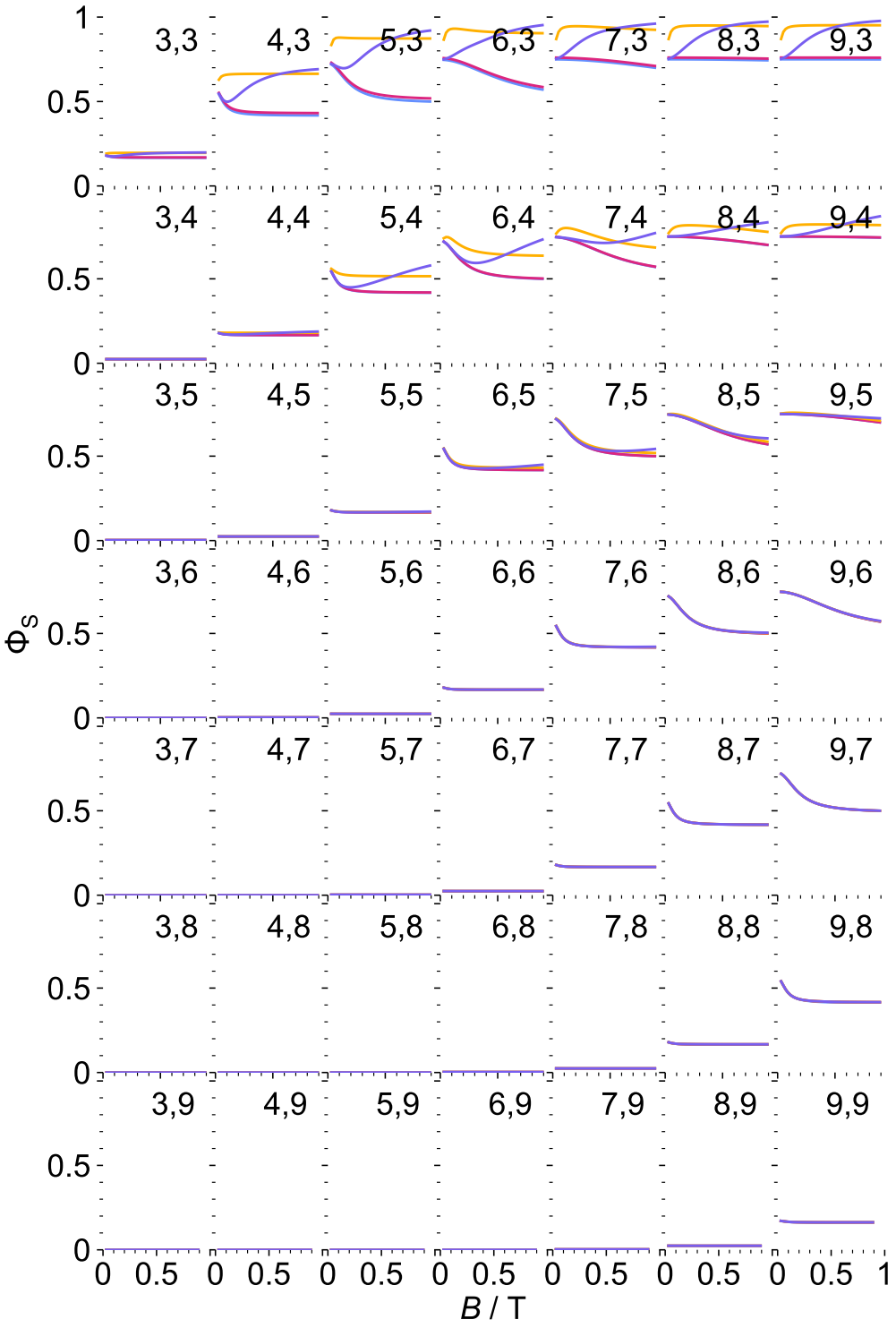

Figure D.7 g-tensor anisotropy relaxation mechanism. Calculated MFEs on the $H^\bullet$ + $CO_2^{\bullet-}$ reaction showing Φ_S as a function of B for $0.03\,T < B < 0.9\,T$. $\Delta g = 0.0107$, $a_H = 50.74\,mT$, and including g-tensor anisotropy relaxation. The rotational correlation time τ_c was taken to be 10^{-6} s (blue), 10^{-8} s (pink), and 10^{-10} s (yellow), and 10^{-12} s (purple), and each panel is labelled with the values of the two rate constants: $\log_{10} k_S, \log_{10} k_D$.

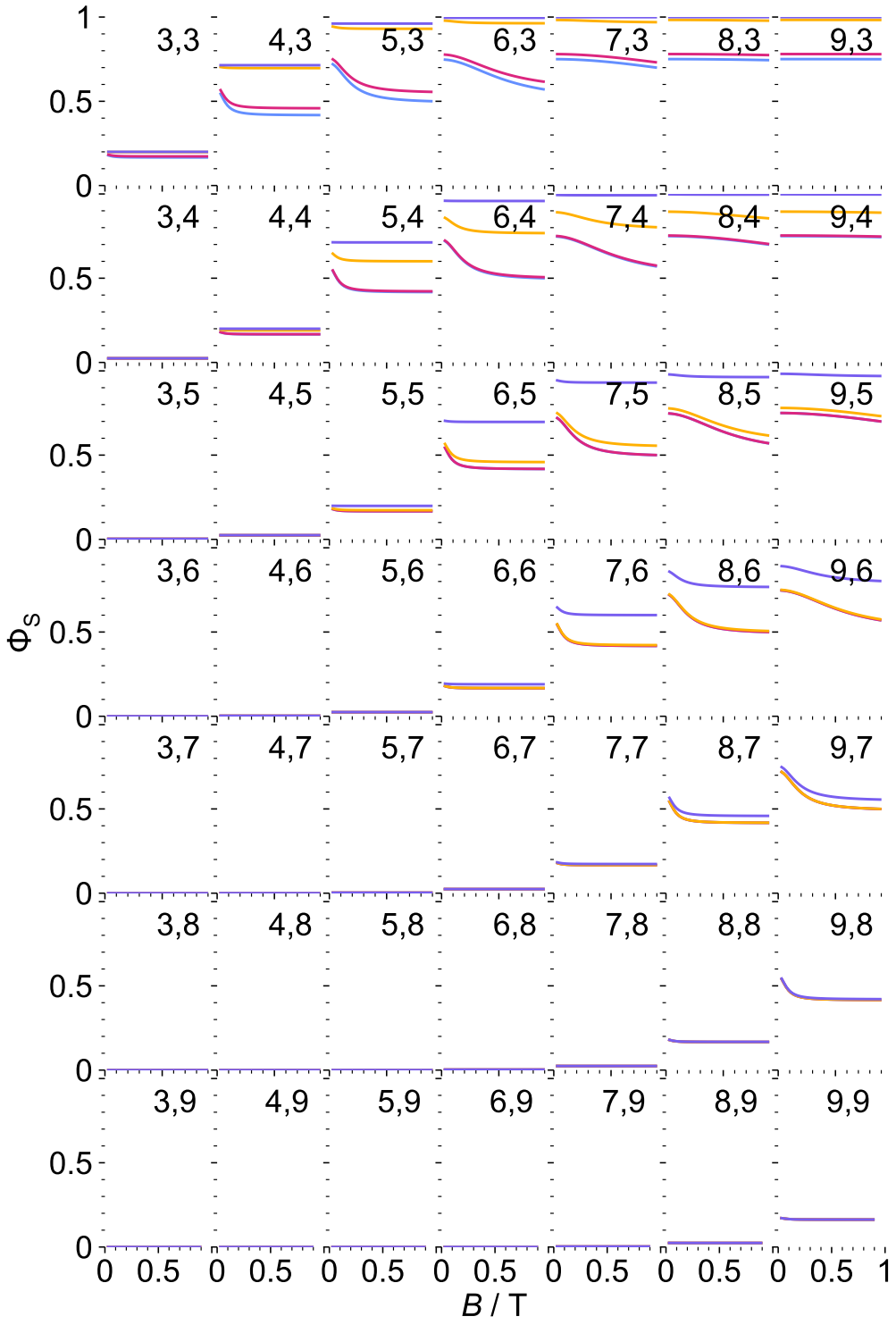

Figure D.8 Spin–rotation relaxation mechanism. Calculated MFEs on the $H^{\bullet}$ + $CO_2^{\bullet-}$ reaction showing Φ_S as a function of B for 0.03 T < B < 0.9 T. $\Delta g = 0.0107$, $a_H = 50.74$ mT, and including spin–rotation relaxation. The rotational correlation time τ_c was taken to be 10^{-6} s (blue), 10^{-8} s (pink), and 10^{-10} s (yellow), and 10^{-12} s (purple), and each panel is labelled with the values of the two rate constants: $\log_{10} k_S$, $\log_{10} k_D$.

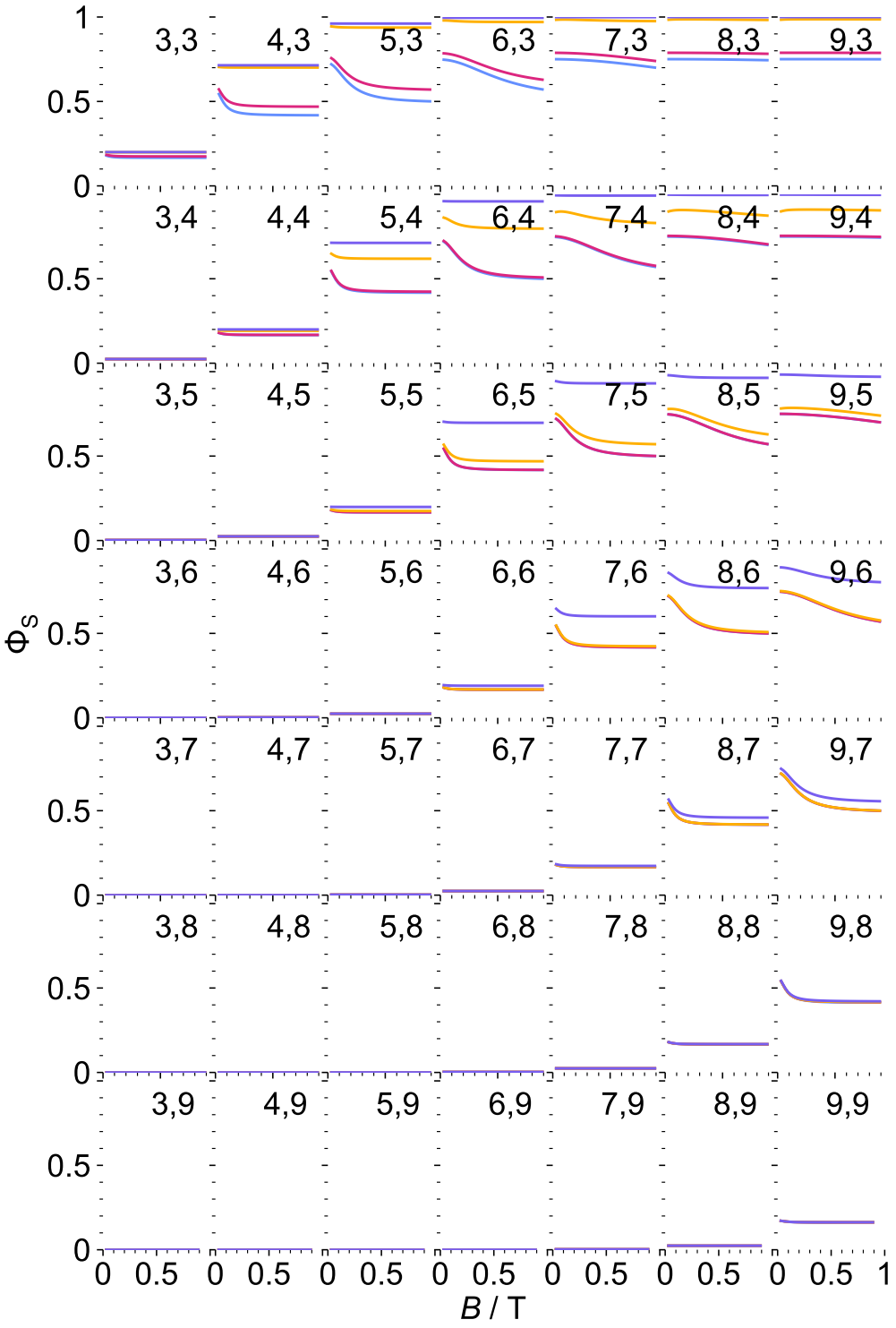

Figure D.9 Spin–rotation and g-tensor anisotropy relaxation mechanisms. Calculated MFEs on the $H^{\bullet} + CO_2^{\bullet-}$ reaction showing Φ_S as a function of B for $0.03\,\mathrm{T} < B < 0.9\,\mathrm{T}$. $\Delta g = 0.0107$, $a_H = 50.74\,\mathrm{mT}$, and including both spin–rotation and g-tensor anisotropy relaxation. The rotational correlation time τ_c was taken to be 10^{-6} s (blue), 10^{-8} s (pink), and 10^{-10} s (yellow), and 10^{-12} s (purple), and each panel is labelled with the values of the two rate constants: $\log_{10} k_S$, $\log_{10} k_D$.